**FLEXIBLE TWIST FOR PITCH CONTROL IN A HIGH
ALTITUDE LONG ENDURANCE AIRCRAFT WITH
NONLINEAR RESPONSE**

DISSERTATION

Vanessa L. Bond, Lt Col, USAF

AFIT/DS/ENY/08-D11

**DEPARTMENT OF THE AIR FORCE
AIR UNIVERSITY**

AIR FORCE INSTITUTE OF TECHNOLOGY

Wright-Patterson Air Force Base, Ohio

AFIT/DS/ENY/08-D11

FLEXIBLE TWIST FOR PITCH CONTROL IN A HIGH ALTITUDE LONG
ENDURANCE AIRCRAFT WITH NONLINEAR RESPONSE

DISSERTATION

Presented to the Faculty

Graduate School of Engineering and Management

Air Force Institute of Technology

Air University

Air Education and Training Command

in Partial Fulfillment of the Requirements for the

Degree of Doctor of Philosophy

Vanessa L. Bond

Lieutenant Colonel, USAF

December 2008

AFIT/DS/ENY/08-D11

FLEXIBLE TWIST FOR PITCH CONTROL IN A HIGH ALTITUDE LONG
ENDURANCE AIRCRAFT WITH NONLINEAR RESPONSE

Vanessa L. Bond
Lieutenant Colonel, USAF

Approved:

Date

_____//SIGNED//_____   __24 Nov 08_
Dr. Robert A. Canfield (Chairman)

_____//SIGNED//_____   __24 Nov 08_
Dr. Donald L. Kunz (Member)

_____//SIGNED//_____   __25 Nov 08_
Dr. James W. Chrissis (Member)

_____1lUKȚ P GF 1l"_____   ""7'F ge'2:___
M. U. THOMAS
Dean, Graduate School of Engineering
and Management

Abstract

Information dominance is the key motivator for employing high-altitude long-endurance (HALE) aircraft to provide continuous coverage in the theaters of operation. A joined-wing configuration of such a craft gives the advantage of a platform for higher resolution sensors. Design challenges emerge with structural flexibility that arise from a long-endurance aircraft design.

The goal of this research was to demonstrate that scaling the nonlinear response of a full-scale finite element model was possible if the model was aeroelastically and "nonlinearly" scaled. The research within this dissertation showed that using the first three modes and the first bucking modes was not sufficient for proper scaling.

In addition to analytical scaling several experiments were accomplished to understand and overcome design challenges of HALE aircraft. One such challenge is combated by eliminating pitch control surfaces and replacing them with an aft-wing twist concept. This design option was physically realized through wind tunnel measurement of forces, moments and pressures on a subscale experimental model. This design and experiment demonstrated that pitch control with aft-wing twist is feasible.

Another challenge is predicting the nonlinear response of long-endurance aircraft. This was addressed by experimental validation of modeling nonlinear response on a subscale experimental model. It is important to be able to scale nonlinear behavior in this type of craft due to its highly flexible nature. The validation accomplished during this experiment on a subscale model will reduce technical risk for full-scale development of

such pioneering craft. It is also important to experimentally reproduce the air loads following the wing as it deforms. Nonlinearities can be attributed to these follower forces that might otherwise be overlooked. This was found to be a significant influence in HALE aircraft to include the case study of the FEM and experimental models herein.

To Mother, Father, Husband and baby-to-be

Acknowledgements

I would like to express my sincere appreciation to my faculty advisor, Prof. Robert Canfield, for his guidance, support and encouragement throughout the course of this dissertation effort. In addition, I would like to thank my committee members, Prof. Donald Kunz and Prof. James Chrissis for their dedicated support and insights.

I am also greatly indebted to my sponsor at AFRL Vehicles Directorate, Dr. Maxwell Blair, whose ideas and conceptions, along with Prof. Canfield, were the foundation of this research.

Two international professors were instrumental in the planning and executing of the experimental portions of this dissertation, Prof. Afzul Suleman and Prof. Jonathan Cooper. Their professional expertise and experience in the specialty and in the laboratory were irreplaceable.

In addition to the academic acknowledgements, the hands-on fabrication and experimentation skills from students, professors and manufacturing professionals at the Portuguese Air Force Academy and the University of Manchester made this endeavor possible: Dr. Pedro Pereira, Dr. Gareth Vio, Mr. Simon Miller, Mr. Richard Gardner, Capt. Maria de Luz Madruga Santos Matos, Capt. José Costa, Mr. Paul Townsend, Mr. William Storey, Mr. Ross Holmes, Mr. Robert Wroe, Mr. Paul Nedwell, and Mr. Gordon Lester.

Lastly, I would like to acknowledge the academic help and support from two of my fellow students, Lt Col Vincent Chioma and Major Timothy Jorris. Their continued support and encouragement made my time at AFIT even more rewarding.

Table of Contents

List of Figures

List of Tables

Nomenclature

α = angle-of-attack

δ_e = angle of elevator deflection

ε = angle between chord and tangential line of pressure port, error

ϕ = remainder mode

ϕ_b = buckling mode

θ = angle of twist, pitch (with subscript)

λ = eigenvalue

μ = viscosity, aeroelastic mass

ρ_∞ = air density

ρ = structural density (with subscript)

σ = stress

ω = frequency

Φ = truncated modal matrix

Φ_{all} = modal matrix

Φ_R = remainder modal matrix

AIC = aerodynamic influence coefficient

AFIT = Air Force Institute of Technology

AFRL = Air Force Research Laboratory

b = wing semi-chord, wing semi-span (with subscript)

B = second derivative of the shape function matrix

c = chord

$C_{L(roll)}$ = rolling coefficient of moment

C_M = pitching coefficient of moment

C_{Lt} = coefficient of lift of the tail

C_{Mo} = coefficient of moment at zero lift

C_{Mcg} = coefficient of moment at the center of gravity

C_N = yawing coefficient of moment

CAD = computer-aided design

CFD = computational fluid dynamics

d = elemental deflections

D = drag, global deflections

ds = surface distance between pressure port

E = Elastic Modulus, constitutive matrix

F_a = aerodynamic forces vector

F_N = normal force

F_T = tangential force

F_x = X component of the resultant pressure force acting on the vehicle

F_z = Z component of the resultant pressure force acting on the vehicle

FEM = finite element model

g = aerodynamic damping

h = plunge

h_{dim} = aerodynamic forces scale factor

H = aerodynamic transfer function

HALE = high-altitude long-endurance
I = moment of inertia
ISR = intelligence, surveillance and reconnaissance
k = reduced frequency
k_{dim} = stiffness scale factor
K = stiffness matrix
K_G = geometric stiffness matrix
L = lift, length (with subscript)
L/D = lift-to-drag ratio
M = mass matrix, mass primary quantity (with subscript)
m_{dim} = mass scale factor
m_{stru} = structural mass per unit length
M_x = X component of moment acting on the vehicle
M_y = Y component of the moment acting on the vehicle
M_z = Z component of the moment acting on the vehicle
MAC = mean aerodynamic chord
K = stiffness matrix
OML = outer mold line
Q = aerodynamic forces matrix
R = reference load
Re = Reynolds number
np = number of pressure ports
q = truncated generalized coordinate
q_B = buckling coordinate
q_∞ = dynamic pressure
q_R = remainder generalized coordinate
p = total pressure, non-dimensional frequency
s = frequency in the Laplace domain
S_{mod} = wing area for the model
t = time
T = transformation matrix
τ = non-dimensionalized time
V = velocity
x = physical coordinate

Subscripts

w = pertaining to the aircraft (wing)
m = pertaining to the wind tunnel model

Superscripts

$(\cdot)$ = generalized non-dimensional matrix, vector

$\overline{(\cdot)}$ = mixed-dimensional matrix, vector

$\overline{\overline{(\cdot)}}$ =   uniform-dimensional matrix, vector

$\widetilde{(\cdot)}$ =   non-dimensional matrix, vector

FLEXIBLE TWIST FOR PITCH CONTROL IN A HIGH ALTITUDE LONG

ENDURANCE AIRCRAFT WITH NONLINEAR RESPONSE

1. Introduction

1.1 <u>Motivation</u>

Information superiority is a key capability in achieving the technological mission of the U.S. Air Force: past, present and future [1]. Today's Air Force must fight smarter, maximizing the delivered effect on the enemy while minimizing its own losses and eliminating collateral damage. This increased requirement for information dominance and support of precision engagements is a key motivator for the Intelligence, Surveillance and Reconnaissance (ISR) role in the 21st century. Employing unmanned aerial vehicles, like the Global Hawk and Predator, with ISR capabilities has already proven the worth of this technology, while at the same time, highlighting the need for increased capability. Future high-altitude long-endurance (HALE) aircraft need to provide continuous coverage of entire theaters of operation. New high-density sensors will provide higher resolution data with fewer constraints, penetrating dense foliage to "see" enemy tanks under trees, for example. Research and development of key enabling technologies is essential in order to bring these new capabilities to the user as soon as possible.
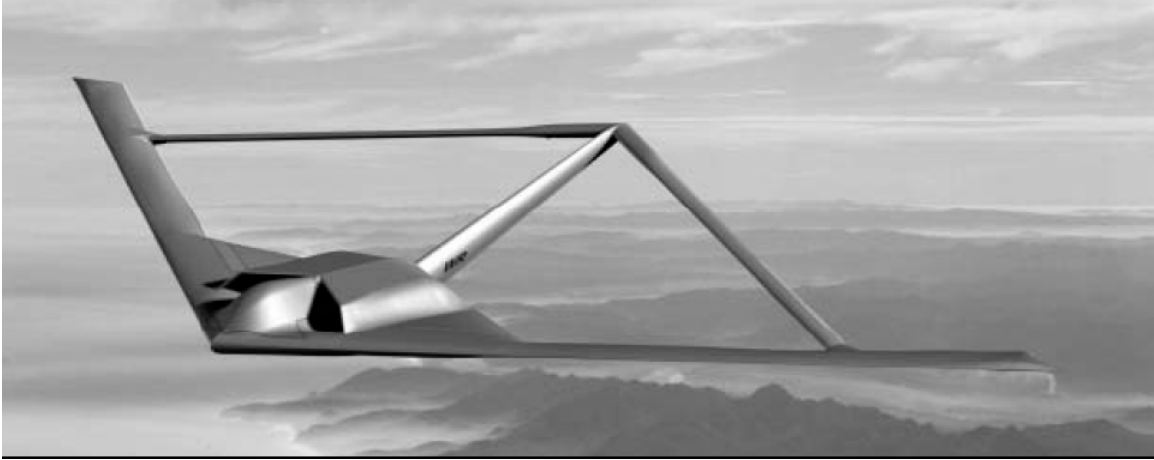
Figure 1-1. Boeing Joined-Wing Sensorcraft [2].

One design philosophy that combines the HALE mission with more capable sensors requires the use of very high aspect ratio wings. These wings contain more fuel for increased endurance and can support large-aperture, embedded antennae in the wing skins for increased sensor performance. With a twistable wing, the metal hardware associated with control surfaces could be eliminated, thus not encumbering the sensor transmissions. Very high-aspect ratio wings also pose some serious design challenges. Overall reduced strength and stiffness can result in large deformations in flight, and large variation in weight due to fuel expenditure can result in constantly changing trim requirements throughout the mission profile. One area of interest which addresses some of these characteristics of HALE aircraft is being able to actively control the shape of the wing, reducing or eliminating standard control surfaces. This allows greater flexibility in structural design of the wing, and reduces interference with sensor placement. The research within this dissertation and future experimental validation are key enablers to fully realize the mission capabilities of next-generation ISR platforms.

One of several design philosophies for the next-generation of ISR platforms with longer missions and higher density sensors is the Joined-Wing Sensorcraft (Figure 1-1). A joined-wing aircraft is one that connects a front wing and an aft wing. The research within this dissertation used a specific joined-wing design to demonstrate pitch trim concepts. The sponsors of the research within this dissertation chose the Boeing Aircraft Company's Sensorcraft design as a case study to help reduce technical risk to the US Air Force Research Lab (AFRL) Sensorcraft program. As Figure 1-1 depicts, it has a forward-swept aft wing that is joined to an aft-swept fore wing to form a diamond-shaped planform from the front and top views. The forward and aft wings lie in a plane tilted from horizontal, and the aft wings are connected to the fuselage by a boom. The full-scale design is comprised of several composite materials; of note is the Conformal Load Bearing Antenna Structure (CLAS) material. It is made of Astroquartz, a material transparent to the sensors, a honeycomb core material and graphite epoxy.

The Joined-Wing Sensorcraft is unique in two major areas. First, it is an aircraft built around its sensors, that is, the sensors are built into the composite skin. In order to maximize the useable wing surface area for the sensors, and avoid interference with the sensors, control surfaces should be minimized or eliminated. The second unique aspect of this design is provided by the joined-wing configuration. Minimizing the control surfaces takes advantage of the Wolkovitch effect of the joined-wing configuration [3]. Unlike a conventional planform, wing bending acts in the plane connecting the fore and aft wings. To resist this bending the wing box structure must maintain a forward spar as far forward and aft spar as far aft as possible (see Figure 1-2). Therefore, conventional control surfaces should be avoided, since the beneficial feature of maximizing the

distance between forward and rear spars leaves little room for leading and trailing edge control surfaces. Additionally, eliminating control surfaces minimizes interference with the sensor array, resulting in a more effective system. To achieve longitudinal trim the composite wing was subjected to flexible aft-wing twist. The aft-wing twist for pitch control was enabled by modifying the aft wing to be torsionally compliant. This was accomplished by removing sections of the ribs and skin such that the shape of the airfoil was held when a coupled force or moment is applied at the aft-wing root. This created a twist in the aft wing with less force required. This twist allows the aft wing to behave like an elevator control surface to control pitch.

Flexibility in the sensor array due to HALE aircraft deformation can be compensated, per previous studies. Thus, the aft-wing twist will not interfere with the sensor capability [4]. Initial experiments [5] were conducted to determine whether the twisted aft wing could produce the forces and moments required for pitch control. Research and experimentation included aeroelastic scaling of a twisted aft-wing model, measurement of the aerodynamic response, and experimental validation of preliminary nonlinear joined-wing design analyses [6, 7, 8, 9]. These were each intended to be scaled from the same full-scale case study. However, due to the stiff nature of the as-delivered model, some modifications and simplifications were necessary while maintaining the objective of the basic research of this dissertation.
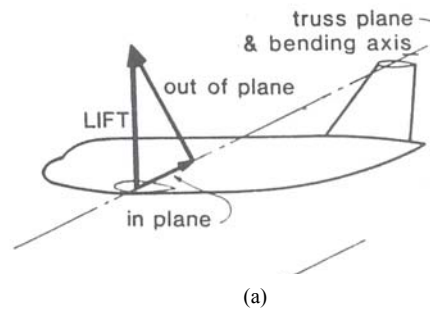
Fig. 5   Tilted bending axis of a joine
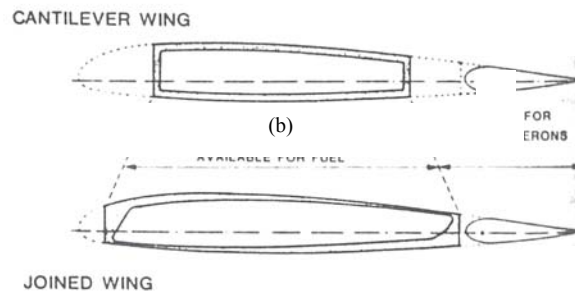
Fig. 6   Optimum wing structures.

Figure 1-2. (a) Tilted bending plane of a joined wing and (b) Optimum wing structures [3].

1.2   Problem Statement

In previous studies [6, 7, 8, 9] an initial assumption was made that pitch control was feasible utilizing flexible wing twist.   The research within this dissertation demonstrates this assumption to be true. Joined-wing designs have not gone forward due to the added risk of structural nonlinearities found during preliminary designs [6,10].   If these nonlinearities could be validated on a subscale FEM and experimental model, significant risk could be mitigated before investing in a full-scale aircraft.   Thus, an endeavor was made to scale nonlinear response for unconventional designs to confirm preliminary analyses of predicted nonlinear response, using the Boeing Joined-Wing Sensorcraft as the case study [6, 7, 8, 9, 10].   This work provides empirical proof for

5

concepts like aft-wing twist for longitudinal control in the linear regime and scaled static response in the nonlinear regime during critical phases of flight of the mission profile. This reduces risk to joined-wing designs by validating the preliminary nonlinear analyses. Scaled experimental models were used to tie in longitudinal control and nonlinearity by measuring forces, moments and pressures on an aerodynamically scaled model and measuring deformation of a static nonlinear response model using follower force load application. Both experimental models were derivatives of the case-study FEM, the Boeing Joined-Wing Sensorcraft. Thus far, reduced scale models for joined-wing aircraft had been tested only with conventional control surfaces, conventional (non-following) static loads, and small deflections [11, 12].

The following problem statement summarizes the objectives of the research in this dissertation:

> Incorporate flexible twist for pitch control in the design of a high altitude long-endurance aircraft, including consideration of nonlinear response, and experimentally validate feasibility.

Due to the nature of the case study there was some disassociation of models used throughout the research in this dissertation. The initial intent was to start with the same model to demonstrate pitch control and nonlinear response both computationally and experimentally. Although these concepts were thoroughly explored, different models were scaled. Within this document the full-scale finite element models are scaled in various ways to demonstrate different parts of the problem statement.

In order to demonstrate nonlinear response on an aeroelastically scaled model a simple model was used—a Goland wing [13] modified to include a strut like a joined wing. In this case it was convenient to use a simple finite element model in order to

demonstrate aeroelastic scaling, which takes into account non-dimensionally scaling mass, length and time, with the added constraint of scaling stiffness, and geometric nonlinearities. This was applied to two experimental models. One validated aerodynamic loads associated with twisting aft wing for pitch control and the other demonstrated nonlinear response. The original (Boeing) case study model was too stiff with no evidence of a nonlinear response. Thus, the model had to be modified in order to be able to exhibit a usable response for the purpose of the research within this dissertation.

The objectives of the research were accomplished by performing the following tasks (Figure 1-3 through Figure 1-5):

1. Demonstrate nonlinear response on an aeroelastically scaled model.
2. Determine aerodynamic forces such that pitch control is realizable.
3. Experimentally validate nonlinear response on a scaled model.

How these tasks were accomplished is discussed in Chapters 4-6.
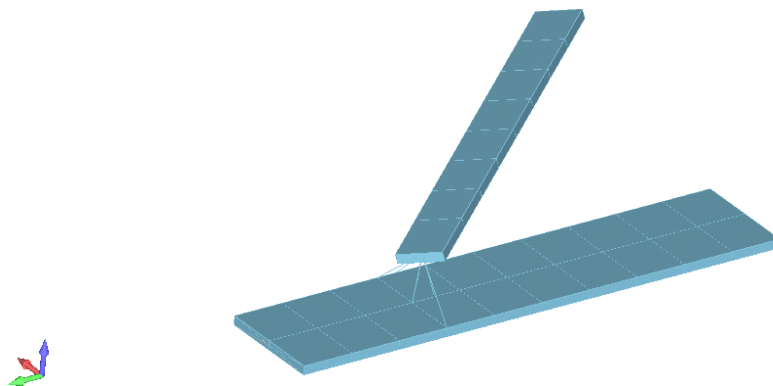
Figure 1-3. Task 1: Demonstrate nonlinear response on a reduced scale model.
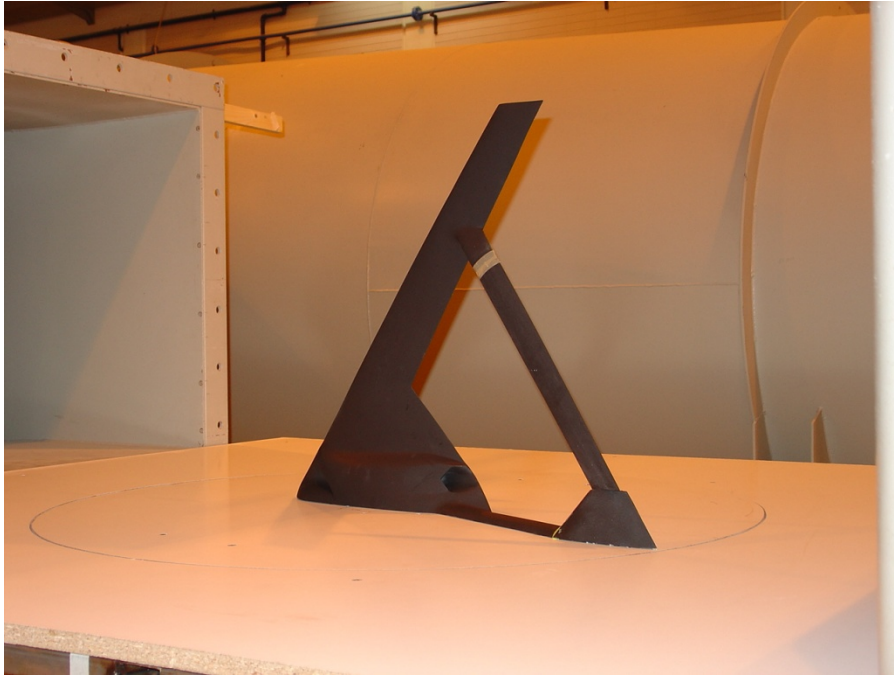
Figure 1-4. Task 2: Determine aerodynamic forces such that pitch control is realizable.
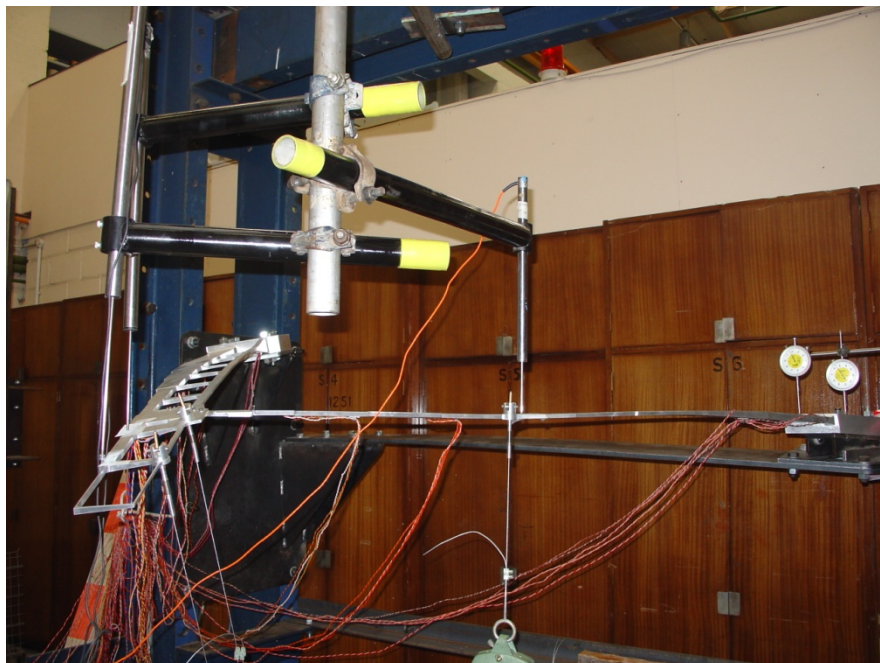
Figure 1-5. Task 3: Experimentally validate nonlinear response on a reduced scale model.

1.3 Overview of Present Work

The body of existing work provides the theoretical, analytical and experimental validation of some technology enablers for future HALE ISR platforms. These enablers have been slow to reach the employment stage due to their technological immaturity and neglect of nonlinear effects. The risks of incorporating these technologies can be reduced by experimental validation. The research within this dissertation focused on experimentally validating flexible twist for pitch control in the linear regime and scaling static response to follower forces in the nonlinear regime.

The first step was to aeroelastically size the full-scale finite element model (FEM) used in this study. To this end, a similar work by Pereira, et al [12] on an AFIT joined-wing design without control mechanisms was analyzed (discussed in the *Aeroelastic and Geometric Scaling*, Section 4.1). The current investigation was performed on a Goland wing and various derivatives to include adding a strut to make it a joined wing. This joined-wing design was then aeroelastically scaled to include the buckling mode. The aeroelastic scaling procedure was extended to incorporate geometrically nonlinear buckling response, for the first time, to the author's knowledge.

The next step was accomplished using wind tunnel models to determine the required aerodynamic forces for pitch control. The method, test and analyses of that model are discussed in Chapter 5. The aerodynamic experiment discussed in this chapter showed that flexible twist is a feasible method for pitch control. This is a significant finding such that is provides validation of assumptions made during in-house investigations into joined-wing design optimization.

9

A flexible aft-wing twist design concept was developed and implemented. The preliminary design of the torsionally-compliant sub-structure, used to build the outer-mold line (OML) of the wind tunnel twisted models, will be described in this document. This configuration was designed in more detail (on the modified Boeing Sensorcraft FEM). The full-scale FEM with aft-wing twist was analyzed for nonlinear response and compared to the nonlinear response observed computationally in a separate reduced scale model. This scale model was tested experimentally in the nonlinear regime and the response was demonstrated statically.

The contributions made through the course of this study were completed through the execution of analytical and experimental demonstration. The experimental portions were in both wind-tunnel and static load evaluations. The first experiment demonstrated that pitch control is realizable using aft-wing twist on an aerodynamically scaled model. The second experimental endeavor validated the extent to which nonlinear response could be scaled. These two efforts were tied together through demonstration of an aeroelastically scaled FEM. The original contribution of the research within this dissertation is in demonstrating that including the critical buckling eigenvalue in addition to natural frequencies and mode shapes does not necessarily allow one to effectively scale a model aeroelastically throughout the nonlinear regime for a post-buckled aircraft. Had this scaling been appropriate, it could reduce significant risk to designing high-aspect-ratio wings typically used in high-altitude long-endurance aircraft to include non-traditional configurations like joined wings.

Previous related studies are outlined in the following Chapter, Section 2.1.1. Some research that remains to be accomplished based on this literature search is covered

in this dissertation. It is noted in the following chapter as gaps in what has already been

accomplished by other researchers.

2. Background

2.1 Previous Work

There have been many studies on the joined-wing concept, aeroelastic model scaling, optimizing for nonlinear response and using wing twist for aircraft control. Some of these studies were completed externally and some local to AFRL and the Air Force Institute of Technology (AFIT). This section provides a review of past studies and develops their role in relation to the present course of investigation.

2.1.1 Previous External Studies

The joined-wing concept was first introduced in 1970s patents by Wolkovitch, who published an overview in 1986 [3]. His concept and patent indicated that there were several potential advantages over conventional aircraft:

1. Lighter weight and higher stiffness
2. Less induced drag
3. Reduced parasite, transonic and supersonic drag
4. Built-in direct lift and side force capability
5. Good stability and control in normal flight and at stall

Wolkovitch also defined a property of the joined-wing configuration that is counter to that of conventional wing aircraft. The out-of-plane arrangement of the joined-wing components results in a wing bending axis which is tilted with respect to the horizontal. This effect drives a structural design which concentrates material near upper leading edge and lower trailing edge (Figure 1-2), referred to here as the Wolkovitch effect [3].

More detailed aerodynamic and structural studies by Kroo, Gallman and Smith [10] have confirmed the Wolkovitch effect and defined some characteristics of joined-wing structures that are advantageous to the design. The joined-wing structure is

12

redundant. Thus, in completing structural optimization the material thickness depends on the internal loads which are, in turn, dependent on the thickness, resulting in an iterative problem. The material thicknesses were found using fully-stressed design [10]. These studies included one in which the material distribution in the structural design accounted for the Wolkovitch effect. Further analysis [10] of nonlinear finite element models demonstrated aft-wing buckling with very large deflections. Typically, preliminary designs do not include buckling or nonlinear analysis. This finding showed that the joined-wing's atypical configuration requires that nonlinear analyses be conducted and accounted for early in the design process.

Lee and Chen [14] indicated that flutter analysis including the front and rear wing buckled structural modes can be used to represent all the structural states. This confirms the necessity of including nonlinearity fin aeroelastic analysis on configurations likely to buckle. Wang and Chen [15] also suggest that HALE aircraft design requires nonlinear aeroelastic analysis due to its large deflections. Additional detailed follow-on work at AFIT also demonstrated this requirement, as well as the need for multidisciplinary optimization, discussed in the next section. Patil [16] studied the nonlinear static and aeroelastic response. The results in linear and nonlinear analyses were similar. However, the experimental results for non-planar joined wings demonstrated much more flexibility than that modeled by a FEM.

Smith and Kroo continued their research along with Cliff and built a demonstrator joined-wing aircraft [11]. The objectives were to demonstrate good handling qualities and validate the design methods used for the joined wing configuration. It was evaluated with wind tunnel tests in a 12-foot wind tunnel at 1/6 of the full-scale. The assessment of

performance, stability and control confirmed that the tools used for design were suitable for a complicated configuration like a joined wing.

At higher angles-of-attack the pitching moment showed a deviation from the typical linear plot for a cantilever wing [11]. A similar phenomenon is discussed in the pitch control results section of the current research, Chapter 5. This nonlinearity in the pitching moment corresponds to the stall angle-of-attack indicating an undesirable amount of pitch-up at stall. This led the researchers to make an improvement to the design by adding a leading edge vortilon on the fore wing of the aircraft. The vortilon made a noticeable improvement. The inboard and outboard elevators and flaps were also shown to be highly effective at -15°. This demonstrates the effectiveness these types of control surfaces have on such a joined-wing design, leading to the topic of the current research—the effectiveness of aft-wing twist for pitch control.

In addition to Smith and Kroo, Tyler, Schwabacher and Carter of AFRL completed complementary computational fluid dynamics (CFD) and wind tunnel examinations [17] of an AFRL generated joined-wing configuration. The primary focus was on three-dimensional on-design performance to determine breakdown in flow due to separation, component interference and combinations thereof. They found some of their computational results could be used to correct the wind tunnel data for the interaction of the sting mount. However, most of the presumed-complementary data was actually collected at different angles or speeds such that the data could not be directly correlated. Their main conclusion was that better comparisons could be made if the test runs experimentally and computationally were planned with this effort in mind. There were

no control surfaces modeled in the wind tunnel or CFD, thus leaving a future study open for research, such as that proposed in this study (Chapter 5).

A survey of joined-wing configurations conducted by Livne explores the fact that the joined-wing concept is of significant interest to a number of disciplines [18]. The joined-wing concept requires a multidisciplinary approach to effectively realize the analysis and design problem. The unconventional configuration requires an optimized design which takes advantage of the interactions between nonlinear structural behavior and aeroelastic response. In fact, sizable in-plane compression on the aft wing requires the inclusion of geometric structural nonlinearities in the structural, aeroelastic and aeroservoelastic analyses. Large in-plane loads can be avoided by optimizing the fore-aft wing joint, which is especially significant when structure suffers at the expense of other sub-system design goals. Lastly, Livne recognizes that there are significant aeroelastic scaling challenges for the joined-wing, a challenge that is addressed in the research within this dissertation (Chapter 4) [18].

Weisshaar and Lee [19] optimized the fore-aft wing joint location as they integrated the structural and aerodynamic analyses to realize the design for an innovative joined-wing aircraft. They found that there is a potentially large weight savings due to out-of-plane stiffening enhanced by rear wing root vertical offset. This weight savings can be realized by optimizing the position of the wing joint along the span of the fore wing, and the rear wing root vertical offset.

Typically, the aft wing of the joined-wing configuration braces the high-aspect-ratio fore wing. To take advantage of this structural redundancy, the joint must be designed to transfer the moment while resisting instabilities. These instabilities include

divergence and flutter caused by excessive moment, shear and axial reaction loads at the joint [20]. Lin, et al [20] investigated joint fixity influence on the stiffness and strength characteristics of a joined-wing. They found that the rigid joint was the best compromise for combined strength and stiffness benefits. It has qualities of reducing main wing roll bending moment and transforming it into a chordwise moment by minimizing joint reaction loads. However, for aerodynamic loads distributed 80% on the front wing and 20% aft wing, the roll bending moment was not as effectively reduced as the 90%-10% combination.

Once a promising configuration is designed, analytical aeroelastic analysis, and then experimental analysis of an aeroelastically scaled model must be accomplished to reduce the risk for full-scale production of this unique configuration. Two recent examples illustrate the detailed steps of these processes with aeroelastic characteristics in mind. The first entails the use of aeroelastic twist for roll control, while the second focuses on scaling a joined-wing model for valid experimental analyses.

AFRL conducted a study [1] on a Joined-Wing Sensorcraft with a goal to twist, by means of embedded piezoceramic fiber composites, the outboard wing with enough roll authority to control the aircraft at critical mission legs. Trim optimization was accomplished to determine the control surface displacements required to trim for roll acceleration at low speed. The minimum twist angle solution deflected each of the surfaces up to 24 degrees, where a control surface was divided into many smaller discrete surfaces to form a whole surface. Discretely dividing the surface in many sections is the precursor to the design in the current study (Chapter 5). Both the twist angle solution and the required aerodynamic moment (150 N-m) were not realizable given the constraints on

16

the design variables. The AFRL study concluded that "twist actuation on the outboard wing section is not adequate for the roll on landing problem" [1].

The AFRL study investigated a concept based on the Active Aeroelastic Wing technology, as realized on a NASA Dryden F/A-18 Hornet modified with active aerodynamic control on the leading and trailing edges and wing twist. For the wing twist, the outboard wing of the joined-wing configuration was divided into discrete control surfaces. As the control surfaces were subdivided, the trends of the resulting hinge moments differed, especially around the joint area. This indicated some aerodynamic response interaction between the outboard wing and the rear wing. As the control surface is further subdivided it begins to more closely approximate a continuously twisted wing, the subject of the current investigation. An added benefit of this design feature is a possible reduction in radar cross section and drag. A more refined panel model was developed to model the smoothly contoured control surface. Although the resulting weight savings or endurance increase was only on the order of 5%, there was a slight improvement in vehicle control performance that is worth further exploration. In addition, Pendleton, Lee and Wasserman [21] of AFRL built and tested an aeroelastically scaled F-16 wing in a 5-foot wind tunnel at 1/5 of full-scale. The model was accurately scaled by matching the bending and torsional stiffness using a simplified structure to the full-scale model rather than duplicating a smaller version of the complex F-16 wing. Continued understanding of this area can be obtained from the observed aerodynamic response of complex configurations of aeroelastically scaled models, in which the current investigation focuses in Chapter 4.

Pereira, et al [12] describe how to scale a model of the joined-wing. The natural frequencies of the model, normalized by a characteristic velocity and length, were matched to that of the full-scale aircraft. Three scaling constraints were applied to length, time and mass. To match the aeroelastic properties, the model had to match the full-scale by duplicating its stiffness to aerodynamic forces ratio and the mass and stiffness distribution.

The method of scaling an aeroelastic model that was studied by Pereira, et al used the natural frequencies, assuming that the reduced frequencies would match since the aerodynamic effects were neglected [12]. Another method of scaling aeroelastically is to match the scaled natural frequencies and mode shapes [22]. Comparison of these two methods is developed in Chapter 4. This shows whether the resulting reduced scale models are aeroelastically equivalent. If they are equivalent, the aeroelastic frequencies throughout the velocity range should be the same or nearly the same once their values are properly scaled. The research within this dissertation matched the natural frequencies and mode shapes since the first method, matching only the natural frequencies, demonstrated that the reduced scale model was not aeroelastically equivalent.

Reduced aeroelastic frequencies and damping are plotted versus the scaled velocity (Figure 2-1) for natural mode three of the AFRL/AFIT-designed joined-wing model, which experienced the first flutter velocity onset [12]. The flutter velocity matches when comparing Pereira's aeroelastically scaled model and full-scale wings with scaled magnitudes, where appropriate, as seen by the zero-crossing of the aeroelastic damping in the lower plot. However, the aeroelastic frequencies, shown in the upper

plot, do not match very well after 20 m/s. This method of scaling may not be acceptable, since 31 m/s is the scaled velocity for the ingress part of the mission profile.
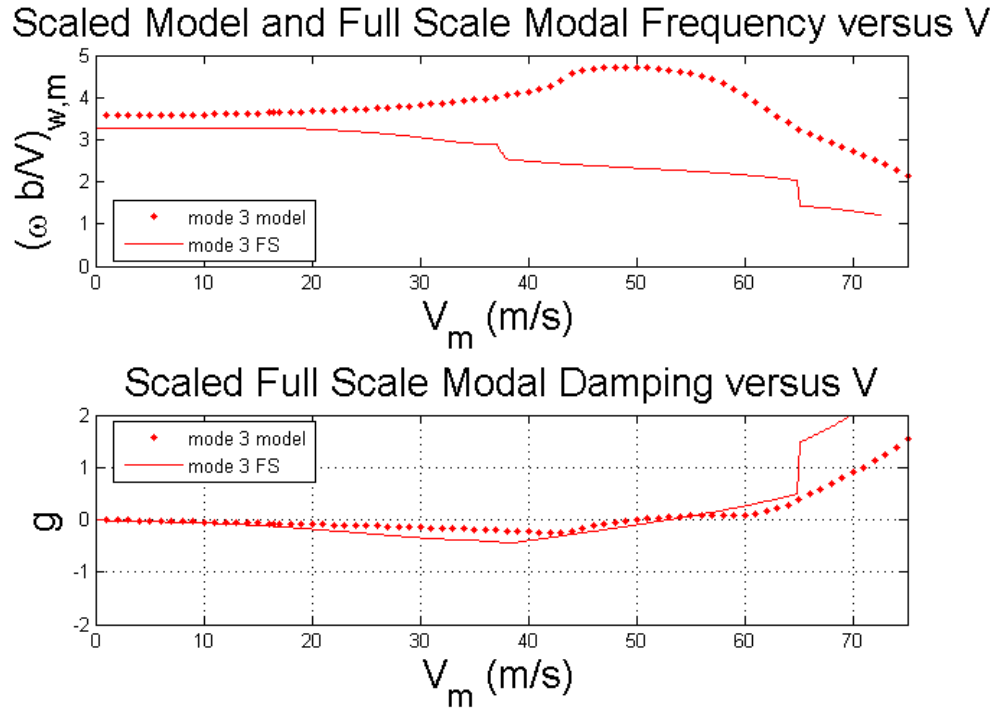
Figure 2-1. Reduced scale model and full-scale modal frequency and damping.

2.1.2   Previous AFIT Studies

Previous internal studies developed joined-wing designs through the use of wind tunnel testing and optimization studying linear and nonlinear effects. These included trials of several joined-wing configurations.

Corneille and Franke tested several configurations of joined-wings [23] in the wind tunnel at AFIT. The model that most closely resembles the configuration of the case study used in the current research has a fore-aft wing sweep of 30° with negative

stagger (the aft wing is higher than the fore wing). They found that the negative stagger had the best lift characteristics, but also had the highest drag. This presents an opportunity to use flexible twist to minimize drag [1]. Pitching moment was not discussed for any of their configurations and they did not include control surfaces in their design.

The high aspect ratio and optimal lift-to-drag ratio (L/D) of the HALE aircraft design requirements drive the joined-wing design to highly flexible wings. Since highly flexible wings experience large deflections, linear assumptions are no longer valid. Traditional preliminary aircraft design investigates only local nonlinearities like skin panel buckling. Due to the design requirements of HALE aircraft, global nonlinearities, such as front or aft wing buckling are anticipated [6].

The nonlinear contributions of large deformations must be accounted for in the implementation of aft-wing twist for longitudinal control in the joined-wing configuration [8]. A greater understanding of these phenomena can be gained by building a scaled physical model. The challenge of this course of action is to correctly scale the nonlinear phenomena. A piecewise linear approach can be taken with an overall nonlinear result. In other words, "the nonlinear system can be divided into several linear subsystems using [a] nonlinear parameter scheme" [24].

Blair and Canfield's [8] study assumed an aft-wing twist mechanism was feasible by actuating pushrods in a vertical tail (assuming there is a vertical tail in the configuration). It takes advantage of a wing design with low torsional stiffness and high bending stiffness. In addition, this study demonstrated larger deformation due to aft-wing twist can be achieved with a soft sub-structure [8]. The research within this dissertation

attempts to verify this assumption with empirical data so that progress can be made with this innovative design.

Previously, joined-wing designers have only considered nonlinear buckling response with respect to the design of the aft wing. Front wing buckling had been overlooked until the high-fidelity model and analysis of Blair, et al [6]. "Because the wing bends up and forward, both the aft and front wings have the potential to buckle whenever compression is present" [6]. "The joined-wing configuration exhibited large geometric nonlinearity below the critical buckling eigenvalue. Thus, nonlinear analysis was required to model correctly this joined-wing configuration" [6]. The research within this dissertation confirms this experimentally to further the understanding of nonlinear response for unconventional designs (Chapter 6).

The torsional stresses resulting from aft-wing twist aggravated the convergence issues during fully-stressed design (FSD) sizing. Thus, aft-wing twist was neglected throughout Roberts' FSD with nonlinear analysis [25]. Further research, which is a concentration of the work presented herein, is required to develop a twist-compliant aft-wing structure that alleviates these torsional stresses. The twist "provides ample control authority with minimal drag" with a twist-actuated aft wing for pitch control [6]. Low torsional stiffness in combination with high bending stiffness allows for a more easily twist-actuated aft wing, while a torque-compliant structure still accommodates the load paths. The aft-wing twist mechanism must maintain bending stiffness to carry the lift load. At the same time reducing twist stiffness relieves the excessive applied twist load to achieve aerodynamic twist required for trim. Placing material in the trailing and leading edges to obtain "maximum leverage to resist bending" suggests that a control

surface or nonstructural material should not be maintained at the fore or aft wing roots at these locations [6].

Blair, Canfield and Roberts [6] concluded that nonlinear deformations were critical in the weight-optimized aluminum joined-wing structure. Rasmussen, et al, continued this vein of research by automating the analyses and investigating various configurations to include joint location, vertical offset, front wing sweep, aft wing sweep, outboard wing sweep, and thickness-to-chord ratio [7]. One significant finding was, "A high vertical offset creates an aft wing structure which resists bending deflections of the front wing.

Concurrent with Rasmussen's studies, further aeroelastic analyses were completed by Sitz [26]. The analysis used a structural model splined to an aerodynamic model. This spline fixes points of the structural model to points on an aerodynamic model so that loads and deformations can be transferred at those points. The more points in the spline, the better the flow conforms to the structural body. The use of aft-wing twist was investigated with results consistent with Roberts. Furthermore, wing twist was modeled by pre-determined twisting from the aft-wing root. The trim angle-of-attack trends were consistent with the mission profile.

After Sitz, Craft [27] investigated the details of drag estimation for the AFIT/AFRL joined-wing configuration. Before Craft, designs were based on constant lift-to-drag ratio assumptions. With a combination of methods, the lift-to-drag ratios were found in the range of upper to mid-20s, rather than the previously assumed constant 24. With actual wind tunnel results (without specialized drag-reducing devices such as blown flaps, etc), the lift-to-drag ratios can be determined, as in this current investigation.

Still a more detailed and physically realizable aft-wing twist design was developed by Kimler, et al [28]. "Closed cross-sections resist torsional loading quite efficiently, especially when the additional stiffness due to the use of composite materials is considered. Thus some means of reducing the torsional rigidity of the aft wing's cross-section needed to be incorporated. One extremely efficient means of doing so is to make the wing cross section open" [28]. Kimler [28] designed a spanwise slit into the aft wing's lower skin just forward of the aft spar to take advantage of the fact that less applied torque is required for an open section versus a closed section. The slit or gap in the lower skin allows the skin to displace fore and aft as the wing twists. The analytical results of the wing with and without the spanwise slit demonstrated strains 50% less in the wing with the slit, in all load cases. Kimler [28] accomplished a cursory examination of laminate ply orientation. He found only a small improvement was made with fiber direction, compared to the spanwise slit of much larger contribution.

One result of this design is the requirement to modify the ribs so as to allow the skin displacement. Without such modification of the ribs, the twist would be counteracted. Kimler [28] modified the ribs by disconnecting them entirely from the bottom skin. This study builds on that approach, using a modified rib that keeps the shape of the skin, yet allows the displacement as discussed. This design is discussed in Section 5.1.4, Twist Tailored Model Design.

2.2 Summary Remarks

While there have been detailed studies of the joined-wing concept, aeroelastic model scaling, optimization for the use of wing twist for aircraft control and nonlinear response, there are issues that require further investigation. These issue include an

experimental proof-of-concept of aft-wing twist and nonlinear response for unconventional design. Each would reduce risk for full-scale developments in the future. Verification of these theoretical concepts will allow these major enabling technologies to be included in future HALE aircraft designs, such as the Joined-Wing Sensorcraft.

The intention was that the three tasks of the problem statement—scaling, the wind tunnel experiment and the nonlinear static experiment—would be undertaken from the same full-scale case study, the Boeing Joined-Wing Sensorcraft. However, the scaling was completed on a simpler model, the Goland wing [13] and a modified Goland wing with a strut. The wind tunnel testing was executed on a model scaled geometrically after modifications for aft-wing twist. Lastly, the nonlinear static testing was executed on a modified Boeing Joined-Wing. However, this time it was modified to make it more flexible such that nonlinear response would be exhibited and could be compared to finite element analysis.

These three efforts combined will satisfy the problem statement of the research in this dissertation. Furthermore, they each fulfill gaps in the community of research that presently exist. That is, including follower forces effect on high aspect ratio vehicles since it is not always negligible due to the large wing deflections in the flight envelope (Chapter 3). Demonstrating whether nonlinear response can be scaled on an aeroelastically scaled model is yet to be shown (Chapter 4). In addition, validating through experiment pitch control by means of aft-wing twist and scaling for nonlinear response are also left to be shown (Chapters 5 and 6).

3. Theoretical Formulation of Scaling and Pitch Control

3.1 Aerodynamic Wind Tunnel Testing Theory

Before testing a full-scale article in an uncontrolled environment, a reduced scale model can be used to gather valuable data from wind tunnel testing under controlled conditions. Not only does this testing reduce cost and mitigate risk to aircraft development, it allows the engineer to control many of the variables associated with flight testing an aircraft. In this way, innovative designs and theories put to practice can be evaluated in a controlled environment with less uncertainty. In addition, a low fidelity analytic model can be corrected through experimental data.

An aerodynamic model that is tested under the same Reynolds and Mach numbers has the same force and moment distribution as the full-scale aircraft [29]. It is generally accepted that incompressible effects can be neglected below 0.4 M [29]. In addition, with Reynolds numbers above $4x10^5$, the oscillatory air forces associated with the Reynolds number are relatively small [30]. Thus, the flutter speed and frequency are relatively unaffected by Reynolds number disparities above $4x10^5$. Also, above $1.5x10^6$ the boundary layer effects are predictable [29].

In the research within this dissertation, Mach and Reynolds numbers could not be matched due to the low speed of the wind tunnel and model size limitations. Although the Reynolds number is close to critical, the collection of pressure data, discussed next, helped account for effects experienced.
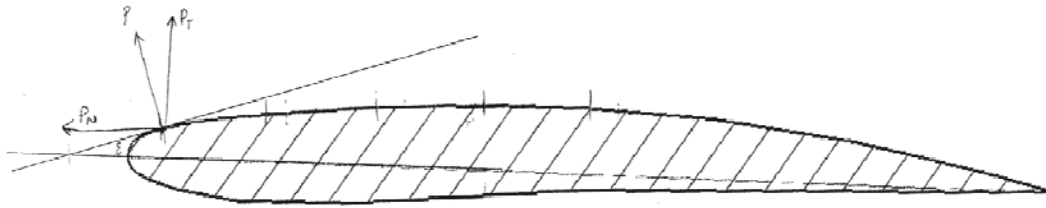
Figure 3-1. Pressure at a point along the chord.

In addition to directly measuring the forces and moments using a balance, pressure measurements were collected in the wind tunnel. The pressure forces can be integrated chordwise along the surface of the airfoil to determine the two-dimensional lift distribution of the airfoil at a specific spanwise location (Figure 3-1). Both lift and drag (not to include drag due to viscous forces) can be calculated from pressure distribution [29]. Integrated static pressures from pressure ports along the chord of the wing are used in this calculation. For a joined-wing aircraft, the majority of the lift comes from the fore wing, since it is the largest. The lift produced by the aft wing, however, is also of interest since this is the surface which is manipulated to control pitch. Therefore, special attention is paid to changes in lift due to the aft wing, with various twist angles.

3.2   Conventional and Wing Twist Stability Derivatives

Conventional aircraft use an elevator or similar control surface on the horizontal tail to change the lift and, in turn, effect a change in the coefficient of moment at angle-of-attack, C_M, to keep the aircraft trimmed at different speeds. The range of required control surface deflection to provide longitudinal control of the aircraft must also be determined for the joined-wing aircraft. In this case, however, the objective is to determine how much twist is required of the aft wing, rather than a control surface

deflection to provide longitudinal control of the aircraft. This can be accomplished by

determining the lift curve slope for the neutral aircraft, $\left. \dfrac{\partial C_L}{\partial \alpha} \right|_{\delta_e = 0}$.
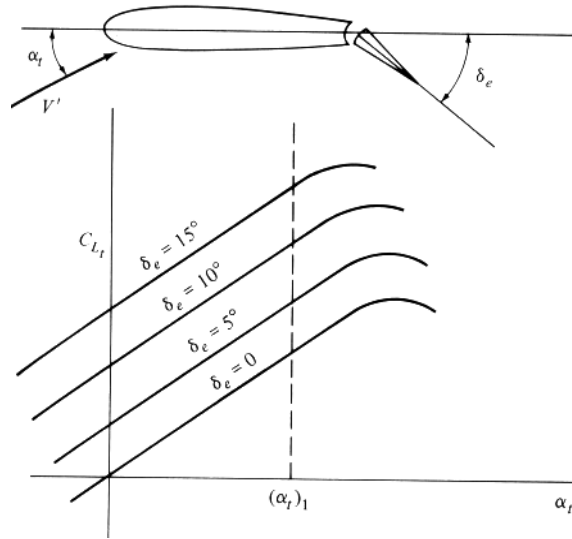
Figure 3-2. Tail-lift coefficient with elevator deflection [31].

For a conventional aircraft, the lift curve slope of the tail remains constant but

shifts to the left as the elevator, δ_e, is deflected downward (positive by convention), as in

Figure 3-2. Plotting C_{L_t} vs. δ_e at a constant angle-of-attack, the curve would be linear

for most conventional aircraft. This stability derivative, $\dfrac{\partial C_{Lt}}{\partial \alpha}$, is a measure of elevator

effectiveness [31]. For the joined wing, elevator deflection, δ_e, is replaced with aft-wing

twist, θ. The moment curve can then be used to measure how well the twist controls the

pitch of the aircraft. The moment referred to includes all the lifting surfaces (fore and aft

wing). Like elevator deflection, where down is positive, positive is designated as aft

wing trailing edge down (Figure 3-3).   Since the aft wing is twisted, it is possible that

this joined wing may not have a constant $\dfrac{\partial C_{Mcg}}{\partial \alpha}$ for various angles-of-twist as with a conventional wing.
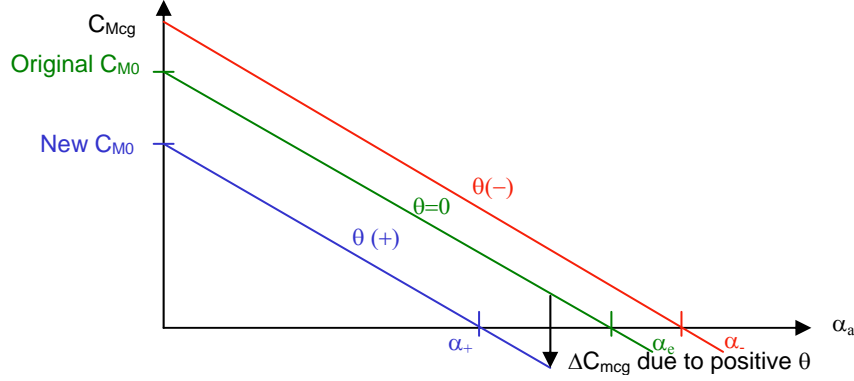
Figure 3-3. Theoretical effect of aft-wing twist on moment coefficient [32].

3.3 Formulation of Non-dimensionalized Scaling Laws

3.3.1 Modeling the Linear System

The first step is to write the aeroelastic equations and non-dimensionalize them. To get a properly scaled aerodynamic equation the variables that can be changed must be recognized, which are dependent on the manufacturability of the reduced scale model. The Aerodynamic Influence Coefficient (AIC) matrix characterizes the air loads of the system. It depends on the deformation due to the combination and participation of the mode shapes. The classical flutter equation is:

$$\left[s^2 \overline{M} + \overline{K} - \overline{q}_\infty \overline{Q}\left(\tfrac{sb}{V}\right) \right]\left\{ \overline{x}(s) \right\} = 0 \tag{3.1}$$

where $\overline{M}$, $\overline{K}$ and $\overline{Q}$ are the mass, stiffness and aerodynamic forces matrices, $\overline{x}$ is the physical coordinate, s is the Laplace counterpart of frequency, b is length, V is velocity and $\overline{q}_\infty$ is dynamic pressure [33, 34].

28

This is the equation that is to be nondimensionalized; derivation of the equation can aid in this process. The following equation goes to the foundation with the equation of motion for an aeroelastic aircraft system:

$$\overline{M}\,\overline{\ddot{x}}(t) + \overline{K}\,\overline{x}(t) = \widehat{F}_a\left[\hat{x}(t), \dot{\hat{x}}(t)\right] \tag{3.2}$$

where $\widehat{F}_a\left[\hat{x}(t), \dot{\hat{x}}(t)\right]$ is a vector of aerodynamic forces due to structural deformation.

Single-barred variables, $\overline{(\cdot)}$, are dimensional.

In approximating an aerodynamic system by a linear system, an aerodynamic transfer function, $\widehat{H}$, relates the aerodynamic forces, $\widehat{F}_a$, to the structural deformation, $\hat{x}(t)$ through the convolution integral

$$\widehat{F}_a\left[\hat{x}(t), \dot{\hat{x}}(t)\right] = \int_0^t \overline{q}_\infty \widehat{H}\left(\tfrac{V}{b}(t-\tau)\right)\hat{x}(\tau)\,d\tau \tag{3.3}$$

with initial conditions at $t = 0$, $\hat{x}(0)$ and $\dot{\hat{x}}(0)$.

In approximating an aerodynamic system by a linear system, an aerodynamic transfer function, $\widehat{H}$, relates the aerodynamic forces, $\overline{F}_a$, to the structural deformation, $\overline{x}(t)$ through the convolution integral,

$$\overline{F}_a\left[\overline{x}(t), \dot{\overline{x}}(t)\right] = \int_0^t \overline{q}_\infty \widehat{H}\left(\tfrac{V}{b}(t-\tau)\right)\overline{x}(\tau)\,d\tau \tag{3.4}$$

Hence, the Laplace domain linear system is

$$\overline{F}_a\left(\overline{x}(s)\right) = \overline{q}_\infty \overline{H}\left(\tfrac{sb}{V}\right)\overline{x}(s) \tag{3.5}$$

where $\overline{\overline{H}}$ is the Laplace counterpart to $\widehat{H}$, $\overline{q}_\infty \overline{H}$ is the aerodynamic transfer function

and where s is $i\omega$. The Laplace transform of (3.3) is

$$\left[s^2 \overline{M} + \overline{K} - \overline{q}_\infty \overline{Q}\left(\tfrac{sb}{V}\right) \right]\{\overline{x}(s)\} = 0 \tag{3.6}$$

In order to unify the dimensions, $\overline{x}$ can be transformed by a matrix, T. Thus,

$\overline{x} = Tx$, where x is a non-dimensional vector of physical coordinates. For example, for a

pitch-plunge (θ, h) system typically used for classical bending-torsion coupling,

$$\{\overline{x}\} = \left\{\begin{array}{c} h_1 \\ \theta_1 \\ h_2 \\ \theta_2 \\ \vdots \end{array}\right\} = \begin{bmatrix} b & & & \\ & 1 & & \\ & & b & \\ & & & 1 \\ & & & & \ddots \end{bmatrix} \left\{\begin{array}{c} h_1/b \\ \theta_1 \\ h_2/b \\ \theta_2 \\ \vdots \end{array}\right\} \tag{3.7}$$

where b is the wing semi-chord. Then, (3.7) can be substituted into (3.1)

$$\left[s^2 \overline{M} + \overline{K} - \overline{q}_\infty \overline{Q}\left(\tfrac{sb}{V}\right) \right] T \{x(s)\} = 0 \, . \tag{3.8}$$

That still leaves the mass, stiffness and aerodynamic force matrices in a mixed

dimensional form, as indicated by the single over-bar. First, they are transformed into a

uniform-dimensional form, indicated by $\overline{\overline{(\cdot)}}$, then a non-dimensional form, $\widetilde{(\cdot)}$, and

finally a non-dimensional generalized form, $(\cdot)$. If, for example, the mixed-dimensional

mass matrix, $\overline{M}$, were transformed by T it would result in a uniform-dimensional mass

matrix; that is, one in which all terms in the matrix carry the same units,

$$\overline{\overline{M}} = T^T \overline{M} T \tag{3.9}$$

$$\bar{\bar{K}} = T^T \bar{K} T \tag{3.10}$$

$$\bar{\bar{Q}} = T^T \bar{Q} T . \tag{3.11}$$

If these same operations were performed on the stiffness and aerodynamic force matrices, the resulting system matrices and equation in the system would be uniformly dimensional. Premultiplying (3.8) by T^T and substituting Equations (3.9) through (3.11) yields the linear aeroelastic equation in terms of dimensionally uniform system matrices,

$$\left[s^2 \bar{\bar{M}} + \bar{\bar{K}} - \bar{q}_\infty \bar{\bar{Q}}\left(\tfrac{sb}{V}\right) \right] \{x(s)\} = 0 . \tag{3.12}$$

To make the matrices non-dimensional, the dimensional scale would be factored out of their respective matrices

$$
\begin{aligned}
\bar{\bar{M}} &= m_{\text{dim}} \widetilde{M} \\
\bar{\bar{K}} &= k_{\text{dim}} \widetilde{K} \\
\bar{\bar{Q}} &= h_{\text{dim}} \widetilde{Q}
\end{aligned}
\tag{3.13}
$$

where m_{dim}, k_{dim}, h_{dim} are scale factors making each matrix non-dimensional. Of course, these scale factors can be in a variety of forms that may be convenient to scaling the full-size aircraft. One such parameter may be the ratio, *EI/L*, for stiffness of classical bending-torsion flutter models, for example. Thus, the non-dimensional flutter equation with the dimensional scale factors is:

$$\left[s^2 m_{\text{dim}} \widetilde{M} + k_{\text{dim}} \widetilde{K} - \bar{q}_\infty h_{\text{dim}} \widetilde{Q}\left(\tfrac{sb}{V}\right) \right] \{x(s)\} = 0 . \tag{3.14}$$

31

The characteristic dimensions for mass, stiffness and aerodynamic force may be reduced to three primary quantities such as length, mass and time. In particular, those appropriate to this study are the three quantities of air density, length and velocity, which are dictated by wind tunnel restrictions:

$$m_{dim} = \rho_\infty b^3$$
$$k_{dim} = \rho_\infty V^2 b^4 \quad\quad\quad (3.15)$$
$$h_{dim} = b^4 \quad,$$

where ρ_∞ is air density, b is a characteristic length such as span, and V is the maximum velocity of interest.

The basis of the optimization objective function and side constraints used in Chapters 4 and 6 is the free-vibration eigenvalue problem

$$K\bar{\phi} = \lambda M \bar{\phi} \quad\quad\quad (3.16)$$

where the eigenvalue is $\lambda = \omega^2$ and ω are the system natural frequencies [35]. Using this modal approach, $x = \Phi q$, where Φ is the modal matrix whose columns contain the lower-order natural modes, normalized so as to be non-dimensional, and the vector, q, are the generalized coordinates.

If each of the mass, stiffness and aerodynamic force matrices in uniform-dimensional form are transformed by the max-normalized mode shapes, the resulting matrices become

$$M = \Phi^T \widetilde{M} \Phi$$
$$K = \Phi^T \widetilde{K} \Phi \quad\quad\quad (3.17)$$
$$Q = \Phi^T \widetilde{Q} \Phi \quad.$$

Thus, the classical flutter equation is constructed in generalized form with non-dimensional generalized mass, stiffness and aerodynamic force matrices,

$$\left[\frac{s^2 m_{\dim}}{k_{\dim}} M + K - \frac{\bar{q}_\infty h_{\dim}}{k_{\dim}} Q\left(\frac{sb}{V}\right) \right] \{q(s)\} = 0. \tag{3.18}$$

The leading non-dimensional ratios are then absorbed into two variables and presented as

$$\left[p^2 M + K - q_\infty Q(p) \right] \{q(s)\} = 0, \tag{3.19}$$

where p^2 and q_∞ become the non-dimensional Laplace variable and the non-dimensional dynamic pressure, respectively.   Thus, the critical non-dimensional generalized aeroelastic Equation (3.1) is formed, which can produce the same response in any vehicle scale, provided the distribution of mass and stiffness, planform shape, and the mode shapes are the same. The physical responses, e.g., frequency or flutter dynamic pressure, are determined from the common non-dimensional frequency, p, and dynamic pressure, q_∞, from the solution of the single non-dimensional equation of motion. For example, the parameter for dynamic pressure values for flutter onset, $\bar{q}_{\infty F}$, can then be determined by

$$\bar{q}_{\infty F} = q_{\infty F} \frac{k_{\dim}}{h_{\dim}}. \tag{3.20}$$

This formulation then allows some freedom in building a reduced scale model that will aeroelastically represent the full-scale vehicle. Such freedom allows the model designer to choose materials and distribution of the materials to accommodate model manufacturing limitations. The task of the model builder is to use this design freedom to produce a model for which the non-dimensional K, M, and Q match those of the full-scale vehicle.

3.3.2 Modeling the Nonlinear System

The system under investigation, which includes the Joined-Wing Sensorcraft and its flight environment, has several nonlinearities associated with it. These nonlinearities can be grouped into two categories: geometric and forcing (Figure 3-4).

The geometric nonlinearity has two subcategories that include the nonlinearities due to material, and those due to the strain-displacement relationship. The system was designed to its required flight envelope, thus the material was exposed to loads beyond the linear region of the material properties. Thus, the material nonlinearity in this system is ignored.

The forcing nonlinearity in this system is the air loads. The Joined-Wing Sensorcraft's high aspect ratio lends itself to large wing deflections. Since air loads are defined as perpendicular to the surface of the aircraft wing(s), the forces follow the wing as it deflects. Typical linear systems neglect modeling changes in the force direction due to wing deflection, since the deflection is small. However, the follower forces effect on high aspect ratio vehicles is not always negligible due to the large wing deflections in the flight envelope.

In order to achieve the same nonlinear response of the system, the geometric nonlinearity due to large strains and the nonlinearity due to follower forces must be modeled so as to match the reduced scale model response to that of the full-scale system.
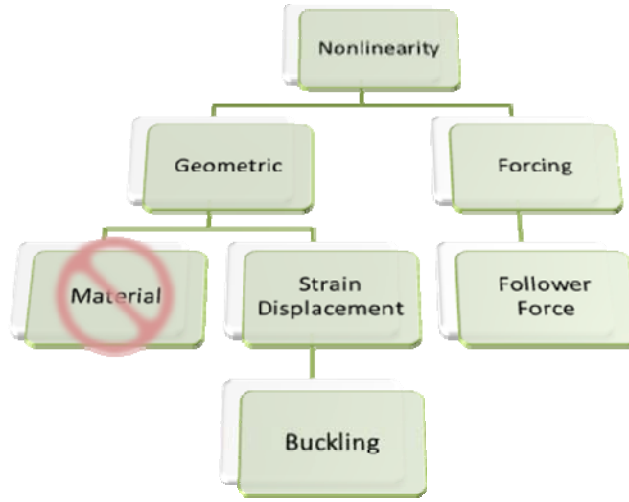
Figure 3-4. Hierarchy of system nonlinearity (material nonlinearities not considered herein).

The nonlinear strain terms appear in the structural stiffness, $\overline{K}$, whereas the nonlinear follower-force air loads appear in the force, as in (3.21) , on the right side of the equilibrium equation;

$$\left[\overline{K}\right]\{\overline{x}\} = \{\overline{F}\}$$ (3.21)

where

$$\overline{K} = \overline{K}_L + \overline{K}_G\left(\overline{x}\right).$$ (3.22)

Buckling analysis is a simplification that treats forces as constant while nonlinear strains develop. These nonlinear strains are examined to determine at what load level the structure becomes unstable. To begin, the reference load must be established, $\{R_{ref}\}$, and the linear internal loads must be solved for

$$\left[\overline{K_L}\right]\{\overline{x}_{ref}\} = \{\overline{F}_{ref}\} \Rightarrow \{\sigma^e_{ref}\} = [E][B]^e\{\overline{x}^e_{ref}\}$$ (3.23)

35

where $\{\sigma\}$ is the vector of element stress components, $\bar{x}_{ref}^e$ is elemental deflection, $[E]$ is the constitutive matrix and $[B]$ is the strain-displacement matrix. Then the geometric stiffness (stress stiffness) matrix, $\left[\bar{K}_G\right]_{ref}$, is constructed from $\{\sigma^e{}_{ref}\}$.

The eigenvalue problem,

$$\left[\bar{K} + \lambda_{cr}\bar{K}_{G_{ref}}\right]\{\phi_b\} = 0 , \qquad (3.24)$$

where

$$\bar{K}_G = \lambda\bar{K}_{G_{ref}} \qquad (3.25)$$

is solved for the buckling load, the critical (lowest) eigenvalue, λ_{cr}, which scales the reference load [36];

$$\left\{\bar{F}\right\}_{cr} = \lambda_{cr}\left\{\bar{F}_{ref}\right\} = 0 . \qquad (3.26)$$

The nonlinear or buckling influence can be included in the overall system such that the full-scale model buckling modes can be solved. Then, this response can be matched in a subscale model and the stiffness non-dimensionalized as in equations (3.13). This is accomplished by scaling the following non-dimensional form of (3.24):

$$k_{\dim}\left[\widetilde{K} + \lambda_b\widetilde{K}_{G_{ref}}\right]\{\phi_b\} = 0, \qquad b = 1, 2, \ldots \qquad (3.27)$$

where λ_b are the eigenvalues for buckling,

$$\lambda_b = \frac{\phi_b^T\widetilde{K}\phi_b}{\phi_b^T\widetilde{K}_{G_{ref}}\phi_b} . \qquad (3.28)$$

36

Equation (3.27) assumes that the $\widetilde{K}$ and $\widetilde{K}_G$ terms are non-dimensional and k_{dim} is the same for both. Thus, if the geometric nonlinearities, $\widetilde{K}_G$, are scaled along with $\widetilde{M}$ and $\widetilde{K}$ the response of the system is the same whether in a full-scale or subscale model.

A similar approach to non-dimensionalizing can be used from the process in Section 3.3.1 to arrive at the following aeroelastic equations incorporating geometric nonlinearity. Transforming $\widetilde{K}_G$ to modal coordinates,

$$K_G = \Phi^T \widetilde{K}_G \Phi \qquad (3.29)$$

where Φ includes the critical buckling mode. Replacing K in (3.18), $K_L + K_G$ gives the non-dimensionalized aeroelastic equation of motion

$$\left[\frac{s^2 m_{\text{dim}}}{k_{\text{dim}}} M + K + \frac{k_{b_{\text{dim}}}}{k_{\text{dim}}} K_G - \frac{\bar{q}_\infty h_{\text{dim}}}{k_{\text{dim}}} Q\left(\frac{sb}{V} \right) \right] \{q\} = 0. \qquad (3.30)$$

For a linear system, the expansion theorem states that any deformation can be described in terms of all the modes, Φ_{all}, times all the generalized coordinates, q_{all}. Typically, the number of modes used is truncated and the approximate solution is usually sufficient. Thus, the truncated modes, Φ, and the remainder of the modes, Φ_R, comprise all of the modes, Φ_{all}. Hence, an approximate solution is

$$x \cong \Phi q, \qquad (3.31)$$

whereas the exact solution may be represented by

$$x = \{\Phi \quad \Phi_R\} \begin{Bmatrix} q \\ q_R \end{Bmatrix}. \qquad (3.32)$$

Chapter 4 demonstrates the primary buckling mode (or its residual) is added to the set of generalized coordinates. The norm of the buckling mode residual is the criterion for determining whether the residual modes are small enough to be neglected,

$$\frac{\|\phi_r\|}{\|\phi_b\|} \ll 1 \qquad (3.33)$$

where the residual is formed by subtracting its projection onto the truncated modal space,

$$\phi_r = \phi_b - \Phi q_B = \phi_b - \Phi^T \Phi M \phi_b. \qquad (3.34)$$

Thus, an approach can be evaluated for use in modeling the geometric nonlinearities due to buckling in an aeroelastic system like the Joined-Wing Sensorcraft.

3.3.3   Scaling Laws

There are three primary ratios that must be considered for scaling the aeroelastic characteristics of the full-scale joined wing. These ratios capture the critical parameters used in scaling the aeroelastic model and are based on physical limitations of a particular test set-up. These ratios include characteristic length ratio, air density ratio and velocity ratio. The length ratio is established by the size of the full-scale vehicle compared to wind-tunnel or ground test restrictions. Thus, it is defined for the wind tunnel test item, as discussed in Chapter 5, as

$$\frac{b_m}{b_w} = \frac{1}{38}, \qquad (3.35)$$

where m and w are reduced scale and full scale, respectively, and as

$$\frac{b_m}{b_w} = \frac{1}{15} \qquad (3.36)$$

for the ground test item (discussed in Chapter 6).

The air density ratio is fixed by the standard day altitude of the wind tunnel and the mission profile,

$$\frac{\rho_{\infty_m}}{\rho_{\infty_w}} = \frac{\rho_{\infty_{541ft}}}{\rho_{\infty_{50Kft}}} = \frac{2040.9 \text{ lb/ft}^2}{243.6 \text{ lb/ft}^2} = 8.3781.$$

(3.37)

The velocity ratio is fixed by the maximum viable speed of the wind tunnel and the mission profile,

$$\frac{V_m}{V_w} = \frac{50 \text{ m/s}}{177 \text{ m/s}} = 0.2825.$$

(3.38)

The aeroelastic equations in the previous section impose an aeroelastic mass ratio of unity;

$$\left(\frac{\mu_m}{\mu_w}\right) = \frac{\left(\dfrac{m_{str}}{\pi\rho_\infty b^2}\right)_m}{\left(\dfrac{m_{str}}{\pi\rho_\infty b^2}\right)_w} = \frac{\left(\dfrac{M}{\pi\rho_\infty b^3}\right)_m}{\left(\dfrac{M}{\pi\rho_\infty b^3}\right)_w} = 1$$

(3.39)

where μ is the aeroelastic mass ratio, m_{str} is the structural mass per unit length, $\pi\rho_\infty b^2$ is the mass of a characteristic volume of air above the wing, and M is structural mass. Thus, since the air density and length ratios are fixed, (3.39) can be written in terms of a mass ratio [29]:

$$\frac{M_m}{M_w} = \left(\frac{\rho_m}{\rho_w}\right)_\infty \left(\frac{b_m}{b_w}\right)^3.$$

(3.40)

Equation (3.39) was used for scaling the applied loads in static ground testing described in Chapter 6, such that

$$\frac{F_m}{F_w} = \frac{M_m a}{M_w a} = \left(\frac{\rho_m}{\rho_w}\right)_\infty \left(\frac{b_m}{b_w}\right)^3. \tag{3.41}$$

The following approach, Chapter 4, demonstrates the use of aeroelastic scaling procedures and nonlinear scaling using the theory contained in this chapter. It accounts for the fact that the equations of motion for the model are already non-dimensionally scaled according to this chapter and takes further steps to constrain the stiffness so as to scale it aeroelastically and nonlinearly.

4. Scaling Approach, Results and Discussion

The method of aeroelastically scaling with mode shapes and/or the aeroelastic reduced frequencies, including geometric stiffness, described in Chapter 3 was carried out on the Goland wing [13] for simplicity and then on the Goland wing modified to include a strut. This simplified joined wing was used to make a comparison to the method used by Pereira [12]. Thus, the validity of aeroelastic scaling using modal frequencies versus modal frequencies and mode shapes was confirmed. In addition to linear scaling with vibration eigenvectors, nonlinear scaling was performed using a buckling eigenvector.

4.1 Aeroelastic and Geometric Stiffness Scaling

A discussion of the theoretical methods for building up from aeroelastic scaling to aeroelastic and nonlinear static scaling are discussed in this section. The use of natural frequencies, a combination of natural frequencies and natural mode shapes and ultimately the combination of natural frequencies, natural mode shapes, buckling eigenvalues and eigenvectors to scale inherently geometric nonlinear aircraft designs is presented.

4.1.1 Scaling with Natural Frequency

The case study made on an AFIT joined-wing configuration by Pereira, et al [12] was used to demonstrate the first method of scaling an aeroelastic model. This method was to scale by matching the scaled natural frequencies. First the length, mass and velocity were scaled according to the scaling laws in Equations (4.1), (4.4) and (4.5). The scaled velocities, V, Pereira et al, started with are governed by [12, 30, 37]:

$$\frac{V_m}{V_w} = \left(\frac{b_m}{b_w}\right)^{1/2} \tag{4.1}$$

where *m* and *w* are reduced scale and full scale, respectively. Equation (4.1) comes from scaling the Froude number, a number used in scaling low-speed aeroelastic models,

$$Fr = \frac{V}{\sqrt{gb}} \tag{4.2}$$

The reduced frequency, *k*, is the non-dimensional ratio related to the natural frequency, ω_n at zero airspeed (not the frequency at which flutter onset occurs):

$$k = \frac{\omega b}{U} \tag{4.3}$$

Hence for models with matched reduced frequency, the following ratio is equivalent:

$$\left(\frac{V}{b\omega_n}\right)_m = \left(\frac{V}{b\omega_n}\right)_w, \quad n = 1,...,5 \tag{4.4}$$

Thus, the inverse of (4.4) are the normalized natural frequencies Pereira et al, sought to match, which leads to the natural frequency ratio,

$$\frac{\omega_m}{\omega_w} = \left(\frac{V}{b}\right)_m \left(\frac{b}{V}\right)_w \tag{4.5}$$

The constant values used on the right side of (4.1) are in Table 4-1 [12]. Comparing the aeroelastic analysis of the resulting subscale model to full-scale at the equivalent scaled velocities shows that matching natural frequencies alone is insufficient for the success of aeroelastic scaling. Figure 2-1 demonstrates that the critical aeroelastic frequency does not match throughout the velocity regime of the mission profile. Thus, the second method of scaling, where the model is also optimized to match natural frequencies and modes or reduced flutter frequencies, may be more appropriate to achieve equivalency throughout the velocity range.

Table 4-1. Values for scaling optimization.

	Full-scale, W	Reduced scale model, M
Semi-span, b	32.25 m	1.0177 m
Velocity, V	177 m/s	31 m/s

4.1.2   Scaling with Natural Frequency and Mode Shapes

The proposed method of aeroelastic scaling could take either of two approaches to match the aeroelastic properties of the full-scale aircraft.   Both methods are derived from matching the non-dimensional scaled equations of motion as described in Chapter 3, particularly Equation (3.18).   The first approach is to match the mode shapes together with scaled natural frequencies and the second is to optimize aeroelastic reduced frequencies and damping (real and imaginary part of aeroelastic eigenvalues).

The first method involves adding more constraints, namely constraints to match mode shapes, than those considered in the related work by Pereira [12].   Additional design variables are needed to satisfy the added constraints. In addition to rib thickness design variables, skin and spar thicknesses were added as design variables.   This technique is less complex than optimizing to match the aeroelastic eigenvalues, if the fidelity of the models is the same, since the latter requires aeroelastic analysis in every cycle of optimization.   This first method can be summarized in the following optimization problem statement,

$$\min\left[\sum_{i=1}^{n} \left\| (\omega_i)_m - (\omega_i)_w \right\| \Bigg|_{V=0} + \sum_{i=1}^{n} \left\| (\Phi_i)_m - (\Phi_i)_w \right\| \right] \tag{4.6}$$

subject to side constraints, where ω_i is a non-dimensional frequency, Φ_i is the mode shape, and the side constraints on design variables are dictated by manufacturing limitations. In general the mode shapes in the second term of Equation (4.6) do not have the same (number of) degrees of freedom. Hence, the displacements of one model (typically the higher fidelity one) must be mapped to the other. For the purposes of this study, the models to be matched had a subset of common physical degrees-of-freedom, $\{x\}$, permitting matching the mode shape to be unambiguous.

The second approach is to match aeroelastic reduced frequencies and damping, which is tantamount to matching modal mass, stiffness, and aerodynamic force matrices in (3.17). This first requires an optimization problem of the flutter analysis. This method can be summarized in the optimization problem

$$\min\left[\sum_{i=1}^{n}\left\|\left(\omega_i\right)_m-\left(\omega_i\right)_w\right\|+\sum_{j=1}^{n_v}\sum_{i=1}^{n}\left\|\left(k_{ij}\right)_m-\left(k_{ij}\right)_w\right\|+\sum_{j=1}^{n_v}\sum_{i=1}^{n}\left\|\left(g_{ij}\right)_m-\left(g_{ij}\right)_w\right\|\right] \qquad (4.7)$$

where k_{ij} is the reduced frequency, g_{ij} is the aeroelastic damping, n is the number of reduced frequencies and n_v is the number of velocities where the aeroelastic equations are discretized. The reduced frequencies and damping come from the common non-dimensional eigenvalue, p, in the generalized form

$$k=\left|\Im\left(p\right)\right|, \qquad \gamma=\left|\Re\left(p\right)\right| \qquad (4.8)$$

where g_{ij} is related to the rate of decay parameter, γ, by

$$g \cong 2\gamma \qquad (4.9)$$

Aeroelastic response at various flight speeds can be addressed by $n>1$ and flutter by $n=1$.

4.1.3   Scaling with Natural Frequency, Mode Shapes and Geometric Stiffness

In order to scale the nonlinear system the geometric stiffness matrix is matched; that is, the buckling mode shapes are addressed in Section 3.3.2 through the use of

$$\left[\frac{s^2 m_{\dim}}{k_{\dim}} M + K + \frac{k_{b\dim}}{k_{\dim}} K_G - \frac{\bar{q}_\infty h_{\dim}}{k_{\dim}} Q\left(\frac{sb}{V}\right) \right]\{q\} = 0 \tag{3.30}$$

where q is the vector of modal coordinates.

The most general scaling problem statement for the fully dynamic aeroelastic problem could be posed as

$$\min \left[\left\| (M)_m - (M)_w \right\| + \left\| (K)_m - (K)_w \right\| + \left\| (K_G)_m - (K_G)_w \right\| + \left\| (Q)_m - (Q)_w \right\| \right] \tag{4.10}$$

for appropriate matrix norms, assuming that the same generalized coordinates may be used for both full vehicle and reduced scale model. These matrices can represent the system of a physical model in which these predicted results can be compared. A more direct approach is to match the nonlinear static aeroelastic solution, where the nonlinear response is captured in

$$\min \left\| \left(\bar{x}_{NL} \right)_m - \left(\bar{x}_{NL} \right)_w \right\| \tag{4.11}$$

subject to side constraint, where $\bar{x}_{NL}$ is the static nonlinear deformation to a particular load or set of loads. In this case study the values $\left(\bar{x}_{NL} \right)_m$ and $\left(\bar{x}_{NL} \right)_w$ from Equation (4.11) was compared between a beam model and a built-up wingbox to validate an approach to match two models nonlinearly and aeroelastically. The natural modal frequencies and mode shapes and the buckling eigenvalue and buckling mode are optimized simultaneously using the approach:

$$\min\left[\sum_{i=1}^{n}\left\|\left(\omega_i\right)_m-\left(\omega_i\right)_w\right\|+\sum_{i=1}^{n}\left\|\left(\Phi_i\right)_m-\left(\Phi_i\right)_w\right\|\right.$$
$$\left.+\sum_{i=1}^{n}\left\|\left(\lambda_{buckling,i}\right)_m-\left(\lambda_{buckling,i}\right)_w\right\|+\sum_{i=1}^{n}\left\|\left(\Phi_{buckling,i}\right)_m-\left(\Phi_{buckling,i}\right)_w\right\|\right]_{V=0} \tag{4.12}$$

subject to side constraints. The use of this approach defined by Equation (4.12) is verified by calculating the difference in nonlinear static response, as in Equation (4.11).

In order to demonstrate the aforementioned theoretical approach, an analytical example follows using the well-known uniform cantilever wing established by Goland [13] for flutter analysis in 1945.

4.2   Demonstration of Aeroelastic Scaling

The aforementioned method to optimize a reduced scale model to a target model is realized using the Goland wing [13] beam model and a built-up wingbox model that could be manufactured. In addition, an uncoupled variant of the wingbox and a wingbox with a strut added will be discussed. These simpler cases replace using the full-scale Boeing Sensorcraft as a case study to demonstrate procedures to match models using natural modes, natural frequencies, buckling eigenvalues, and buckling eigenvectors.

4.2.1   Goland Wing Beam and Wingbox Model Descriptions

The wing beam model developed by Goland was a uniform cantilever wing to analyze flutter that coupled the bending and torsion modes [13]. The wing is modeled as a one-dimensional beam.

The built-up wingbox used in the analytical portion of this study was used for several tasks. It is derived from the heavy Goland wingbox, known as Goland$^+$ [38] to match the frequency and mode shapes of the original Goland wing beam model [13],

subsequently comparing the aeroelastic response of each and comparing nonlinear response (wingbox with strut). In addition, the built-up wingbox was matched in frequency alone without matching mode shapes to demonstrate the need to match mode shapes.

A preliminary version of a Goland wingbox derivative, referred to here as Goland$^{\pm}$, was developed from the heavy Goland wingbox, Goland^{+}, by matching the mass distribution of the original Goland beam model. The properties of the original Goland wing beam model [13], Goland^{+} [38], and Goland$^{\pm}$, are summarized in Table 4-2. The Goland$^{\pm}$ wing is depicted in Figure 4-1. In addition, the Goland$^{\pm}$ FEM has a subset of common physical degrees-of-freedom at the elastic axis, permitting matching the mode shape to be unambiguous.
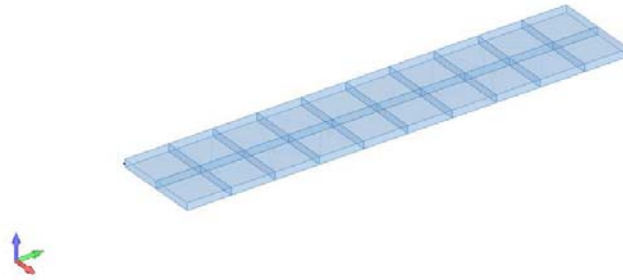
Figure 4-1. Goland$^{\pm}$ wing.

Table 4-2. Goland Beam, Goland⁺ wingbox and Goland± wingbox properties

Property	Goland beam [13]	Goland⁺ wingbox [38]	Initial Uncoupled Goland± wingbox
E, Young's Modulus	N/A	$1.476e9$ lbs/ft^2	$1.476e9$ lbs/ft^2
G, Shear Modulus	N/A	$5.16e8$ lbs/ft^2	$5.16e8$ lbs/ft^2
EI_1/m	$31.7e6$ lb-ft/slug	N/A	N/A
$GJ/I_{ea/L}$	$1.23e6$ lb-ft/slug	N/A	N/A
$I_{ea/L}*L \equiv J_m$ Mass moment of inertia about the elastic axis	38.86 slug ft^2	N/A	33.57 slug ft^2
$I_{cg/L}*L \equiv I_{cg}$ Mass moment of inertia about the center of gravity	33.57 slug ft^2 (38.86 slug ft^2 uncoupled)	50.34 slug ft^2	33.57 slug ft^2
Base	3 ft	4 ft	4 ft
Height	N/A	0.3334 ft	0.3334 ft
Length of span	20 ft	20 ft	20 ft
Leading /Trailing edge Spars, t_1	N/A	0.0006 ft	0.0006 ft
Center Spar thickness, t_c	N/A	0.0889 ft	0.0889 ft
Rib thickness	N/A	0.0347 ft	0.0347 ft
Skin thickness, t_2	N/A	0.0155 ft	0.0155 ft
mass	14.91 slugs	224.98 slugs	14.92 slugs
Leading /Trailing edge Spar cap areas, A_1	N/A	0.0416 ft	0.0416 ft
Center spar cap area, A_3	N/A	0.1496 ft	0.1496 ft
1st bending frequency	8[$]/ 7.88[§] Hz (uncoupled)	1.97 Hz[§]	8.1 Hz*/10.1 Hz[§]
1st torsional frequency	14[$]/ 13.83[§] Hz (uncoupled)	4.05 Hz[§]	14 Hz*/15.2 Hz[§]

[$]Goland paper values [13]
*Hand-calculation
[§] frequency estimate with NASTRAN FEM

4.2.2 Goland Wing Beam and Goland± Wingbox Model Uncoupled Optimization

The uncoupled Goland± model was developed from the Goland⁺ model by replacing the FEM concentrated masses that were located at each spar-rib junction with non-structural mass to match the method used in the beam FEM. This comprised nonstructural mass per length in bar elements along the elastic axis and concentrated masses along the elastic axis with only the torsional degree-of-freedom active. The total

mass matches the beam FEM which equals the total Goland wing mass of 217.74 kg (14.92 slugs).

Thus, the uncoupled Goland$^{\pm}$ wingbox was formed, where the bending and torsion frequencies match within 0.07% of the Goland beam uncoupled frequencies (column 2, Table 4-2 and Figure 4-2(a) and (b)). This match was achieved by minimizing the difference between the eigenvalues of the wingbox and beam, as in the first term in Equation (4.12).

(a) ω_1=7.88 Hz   (b) ω_2=13.84 Hz
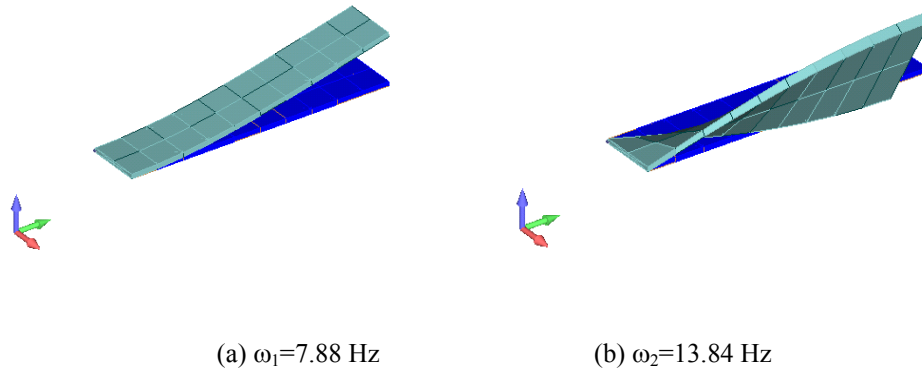
Figure 4-2. Goland$^{\pm}$ wingbox uncoupled natural frequencies and mode shapes

The constant properties for the uncoupled models included: E, Young's Modulus, G, shear modulus, $I_{ea/L} \times L \equiv J_m$, , mass moment of inertia about the elastic axis, $I_{cg/L} \times L \equiv I_{cg}$, mass moment of inertia about the center of gravity, base, height and span (Table 4-2). The design variables were the thickness of the spars, ribs, and skin, and spar cap areas. Their property values before and after optimizing are summarized in Table 4-3.

.

Table 4-3. Uncoupled Goland$^{\pm}$ wingbox properties matched frequencies/mode shapes

Property	Initial Uncoupled Goland$^{\pm}$ wingbox	Freq/Mode Shape matched Uncoupled Goland$^{\pm}$ wingbox
1st modal frequency	8.1 Hz*/7.51 Hz§ (bending)	7.88 Hz§ (bending)
2nd modal frequency	14 Hz*/14.36 Hz§ (torsion)	13.84 Hz§ (torsion)
Leading /Trailing edge Spars, t_1	0.0006 ft	2.15e-4/4.60e-4 ft
Center Spar thickness, t_c	0.0889 ft	0.341 ft
Rib thickness	0.0347 ft	0.0347 ft
Skin thickness, t_2	0.0155 ft	2.30e-3/5.06e-3 ft
Total mass	14.92 slugs	14.92 slugs
Leading /Trailing edge Spar cap areas, A_1	0.0416 ft^2	8.30e-3 ft^2
Center spar cap area, A_3	0.1496 ft^2	0.235 ft^2

*Hand-calculation
§ NASTRAN FEM Calculation

The modal displacements were matched at the common physical degrees-of-freedom at the elastic axis in the optimization objective function, while the first two eigenvalues were constrained to remain within 0.01% of the target. This match was achieved by constraining the frequencies and optimizing the bending and torsion mode shapes in NASTRAN. The difference between the eigenvectors of the wingbox and beam were minimized at nodes aforementioned along the span.   The design variables previously noted were allowed to vary within 10% to 1000% of the initial value. The values that remained constant even with optimization were the rib thickness at 0.0347 ft, the rib caps at 0.0422 ft^2, and the posts at 0.0008 ft^2. In order to match the wingbox properly, all the degrees-of-freedom in the original beam model were released to allow responses such as in-plane bending to match that of a wingbox. In addition, in-plane bending and axial properties were used for the beam when those degrees-of-freedom were released (they were derived from the uncoupled wing once the previous sections

results were found). For consistency with the wingbox model, the beam model allowed transverse shear deformation (i.e., a Timoshenko beam), explaining the difference with the hand calculation in Table 4-3.

4.2.3   Goland Wing Beam and Goland$^{\pm}$ Wingbox Model Coupled Optimization

Given the uncoupled model was useful in demonstrating the proper modal scaling procedure, the coupled model analysis provides more utility in demonstrating proper aeroelastic scaling procedure. In addition, flutter generally occurs when the bending and torsion modes coalesce, and this is likely produced in a coupled cantilever wing like the Goland$^{\pm}$ wing. This is not the case, as expected, for the uncoupled model.

The coupled Goland$^{\pm}$ model was developed from the uncoupled Goland$^{\pm}$ by putting an offset from the elastic axis into the elements with nonstructural mass to match the mass moment of inertia about the elastic axis, I_{ea}, and center of gravity, I_{cg}, while keeping the total mass constant (Table 4-2). In the uncoupled model, the mass moment of inertia values at the center of gravity and at the elastic axis are equivalent.   However, to match the coupled Goland wing, where the center of gravity is 10% of chord further from the leading edge than the elastic axis, all three values must match. This was done by the offset of mass. Then the first two eigenvalues and mode shapes were matched using the same method as the uncoupled wing in the previous section, using stiffness design variables only to include thickness of the spars, ribs, and skin, and spar cap areas.

In order to show that just matching natural frequencies is not sufficient to scale a wing aeroelastically, the frequency values were matched, while the torsion mode was the lowest frequency and the bending next. This is in reverse order from the original Goland wing. Assume the uncoupled modes started in reverse order based on the thickness and

51

areas chosen for a wingbox. To demonstrate this example, the initial condition previously stated was reached by solving two equations in two unknowns for target area moment of inertia and torsional constant, I_1 and J as in Equation (4.13). Next, a set of stiffness design variables that produce the target I_1 and J as the new initial point was found. Then the FEM was tuned to match only the frequency values starting with initial design values:

$$\omega_{bending} = 8 \text{ Hz} = \frac{3.55}{L^2}\sqrt{\frac{EI_1}{m}} \Rightarrow I_1 = \left(\omega_{bending}\frac{L^2}{3.55}\right)^2 \frac{m}{E}$$

$$\omega_{torsion} = 14 \text{ Hz} = \frac{\pi}{2L}\sqrt{\frac{GJ}{I_{ea}}} \Rightarrow J = \left(\omega_{torsion}\frac{2L}{\pi}\right)^2 \frac{I_{ea}}{G} \qquad (4.13)$$

The I_1 and J from the uncoupled equations for first bending and first torsion natural frequency were solved, using the normal frequencies in reverse

$$I_{target} = \left(2\pi(14 \text{ Hz})\frac{L^2}{3.55}\right)^2 \frac{m}{E}$$

$$J_{target} = \left(2\pi(8 \text{ Hz})\frac{2L}{\pi}\right)^2 \frac{I_{ea}}{G} \qquad (4.14)$$

To match the FEM frequencies precisely the model was tuned using NASTRAN to optimize. Then another optimization scheme in NASTRAN was used to swap the mode shape order. The NASTRAN FEM was first optimized to match the first two eigenvalues. The thicknesses and areas were allowed to vary, the results shown in Table 4-4 column 2. The next step (results in Table 4-4, column 3) constrained the first two eigenvalues and matched modal deflections of several nodes along the span of the wing. The resulting frequencies when only the frequencies were matched were within 0.32% of the Goland wing beam coupled natural frequencies. As depicted in Figure 4-3, the blue wingboxes, (a) and (b), match the Goland coupled beam mode shapes and the yellow

wingboxes, (c) and (d), do not, although in both cases the modal frequencies match the Goland beam.

(a) ω_1=7.61 Hz   (b) ω_2=15.18 Hz

(c) ω_1=7.64 Hz   (d) ω_2=15.12 Hz
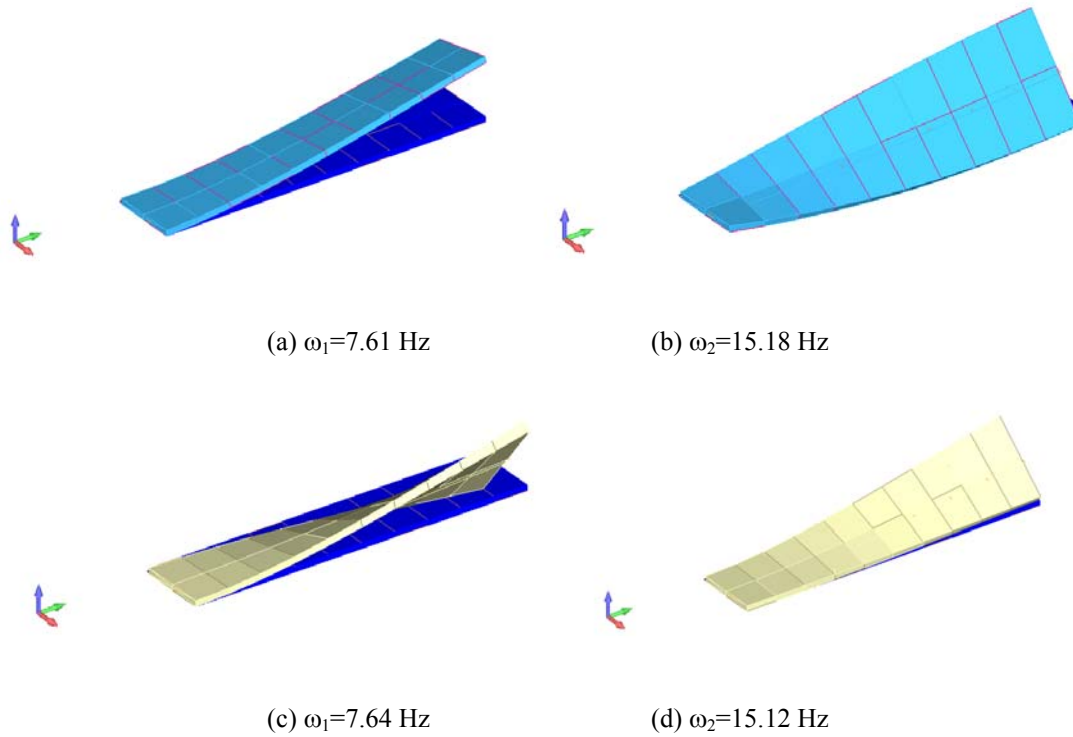
Figure 4-3. Goland$^\pm$ wingbox coupled natural frequencies and mode shapes.

Table 4-4. Coupled Goland$^\pm$ wingbox properties matched frequencies/mode shapes and matched frequencies only

Property	Initial Coupled Goland$^\pm$ wingbox	Frequency matched only Coupled Goland$^\pm$ wingbox	Freq/Mode Shape matched Coupled Goland$^\pm$ wingbox
1st modal frequency	8.17Hz*/7.70 Hz§	7.64 Hz§	7.61 Hz§
2nd modal frequency	14.03 Hz*/ 15.77 Hz§	15.12 Hz§	15.18 Hz§
Leading /Trailing edge Spars, t_1	0.0006 ft	1.31e-005/1.30e-005 ft	8.71e-4/5.46e-4 ft
Center Spar thickness, t_c	0.0889 ft	0.442 ft	0.19955 ft
Skin thickness, t_2	0.0155 ft	0.0484/0.127 ft	LE/TE: 9.98e-3/5.32e-3 ft
Leading /Trailing edge Spar cap areas, A_1	0.0416 ft^2	0.0477 ft^2	0.0083 ft^2
Center spar cap area, A_3	0.1496 ft^2	0.267 ft^2	0.226 ft^2

*Hand calculations
§ frequency estimate with NASTRAN FEM

The constant properties for the coupled models were the same as the uncoupled model previously mentioned with the exception that the $I_{ea/L} \times L \equiv J_m$, mass moment of inertia about the elastic axis was 38.85 slug ft^2 and the mass moment of inertia about the center of gravity, $I_{cg/L} \times L \equiv I_{cg}$ was 33.57 slug ft^2 to match the FEM beam model produced from the Goland wing specifications.

To characterize how the swapping of the mode shape-natural frequency pairs affects the aeroelastic properties of the wing, flutter analysis was compared on the panel model splined to each of these models. Figure 4-4 demonstrates how the aeroelastic response of two Goland$^{\pm}$ wingbox models with first and second natural modal frequencies with values within 0.45% of each other (their mode shapes are practically swapped) have drastically different aeroelastic responses. If the two models were aeroelastically equivalent, both the real and imaginary parts of the roots would match. Thus, the frequency and damping should be consistent. Here it is demonstrated that, when only the frequency is tuned, the aeroelastic frequency trends for the frequency-only-matched case are opposite relative to each other (i.e., bending relative to torsion modes). In addition, the damping indicates flutter speed is about 500 ft/s slower than the beam model it is attempting to match. Hence, the frequency and damping are inconsistent with the beam model and demonstrate that models matching in frequency only are not necessarily aeroelastically scaled. In contrast, the frequency-plus-mode-matched case has equivalent aeroelastic frequencies throughout the speed regime.
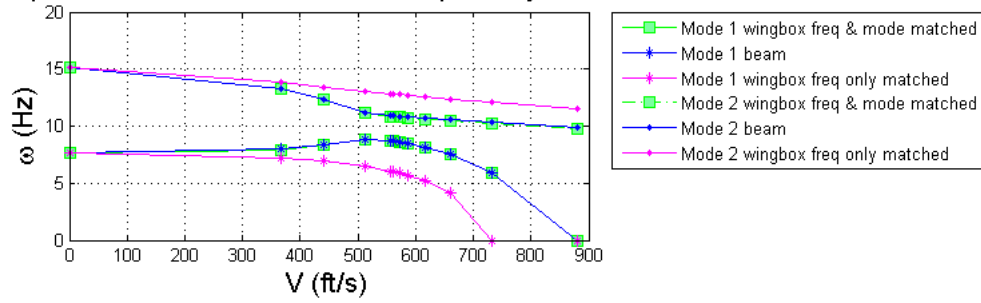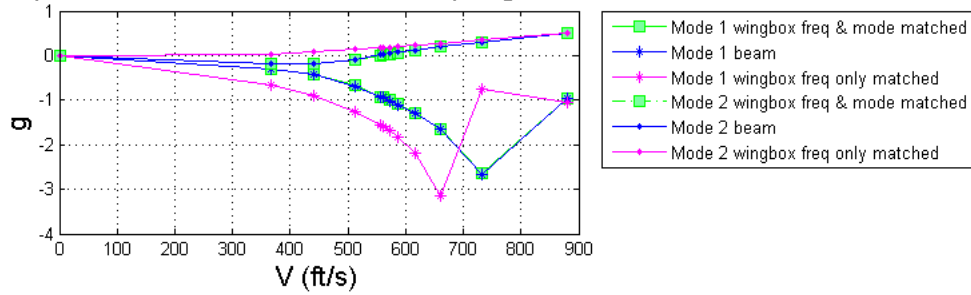
Figure 4-4. V-g, V-ω plots for the freq/mode shape matched and frequency only matched models.

4.3   Demonstration of Scaling Nonlinear Response

The theory discussed earlier in this chapter suggests that the geometric stiffness can be matched by matching the buckling eigenvalue and mode shape in addition to the natural modes and eigenvalues (as in the test cases in Sections 4.2.2 and 4.2.3). The hypothesis is that, if the geometric stiffness is matched, then nonlinear analysis will yield similar results for both models.   In order to test this hypothesis, the geometric nonlinearity associated with global buckling of a joined wing was analyzed.

4.3.1   Joined Wing Vibration Optimization

To simplify this analysis, the case study was the Goland$^{\pm}$ wingbox with a two-spar strut added (Figure 4-5) rather than the Boeing Sensorcraft used in the experimental case studies in Chapters 5 and 6 .

Front

Top

Side
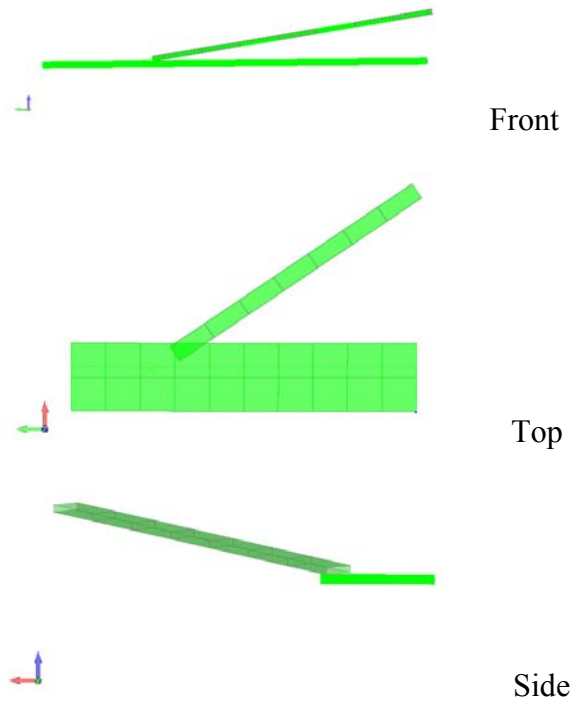
Figure 4-5. Goland wingbox with two-spar strut.

The first step was to match the frequencies and mode shapes in the same manner as described in the previous section. In this case, each wing was optimized separately and then joined. The first three frequencies and mode shapes for the beam strut and wingbox strut before scaling are depicted in Figure 4-6 and compared in Table 4-5. The relative error norm for each mode in the pitch and plunge directions, T3 and R2, are presented in Table 4-5. These values indicate the match is not valid.

(a) ω_1=10.82 Hz (bending) (b) ω_2=14.85 Hz (torsion/aft-wing bending) (c) $\omega_3$17.64 Hz (torsion/aft-wing bending)

(d) ω_1=11.36 Hz (bending) (e) ω_2=16.48 Hz (torsion/aft-wing bending) (f) ω_3=23.33 Hz (torsion/aft-wing bending)
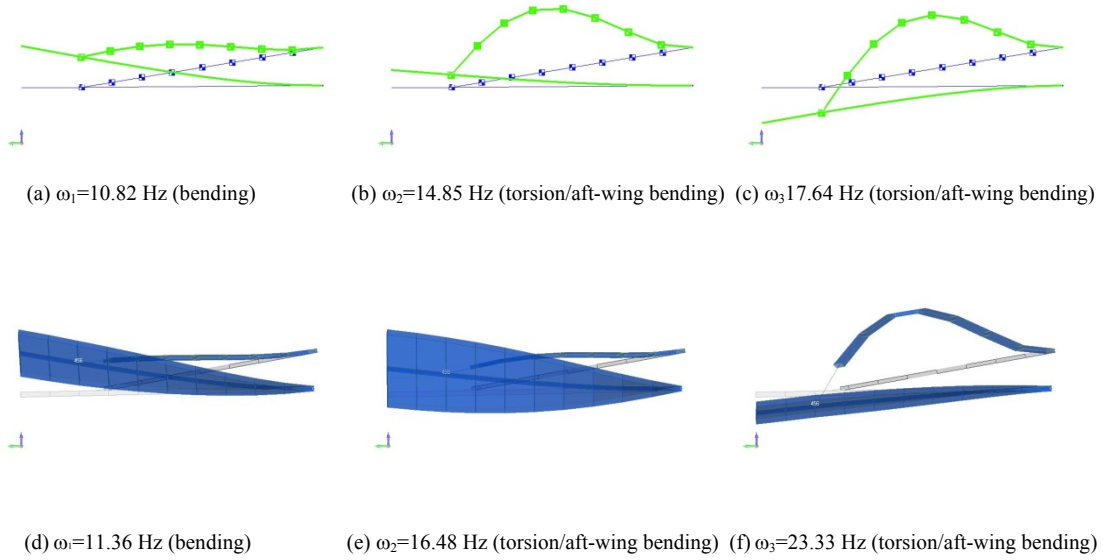
Figure 4-6. Natural modes of beam strut (a-c) and wingbox (d-f) models where fore and aft wings optimized separately to match natural frequencies and mode shapes.

Table 4-5. Comparison of wingbox before scaling compared to beam modes.

Mode	$\dfrac{\left\|\bar{\phi}_n - \bar{\phi}_{n,tgt}\right\|}{\left\|\bar{\phi}_{n,tgt}\right\|}$
T3 & R2 Mode 1	0.1608
T3 & R2 Mode 2	0.5412
T3 & R2 Mode 3	0.5399

To verify whether the models were aeroelastically matched, given the bending and torsion natural frequencies and mode shapes were matched, the models were analyzed for flutter in ZAERO as in the previous cases. The panel model and wingbox used in this analysis are depicted in Figure 4-7. The wingbox and beam V-g and V-ω comparison depicted in Figure 4-8 demonstrate that the two models are not aeroelastically matched in frequency or damping.
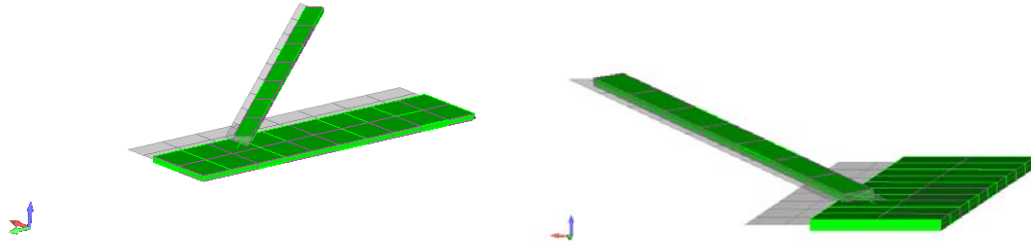
Figure 4-7. Aerodynamic panel (gray) and wingbox model (green).
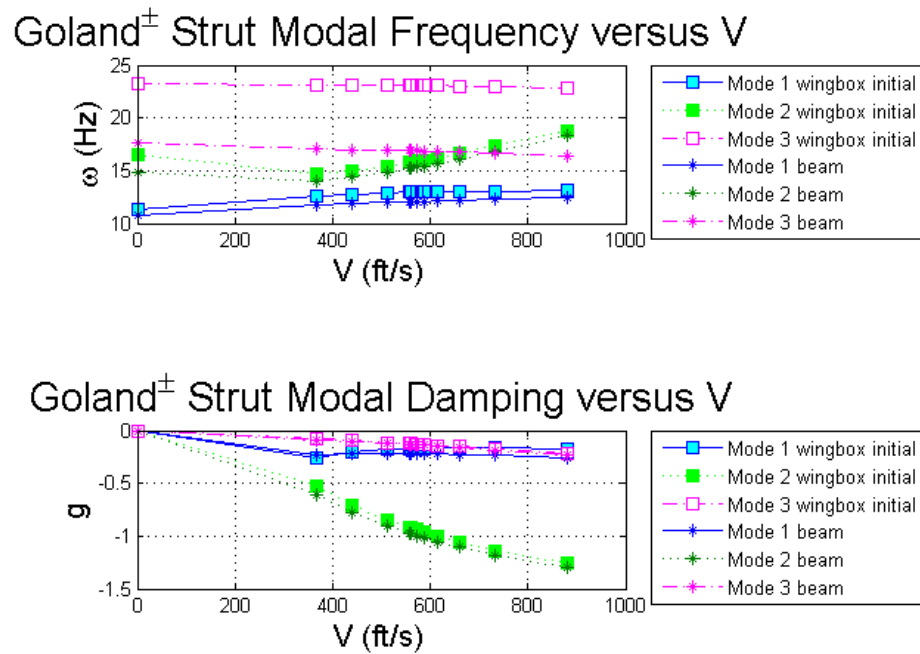
Figure 4-8. Aeroelastic roots for Goland$^{\pm}$ with strut FW and AW matched separately.

4.3.2   Joined Wing Vibration and Buckling Optimization

The next step was to match the critical buckling eigenvalue and eigenvector. The hypothesis asserted in Section 4.1.3 states if the models' buckling eigenvalue and eigenvector in addition to the natural frequencies and mode shapes are matched, the nonlinear response also corresponds. The vibration eigenvalues and mode shapes and critical buckling eigenvalue were then optimized to match the beam model by changing

the wingbox property design variables (Figure 4-9). The property values for the wingbox strut FEM are summarized in Appendix E, Table E-1. This resulted in less than 0.5% error in the first three vibration eigenvalues and less than 0.45% error in the critical buckling eigenvalue. The relative error norm for the vibration mode shapes was 0.0398, 0.1314 and 0.1464 for the first three modes, respectively (Table 4-6). This indicates a valid match. The relative error norm would be even smaller if only the buckling eigenvalue was matched without constraining the vibration eigenvalues. The buckling mode shape with a load at the wingtip is depicted in Figure 4-11 and compared in Figure 4-12. The comparison of buckling and vibration eigenvalues, summarized in Table 4-6, demonstrates an excellent match of the beam and optimized models.

Table 4-6. Summary of vibration and buckling matching

	beam	(1) joined wingbox before scaling		(2) joined wingbox after buckling and vibration opt	
eigenvalue	eig	eig	% diff	eig	% diff
vib mode 1	4.62E+03	5.10E+03	9.39%	4.63E+03	0.32%
vib mode 2	8.71E+03	1.07E+04	18.76%	8.72E+03	0.15%
vib mode 3	1.22E+04	2.14E+04	42.97%	1.22E+04	-0.13%
critical buckling eig	8.88E+03	1.58E+04	43.86%	8.88E+03	0.00%

(a) ω_1=10.82 Hz (bending)   (b) ω_2=14.85 Hz (torsion/aft-wing bending) (c) ω_2=17.64 Hz (torsion/aft-wing bending)

(d) ω_1=10.79 Hz (bending)   (e) ω_2=14.75 Hz (torsion/aft-wing bending) (f) ω_3=17.38 Hz (torsion/aft-wing bending)
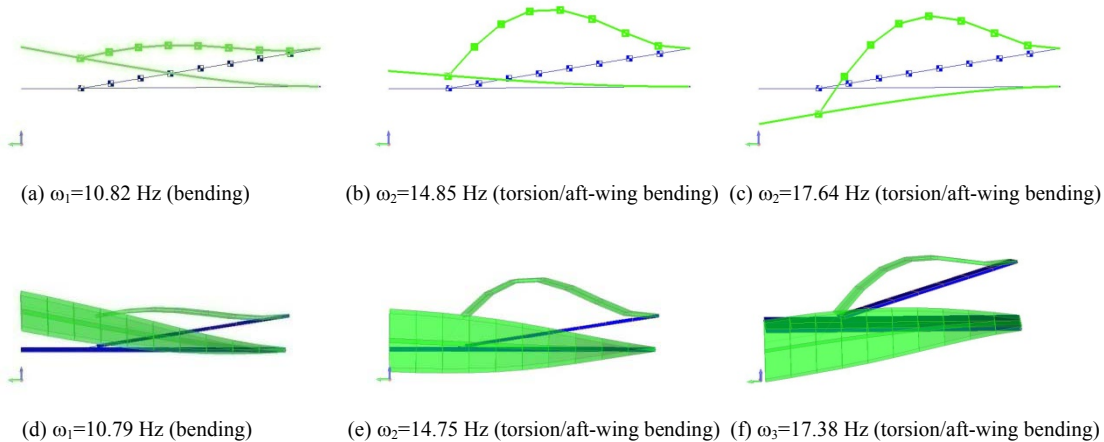
Figure 4-9. Goland$^{\pm}$ mode shapes for beam strut (a-c) and wingbox (d-f) models, matched 1st and 2nd frequencies/mode shapes, optimized with natural frequencies and mode shapes and critical buckling eigenvalue.
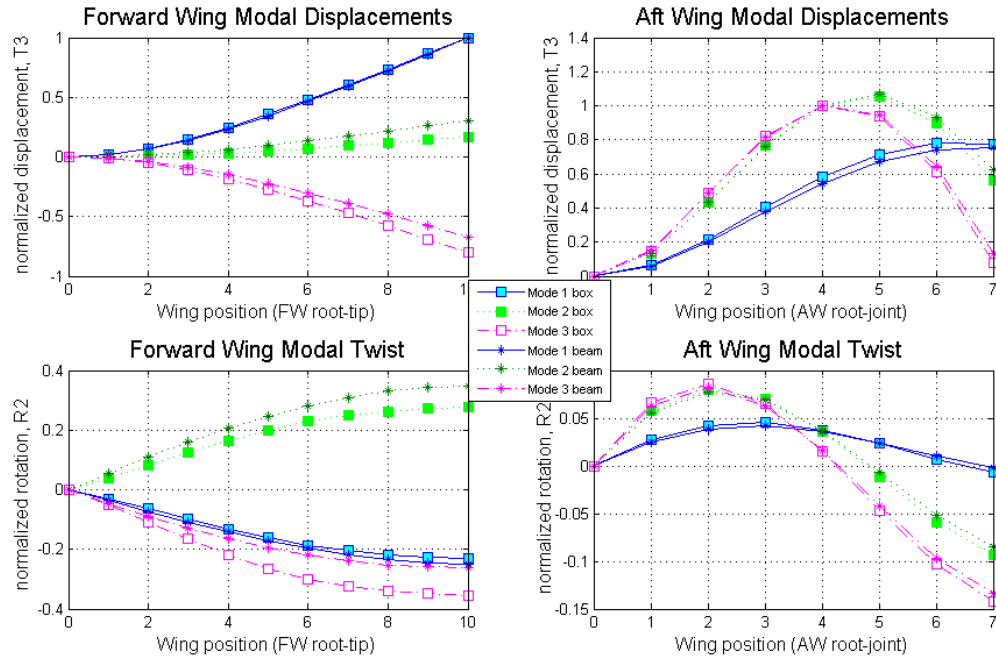
Figure 4-10. Natural modes of matched wingbox and beam strut models optimized with natural frequencies and mode shapes and buckling eigenvalue.

Table 4-7. Comparison of Wingbox vibration modes after scaling to beam modes.

Mode	$\dfrac{\left\|\overline{\phi}_n - \overline{\phi}_{n,tgt}\right\|}{\left\|\overline{\phi}_{n,tgt}\right\|}$
T3 & R2 Mode 1	0.0398
T3 & R2 Mode 2	0.1314
T3 & R2 Mode 3	0.1464
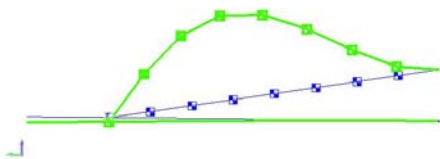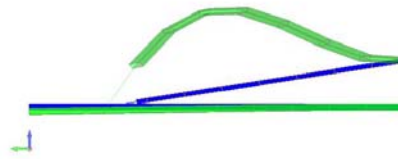
(a) λ= 8876.8   (b) λ= 8981.6

Figure 4-11. Critical buckling mode shape of beam strut (a) and wingbox (b) models.

60
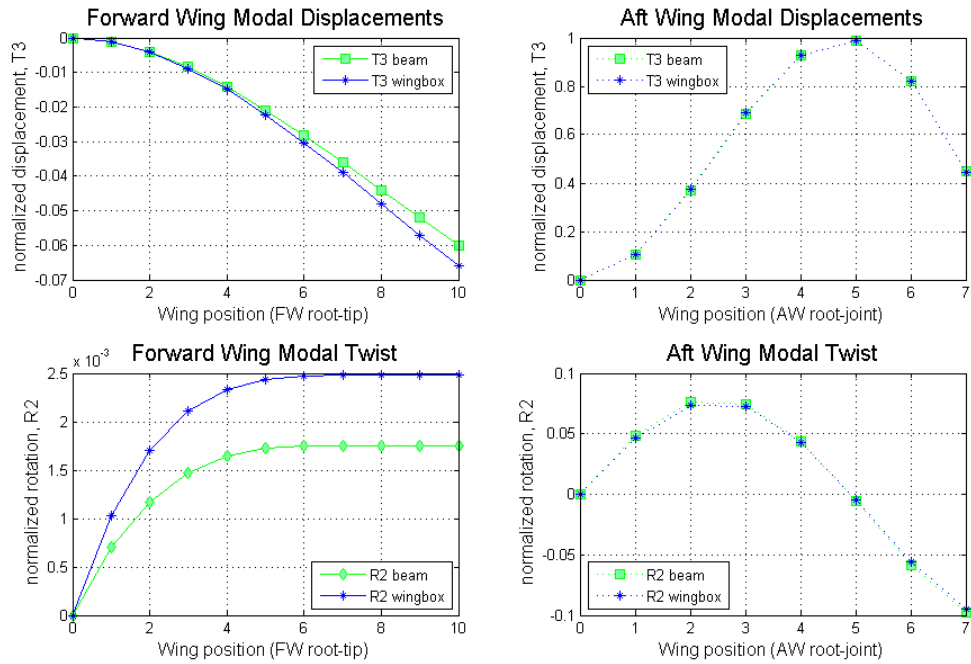
Figure 4-12. Critical buckling modes of matched wingbox and beam strut models.

Once the natural and buckling eigenvalues and eigenvectors were shown to match the beam model, the aeroelastic roots were analyzed to determine whether the models were equivalent at velocity greater than zero. Figure 4-13 depicts that the aeroelastic roots match much more closely throughout the velocity range than the wingbox model did in its initial configuration.
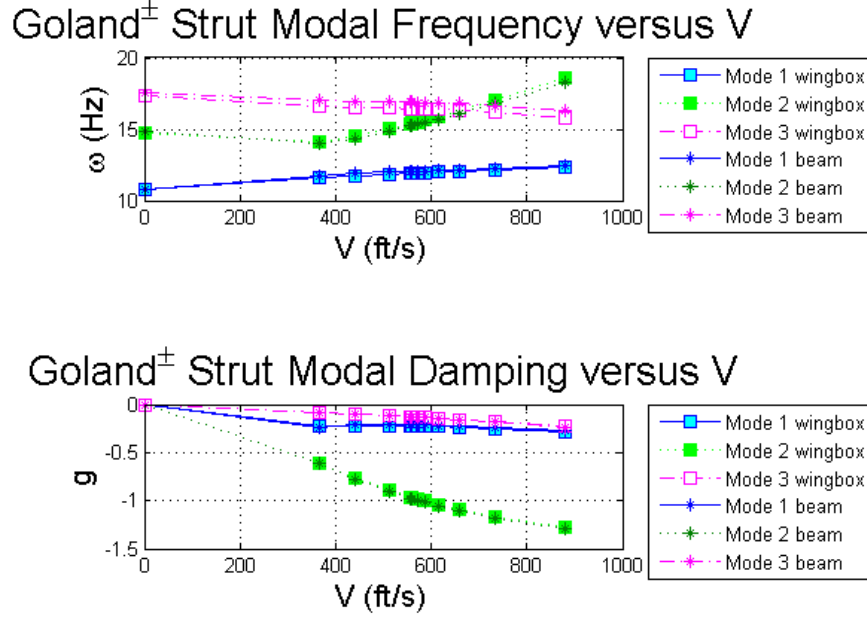
Figure 4-13. Aeroelastic roots for Goland$^\pm$ with strut after buckling and vibration optimization.

The wingbox model matches the beam model both aeroelastically and in fundamental buckling. This was demonstrated by the aeroelastic frequencies and damping matching (Figure 4-13). In addition, the natural frequencies matched within 0.32% and the natural mode shapes relative norms are 0.14 for the first three modes. The critical buckling eigenvalue difference was less than 0.45% and its relative error norm was 0.0066, which included transverse deflection (T3) and twist (R2),

$$\frac{\left\|\bar{u}_b - \bar{u}_{b,tgt}\right\|}{\left\|\bar{u}_{b,tgt}\right\|} \quad . \tag{4.15}$$

4.3.3   Joined Wing Nonlinear Analysis

The nonlinear analysis carried out in this section was the final step in determining whether the aforementioned scaling process was successful in predicting nonlinear

deformations. The displacements for the beam and wingbox were found through nonlinear analysis of a follower force at the wingtip. The magnitude of the maximum force was the buckling load for the beam and wingbox, respectively, as noted in Figure 4-11. Increments of 10% of the load were analyzed for the model before scaling (Figure 4-14). The load was applied at the wing tip from a node at the tip through a node directly above the tip that was rigidly connected to it in all degrees-of-freedom. This method ensured that the force would act like a simulated aerodynamic load force by remaining perpendicular to the surface. Hence, this force followed the deflection of the surface of the flexible wing.

The nonlinear deflections of the wingbox were in better agreement with the beam strut model in the T3 direction than the R2 direction. Like the natural mode shapes, the nonlinear deflection match is quantified by the relative error norm given by Equation (4.11). For T3 this ratio is 0.0071 at 10% of the buckling load and 0.3425 at 100% of the load, where the 100% load is equal to the critical buckling load. For the R2 rotations this ratio ranges from 0.5815 to 0.9169. This demonstrates that the deflections do not match well for nonlinear deformations.

The beam was more flexible than the scaled wingbox. Thus, the critical buckling eigenvalue of 15,813 was more than 40% higher than the initial wingbox. Before the optimization, the wingbox model deflections were lower than the linear analysis of the beam and only within 20% of the beam deflections up to 70% of the buckling load of the wingbox in the fore wing and only accurate up to 50% of the buckling load in the aft wing. However, the scaled wingbox is within 20% of the beam displacements for up to 80% of the buckling load in the fore wing and up to 60% in the aft wing (Figure 4-15

through Figure 4-17). In practice a design would not be taken to the buckling load. However, mathematically applying the buckling load is important for comparison of the nonlinear deflections. It is apparent at all three positions shown that the reduced scale model response does not match that of the target model.

The target Goland aft wing was designed to be very flexible to ensure that it would be the first to buckle as do other joined-wing designs. The aft wing deflection moved in the upward direction and then in the downward direction as the load was increased (Figure 4-17). This is likely due to imposing a supple aft wing and applying the buckling reference load at the tip. The whole structure did not go unstable, since no load was applied to the aft wing.

If the nonlinear response of the target wings was captured correctly, the reduced scale model would demonstrate a similar response. This was not the case and is consistent with the high calculated relative error norms at 100% load. It is valid to look at the nonlinear response at and beyond the buckling load, because the fore wing continues to carry load after the aft wing buckles.
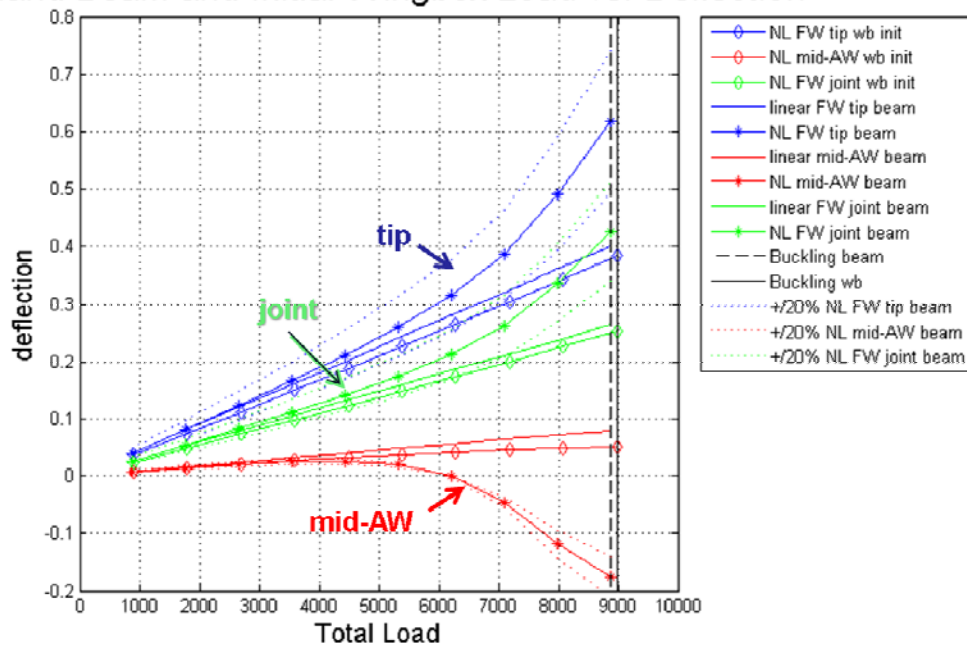
Figure 4-14. Nonlinear deflections due to buckling load applied to initial wingbox and beam.

Figure 4-15. Nonlinear deflections at the wing tip due to buckling load applied to wingbox (before and after scaling) and beam.

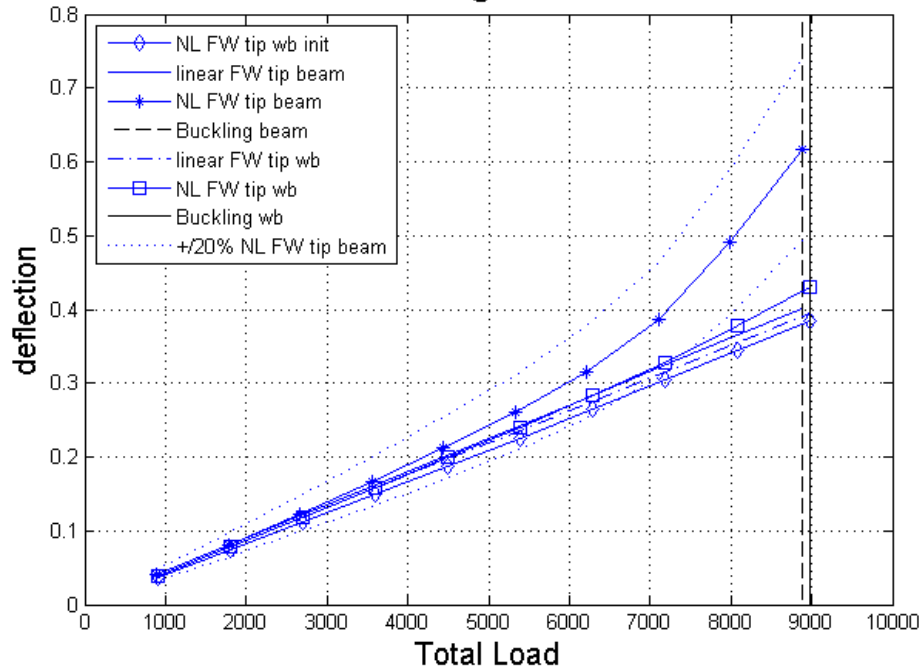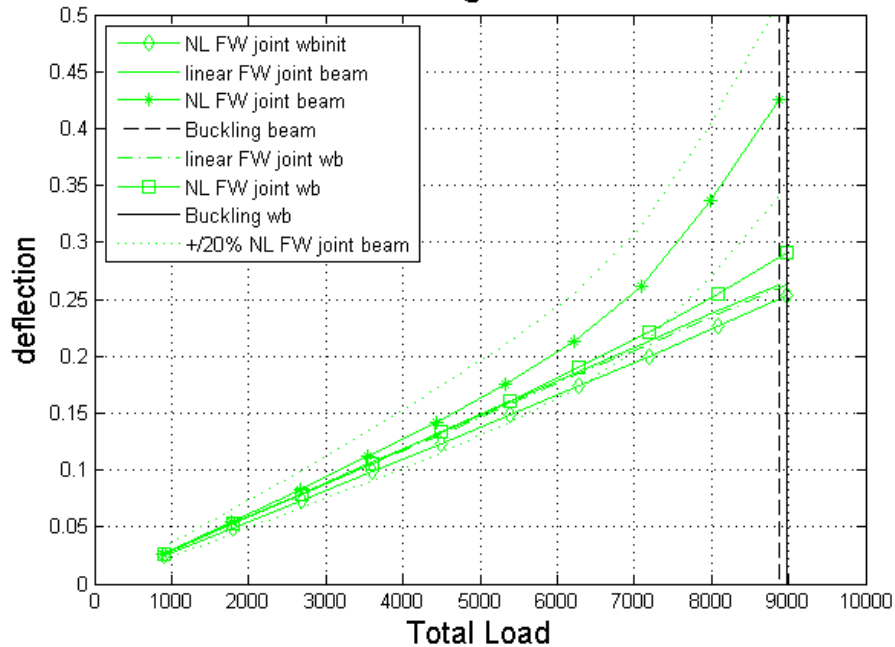**Figure 4-16. Nonlinear deflections at the joint due to buckling load applied to wingbox (before and after scaling) and beam.**
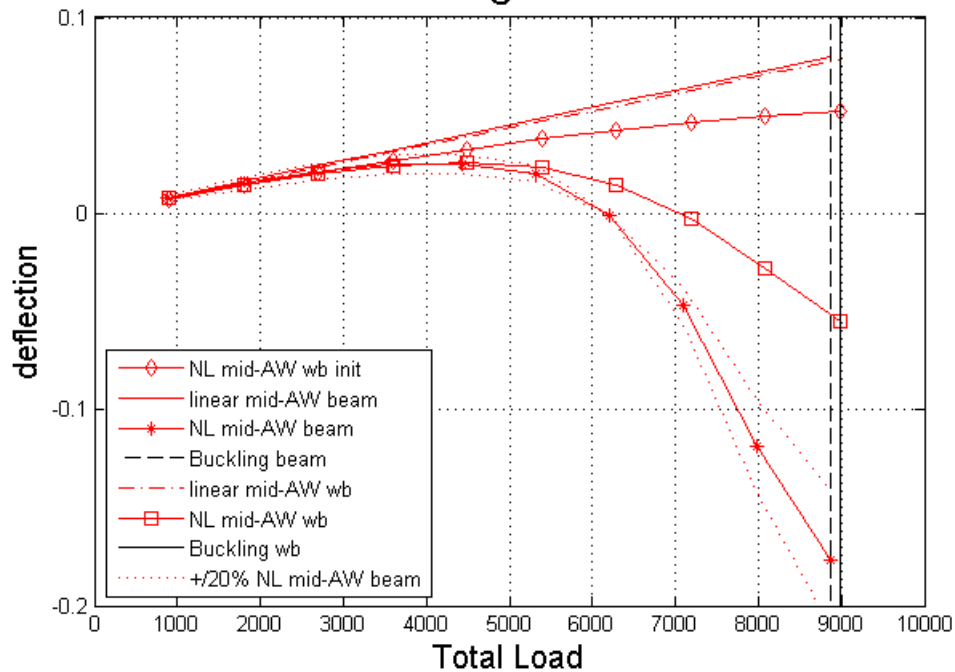
Figure 4-17. Nonlinear deflections at the mid-aft wing due to buckling load applied to wingbox (before and after scaling) and beam.

66

4.4   <u>Scaling Discussion</u>

Using the Goland wing and several variants in this case study, it is evident that aeroelastic scaling requires the proper matching of natural mode shapes, in addition to natural frequencies. It was clear that if only the natural frequencies are matched, there is potential for the aeroelastic properties to be unmatched for two models. In addition to linear scaling with the modal vibration eigenvalues and eigenvectors, the buckling eigenvalues and eigenvectors were considered in order to include scaling the nonlinear effects.

For this case of follower-force type of nonlinearity, the reduced scale model underestimated the nonlinear deformations of the model it was attempting to match. Apparently, it may be necessary to match the entire geometric stiffness matrix, and perhaps more vibration modes, to scale nonlinear response. Geometric stiffness depends upon element internal loads, which should be examined more closely for this case. Specifically, whether internal beam forces are faithfully reproduced by wingbox internal forces transferred to the elastic axis by rigid ribs, used here, should be verified.

The hypothesis explored in this chapter was that if the vibration eigenvalues and eigenvectors were matched along with the first buckling eigenvalue and eigenvector the nonlinear response would be sufficiently scaled. The following recommendations may prove useful to properly scale nonlinear response for further research, since the aforementioned hypothesis was proven untrue.

First, only the critical buckling mode was matched for the Goland joined-wing case study. The case study in this chapter demonstrated aft-wing buckling while the rest of the aircraft continued to carry load. Matching higher buckling modes may aid scaling

the nonlinear response. Buckling modes after critical buckling may significantly contribute to the nonlinearities that occur.

Second, geometric stiffness for the buckling mode relies on the internal load being equivalent in the target and reduced scale models. The internal loads in a beam may not be represented well in the wingbox internal loads. The case study matched axial loads for the beam that represents the elastic axis of the wingbox. However, the internal loads in the wingbox are in the skins and spars. Rigid ribs transferred the internal loads to the elastic axis nodes. The transfer of internal loads through rigid ribs to the skins and spars may not have produced the same geometric stiffness.

Lastly, a less convenient technique discussed in the theory section, Chapter 3, was to wrap an optimization scheme around nonlinear analysis. This more direct method may prove useful if the trials mentioned here also fail.

Here the scaling method determined if the nonlinear response of a subscale model would have the same nonlinear response as a full-scale model. This method attempted to fill the gap between an aeroelastically scaled model response in the linear regime to that of an aircraft configuration, like a joined-wing. This particular joined wing, the Joined-Wing Sensorcraft, requires preliminary design investigation in the geometrically nonlinear regime due to its high-aspect ratio wings.

The demonstration in this chapter of scaling a FEM with an aft wing is tied to the two experiments shown next in that they are parametrically scaled. Their aerodynamic and nonlinear responses are experimentally demonstrated. In the first experiment an aerodynamically scaled joined wing with aft-wing twist verifies flexible twist pitch

control is feasible (Chapters 5). The second experiment characterizes nonlinear response

(Chapters 6).

5. Pitch Control Experimental Approach, Results and Discussion

5.1   Wind Tunnel Model Design and Research Requirements

5.1.1   Scaling Requirements

As mentioned in Section 3.1, one of the primary considerations for scaling the aerodynamic characteristics of the full-scale article is matching the Reynolds number. In addition, there are real world limitations which must be taken into account, such as the size and speed of the wind tunnel, the instrumentation used, and the ability to produce an accurate model at the final scale factor.

The scale of the test model was determined primarily by the physical constraints of the Gottingen wind tunnel at the Portuguese Air Force Academy, where the tests were accomplished. The tunnel was used in an open test-section configuration with a cross section of 1.2×0.8×2 m. To avoid turbulence, the usable test area must maintain uniform flow velocity (less than 0.8% in pressure variation), limiting the testable area to 1.1×0.6×1.4 m. A six-degrees-of-freedom Schenck wind tunnel force balance was used to measure the forces and moments experienced by the model, which dictated that the wing be mounted vertically. With these constraints, the wind tunnel model was limited to 0.6 m for half-span.

5.1.2   Design Requirements

The full-size Joined-Wing Sensorcraft was sized appropriately for a 0.6m half-span, resulting in a 1:38 scale model. Recent experience with this wind tunnel has shown that this size model remains outside the shear layer induced by the wind tunnel at flow velocities up to 50 m/s. The test velocities were approximately 20, 30, 40 and 50 m/s, respectively. At these lower speeds, however, it was anticipated that the pressure sensors

would be unable to record valid data. The usable pressure data test conditions were 30, 40 and 50 m/s.

With the given constraints, it was not possible to match the Reynolds number in this wind tunnel. To calculate Reynolds number the following equation was used with fore wing mean aerodynamic chord (MAC) as the characteristic length:

$$\text{Re} = \frac{\rho_\infty V L}{\mu} \qquad (5.1)$$

The values in Table 5-1 illustrate that the Reynolds number of the wind tunnel testing and the full-scale aircraft are different by two orders of magnitude. As mentioned in the Theoretical Formulation, Chapter 3, the Reynolds number effects may account for the high drag measured during testing, since the wind tunnel model Reynolds number is below the critical Reynolds number of $5\text{x}10^5$.

Table 5-1. Reynolds number comparison for wind tunnel and full-scale aircraft.

	Wind tunnel testing	Full-scale aircraft loiter	Full-scale aircraft ingress/egress
V_i (m/s)	30-50	118	177
L (m)	0.097	3.68	3.68
μ (Pa-s)	1.82e-5	1.82e-5	1.82e-5
MAC (m)	0.097	3.68	3.68
ρ (kg/m^3)	1.19	1.19	1.19
Re	1.90e5 - 3.23e5	2.89e7	4.33e7

5.1.3 Measurement Requirements

In designing the wind tunnel model, the measurement requirements were taken into account. Lift, drag and side force coefficients were measured by the Schenck wind tunnel force balance, which also dictated that the half-span model be mounted vertically (Figure 5-1). The right half-span was chosen arbitrarily. The equations used to transform the forces are

$$L = F_x \sin\alpha + F_z \cos\alpha \qquad (5.2)$$

$$D = -F_x \cos\alpha + F_z \sin\alpha , \qquad (5.3)$$

where L is lift , D is drag, F_x and F_z are the components of the resultant pressure force

acting on the vehicle measured by the Schenck balance, and α is the angle-of-attack.
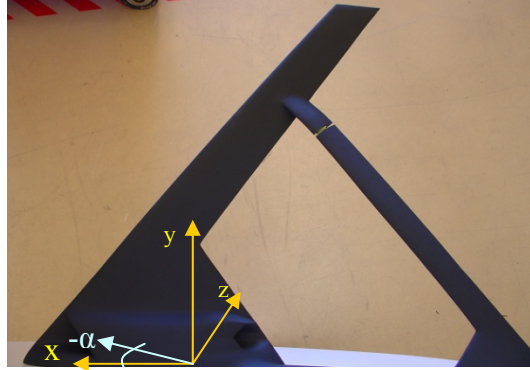
Figure 5-1. Wing tunnel model with nominal aft wing.

5.1.4   Twist Tailored Model Design

This study made use of an existing design, supplied as a FEM by the Sensorcraft

program office for the purpose of risk mitigation to their program (Figure 5-2). The FEM

was used to create the shape of the wind tunnel model, both in the nominal configuration,

and also with ±15˚ of aft-wing twist. Structural modifications were made to the FEM to

enable a twisted aft wing, and then the OML of the twisted configurations was used to

create the wind tunnel shapes.

The ±15° aft-wing twist requirement value was chosen based on calculations for

pitch control on the AFRL/AFIT-designed wing [25], although it is an otherwise arbitrary

value for the purpose of this design. In order to reduce the force required to achieve wing

twist, simulating a realizable actuator, the aft-wing FEM was modified in two ways.

First, a slit was made spanwise in the skin of the aft wing to allow for a more unrestricted

twist (Figure 5-2). Then the ribs of the FEM (Figure 5-4) were modified from a solid section to a three-sided rod design to allow for the skin to deform without the restriction of the rib near the location of the slit (Figure 5-3). These modifications allowed for the use of a 49,856 N (11,208 lbs) actuator, which is less than that used in the Boeing F-15 Eagle elevator actuator of 124,550 N (28,000 lbs) [28] to achieve 15 degrees of change in control-surface angle. The wind tunnel model was not designed to twist dynamically, but to have a fixed twist built into the rigid model. Therefore, to accomplish the required test objectives, three different wind tunnel model configurations were required. The OML of the nominal wing (no twist), and resulting wing twisted up and down 15° were given to a computer-aided design (CAD) modeler to make detailed drawings from which the wind tunnel models were fabricated.
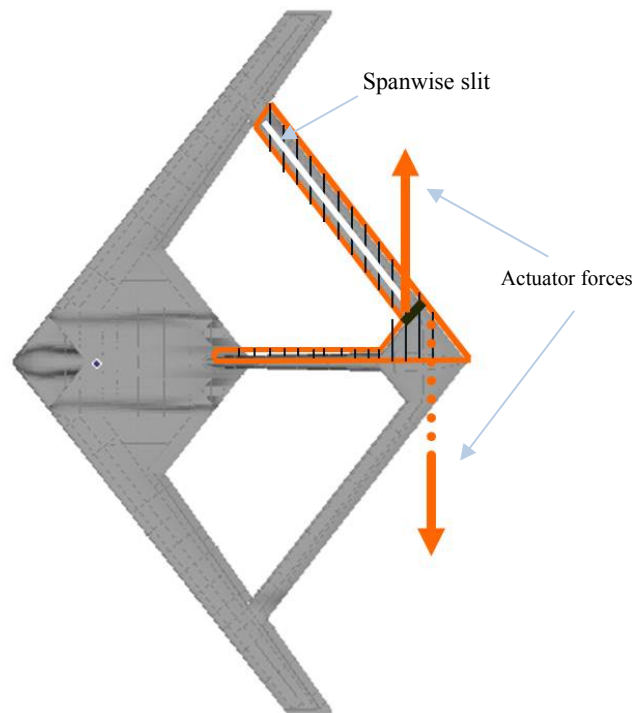
Figure 5-2. Aft wing with spanwise slit (not to scale).
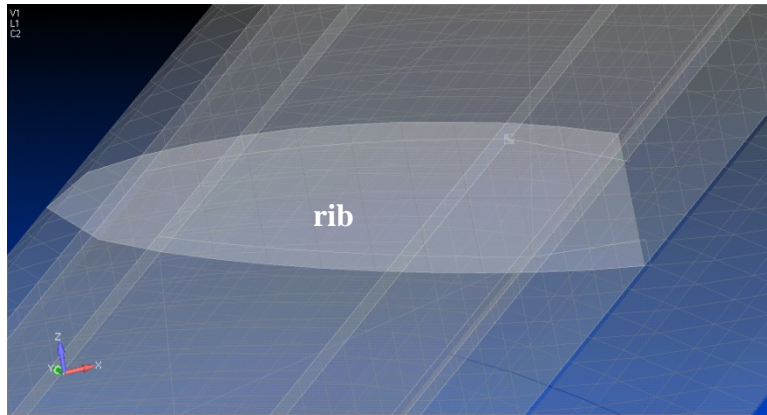
Figure 5-3. Original rib (white).
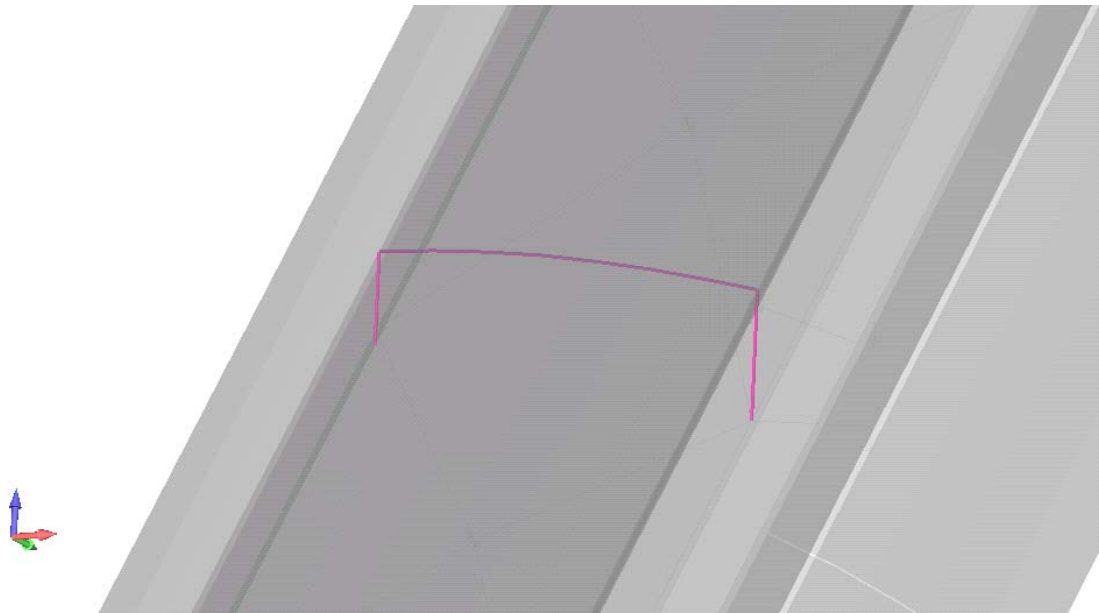
Figure 5-4. Modified rib for torsional compliance (magenta).

5.1.5   Wind Tunnel Model Fabrication

The wind tunnel models were fabricated from foam, balsa wood and fiberglass. Placement of the pressure ports was also finalized during fabrication and was complicated by the small size of the 1:38 scale model. The leading-edge-down twist is illustrated in Figure 5-5. This depicts the FEM prediction of the OML of the wing

twisted down 15°. Note that the primary area of twist occurs at the root, which is expected, given the location of the actuation force is a coupled force at the aft wing-tail joint (Figure 5-2).
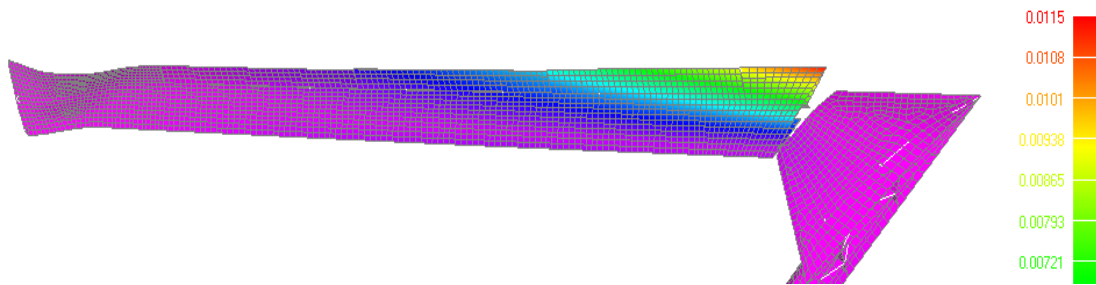
Figure 5-5. Aft wing total transition with spanwise slit.

Due to the complexity of the design, it was decided to build just one model with a reconfigurable aft wing. The nominal aft wing could be replaced by either of the twisted (15° up or down) aft wings (Figure 5-6).
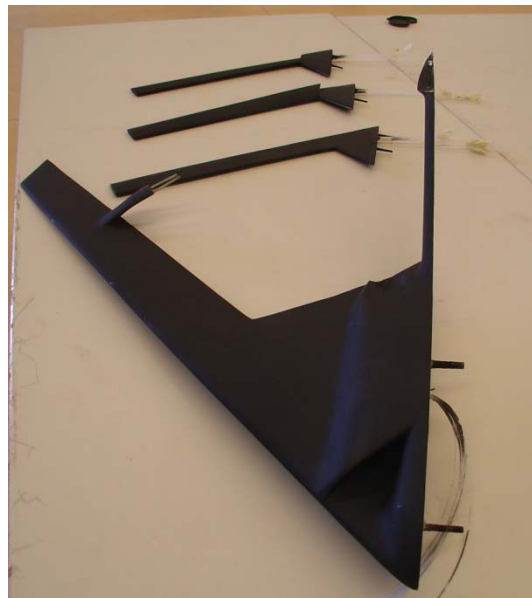
Figure 5-6. 0.6 m half-span model with nominal, 15 down and 15 up (front to back) twisted aft wings.

5.2 Wind Tunnel Testing

5.2.1 Test Equipment Description

A Schenck force balance was used to measure the forces and moments in the x, y, and z directions (see Figure 5-1). The model was mounted on a platform which sits on top of the Schenck scale. The platform has a disk cutout such that the model could be rotated to new angles-of-attack without adjusting the wind tunnel conditions. The coefficient of pitching moment, C_M, coefficient of moment in roll, $C_{L(roll)}$, and yaw, C_N from the mount position are normalized as follow:.

$$C_{L(roll)} = \frac{M_x}{q_\infty \frac{S_{mod}}{2} b}, \quad C_M = \frac{M_y}{q_\infty \frac{S_{mod}}{2} c}, \quad C_N = \frac{M_z}{q_\infty \frac{S_{mod}}{2} b}. \tag{5.4}$$

Testing was accomplished in the Portuguese Air Force Academy's Gottingen wind tunnel (Figure 5-7). The closed circuit horizontal tunnel was used in the open test-section configuration, a contraction ratio of 1:5.53, and a test velocity range from 5 to 70 m/s. The test limitations particular to this study are described in the Scaling Requirements, Section 5.1.1.

Figure 5-7. Gottingen Wind Tunnel Diffuser.

The test set-up also included a control room where pressure, temperature, force and moment measurements could be monitored and wind tunnel test functions controlled. Computer recording pressure measurements, display for outside pressure, computer recording balance measurements, laptop for analyzing data real-time, angle-of-attack controller for the balance are shown left to right in Figure A-6. Wind tunnel power was controlled via the panel depicted in Figure A-7. The wind tunnel was cooled by a water cooling system controlled via the panel depicted in Figure A-8. Tunnel temperature (deg C), tunnel air velocity, velocity controller knob are shown top to bottom and emergency power shutoff shown lower left (Figure A-9).

Pressure measurements were taken from a single span location on each of the front and aft wings. The location was chosen halfway between the joint and root on each wing to minimize flow interaction from another surface. Figure 5-8 depicts the approximate cross-sectional locations of these ports, while Table 5-2 lists the exact locations with respect to the leading edge of each wing.
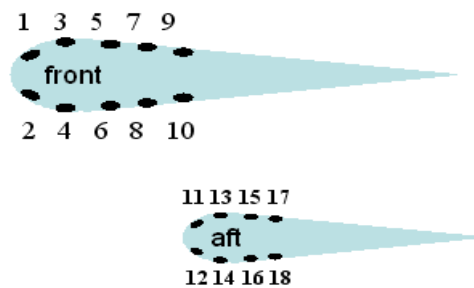

Figure 5-8. Pressure port locations of fore and aft wings.

Table 5-2. Port position relative to the leading edge.

Port number *	Fore Wing position (mm)	Port number*	Aft Wing position (mm)
1/2	5	11/12	3
3/4	16.5	13/14	8.5
5/6	29	15/16	14.5
7/8	41	17/18	20
9/10	53		
*Note: Odd port numbers are on the top of the wing and even are on the bottom.			

Each of the 18 pressure ports were connected to two pressure transducers (Figure A-10) via NetScanner™ Model 9016 Ethernet Intelligent Pressure Scanners to acquire the 18 discrete measurements (Figure A-11). The system scanners were connected to a National Instruments data acquisition system (Figure A-10), which in-turn was connected to a personal computer, used to run LabVIEW software and record the data. A schematic of the LabVIEW sequence, the pressure measurement test and force balance set-ups are shown in Figure A-12, Figure A-13 and Figure A-14, respectively.

5.2.2   Test Procedures

Prior to operating the wind tunnel, the ambient values of the forces and moments were recorded at each angle-of-attack. The force and moment measurements were taken until each was within 0.05 N or N-m, respectively. Once this tare was recorded, the data acquisition systems were configured for the test run.

For wind tunnel operation, the outside air pressure was recorded for use in determining the dynamic pressure of the test run. The tunnel was turned on and adjusted to the speed required for the data capture. The wind tunnel air flow temperature was monitored until the temperature was stable, indicating steady flow and readiness for test.

Once the desired angle-of-attack was set, two to three force and moment measurements were typically recorded while pressure data was simultaneously collected.

Then, the angle-of-attack was incremented by one degree and the process repeated. This process was repeated at each airspeed for each configuration, nominal and ±15° aft wing. The test matrix is outlined in Table 5-3.

Table 5-3. Wind Tunnel Test Matrix

Aft-wing twist (deg)	Velocity (m/s)	AOA (deg)
Nominal	20, 30, 40, 50	-15 to +15
+15	20, 30, 40, 50	-15 to +15
-15	20, 30, 40, 50	-15 to +15

5.2.3 Test Set-up

Initial flow visualization testing was accomplished in an attempt to show stall characteristics. Although testing was accomplished through a wide range of angles-of-attack, stall was not apparent. It would have been interesting to determine where stall occurs for a joined-wing configuration where the forward and aft wings are not inline, but vertically offset. In this case, the vertical offset produced a joint angle (fore wing dihedral plus aft wing anhedral) of over 16° (Figure 5-9).

Each configuration, nominal, twist-up and twist down was tested at varied conditions given in Table 5-3. Since the focus of this study is on pitch control, changes in angle-of-attack were the primary focus. Testing was accomplished at angles-of-attack from -15º to +15° in 1° increments.

Figure 5-9. 16 degrees of offset between the front and aft wings.

Experimental results obtained using the method of test described in this section are analyzed and discussed in the next section. The measured results are compared to panel-method aerodynamic predictions. It will show how the use of aft-wing twist was experimentally feasible on a subscale aerodynamic model.

5.3   Analytical and Experimental Test Force and Moment Results

The following discussion focuses on pitch control, but also highlights some characteristics worthy of note based on these tests. The remainder of the experimental force and moment data and experimental pressure data are deferred to Appendices A and B, respectively.

Most important to this portion of the study is the second task of the problem statement:

Determine aerodynamic forces such that pitch control is realizable.

Not only does coefficient of pitching moment, C_{My}, come into play to demonstrate wing twist effectiveness, but also features such as the usable range of angle-of-attack before separation occurs, and possible contribution from Reynolds number not equivalent to the full-scale FEM.

Since the data are normalized in coefficient form, the $C_{L\alpha}$ curves are consistent for the various airspeeds in the nominal aft wing configuration (Figure 5-10). The analytical results produced in MSC/NASTRAN from the aerodynamic panel model were also reasonably consistent with the experimental data within the linear regime (Figure 5-10). However, since camber and thickness were not modeled in MSC/NASTRAN, zero lift occurs at -2˚ angle-of-attack for the experimental data and -3.5˚ angle-of-attack

for the analytical results. If the lift coefficient is plotted such that zero lift occurs at zero angle-of-attack, the results and data match in the linear regime (Figure 5-11).
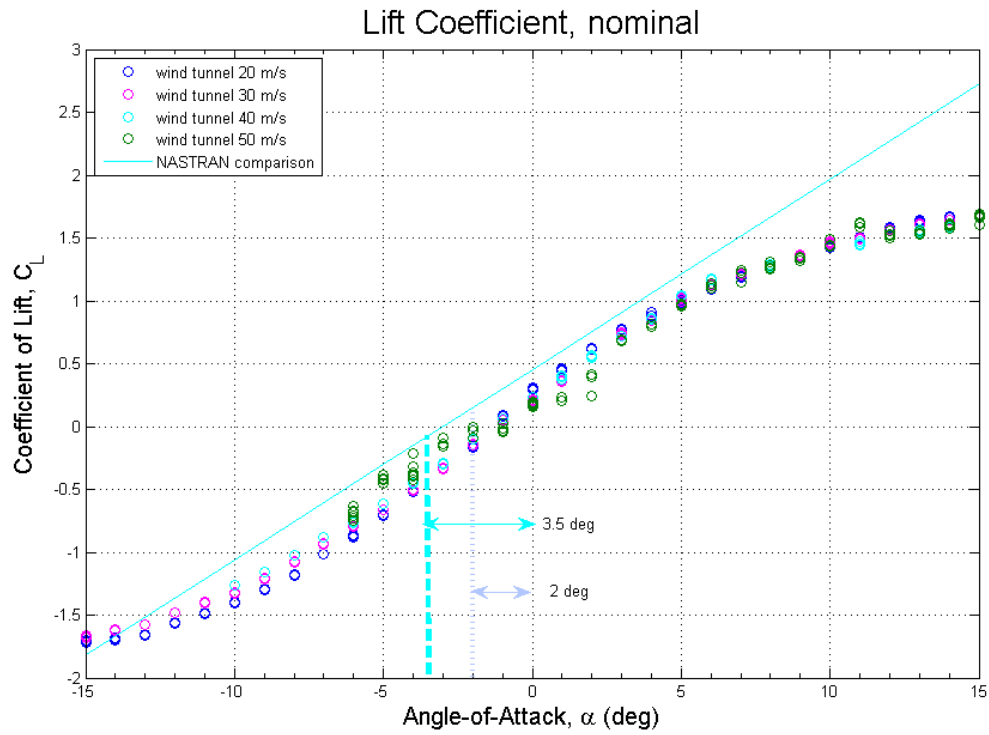
Figure 5-10. Lift curves for nominal aft wing configuration.
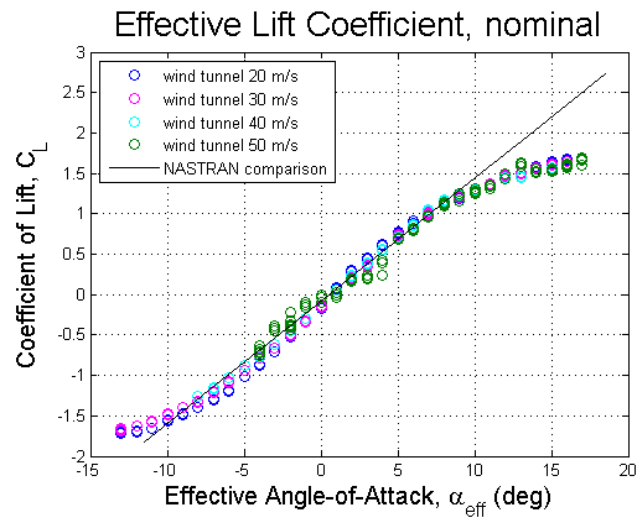
Figure 5-11. Experimental and analytical lift adjusted for the zero-lift angle-of-attack.

While the lift curves are fairly consistent, the wing twist effectiveness seems to be affected by the higher velocity (Figure 5-12), possibly due interference from the fore wing.

Figure 5-12. Wing twist effectiveness for nominal aft wing configuration adjusted for the zero lift angle-of-attack.

Figure 5-13. Experimental to analytical ΔC_{My} for nominal aft wing configuration.

The analytical results produced in MSC/NASTRAN from the panel model after correction for zero lift angle-of-attack still show a ΔC_{My} from the experimental results (Figure 5-13). The delta can be calculated by:

$$
\begin{aligned}
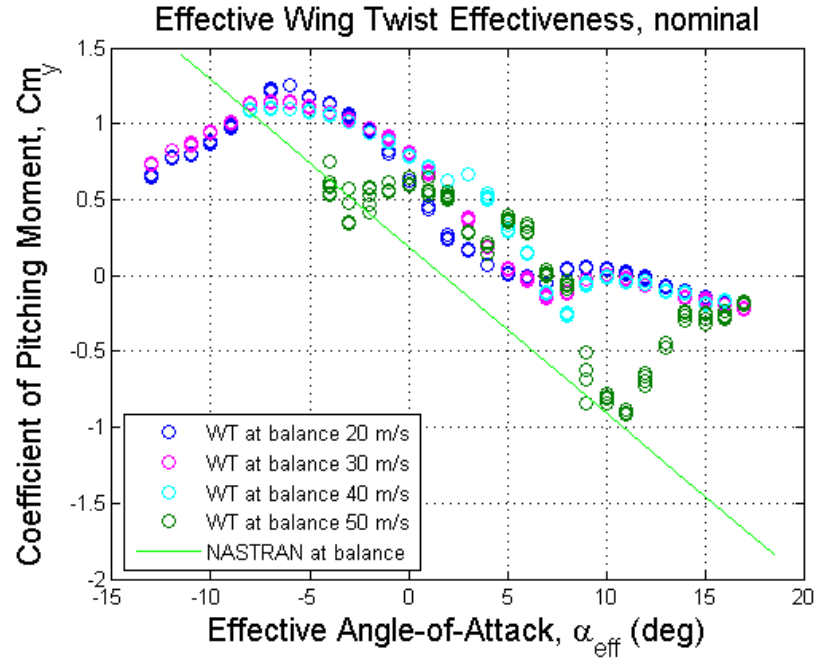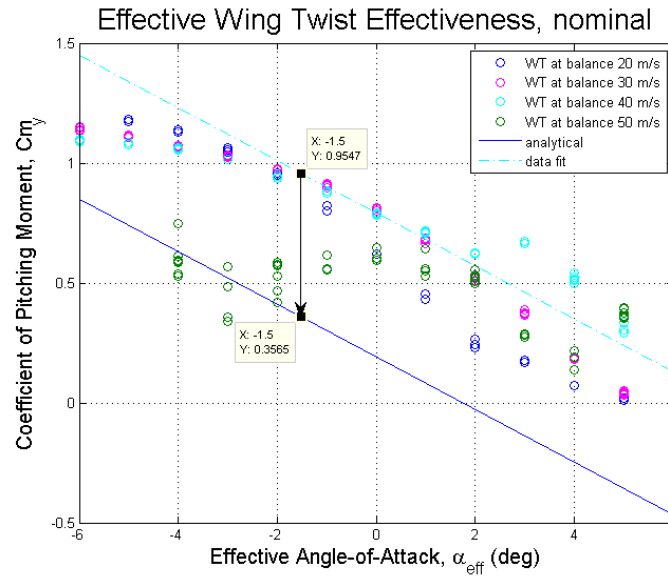\Delta C_{My} &= \left(C_{My}\right)_m - \left(C_{My}\right)_w \\
&= \left(\frac{L_{c.p.}}{\frac{1}{2}q_\infty S}\right)_m \left(\frac{d}{c}\right)_m - \left(\frac{L_{c.p.}}{\frac{1}{2}q_\infty S}\right)_w \left(\frac{d}{c}\right)_w \\
&= \left(C_L\right)_m \left(\frac{d}{c}\right)_m - \left(C_L\right)_w \left(\frac{d}{c}\right)_w
\end{aligned}
\tag{5.5}
$$

where $L_{c.p.}$ is the lift at the center of pressure, c is the chord of the fore wing (subscripts w and m represent the full-scale and subscale, respectively) and d is the moment arm used to calculate the pitching moment, C_{My}, of the vehicle to include both wings. Based on the aforementioned exercise of aligning the full-scale (analytical) and subscale wind tunnel results, $\left(C_L\right)_m = \left(C_L\right)_w$. Thus, (5.5) can be simplified

$$
\Delta C_{My} = \left(C_L\right)\left[\left(\tfrac{d}{c}\right)_m - \left(\tfrac{d}{c}\right)_w\right]
\tag{5.6}
$$

A correction factor moment arm, Δd, can be applied to equate the analytical to experimental pitching moment coefficient, $\left(C_{my}\right)_w$,

$$
d_{corrected} = d_w + \Delta d_w
\tag{5.7}
$$

such that

$$
\left(\frac{d_{corrected}}{c}\right)_w = \left(\frac{d}{c}\right)_m
\tag{5.8}
$$

Solving for d_w and substituting, (5.6) becomes,

$$\Delta C_{My} = (C_L)\left[\left(\tfrac{d}{c}\right)_m - \left(\left(\tfrac{d_{corrected}}{c}\right) - \left(\tfrac{\Delta d}{c}\right)\right)_w\right] \quad (5.9)$$

Applying Equation (5.8),

$$\Delta C_{My} = (C_L)\left(\tfrac{\Delta d}{c}\right)_w, \quad (5.10)$$

and solving for the correction factor moment arm using the experimental data at -1.5 degrees angle-of-attack,

$$\begin{aligned}
\Delta d_w &= (c)_w \frac{\Delta C_{my}}{C_L} \\
&= (3.68\text{m})\frac{0.5985}{-0.3028} \quad (5.11)\\
&= -7.27\text{ m}
\end{aligned}$$

This is evidence of the need for experimental results, since this correction factor can be applied to correct future analytical models. The sign convention of the correction factor moment arm is consistent with the angle-of-attack. This is a significant center of pressure correction, nearly two mean aerodynamic chord lengths. Thus, modeling camber in NASTRAN may be important for predictions.

Examination of force data revealed that the deflection of the twist-down aft-wing configuration was not as continuous as the nominal and twist-up configurations. For instance, Figure 5-14 indicates a 71% change in pitching moment between 5° and 6°, whereas the change between 4° and 5° is only 22%. There is a noticeable break at the outer-mold line to allow freedom of movement at the root joint (Figure 5-5). A shroud, planned for later models, possibly would decrease the drag, especially noticeable for the twist-down configuration (Figure 5-17).
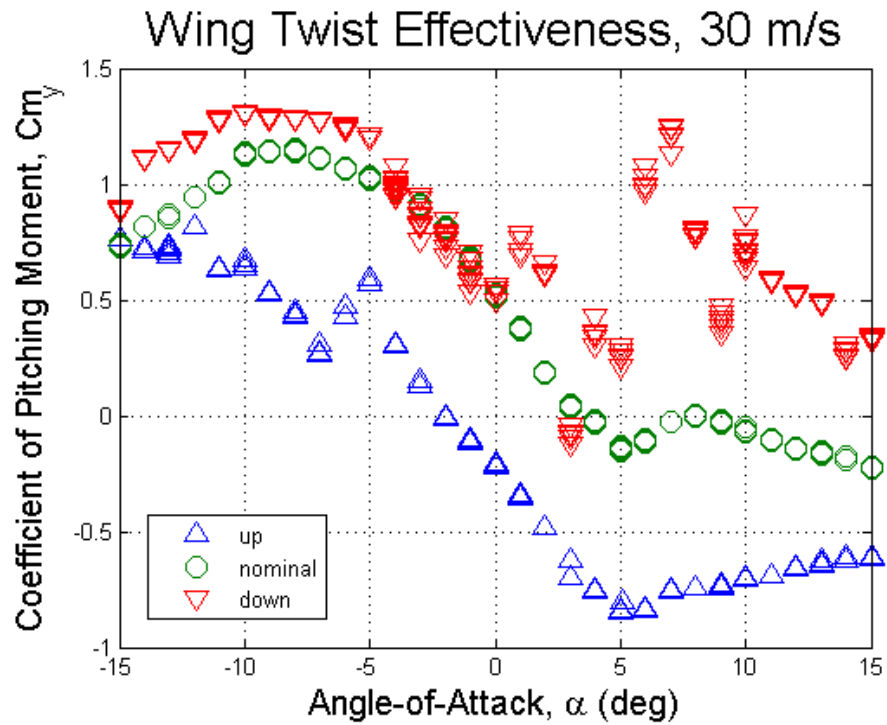
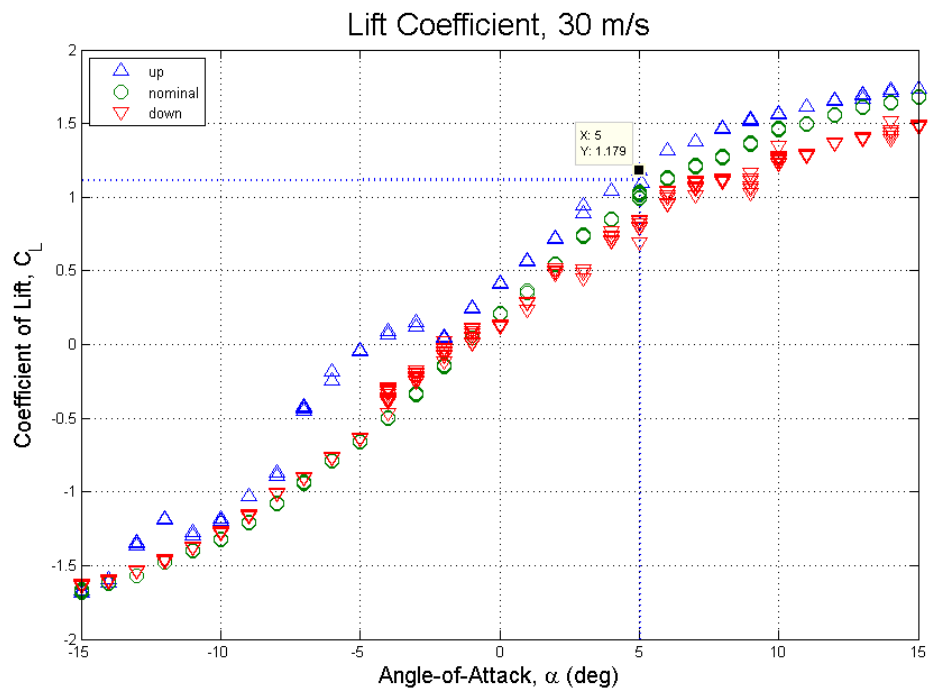**Figure 5-14. Twist effectiveness for twist up, down and nominal configurations.**

Figure 5-15. Lift curves for twist up, down and nominal configurations.

Figure 5-15 indicates a possible separation for the twist-up configuration below -2° angle-of-attack, possibly due to flow from the fore wing impinging on the aft wing. Figure 5-16 reveals that the drag at low angles-of-attack contributes the most to the drag polar in the twist down configuration. Twist-down apparently leads to separation above -5° angle-of-attack. Severe restriction of the flight envelope would have to be avoided by an improved aerodynamic design. Nominal and twist-up minimum drag appears at about -4° or -5° angle-of-attack, which is also not ideal. An improvement to this design would have $C_{D_{min}}$ at a C_L greater than zero. Further, Figure 5-17 indicates the best lift-to-drag ratio occurs at a C_L of 1.18, which is just beyond linear range of Figure 5-15 near 5° angle-of-attack.
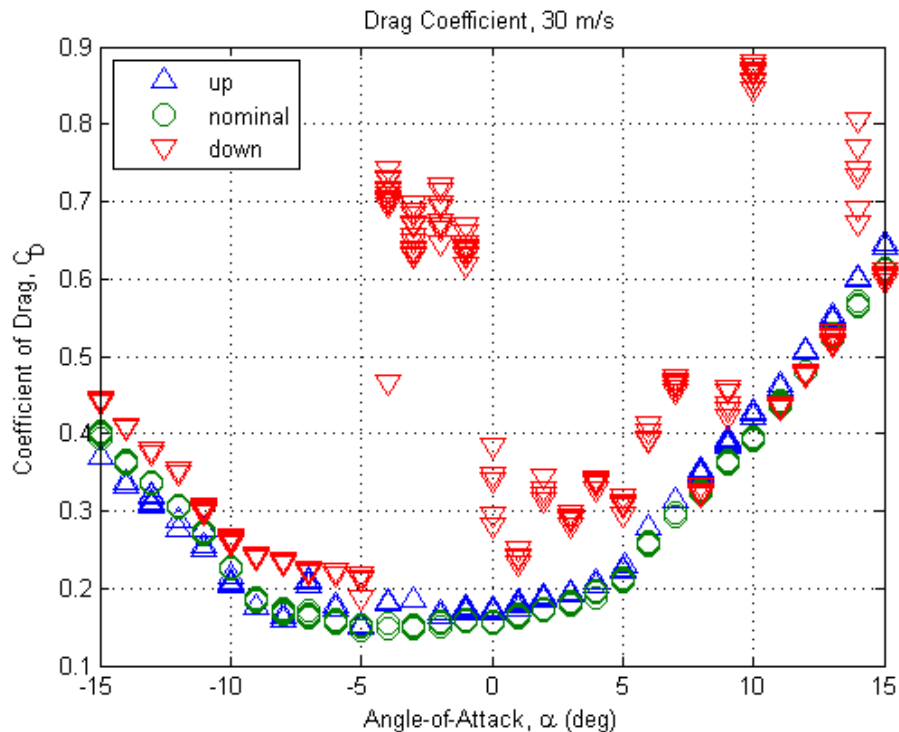

Figure 5-16. High drag at low angles-of-attack in the twist down configuration.
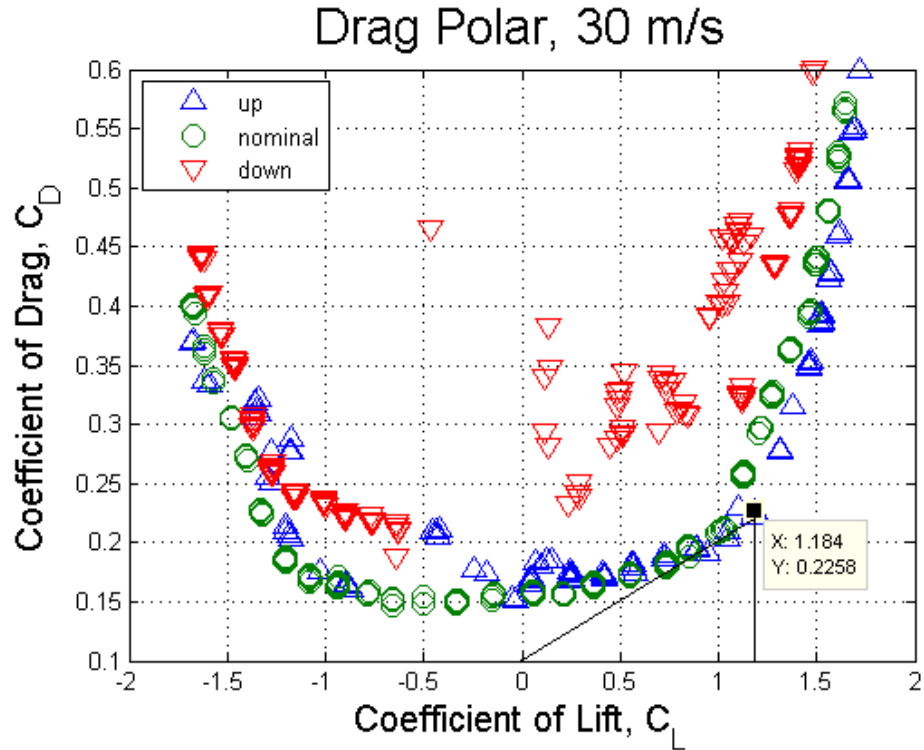
Figure 5-17. Drag polar for twist up, down and nominal configurations.

Further examination suggests that there is a breakdown in the flow due to separation at low angles-of-attack [39]. It is evident from the departure from the linear region in the axial force plot that this occurs above 5 degrees angle-of-attack at most velocities (Figure 5-18 and Figure 5-19).

Maximum L/D at 5 degrees angle-of-attack in Figure 5-20 is consistent with Figure 5-15 and Figure 5-17 at less than 6. Due to the breakdown in flow this is contrast to the L/D=24 assumed in Roberts and Rasmussen studies and L/D of mid to high 20's found by Craft, as mentioned in Chapter 2.

Figure 5-18. Separation onset at low angle-of-attack.

Figure 5-19. Separation onset delayed at higher Reynolds number.
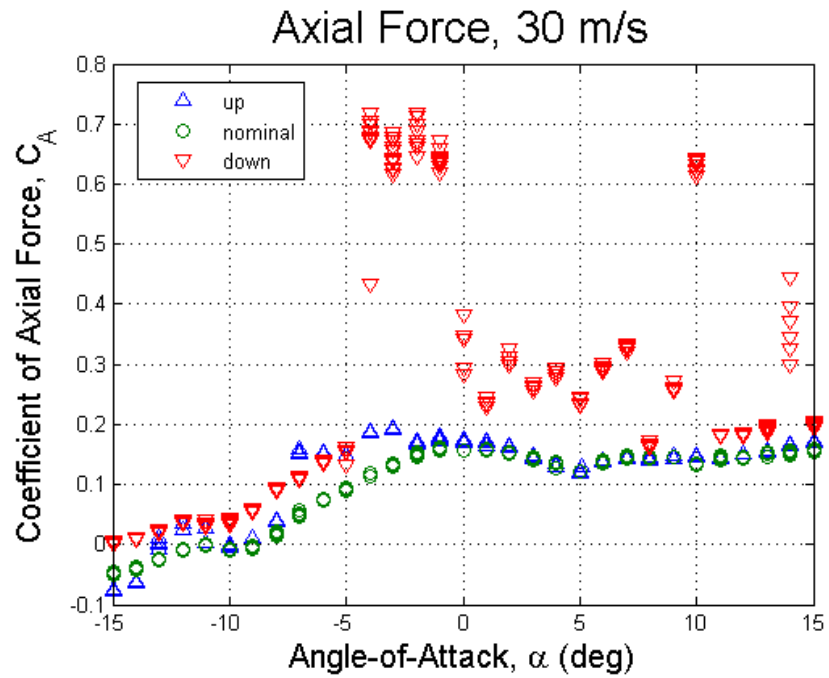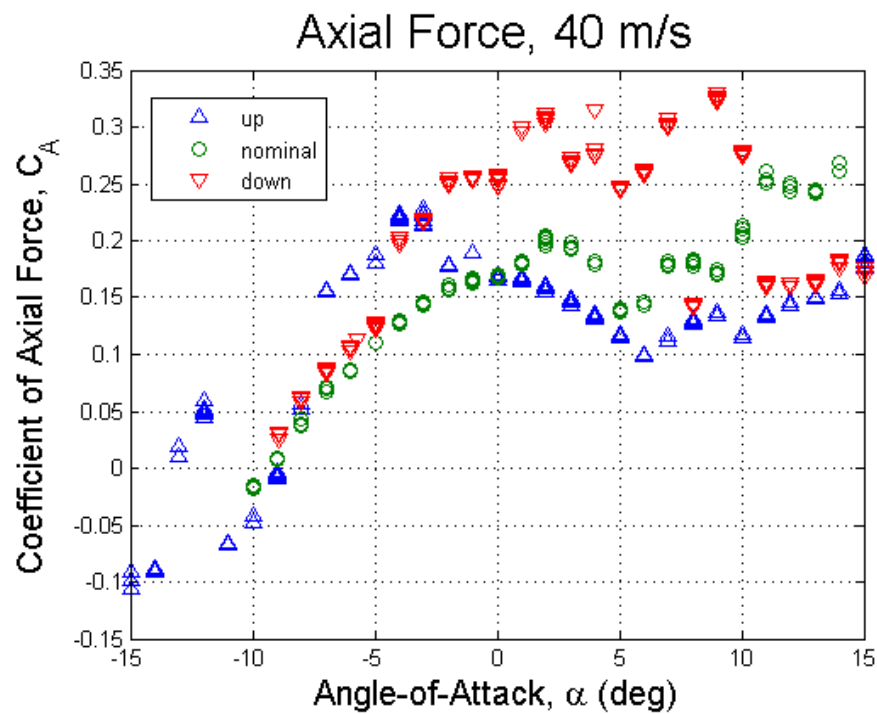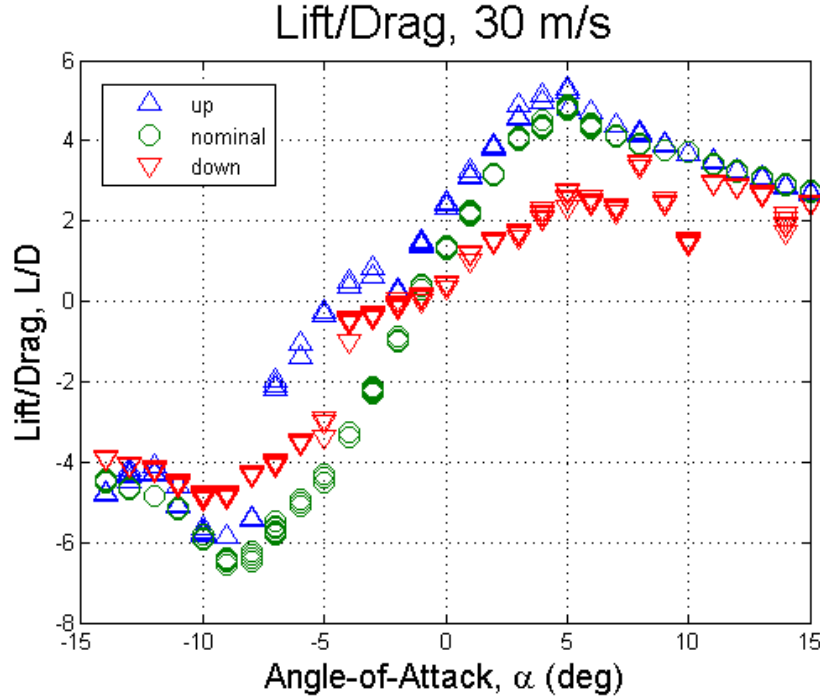
Figure 5-20. Lift-drag ratio for twist up, down and nominal configurations.

The trends in the experimental force and moment data indicate that there is an extremely tight angle-of-attack range in which the vehicle is not stalled or in a turbulence region. Thus, the airfoil design and twist mechanism are critical to prevent such an early stall. In addition, shrouding the joint is important to decrease the stall explicitly evident in the aft-wing twist down configuration. Also, the calibration for zero lift angle-of-attack and $d_{c.p.}$ found in the $C_{L\alpha}$ and C_{My} curves is useful for the validity of the present doublet-lattice aerodynamics and for the next-generation design.

5.4   Analytical and Experimental Test Pressure Results

In addition to force and moment, the pressure was measured at the mid-section of each of the wings. The intent was to use this to help explain phenomena in the force and

moment data that may not be fully understood. The 30 m/s case is presented here with a comparison to the analytical results produced in MSC/NASTRAN from the aerodynamic model (Figure 5-21).
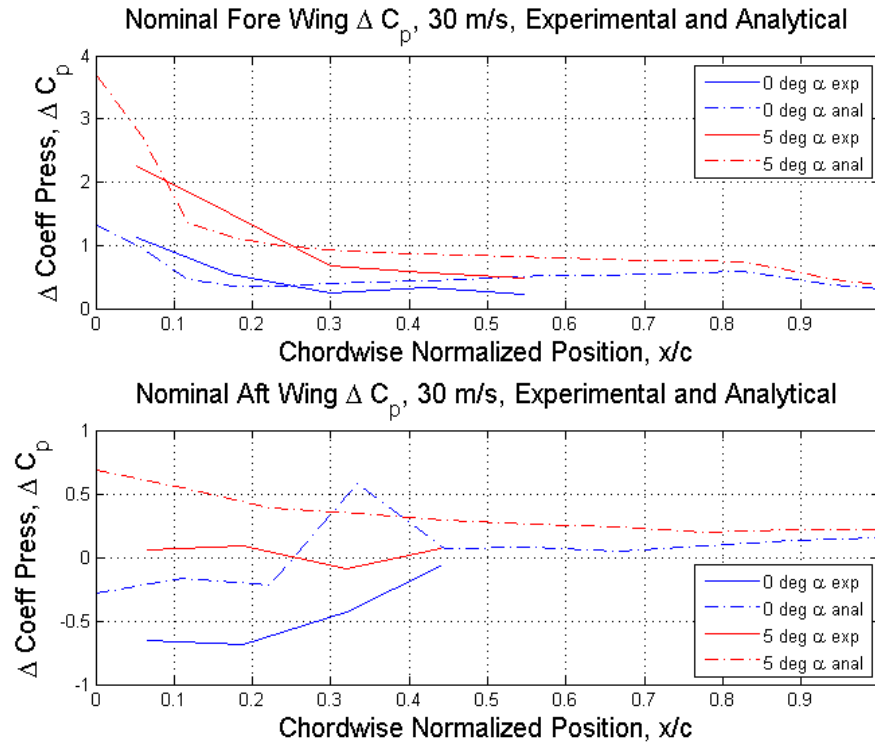
Figure 5-21. Analytical and experimental pressure results with nominal aft wing configuration.

The drastic change in pressure between 5 and 10 degrees angle-of-attack (top plot in Figure 5-22) may account for the "dip" in C_{My} between 5 and 10 degrees angle-of-attack (Figure 5-14).

5.5   Pitch Control Discussion

Although there is a small linear range of angle-of-attack for this case study, it was useful in projecting the possibility for designers of configurations of this type to use a wing-twist mechanism for pitch control. It was clearly shown that the effectiveness of

the control mechanism is a viable alternative to control surfaces. This will allow more room in the wing for sensor placement as well as take advantage of the Wolkovitch effect by separating the leading and trail-edge spars. In addition, the experimental data demonstrates that improvements to the OML may be in order due to the decrease in lift at relatively low angles-of-attack.

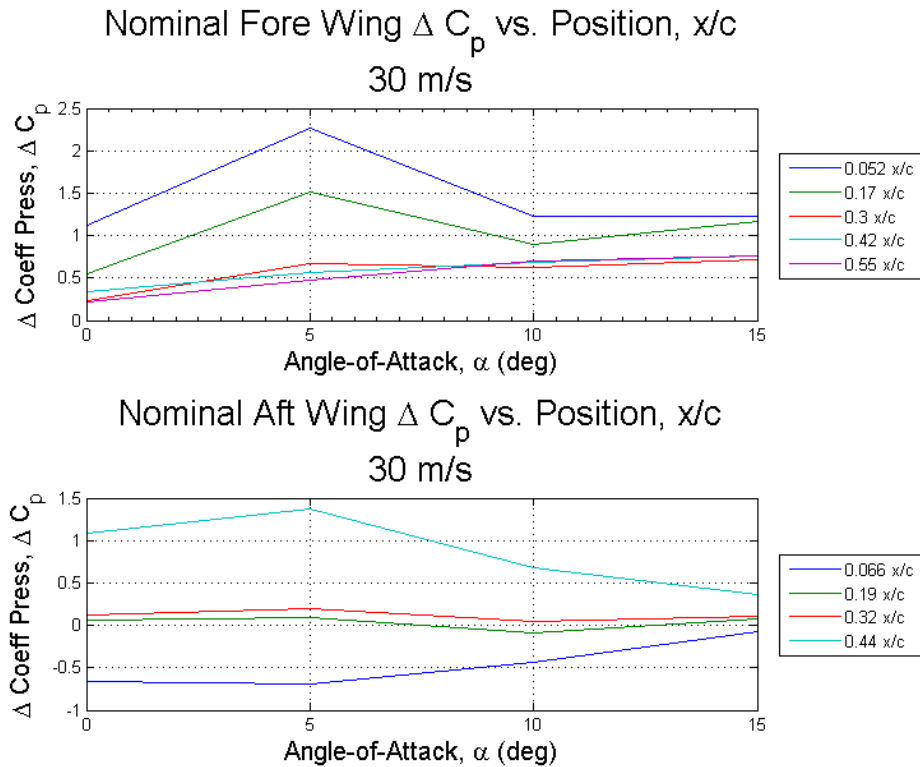**Figure 5-22. Experimental results for the nominal aft wing configuration.**

This chapter demonstrated that experimentally determined aerodynamic forces showed that pitch control using a flexible aft-wing is possible. The pitch control was shown to be effective by the fact that the coefficient of moment was affected by the wing twist throughout the range of angles-of-attack as discussed in Section 3.2. Until now,

only conventional controls were investigated on joined-wings. In addition, in-house studies that presumed this method of pitch control was feasible are now validated.

While the aerodynamic experiment discussed in this chapter showed that flexible twist is a feasible method for pitch control, a complementary experiment is defined in the following chapter. It outlines the method by which static nonlinear response can be demonstrated. Although it does not have skin like the aerodynamic experimental model, the substructure was intended to fit inside an OML similar to that of the Boeing Joined-Wing Sensorcraft used for the wind tunnel model described in this chapter. In fact, the twist in wind tunnel model came from modifications to full-scale FEM described in next chapter.

6. Nonlinear Response Experimental Approach, Results and Discussion

6.1   Nonlinear Response Analysis

The modifications to the as-delivered FEM for aft-wing twist were used to find the shape of the aft wing for the rigid wind tunnel model discussed in the previous chapter. They were originally intended to also be used for the scaling of nonlinear response, but were abandoned (except for rib adaptations) when the full-scale model was found too stiff.

This chapter discusses these modifications to incorporate aft-wing twist and those to prepare the design prior to scaling for the static nonlinear response experiment. The method of test for static nonlinear response is also discussed here. The approach to fulfilling task 3, experimentally validating nonlinear response on a reduced scale model, is established in this chapter. Task 1, to demonstrate nonlinear response on an aeroelastically scaled experimental model, was originally intended to scale the test article used in task 3. However, now the two tasks are disconnected due to the stiff nature of the case study.

6.1.1   Twist Tailored FEM Design Revisited

A revised Boeing FEM 410E5-04 was delivered to the USAF in August 2006. In a fashion similar to that described in Section 5.1.4, a slit was made spanwise in the skin of the aft wing of the revised Boeing FEM. However, the slit was moved to a position close to the forward spar rather than the aft spar, as in the previous FEM used for the OML of the experimental wind tunnel model. This was to take advantage of the Wolkovitch effect by avoiding the load path where there is build-up of material near the lower-rear spar (Figure 1-2). The ribs of the FEM were also modified for torsional

compliance. The three-quarter rib design was altered from the design in Section 5.1.4 to maintain the load-bearing characteristics of a rib (Figure 6-1).

To take into account the Wolkovitch effect of the joined-wing design, the aft wing trailing edge closeout spar was removed and the middle spar moved its place. The ribs in the fore wings and the bulkhead in the tail that were attached to this spar were moved to accommodate this change.
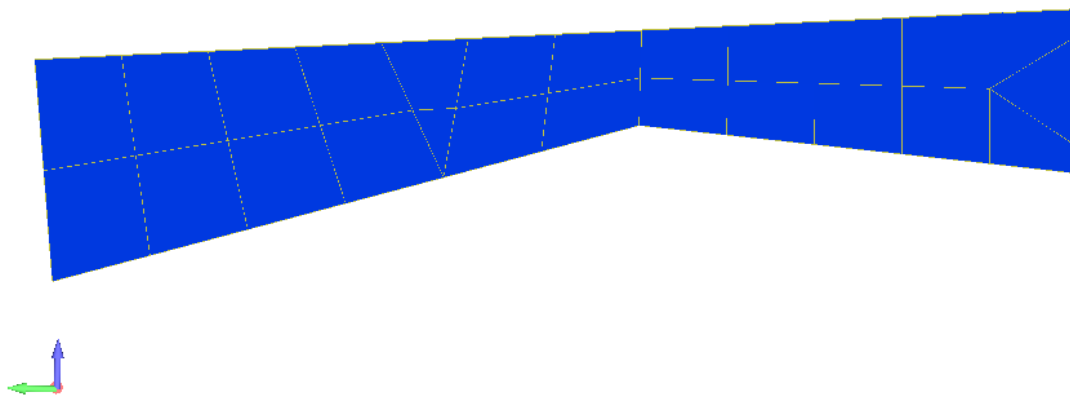
Figure 6-1. Torsionally-compliant aft-wing rib.

6.1.2 Aeroelastically Scaled FEM

As mentioned in Chapter 1, the Boeing Aircraft Company's Sensorcraft design is the case study for the research within this dissertation. However, the FEM delivered at the time the aeroelastic scaling process was initiated did not exhibit large deflections. In fact, the maximum linear deformation was only 0.787 m (31 inches) for a load of 466,712 N (104,921 pounds) per side (Figure 6-2). Thus, it was not reasonable to aeroelastically scale this FEM as-is to study the nonlinear response.

The full-scale FEM was sized to the subscale FEM after it was modified for aft-wing twist (Section 6.1.1) using a geometric length scale of 1:15 and scaling load magnitude to maintain the same proportionate deformation. The loads were scaled using the ratios described in Equation (3.37). This scale was dictated by the size of the wind tunnel where the experimental model was intended to be used for future dynamic studies. Aluminum was used for the subscale experimental model material at the request of the model builders at the University of Manchester, UK, where the test was completed. Stiffness was determined to maintain the same proportionate deformation. The design was optimized with multiple spar and rib design variables. The optimization objective was to have the most flexible design without overstressing the material for the given scaled load. This was accomplished such that the maximum deflection of the FEM was reached with the stress as side constraints.
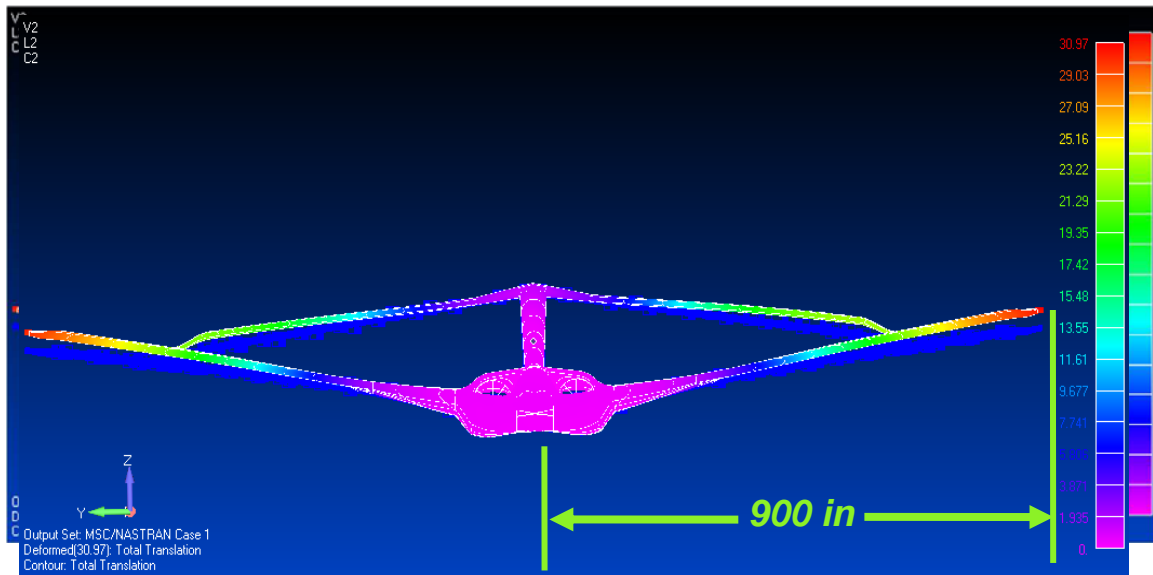

Figure 6-2. Boeing Joined-Wing FEM, 410E5, delivered August 2006 (blue is un-deformed, contours are deformed model).

6.1.3 Full-Scale FEM Evolution

The as-delivered Boeing FEM was modified prior to aeroelastic scaling as follows. The panels were thickened to avoid panel buckling, the aft wing made torsionally compliant, the gust load replaced by equivalent cable loads, the boom was replaced by equivalent springs, and the cable loads were repositioned. The steps taken to adjust the full-scale FEM to exhibit a nonlinear response are summarized in Figure 6-3, where the value in each block is the tip deflection. The details are explained in the following paragraphs. The design point was the worst case load—the Boeing gust load labeled '31411'. Constraints of the static tests (follower forces in particular) required the load be applied at three points. To simulate a gust load in the experimental set-up, the gust load was represented by cable loads that resolved the sum of forces, bending and torsional moments about the aft wing. Since the load case is also a case study in proving the process of aeroelastically scaling a torsionally compliant aft wing, the applied load case was modified to maintain the sum of forces and moment about the aft wing only. This was critical for two reasons. First, the aft-wing buckles, so force and moments applied to it must be maintained. Second, it was critical to demonstrate viability of a flexible aft-wing for pitch control. The torsional moment sum was neglected, since the required moment arm forced an excessive reaction of the load into the clamped fuselage. This allowed the freedom to move the cable along the fore wing, while maintaining the net sum of forces and moments about the aft wing.
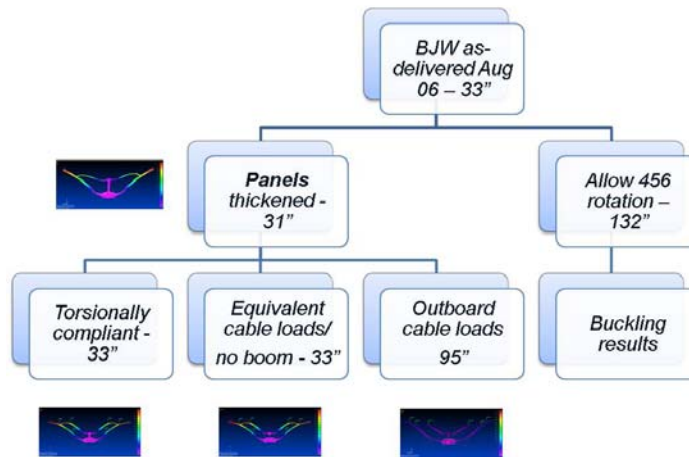
Figure 6-3. Full-Scale FEM Evolution.

Figure 6-4 depicts the worst Boeing-supplied gust load case (31411) applied to the full-scale FEM after the panel thicknesses were increased to eliminate panel buckling. The study and detailed modification of the panel thicknesses, based on the buckling analysis, was completed by Adams [40]. It was modified by increasing some of the panel thicknesses to decrease the number of local buckling modes such that the global buckling could be observed within the first 50 eigenvalues. This process also increased the first global buckling eigenvalue.
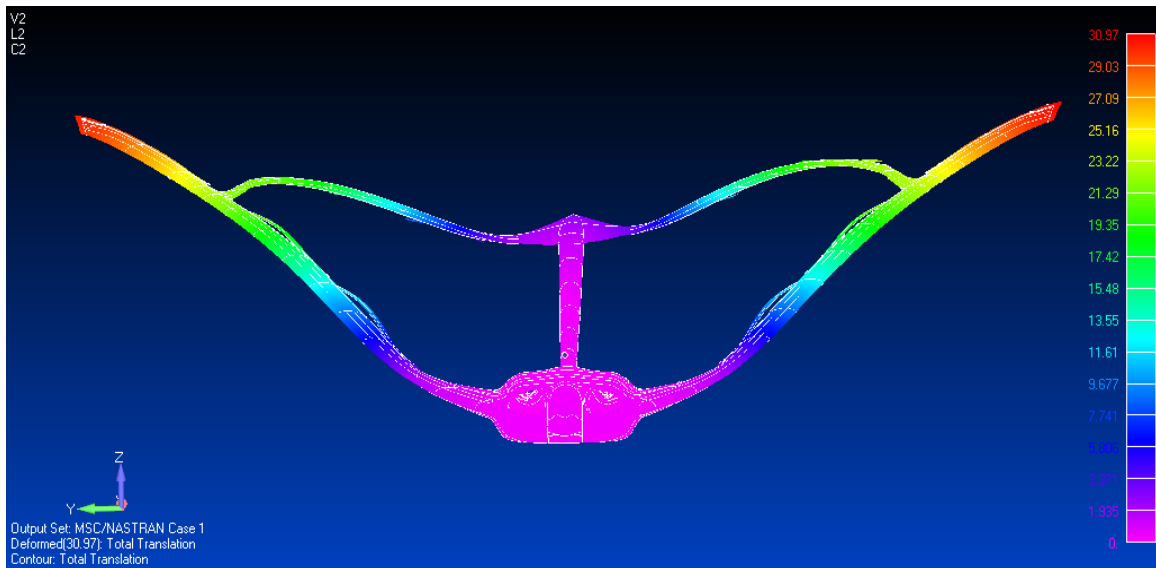

Figure 6-4. Gust Load 31411 Applied to Full-scale FEM (inches).

Next the gust load was resolved into cable loads as previously mentioned to produce statically equivalent loads. The deformation depicted in Figure 6-5 qualitatively demonstrates they are equivalent in comparison to Figure 6-4 since the maximum deflection and shape were approximately equal. The next figure depicts the same load on the torsionally-compliant FEM (Figure 6-6).
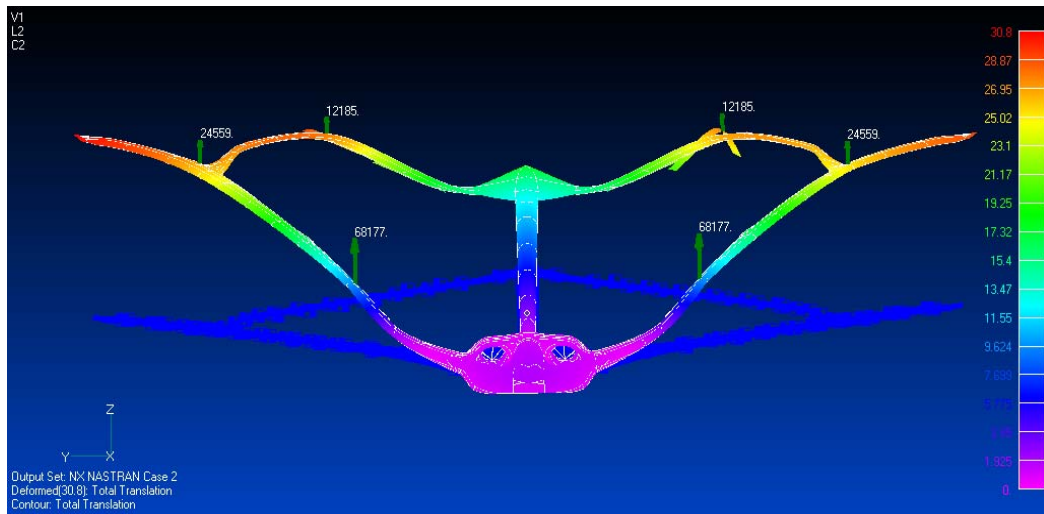

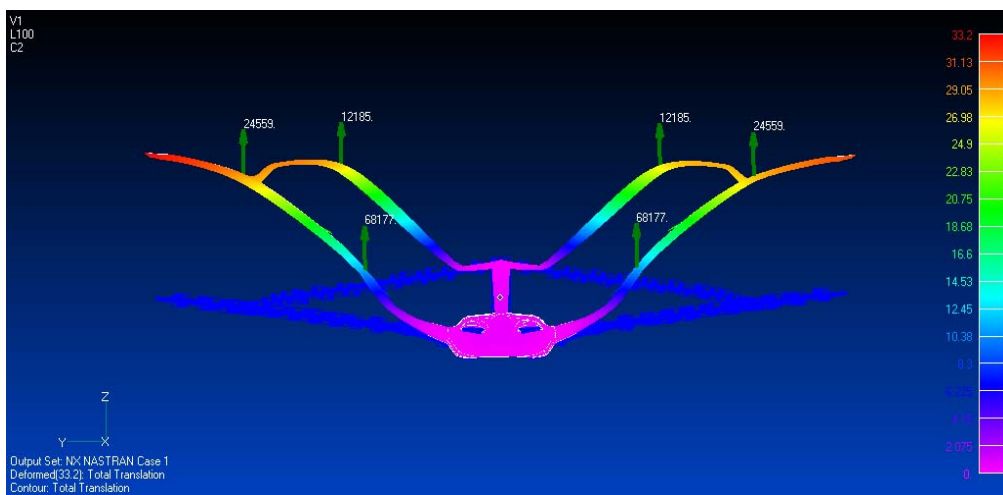**Figure 6-5. Equivalent Static Load applied to full-scale FEM**

Figure 6-6. Equivalent Static Load applied to full-scale torsionally compliant FEM

Figure 6-7 illustrates the same cable load on the torsionally-compliant (Section 6.1.1) FEM in which the boom was replaced with equivalent pitch and plunge springs. This was requested by the model builders for simplification as the experimental model was to be half-span. Two static load cases were used to apply a unit load and unit moment at a node at the center of the tail.

$$F = k_w \Delta x, \qquad M = k_\theta \Delta \theta \qquad (6.1)$$

The deflection at a central node at the fuselage-boom connection is then used to solve for the spring constants.

$$k_w = 751.73 \text{ lbs/ft}, \qquad k_\theta = 89.38 \times 10^6 \text{ ft} \cdot \text{lb} \qquad (6.2)$$
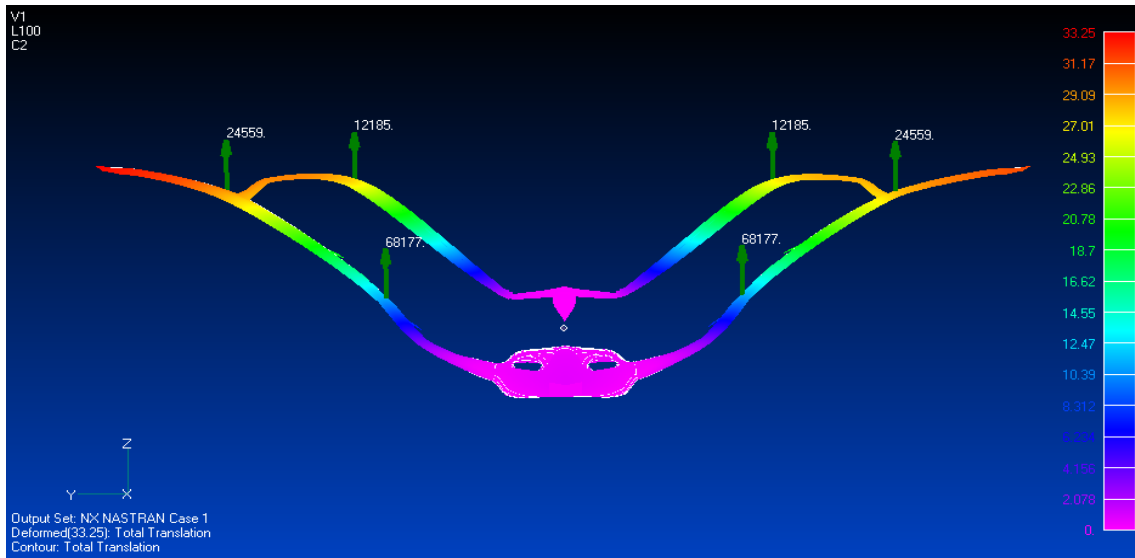
Figure 6-7. Full-scale torsionally compliant FEM where the boom is replaced with equivalent springs

Due to large reaction loads into the fore wing, the cable loads were adjusted to maintain net force and moment only, and one cable was moved to the outboard wing (Figure 6-8). The cable in the fore wing caused excessive fore-wing-root stress for the moment it produced. The cables in the original configuration would have required

99

unnecessary strengthening at the forward-wing-root attachment since the primary interest was the response in the aft wing.

The last modification to the full-scale FEM before scaling was to investigate the curvature of the deflected FEM. The curvature of the outboard wing was atypical of the given applied load on a high-aspect-ratio wing. Upon further investigation, incorrect boundary conditions were discovered on the as-delivered FEM. The rotations had been incorrectly constrained in the wing in an attempt to remedy convergence problems with nonlinear analysis. The maximum deflection of the as-delivered FEM with corrected boundary conditions subject to gust loads was approximately 2.29 m (90 inches) for a half-span of 22.9 m (900 inches).
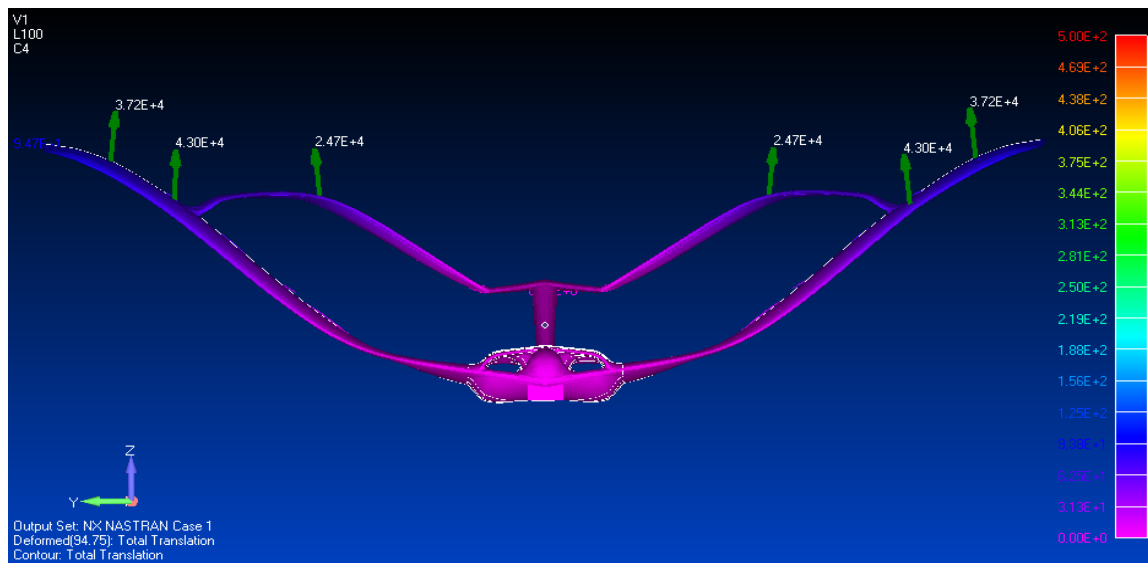

Figure 6-8. Full-scale torsionally-compliant FEM, sum of forces and bending moment resolved only and cable location change.

6.1.4   Subscale Experimental Model

The manufacture of the test item was accomplished at Goldstein Laboratories, University of Manchester, under contract to Northwest Aerodynamics Models Ltd., New

Mills, Derbyshire, UK. In order to describe a feasible design for manufacturing there, they requested the restrictions given in Table 6-1 be incorporated in the subscale FEM.

Table 6-1. Summary of manufacturing constraints of nonlinear response scale model.

Modification	Restriction
Geometric scale	1/15
Minimum rib/spar thickness	5 mm
Model materials	Aluminum
Boom	Replace by two springs
Fore-Aft wing Joint	Straightened
Spar design	Two-spar design

The boom was removed and replaced by two springs, whose pre-optimized stiffness values were scaled based on the stiffness of the boom of the full-scale FEM as previously mentioned in Section 6.1.3. The spring values are 10873.9 N/m for the plunge spring and 9213.68 N·m for the pitch spring. The fore-aft wing joint was straightened such that no kink existed in the aft wing. In addition to the modifications made to the aft wing in the full-scale design, the fore-wing center spar was removed in the subscale design. Table 6-2 contains the dimensions of the aircraft half-span model and Figure 6-9 the CAD from which the fore and aft wings were milled.

Table 6-2. Full-scale and subscale model half-span dimensions.

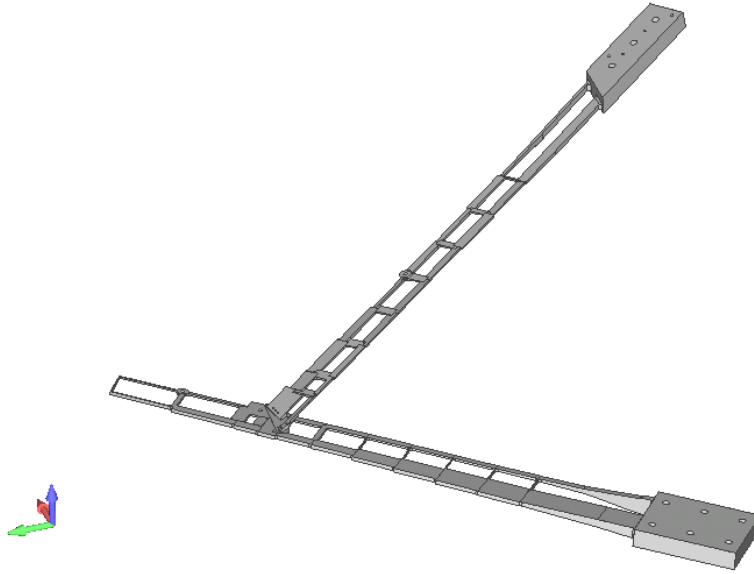|	Height [m (in)]	Length [m (in)]	Span [m (in)]
Full-scale aircraft	8 (315)	30 (1181)	45 (1771.7)
Subscale model	1.5 (59)	2 (78.7)	0.4 (15.7)

Figure 6-9. CAD of experimental model of test item.

With these constraints, the optimization process began.   After numerous iterations, it was determined that an all-aluminum FEM to include internal structure and skin was not flexible enough to meet the demands while maintaining structural integrity. Since the test did not require air-on loads, the skin was not a necessary element. Once the skin was removed the FEM proved to be much more flexible and the optimization process continued.

Whereas the as-delivered FEM was too stiff to match, the scaling strategy was modified to make the subscale FEM as flexible as possible while maintaining the basic shape as the full-scale deformation under worst case gust load. The optimization scheme started with maximizing the joint deflection. To maintain a similar shape to the full-scale, the next optimization scheme maximized the joint deflection while constraining the joint-tail deflection ratio to the same as that of the full-scale ratio, 0.7. Both of these

schemes were subject to stress constraints. Root stresses were high in the matched subscale case for both the gust load and cable load case. Since these stresses were too high in order to maintain the integrity of the aluminum FEM, the root was significantly fortified. The FEM was optimized subject to constraints applied to the nonlinear static analyses and linear buckling analyses. A compromise was made, since the nonlinear analysis reached the maximum load at 62.8% of the full load, indicating a possible approach to collapse load. The material was defined in the FEM as elastic-perfectly-plastic. The buckling eigenvalue was constrained to only 80% of design gust load, yielding a design with both nonlinear stress and buckling constraints merging (Figure 6-11) to make the most flexible design without overstressing the test article. The maximum deflection, a measure of the flexibility of the subscale FEM, was 0.166 m (6.54 in), Figure 6-10. The FEM is 1/15 scale and the resulting linear deflection is 1/14 that of the full-scale maximum deflection subject to similar scaled loads. The nonlinear deflections of cable attachment points occur at 10% load increments in the plot in Figure 6-11. An envelope of ±20% is depicted around each nonlinear curve. The threshold established to proceed with manufacture was 20% margin above the linear deflection to ensure a nonlinear response could be observed. The increments are overlaid and depicted in Figure 6-12.
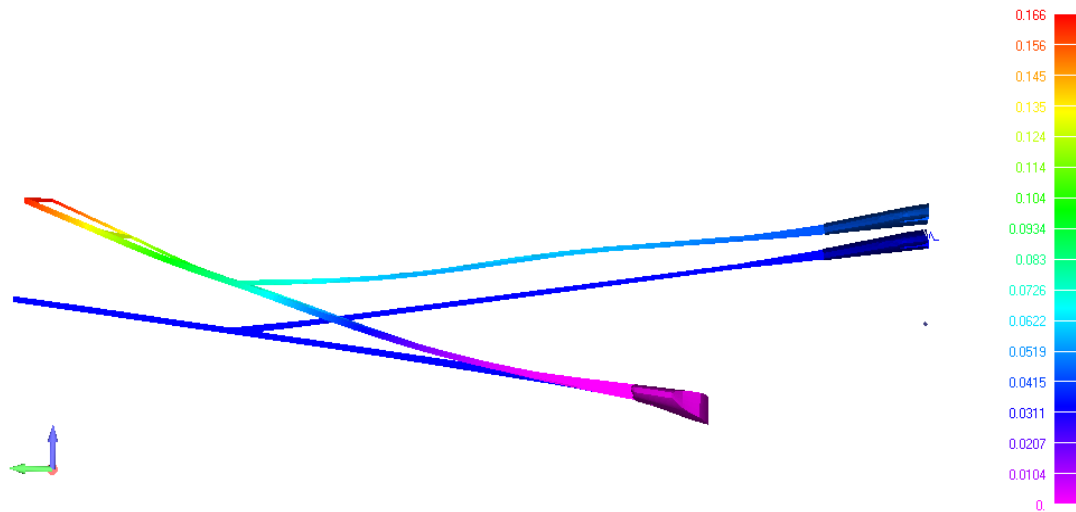
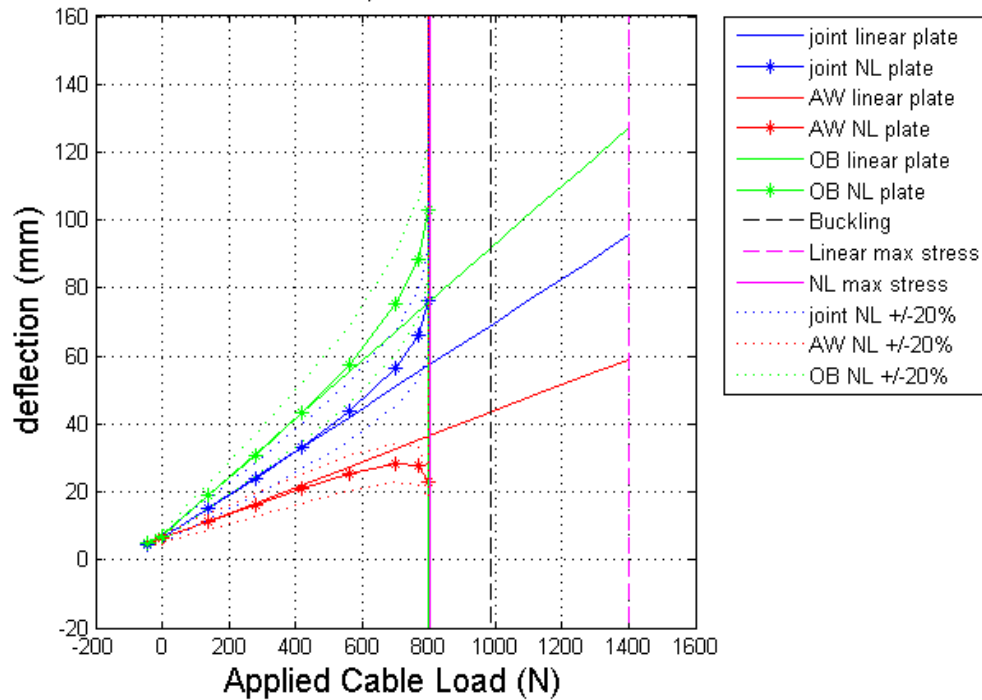**Figure 6-10. Linear analysis yielded maximum deflection of 0.166 m (6.54 in).**

Figure 6-11. Final subscale design: Load versus linear and nonlinear (NL) deflections of cable attachment points (joint, aft wing (AW) and outboard wing (OB)).
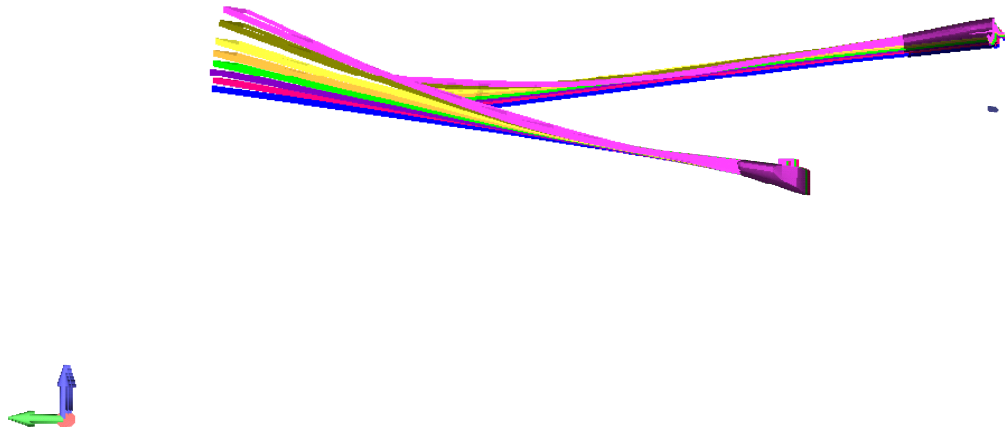
Figure 6-12. Nonlinear response of 10-62.8% load of final subscale design.

6.2   Method of Test – Experimentally Measure Nonlinear Static Response

The third task of the problem statement was to experimentally demonstrate nonlinear response on the flexibly-tailored model. This involves devising a method of test that can simulate follower forces such that the air loads act perpendicular to the wing surface. Due to the large deflections of the high-aspect-ratio wing, the aerodynamic force vector is up and toward the center. Typically, the experimental model is turned upside down and sand bags are placed appropriately on the wings to simulate air loads in the gravity direction only. Since this would not suffice, a device was manufactured using a system of cables to simulate the air loads and with the correct vectors.

6.2.1   Test Set-up

The test set-up consisted of cables attached to scales and turnbuckles in line to a weight on the floor. This system allowed for tension on the cable to measure the applied

load. The system also allowed the applied load to be maintained perpendicular to the wing by adjusting the position of the weight on the floor. The cable, scale and wing system is depicted in Figure 6-13 through 6-18. The test item was oriented such that the forces acted perpendicular to the top of the wings to simulate an air load.

Figure 6-13. Test Article (gray), support structure (blue) and beam constraint structure (brown).

Figure 6-14. Test article, load application and measurement devices

Figure 6-15. Test article, tension scales and strain gage wires.

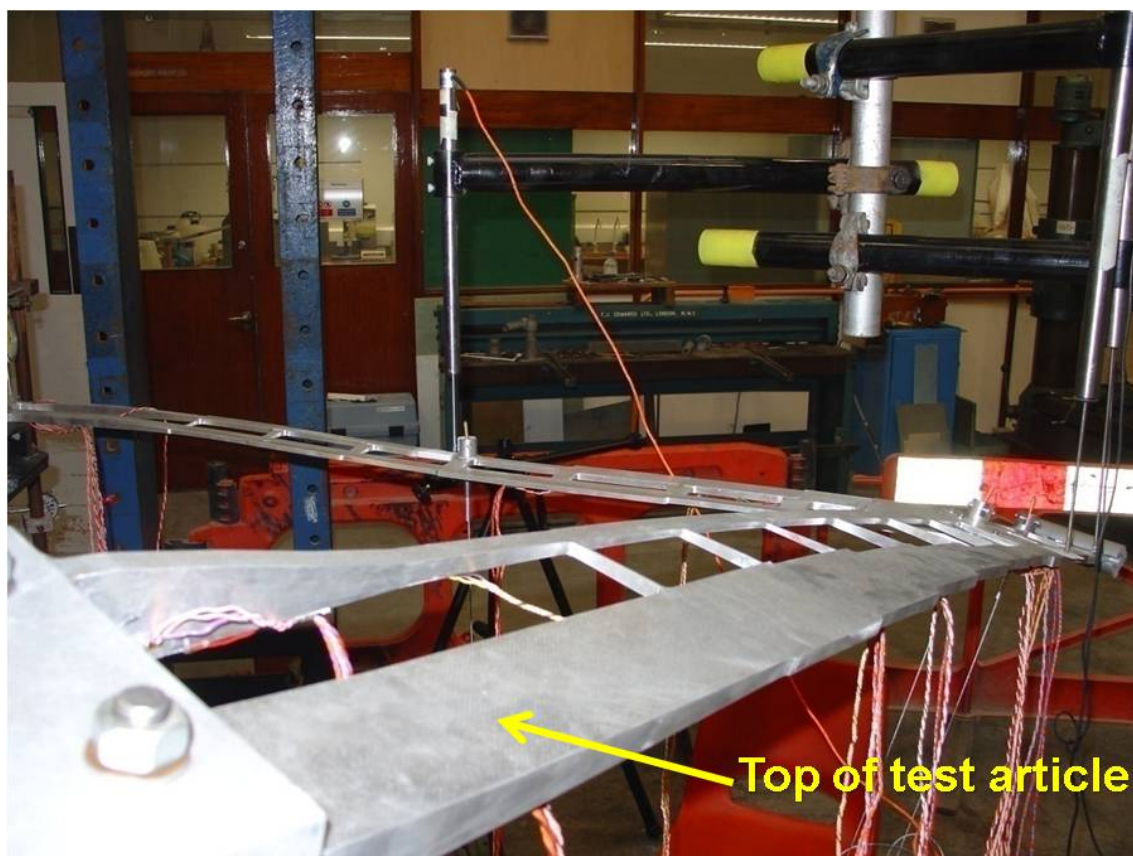**Figure 6-16. Scales in line with cable, turnbuckles and weights.**

Figure 6-17. Top of Test Article.

6.2.2 Instrumentation

Displacement: Displacement probes were used to measure displacement to 0.1 mm accuracy (Figure 6-18). The measurement range required was 0.01 to 0.16 m. The probes were placed at the joint (Figure 6-19 and Figure 6-20), rib between the joint and the tip/leading edge spar junction (Figure 6-21 and Figure 6-22), and aft wing mid-span (4th rib from root/leading-edge spar junction, Figure 6-23).
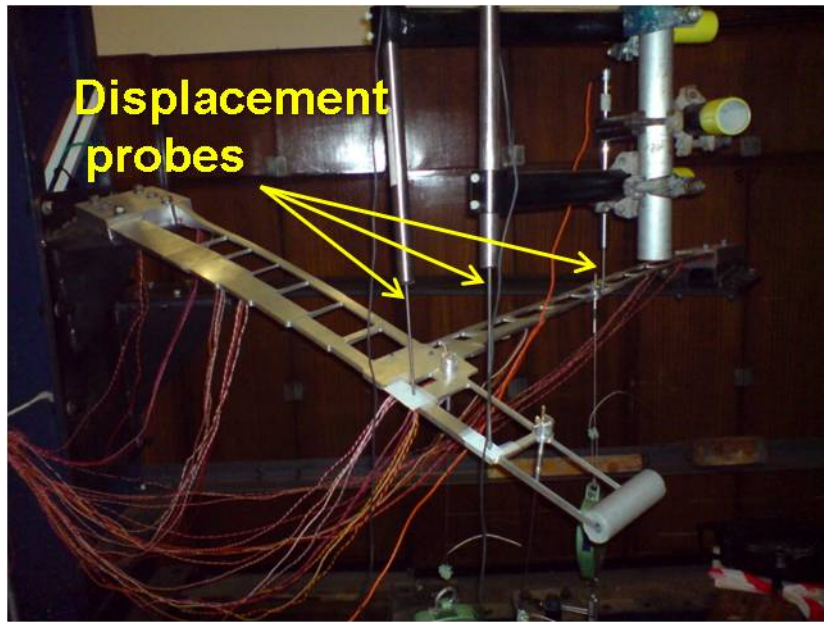
Figure 6-18. Displacement probe locations.

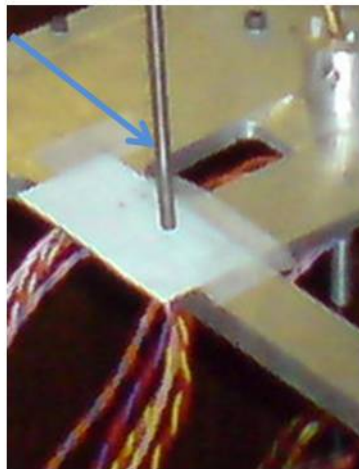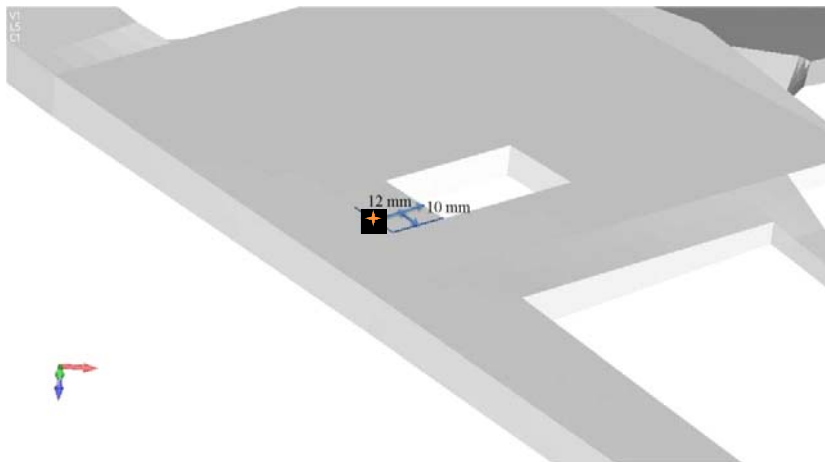**Figure 6-19. Displacement probe at joint location.**

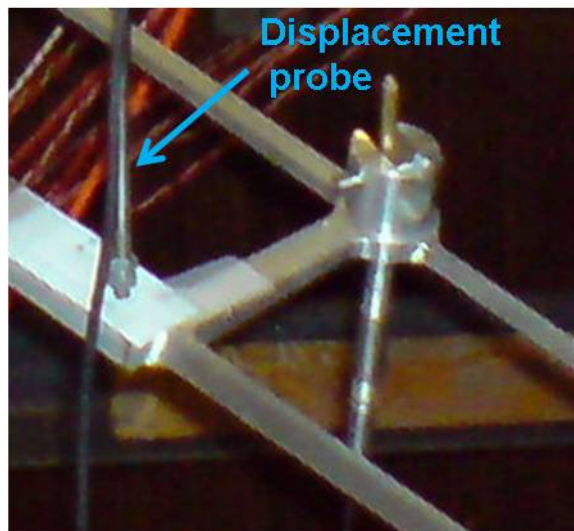**Figure 6-20. Joint probe location on FEM (orange star).**

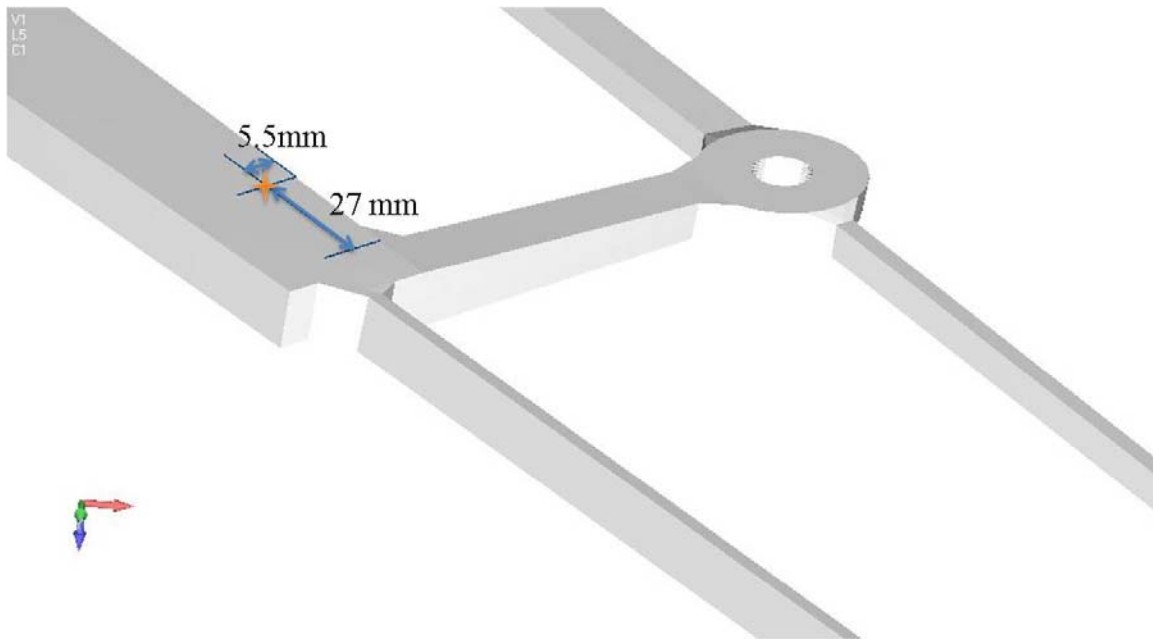**Figure 6-21. Displacement probe at outboard location.**

Figure 6-22. Outboard probe location on FEM (orange star).
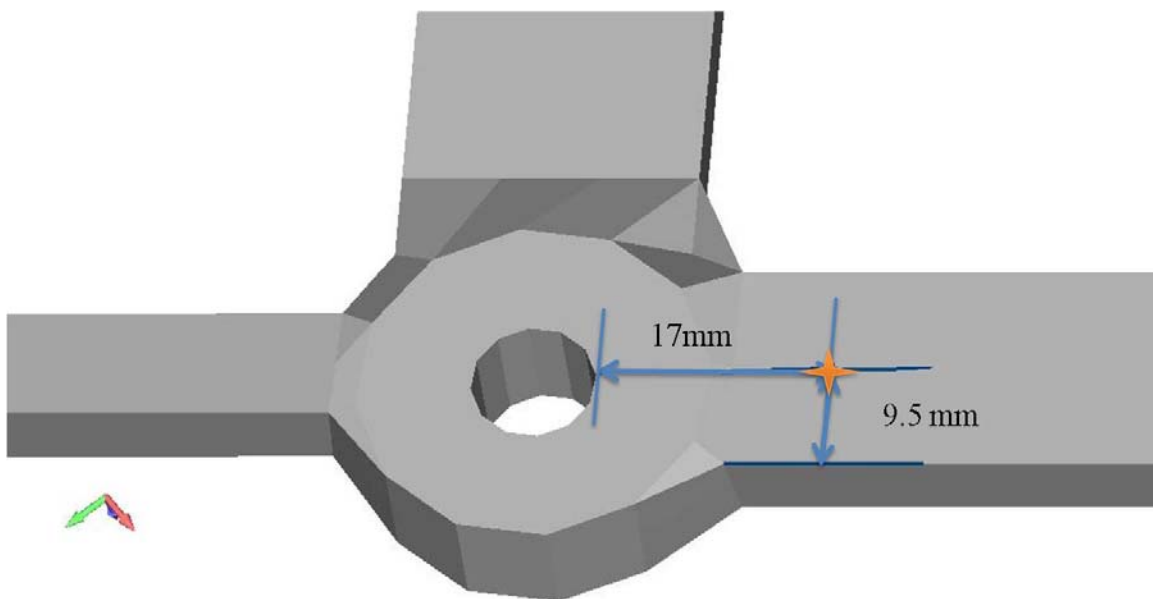
Figure 6-23. Aft-wing probe location on FEM (orange star).

Strain: Strain gages were placed at computationally-determined critical areas (Figure 6-24 and Table 6-3).
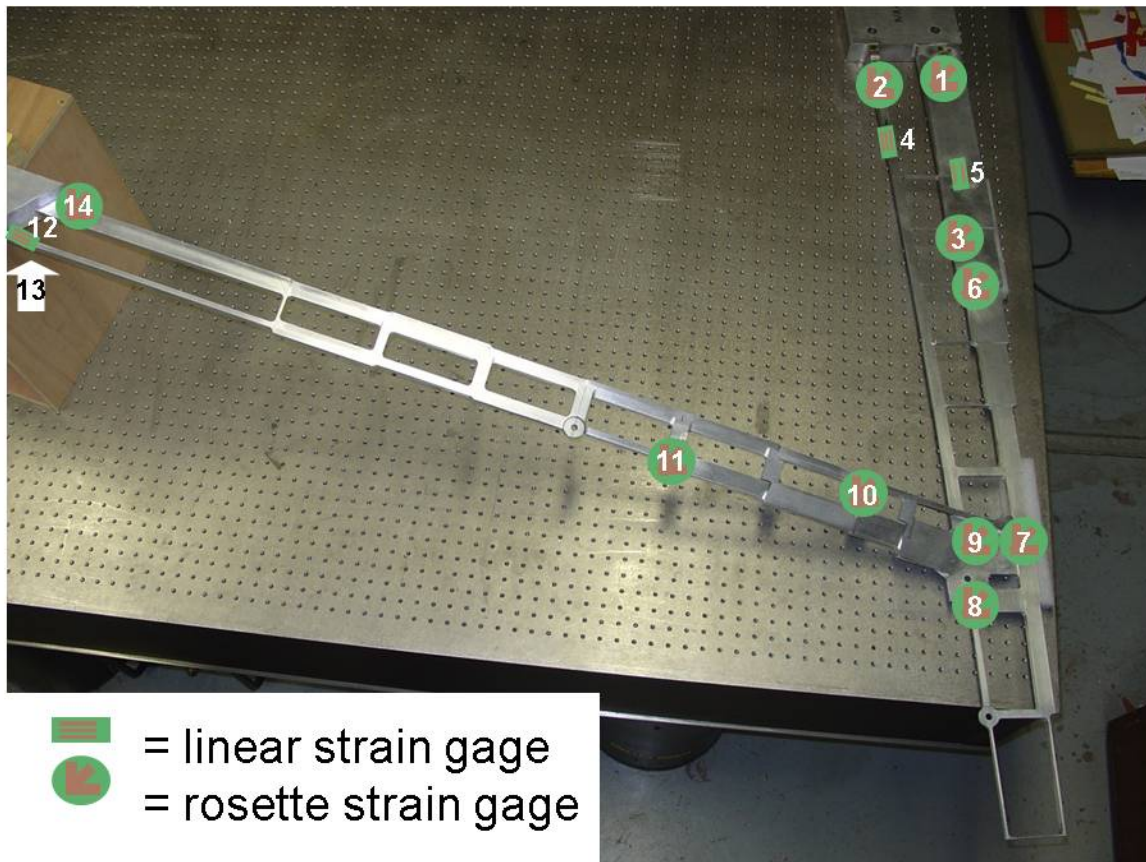
Figure 6-24 Strain gage placement. Placed on top and bottom only at location with white arrow.

Table 6-3. Strain Gage Locations[1]

Location	Fore wing	Location	Aft Wing
1	Root-leading edge (LE) spar junction	8	Rib- trailing edge (TE) spar junction
2	Root- TE spar junction	9	Joint-LE spar junction
3	Rib-LE spar junction	10	Rib- LE spar junction
4	Midpoint between root-1st rib on TE spar	11	Rib- TE spar junction
5	Rib-LE spar junction	12,13 (bottom)	Root-TE spar junction
6	Rib-LE spar junction	14	Root-LE spar junction
7	Rib-LE spar junction		

---

[1] Strain gages were placed on the top of the wing (unless annotated).

Both the displacement and strain information was converted to engineering units of millimeters and microstrain, respectively through an Orion Solartron 352 Data Logging System. The strain gages were of the linear and stacked rosette type, Kyowa strain gages (Table 6-4).

Table 6-4. Strain gage specifications

Strain gage	linear	stacked rosette
Type	FLA-6-23	KFG-5-120-D17-23
Gage length	6 mm	5 mm
Resistance	120Ω	120Ω
Coefficient of thermal expansion	23e-6/°C (matched for aluminum)	23e-6/°C (matched for aluminum)
Gage factor	2.15	2.15

6.2.3 Test Procedures

To increase the applied load on the wing, the turnbuckles were tightened to increase tension. Each of three cable systems was moved along the floor until the cable was perpendicular (by inspection) to its associated spar for each incremental weight (test point) in Table 6-5. Deflections were measured for each test point while strains were continually monitored for safety of test. The collected data includes strain and deflections at various locations on the test item mentioned in Section 6.2.2.

Table 6-5. Test matrix[*]

Mass	Approx % Total gust equivalent load	Location #1 Aft Wing Mid-span (lbs)	Location #2 Joint (lbs)	Location #3 Outboard Wing (lbs)	Total (lbs)
1	10	7.5	13	11	31.5
2	20	14.5	25.5	22.5	62.5
3	25	18.5	32	27.5	78
4	30	22	38.5	33.5	94
5	32	23.5	41	35.5	100
6	34	25	44	38	107
7	36	26.5	46.5	40	113
8	38	28	49	42.5	119.5
9	40	26.5	49	42.5	118
10	42	31	54	44.5	129.5
11	44	32.5	56.5	49	138
12	46	34	49	51	134
13	48	35.5	62	53.5	151

*Measurements taken at least 3 times as the load was increased. Repeated
measurements as the load was decreased.

Using the method of test described in this chapter, the next section discusses
analyses and results by comparing to a FEM. It will show how the use of follower forces
affects an experimental model that was scaled for geometric stiffness.

6.3   Analytical and Experimental Nonlinear Response Test Results

The static nonlinear response test was completed to demonstrate the
characteristics inherent in a nonlinear system like that of a joined-wing-aircraft
configuration and validate FEMs that are used in analysis methods. The displacement
and strain of the experimental model under load was recorded from the experiment. The

following discussion focuses on the comparison of the displacement and strain of the test article to the FEM which represents it.

6.3.1   Compare Predicted and Experimental Displacements

Analysis of the FEM was compared to the experimental results.   To correctly evaluate the experimental results against the predictive analysis, the FEM was adjusted to account for differences from the test article as fabricated and tested (Table 6-6).

Table 6-6. Corrections for Comparison of FEM and experimental model

Correction	FEM	Experimental model
1	Nodal displacements	Measured locations
2	Apply gravity load	Affixed model upside down
3	Apply weight of scales	Scales used to measure load
4	Spring constants	Support beam

Nodal displacements (correction 1 of Table 6-6) from the FEM required adjustments before comparison to the experimental results. Initially, the predicted results were reported at the same location where the force was applied. However, there was a device to hold the cable in place and distribute the load at that location. Thus, the measurements were not taken at the cable attachment points (Section 6.2.2). The locations in the FEM that were plotted for comparison had to be changed to match the experimentally-measured locations. Since the measurement devices were held fixed, as the experimental model deflected the points measured on the fore-wing were significantly different as the load was applied. The movement of the probe along the wing was measured at each test point in relation to the original location. The measurements were taken spanwise and chordwise. An inclinometer was also used to measure the angle that the experimental model was deflecting so that the new position could be computed at

115

each test point and the differences could be accounted for when comparing the results. This is illustrated in Table D-1 and Figure D-1 in Appendix D. There was little change in the aft-wing measured location. The outboard wing location was corrected with the same correction measurements as that taken at the joint since the probes were moving approximately along the same span.

It was convenient to apply experimental loads downward, simulating aerodynamic loads on the experimental model. Thus, it was affixed upside-down with respect to its normal flight configuration. Without additional applied loads, gravity displaced the experimental model. Therefore, the nonlinear FEM must account for that regardless of amount of load applied (correction two of Table 6-6). A gravity load case was added to the FEM to combine with the applied loads at each test point.

The tail boom of the full-scale FEM was represented by a steel beam attached to the aft wing root. However, the experimental model was affixed at an angle different than the FEM due to several extra centimeters of length erroneously added at the wing roots during fabrication. Not only did this extra length contribute to larger deflections, but it also offset the steel beam support (representing the tail boom) from the centerline. Hence, the springs representing the tail boom in the FEM that were limited to pitch and plunge either needed more degrees of freedom to capture the experimental orientation, or the steel beam attached to the experimental model had to be added to the FEM analysis. The latter was chosen to increase the accuracy of the FEM. This extra length was also accounted for in the FEM (correction four in Table 6-6).

Incorporating the corrections, the FEM and experimental displacement both exhibit nonlinear response with similarly-shaped load-deflection curves. However, the

116

experimental results revealed the test article is about 40% more flexible than the FEM (Figure 6-25).   The plots in Figure 6-25 refer to the linear, nonlinear (NL) and experimental (exp) deflection at the joint, fore wing (FW), and aft wing (AW). In addition, the buckling load (Buckling), loads at which the linear (linear max stress) and nonlinear (NL max stress) analyses determined stress is maximum are also plotted. For reference, plus and minus 20% of the nonlinear analyses at each location is also depicted (joint, AW and OB NL+/-20%).   Similar legends with the addition of solid analyses are used in the remainder of the figures in this chapter.

In order to compare the experimental data to FEM analysis some definitions were taken under consideration and included in the figures in this chapter, as well. First, the gravity load, is defined as when the displacement probes were tared (Figure 6-26). This was plotted by subtracting the measured displacement (within the error of the measurement device) versus the force exerted due to the weight of the experimental model. This force is approximately 3.18% of the total gust equivalent load (1400 N), the basis of the force increments in the experiment (Figure 6-5). Hence, there is a negative load. Second, the scales used to measure the load applied displaced the experimental model due to the weight associated with each of them. The second point on each curve indicates the displacement due to the load of the scales hanging without applying tension to the cables, hence a positive displacement at zero on the x-axis relative to the deflection due to the structural weight. The remainder of the FEM and experimental points on the plots have load applied as measured by the scales in the follower force direction, ranging from 10% through 100% of the total gust equivalent load.
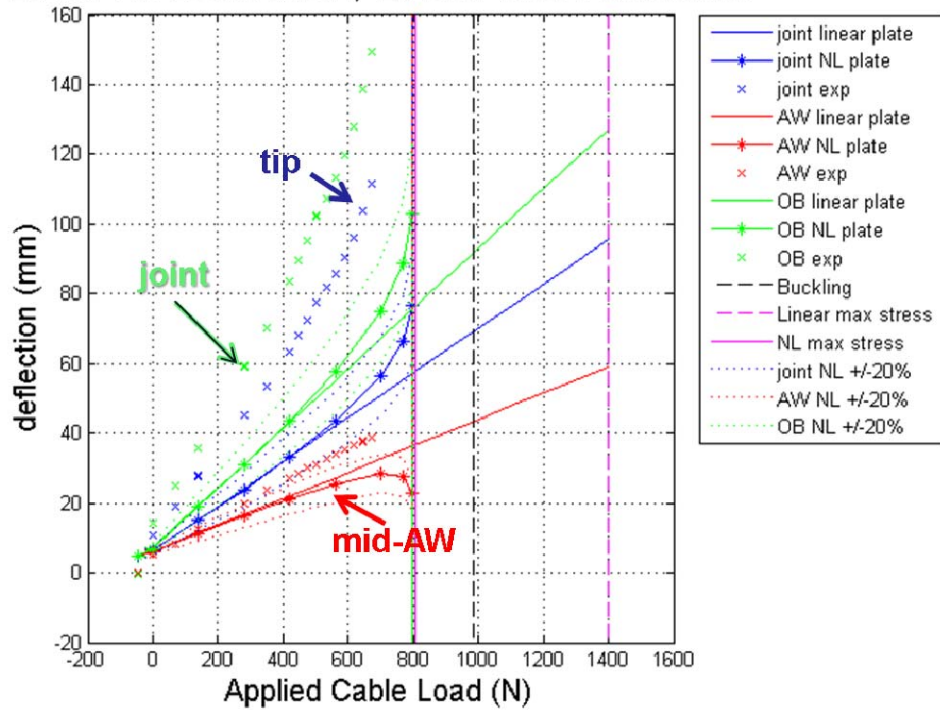
Figure 6-25. FEM and experimental displacement.
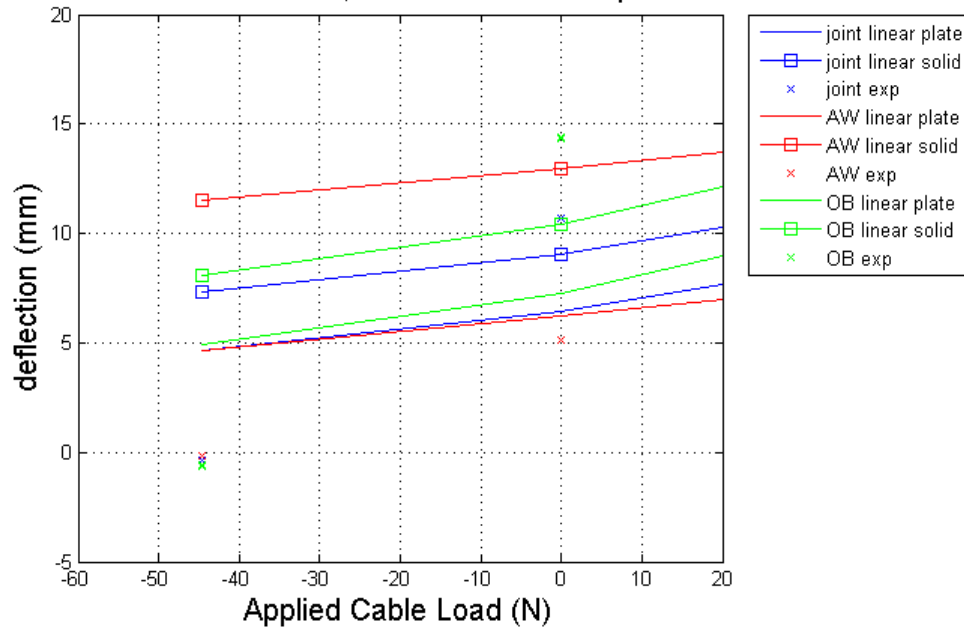

Figure 6-26. Previous figure low end expanded.

118

There are several factors that may contribute to this difference in response. The FEM uses plate elements (Figure 6-27) with thicknesses much greater than height. The plate element was chosen since it is less complex than solid elements for optimization. To investigate the error due to violating the plate geometry assumption, a solid FEM was meshed by Armani, Nye, Stevens, and Swenson [41] (Figure 6-28) from the as-built CAD geometry as the experiments were completed. The fidelity between plate and solid FEM does not account for the source of displacement differences between FEM and experimental results. In fact, the solid element strains widely varied in neighboring elements, indicating that the mesh was not refined enough. The linear deflection from the solid FEM showed about a 10% increase over the linear plate FEM displacements (Figure 6-29). However, the nonlinear results for the solid FEM are further from the experimental results than the plate FEM (Figure 6-30).
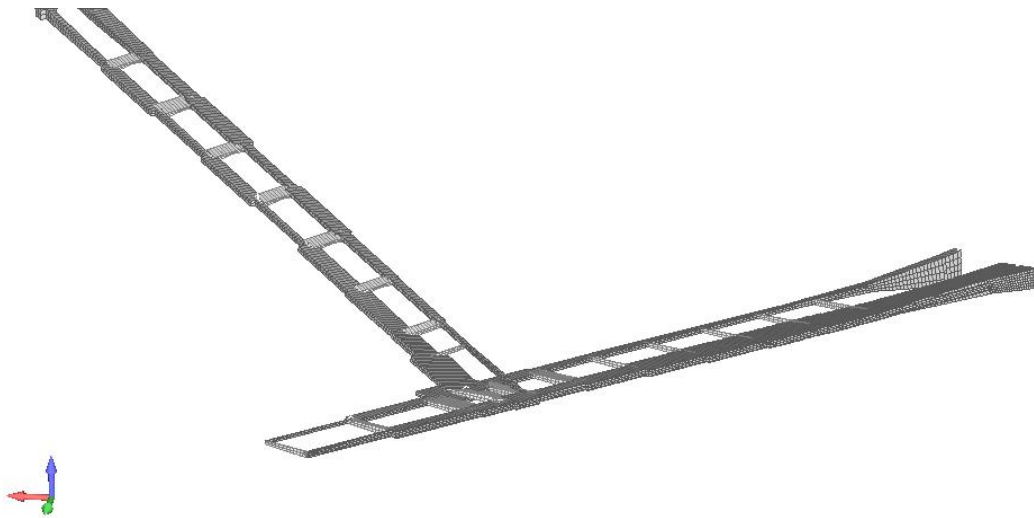

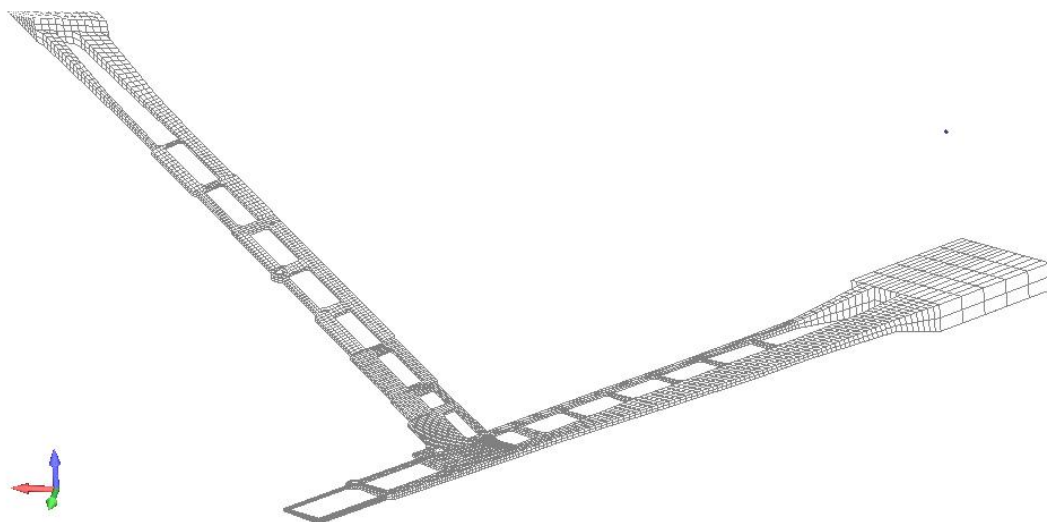**Figure 6-27. Plate mesh finite element model with cross-section illustrated.**

Figure 6-28. Solid mesh finite element model.

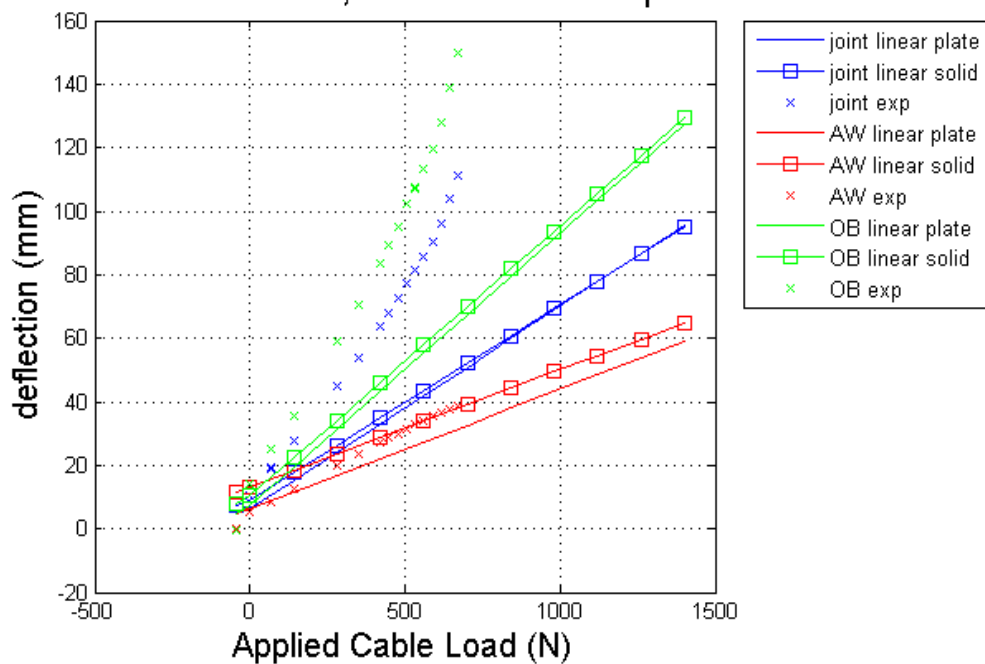**Figure 6-29. Experimental linear plate and solid load-deflection results.**
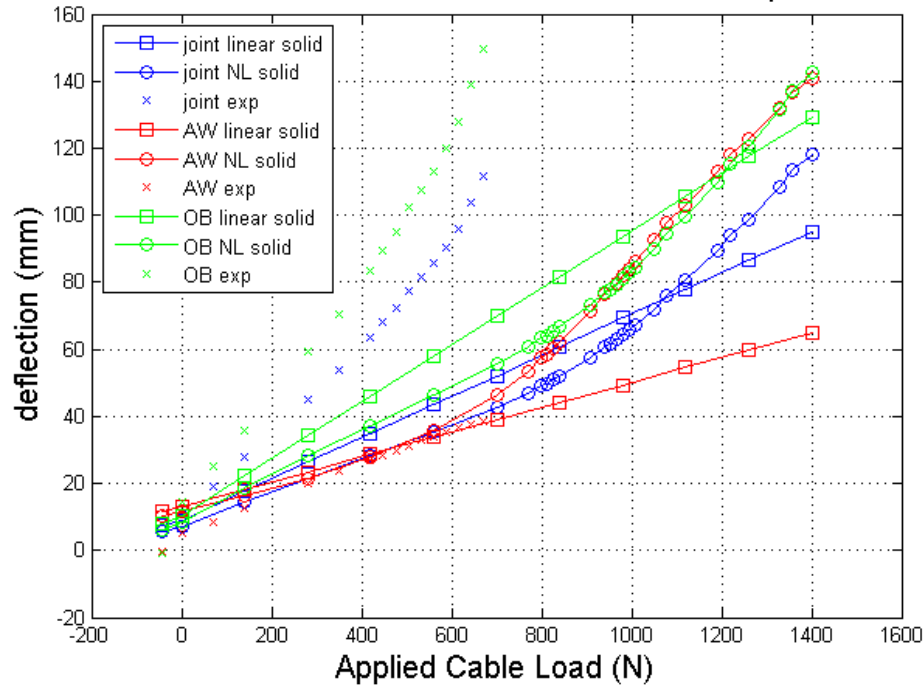
Figure 6-30. Experimental, linear and nonlinear solid element FEM.

The disparity in displacement between the experimental and the various finite element model results led to investigation of the boundary conditions. The boundary condition used in the FEMs was fixed at the support structure attachment. In order to test whether the experimental set-up may have had a hinge effect at the "fixed" locations, a torsional spring at each wing root was modeled in the plate FEM to allow rotation about the root axes in the bending plane of each wing. The spring constants were optimized by matching the deflection of each of the three measured locations at 30% load (420 N). These values were matched within 11% using optimization with linear analysis (Figure 6-31). The resulting spring constant values were at 7853.6 and 88933.7 N·m at the fore-wing root and beam support root, respectively. The results throughout the load application test points were within ±20% of the experimental values, which is consistent

121

with the strain discrepancy (Figure 6-31). The FEM without the springs was at least 40%
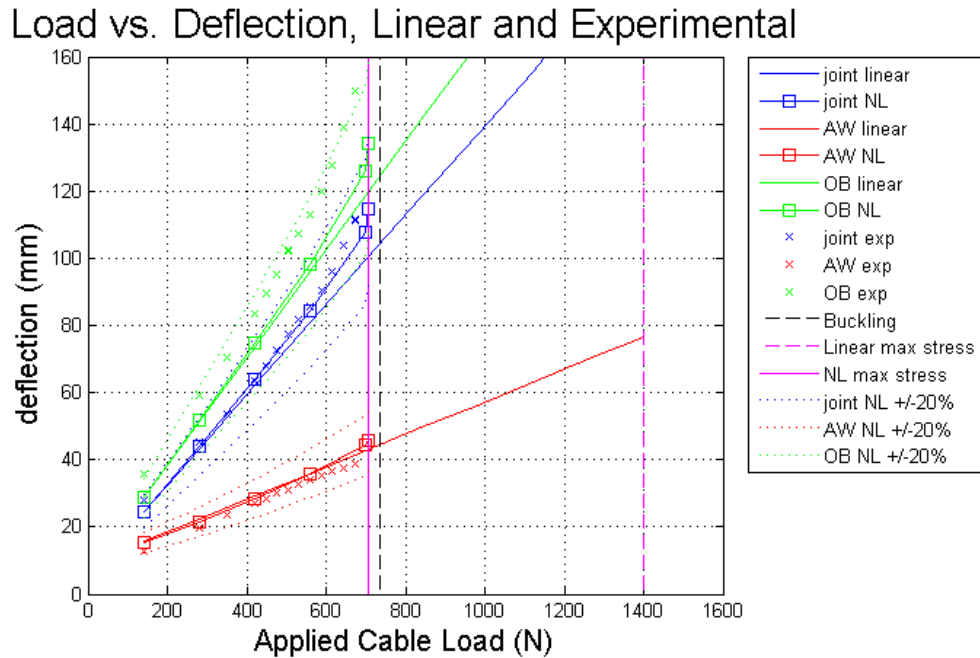
less than the experimental deflections.

Figure 6-31. Experimental, linear and NL plate results with spring boundary conditions.

6.3.2   Compare Predicted and Experimental Strains

The strain was measured at locations described in Table 6-3 and Figure 6-24. In

some cases these were compared to those on the plate FEM used in the design process.

The FEM nonlinear strain results were from the edge of the mid-plate, which is where the

strain gages were placed, rather than one side or the other. The yield stress of Aluminum

is 200-250 MPa. Thus, the associated strain is 3,429 μstrain given a Young's Modulus,

E, of 72.9 GPa.

The axial normal strain (Figure 6-32), the strain in the spar direction of each wing

is the greatest in compression at location 5, the fore-wing leading edge at the spar and

first rib junction. The greatest in tension was at location 13, the aft-wing trailing edge

root. The smallest amount of strain measured was at location 2, the fore-wing leading

122

edge root. However, on a previous set of test points, this gage was faulty. Thus, the data from this gage may be suspect. Locations 12 and 13 are located at the aft-wing root on the top and bottom of the spar, respectively. The strain here has opposite signs, as expected. In addition, the rate of change of the strain at these two locations is changing sign as the load is increased. The strain plots at other locations on the aft wing, Locations 11 and 14, also have some curvature, although less apparent. This curvature may indicate a hardening occurring in the aft wing on the trailing edge spar locations. Another possibility is that the aft wing could be showing signs of initial buckling as in the Goland joined wing in Chapter 4. Figure 6-33 depicts how the aft wing deflection in the plate FEM reverses direction at consecutive load increments (67% total gust equivalent load - orange and blue-green is at 67.43137%).
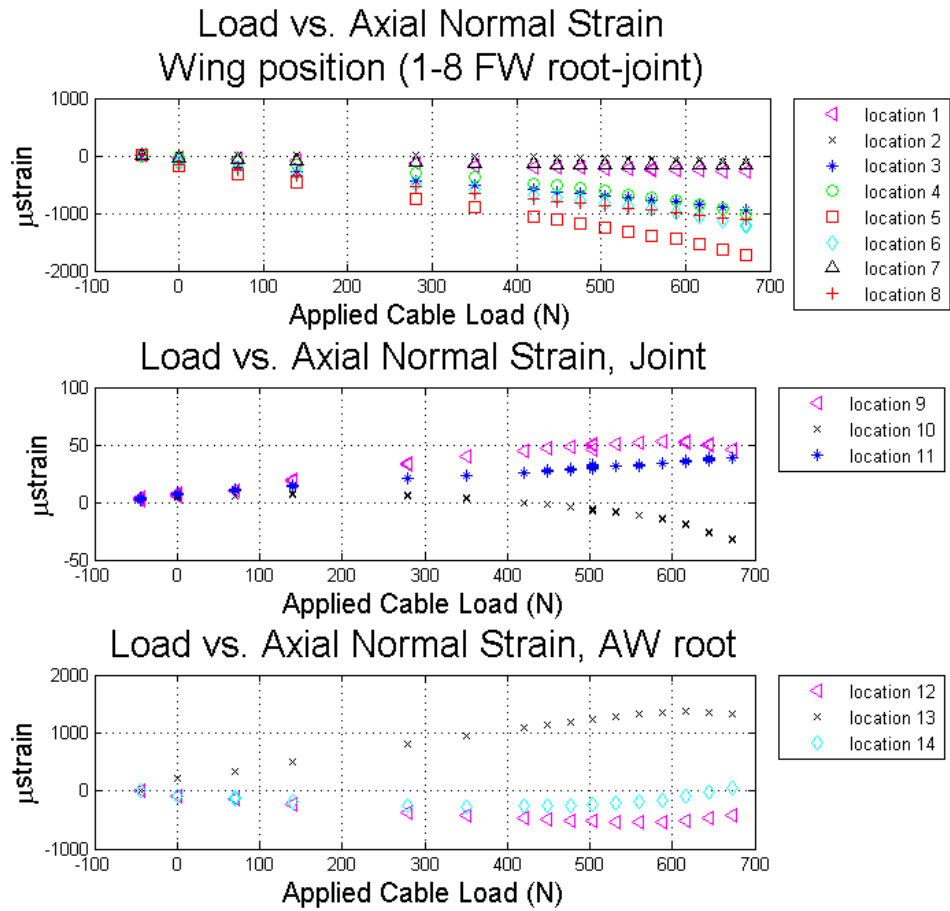
Figure 6-32. Experimental axial normal strain versus load.

Figure 6-33. Plate FEM nonlinear response last two feasible responses.

124

A comparison of axial strain was made at a few select points with the FEM (Figure 6-34). The strain in the FEM at location 5 was nearly 60% larger than that from the experimental results. Normally, larger strains would coincide with larger displacements, yet the FEM displacements were significantly less than the experimental displacements. This is an indication that the fixity of the boundary condition may be suspect.
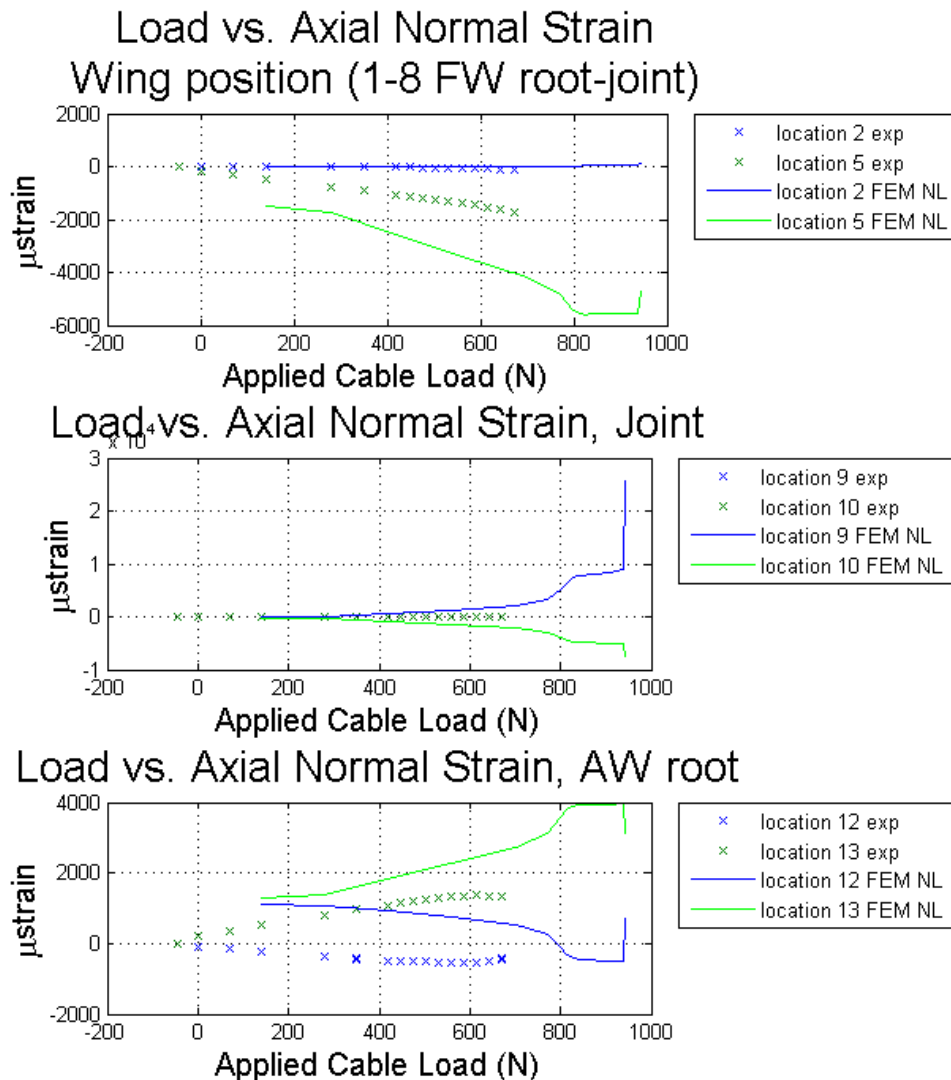

Figure 6-34. Experimental and FEM axial normal strain versus load at select points.

Signs of axial normal strain reverse in locations other than the spars, since the bending plane is not parallel to the chord of each wingbox but rather at an angle to the wing chord, in a plane containing the elastic axis of the two wings. The forward spar ends up above the bending plane, thus in compression. The rear spar of the aft wing is below the bending plane and in tension. This is demonstrated in Figure 6-35.
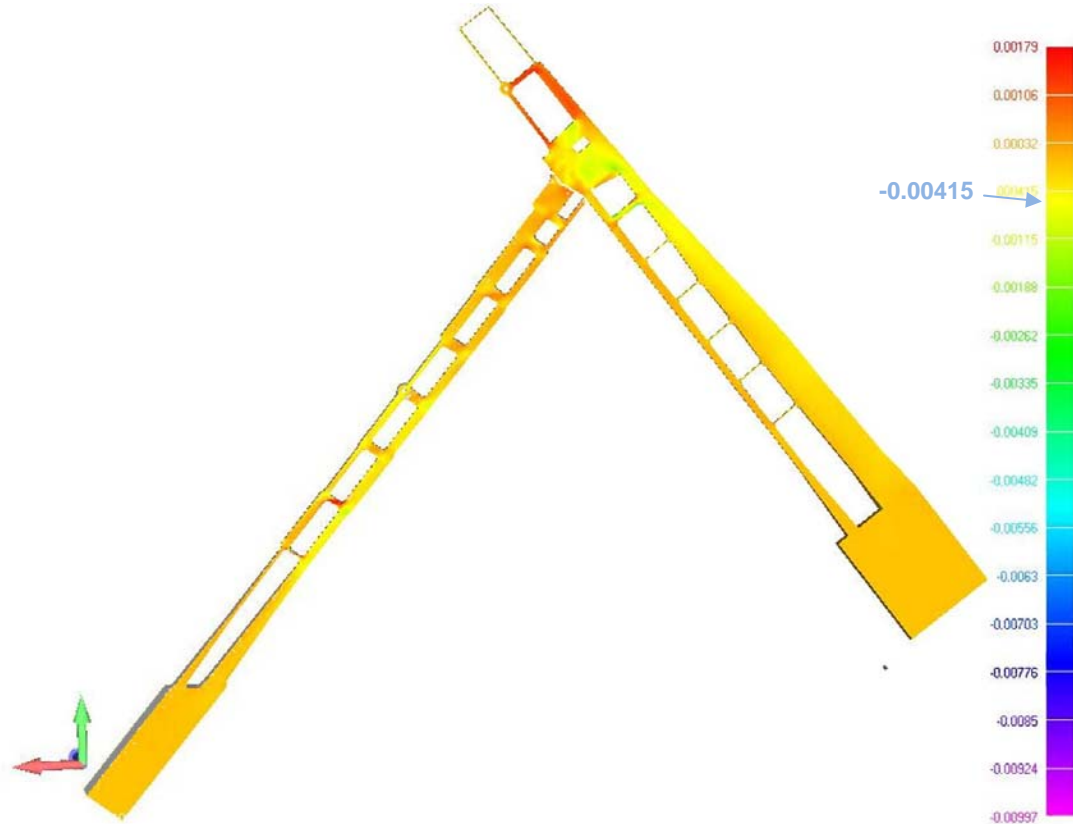

Figure 6-35. FEM normal strain along the spars, load applied side (note yellow areas).

Additional observations can be made with regard to the strain. Since the spars primarily carry bending, their transverse strain has an opposite sign due to Poisson effect. The transverse strain measured along the top of the spars is strain in the chordwise direction of each wing. This transverse strain is in compression where the maximum

occurs at location 6, the fore-wing leading edge at the spar and third rib junction (Figure 6-36).   The shear strain is also at its maximum at location 6 (Figure 6-37). Locations 4, 5, 12, and 13 are not shown because these positions only had linear strain gages, while the rest were rosettes.
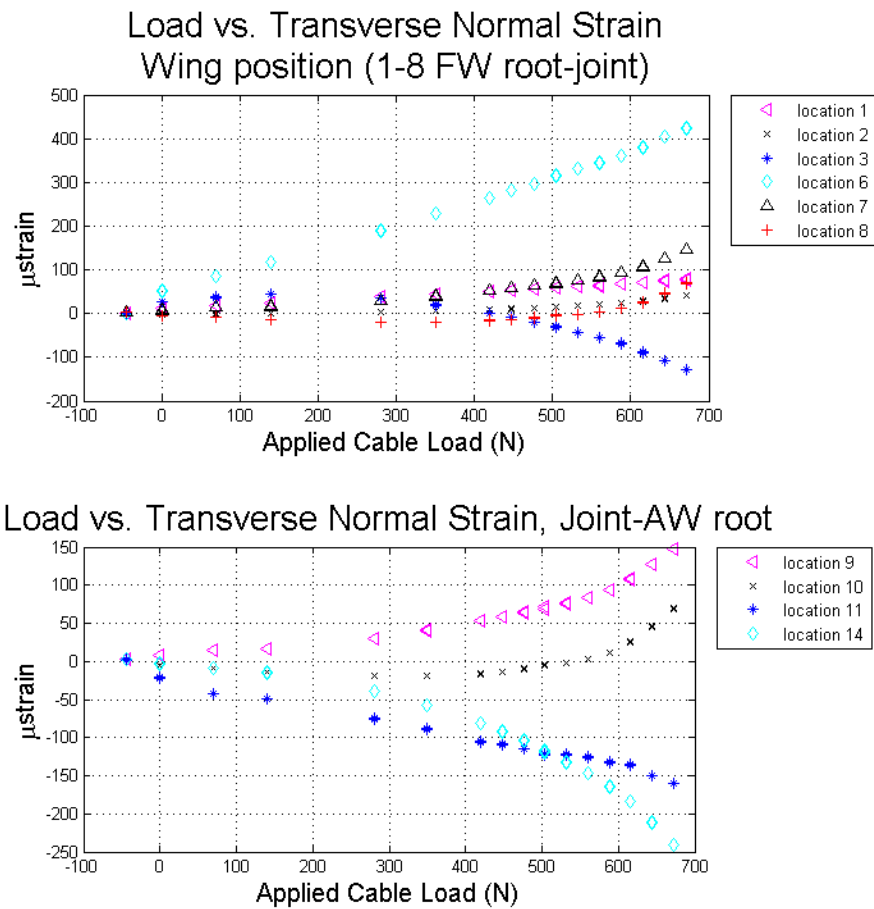

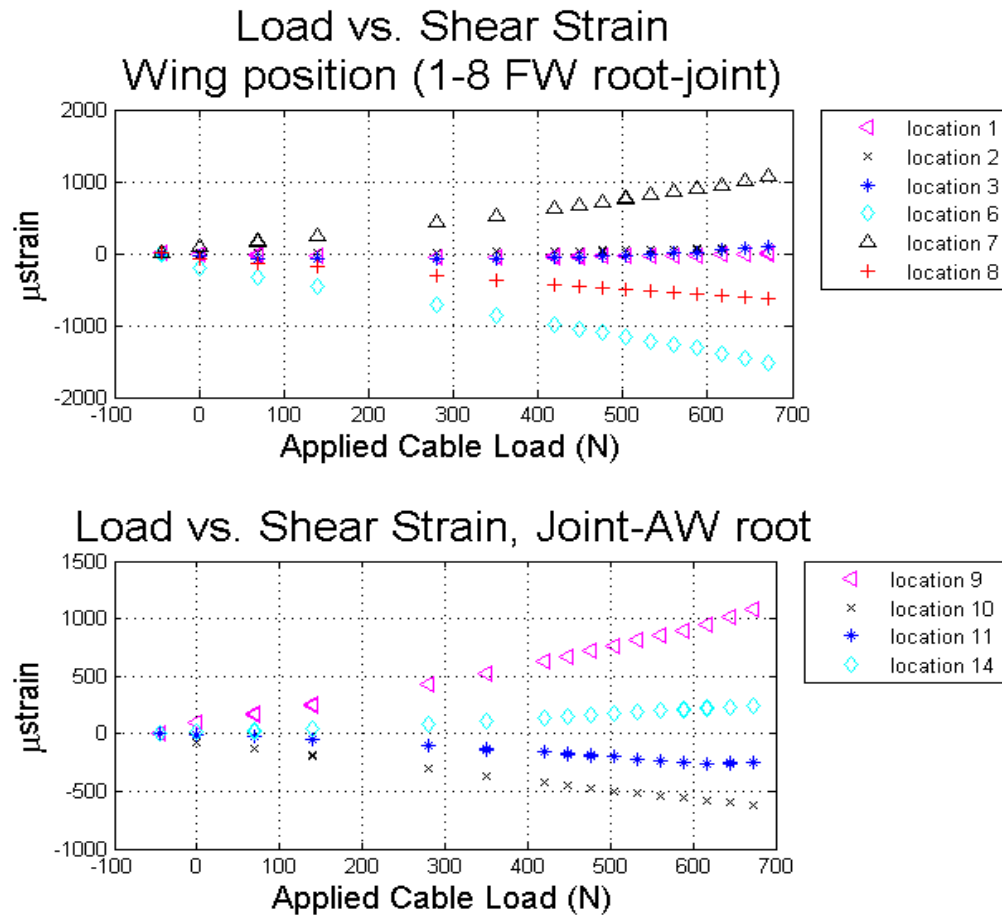**Figure 6-36.   Experimental transverse normal strain versus load.**

Figure 6-37. Experimental shear strain versus load.

Because the FEM primarily consists of plate elements, the FEM spar transverse strain is in the vertical direction of the spars. Since the stress of interest was in the individual wing bending planes, the strain gages were affixed to the top or bottom of the wings. Thus, a comparison of the experimental versus FEM shear strains in the spars is not shown. However, the rosette strain gages that are located at rib-spar junctions, 3, 6, 10, and 11, could be compared to the FEM transverse shear strain. A comparison of location 10, near the joint is depicted in Figure 6-38. The disparity between them is over 100%. This is possibly due to the boundary condition fixity, the FEM fidelity or the need
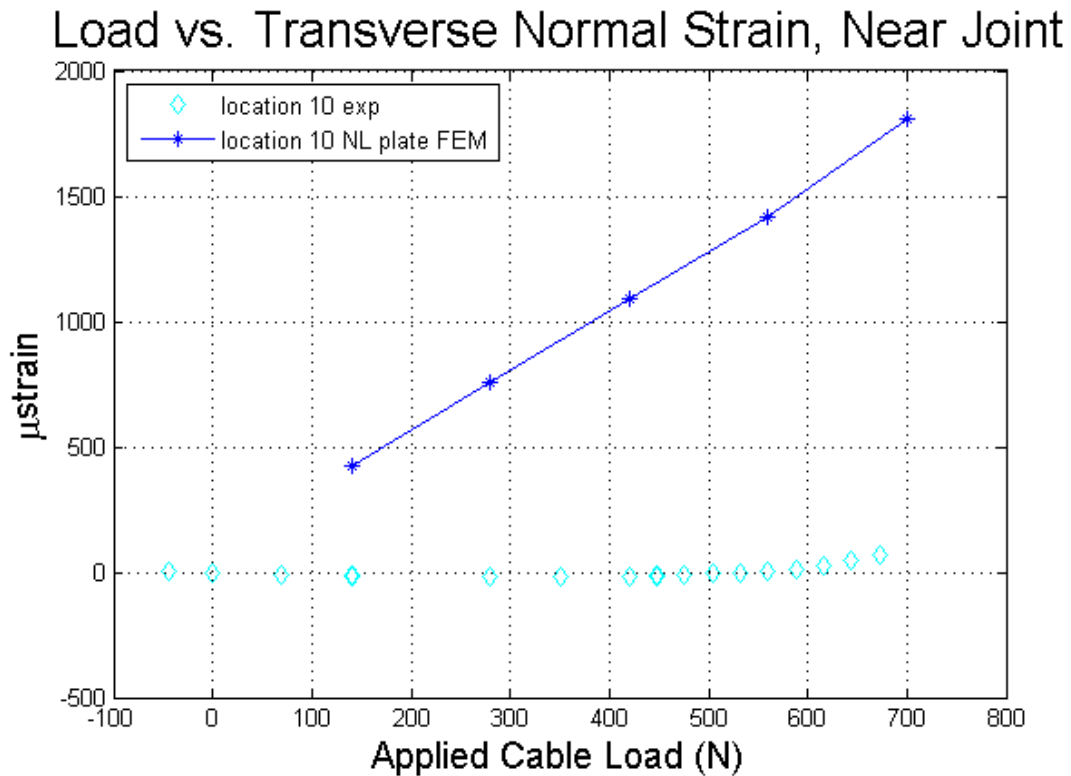
for solid elements in some regions.

Figure 6-38. Transverse load comparison at a spar-rib, location 10.

The same disparity in displacements that led to boundary condition investigation holds true for strains. The axial normal strain in the FEM without the springs was as much as 60% higher than the experimental results (Figure 6-34). However, with the spring boundary conditions, the strain at Location 5 is closer to the experimental results, within 2% (Figure 6-39). At other locations only varied improvements were made (Table 6-7). Since the boundary condition spring constants were determined by matching experimental displacements without regard to strains, the higher correlation of strains after springs were added to the FEM are strong evidence that the experimental structural attachments were not completely clamped. However, because not all the strains are well

matched, the FEM still appears to be deficient in some respect.

Table 6-7. Experimental axial normal strain versus FEM with and without spring BCs.

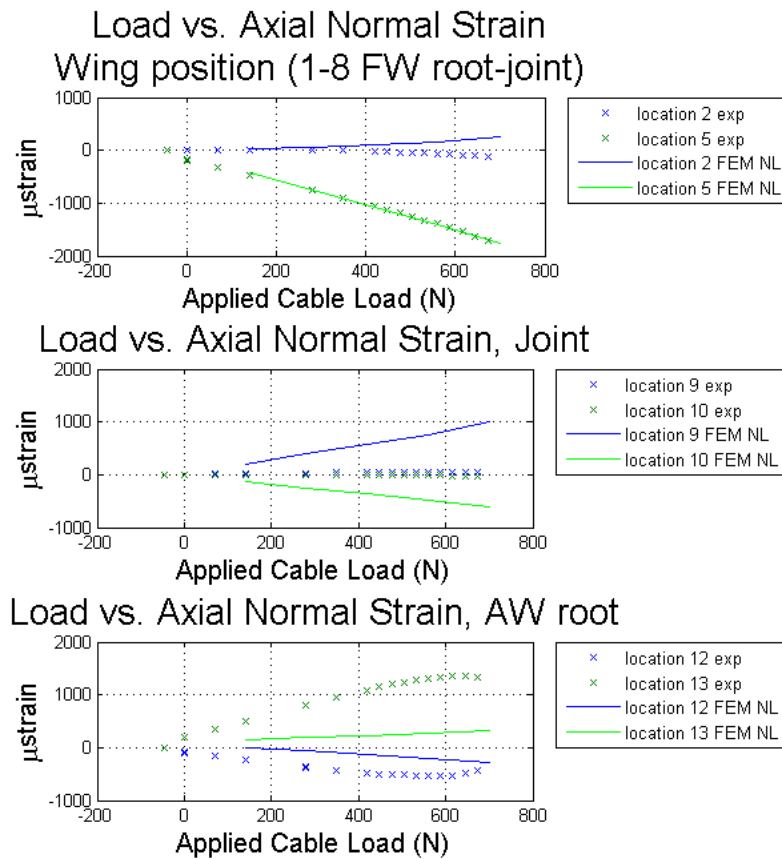| location	experimental	with spring BCs	% diff	without spring BCs	% diff
2	-20.6	99.36	120.73%	-5.186	-297.22%
5	-1053	-1075	2.05%	-2581	59.20%
9	44.8	576.1	92.22%	492.9	90.91%
10	-0.2	-364	99.95%	-900.7	99.98%
12	1089	-129.7	939.63%	938.4	-16.05%
13	-479.2	232.9	305.75%	1833	126.14%

Figure 6-39. Experimental and FEM (with spring BCs) axial normal strain versus load at the fore wing leading edge.

6.4   Nonlinear Response Discussion

If one compares the displacement of the plate and solid finite element models with fixed boundary conditions at the FW root and beam support root (the AW is connected on one side to the FW and to the beam support on the other side), there is much agreement. In fact, the purpose of that exercise was to validate the use of plate elements, despite the fact that the thickness of the plate was several times more than its height. The use of a plate-element model was necessary to simplify the optimization technique to design the structure in the initial stages. Once the experimental model geometry was finalized, a solid mesh was developed to compare to the experimental and plate results. Figure 6-40 depicts a comparison of the experimental versus the plate and solid FEM strain for selected points on the model. The solid elemental normal strains are those surrounding the nodal strain in the plate FEM at a strain gage location. There is a wide disparity among the solid elements surrounding most locations (several elements at each location are plotted in Figure 6-40), indicating a more refined mesh is needed before comparing to experimental data.
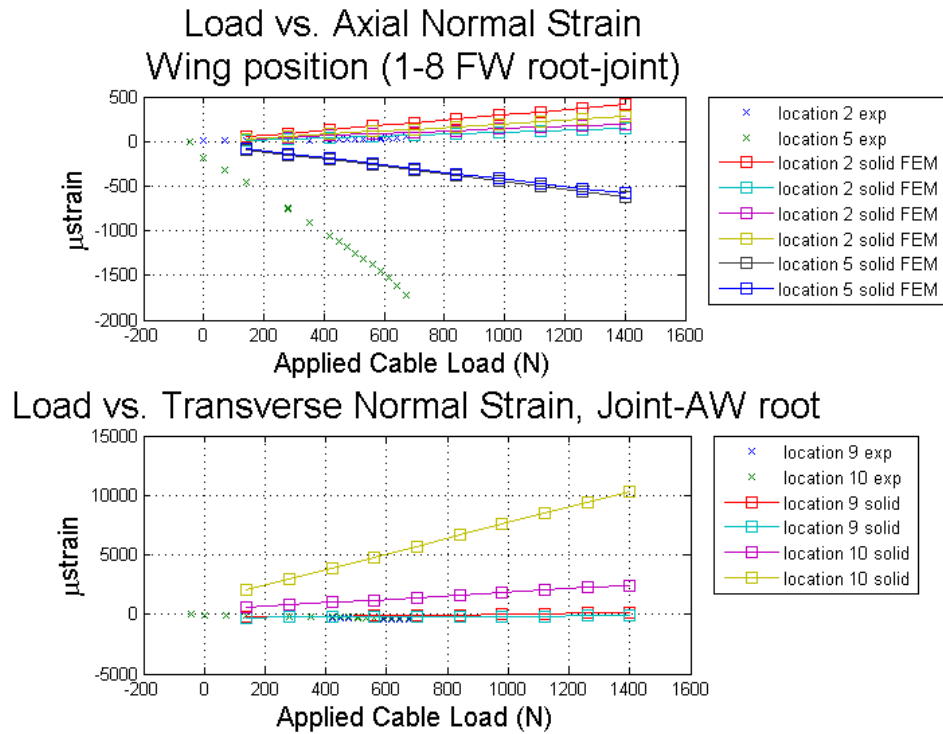
Figure 6-40. Experimental strain versus FEM plate and solid strain.

The FEM displacements correlated well with the experimental results once the springs at these locations were introduced to enforce these results in the plate-element model at the support locations in the experimental set-up. The strain results supported the hypothesis that a hinge effect may have occurred at the support locations in the experimental set-up. In addition, the solid FEM strains are similar to the plate-element strains (Figure 6-40).

This chapter demonstrated that nonlinear response could be experimentally validated on a scaled model. Prior to this test, nonlinear response on a scaled joined-wing model was not available as a predictive tool prior to full-scale flight test. In fact, to the author's knowledge, ground test using air loads, i.e. follower forces, were not captured prior to flight even for full-scale aircraft. Such ground tests on the full or

132

subscale model were suggested in the findings of the mishap report of at least one HALE aircraft [42].

This chapter also showed successful demonstration of an experimental procedure for follower forces. The trends experimentally validated those predicted by FEM analysis for nonlinear response to these follower forces. Also, a range of uncertainty was established between the nonlinear plate model and experiment. Likely sources of error were identified.

Next, the discussion and results in this chapter and those preceding are summarized. The impact and contribution of this body of work both analytically and experimentally are also discussed in the following chapter.

7. Conclusions, Contributions and Recommendations

7.1 Conclusions

In summary, the subject matter addressed can be reduced to this problem

statement:

> Incorporate flexible twist for pitch control in the design of a high altitude
> long-endurance aircraft, including consideration of nonlinear response,
> and experimentally validate feasibility.

This was accomplished by performing the following tasks:

1. Demonstrate nonlinear response on an aeroelastically scaled model.
2. Determine aerodynamic forces such that pitch control is realizable.
3. Experimentally validate nonlinear response on a scaled model.

The first task was to demonstrate whether scaling the nonlinear response was

possible if the model was aeroelastically scaled to include the critical buckling eigenvalue

(Chapter 4). The next task was accomplished by means of wind tunnel experimentation,

as discussed in Chapter 5. Lastly, task three (Chapter 6) was to scale the full-scale

model, while maintaining the nonlinear properties. Then a physical subscale model was

built and tested experimentally for the resulting static nonlinear response. The

verification was the comparison of load-deflection curves for the full and subscale

models.

In analyzing the results of these three tasks, one can conclude that physical

experimentation is a necessary practice to undertake, especially to understand the

response of geometric nonlinearities. Finite element models are useful in predicting

rough order-of-magnitude results, but they are only as good as the assumptions made,

which is the case for all models attempting to represent real physical characteristics.

George Box is credited with stating that "all models are wrong, some are useful," [43]

which is a lesson that is highlighted when comparing analytical, computer, or physically reduced-scale models to full-scale prototypes. All models by definition are a simulation of the real article, given certain simplifying assumptions. Which assumptions are used and in what manner can make the model more closely resemble the real artifact or force it further from the truth.

A model whose mode shapes match in addition to natural frequencies was crucial to aeroelastically scaling models. The case study simplified what an aircraft design might face in scaling a full-scale to a subscale model for manufacture and test to gain confidence in innovative, possibly high-risk, designs. Models differing in fidelity and construction technique were used, yet the same geometric scale was maintained. Since scaling geometrically is a simple step, it was forgone to demonstrate this procedure. If only natural frequencies are matched, the model can only match the target model with confidence at zero velocity. Throughout the velocity profile, there is no guarantee that these models will match aeroelastically. However, matching the vibration eigenvectors and eigenvalues proved to have satisfactory results throughout the velocity range.

In addition to scaling linear results, a method for scaling the nonlinear static results was demonstrated. Typically, this is not a requirement for aircraft that undergo small wing deformations in flight. However, with wings prone to large deformations, designing for nonlinear deflections is imperative.

With this dissertation several implications can be concluded. For one, scaling geometric nonlinearities on a reduced scale model was infeasible with the technique used herein. The demonstrated method augments the aeroelastic scaling with natural frequencies and mode shapes by scaling with the critical buckling eigenvalue and

eigenvector. With all four of these constraints (natural eigenvalues and eigenvectors, and buckling eigenvalues and eigenvectors) to match simultaneously, the reduced scale model did not sufficiently match the static nonlinear response of a target model. This was a hypothesis at the start of this dissertation. Second, the follower-force effect cannot be overlooked. Thus, load application perpendicular to wings with large deformations should be taken into account, since they have a significant impact on the response.

The wind tunnel experiment demonstrated that an actuated twist mechanism in the aft wing of a joined-wing configuration is a viable alternative to conventional control surfaces for pitch control. There were some drag issues at relatively low angles-of-attack that should be addressed for this particular case study. However, the overall determination that wing twist could produce effective control was affirmed. The wing twist emulated the same type of behavior that an elevator would provide and was realizable within a reasonable angle-of-twist and with force that can be activated by readily available actuators.

The static nonlinear analysis also emphasized that the correct load application is an assumption that must be included in a model simulation. It was necessary to apply the correct direction airloads acting on a surface of a high-aspect ratio wing. Since high-aspect ratio wings typically have large deformations, the load direction will significantly change in order to remain perpendicular to the wing. This was apparent in comparing the linear results, in which follower forces were not employed, to nonlinear results in the FEM analysis and the experimental results. It was also critical to apply boundary conditions that resemble the experiment. In a FEM, the boundary conditions can be perfectly fixed, for example. However, under physical examination one possible

explanation is that the boundary conditions were not perfectly fixed, since there was more measured deflection than expected. This may have been due to some hinge effect at the "fixed" locations. The way the experiment was conducted made it difficult to distinguish the rigid displacement due to rotation at this hinge from the deflection due to flexibility. While displacements were larger than expected, strains were less than expected. Since larger strains normally accompany larger displacements, this lends further credence to the hinge hypothesis whereby a hinge results in rigid body rotation that has no accompanying strain.

7.2   Contributions

Employment of high-altitude, long-endurance aircraft to provide continuous coverage in theaters of operation is the key motivator for developing a joined-wing configuration. This type of platform has the advantage of employing higher resolution sensors. However, with advanced concepts such as this design configuration, several challenges emerge due to the structural flexibility. This author contributed an understanding of and means to combat these challenges for the structural and multidisciplinary optimization community, and the benefactors of persistent coverage in theater.

One challenge facing this type of configuration was to maximize the useable wing surface area for the sensors and avoid interference with them. This challenge was met by replacing pitch control surfaces with an aft-wing twist design and demonstrating the concept is physically realizable by experimental validation on a reduced scale model via force and moment collection due to airloads. These experimental wind-tunnel results demonstrated that aft-wing twist is effective for pitch control in the reduced scale model

for $-15º \leq \alpha \leq 15º$. In addition, the wind-tunnel corrections for camber and center of pressure found through experiment are useful to calibrate low-fidelity finite element models.

The second challenge was the ability to predict nonlinear response of long-endurance aircraft. This was addressed by experimental validation of nonlinear response on a reduced scale model. Design risks inherent to nonlinear configurations such as a HALE aircraft are reduced by employing the scaling procedures developed and validated in the experimental portion of this study. The nonlinearities attributed to the air load following the wing were modeled and experimentally carried out. The demonstration here of capturing the nonlinear response on a reduced scale model using predictive methods is a contribution that can significantly reduce risk to high-aspect ratio wing designs.   Although the FEM predictions were about 40% lower than experimental nonlinear deflections, this was brought to within 10-20% with the correction of the boundary condition fixity problem. The endeavor was valuable to demonstrate that linear predictions, which are the industry norm, are not satisfactory when addressing systems with large deflections due to follower forces. The linear predictions can be 10-20% more conservative than the nonlinear predictions.   The predictive method herein included scaling the aeroelastic characteristics of an aircraft in the model that represents it, and capturing the nonlinear response.

In summary, the contribution to this field of study is three-fold. An aeroelastic scaling procedure that extends to incorporating nonlinear buckling response was developed. Secondly, implementation of flexible twist for pitch control was developed and validated on a wind tunnel model of a high-altitude long-endurance joined-wing

aircraft. Lastly, the experimental validation of modeling nonlinear response on a reduced scale model addressed the necessity of incorporating follow-force effect and the non-trivial nonlinear response in preliminary design of highly flexible aircraft like the Joined-Wing Sensorcraft. The research within this dissertation set the stage for future examination of the physical model used here for nonlinear response.

7.3   Recommendations

The hypothesis that equations of motion for geometrically nonlinear response to follower forces could be scaled by matching vibration eigenvalues and eigenvectors, along with the buckling eigenvalue and eigenvector was analyzed in the research within this dissertation. Using the first three vibration modes and the first buckling mode was not sufficient for proper scaling. There are several recommendations that may prove beneficial in properly scaling nonlinear response for further research.

First, match higher buckling modes to aid in scaling the nonlinear response, since they may significantly contribute to the nonlinearities that occur. Second, investigate whether internal loads are equivalent in the target and reduced scale models to ensure proper geometric stiffness for the buckling. Lastly, as discussed in the theoretical section, another option is to wrap an optimization scheme around nonlinear analysis. The purpose of the procedure examined in Chapter 4 was to avoid this more time-consuming, complicated procedure. However, it may be necessary to scale nonlinear response by attempting to match the nonlinear response directly, and in an iterative fashion.

The following future work is recommended in order that aircraft designers might find the risk acceptable to take advantage of a joined-wing configuration. First, a study like that demonstrated with the Goland$^{\pm}$ beam and strut model case should be

accomplished. For example, extend the scaling procedure to incorporate more buckling eigenvalues, match more modes and modal geometric stiffness, or optimize about nonlinear analysis. In addition, consider a more general case of dissimilar degrees-of-freedom. Furthermore, it would be prudent to take the Boeing Joined-Wing Sensorcraft model, once it is optimized for weight such that it becomes a highly-flexible design, through the processes developed and demonstrated in this work. For instance, a reduced scale model of the more flexible Boeing model should be designed by matching natural frequencies and modes shapes, and at least the first buckling eigenvalue and mode shape.

Second, a simple load case was used on the model in the research within this dissertation. A method for adjusting the aerodynamic panel such that the load is applied to the deformed shape due to the highly flexible nature of the wing was developed by Garmann and demonstrated by Adams [40]. The application of this loading would more closely model conditions the Sensorcraft may experience in flight such that nonlinear predictions are more accurate for a variety of flight conditions.

Lastly, one more step could be taken to verify whether the plate-element model is valid for the purpose of modeling the nonlinear response due to static loads. This step is to analyze the displacements in the solid-element model with the same torsional springs at the root boundary condition locations. This was out of the scope of the dissertation since the predictions were a comparison of the optimized FEM to the experimental results. Since the optimization was simplified by the use of a plate-element model, further refining of the FEM was not required in this development.

8. Bibliography

[1] Reich, G., Bowman, J. and Sanders, B. , "Large-Area Aerodynamic Control for High-Altitude Long-Endurance Sensor Platforms ," *Journal of Aircraft*, 42(1): 237-244 (January 2005).

[2 Boeing Aircraft Company Sensorcraft design

[3] Wolkovitch, J., "The Joined Wing: An Overview," *Journal of Aircraft*, 23:161-178 (March 1986).

[4] Smallwood, B., Canfield, R., Terzuoli, A., "Structurally Integrated Antennas On A Joined-Wing Aircraft" AIAA-2003-1459, 44th AIAA/ASME/ASCE/AHS Structures, Structural Dynamics, and Materials Conference 7-10 April 2003, Norfolk, Virginia

[5] Bond, V. , Canfield, R., Matos, M., Suleman, A., and Blair, M., "Wind Tunnel Testing of Twisted Wing for Longitudinal Control in a Joined Wing Aircraft", 47th AIAA/ASME/ASCE/AHS/ASC Structures, Structural Dynamics and Materials Conference, Honolulu, HI, April 2007.

[6] Blair, M., Canfield, R., Roberts, R., "Joined-Wing Aeroelastic Design with Geometric Nonlinearity", *Journal of Aircraft*, 42(4):832-848 (July-August 2005).

[7] Rasmussen, C., Canfield, R., Blair, M., "Joined-Wing Sensorcraft Configuration Design", *Journal of Aircraft,* 43(5): 0021-8669 (2006).

[8] Blair, M. and Canfield, R., "A Joined-Wing Structural Weight Modeling Study", AIAA 2002-1337, 43rd AIAA/ASME/ASCE/AHS/ASC Structures, Structural Dynamics, and Materials Conference, Denver, Colorado, April 2002.

[9] Roberts, R, Canfield, R., Blair, M, "Sensor-Craft Structural Optimization and Analytical Certification", AIAA Paper 2005-2015, 46th AIAA/ASME/ASCE/AHS/ASC Structures, Structural Dynamics & Materials Conference, Austin, Texas, April 2005.

[10]   Kroo, I.M. , Gallman, J.W. and Smith, S.C., "Aerodynamic and Structural Studies of Joined-Wing Aircraft," *Journal of Aircraft*, 28(1): 74-81 (January 1991).

[11] Smith, S.C., Cliff, S.E., and Kroo, I.M., "The Design of a Joined-Wing Flight Demonstrator Aircraft", AIAA/AHS/ASEE Aircraft Design, Systems and Operations Meeting, St. Louis, MO, September 1987.

[12] Pereira, P, Almeida, L., and Suleman, A., Canfield, R. Bond, V., Blair, M., "Aeroelastic Scaling And Optimization Of A Joined-Wing Aircraft", AIAA-2007-1889, 47th AIAA/ASME/ASCE/AHS/ASC Structures, Structural Dynamics and Materials Conference, Honolulu, HI, April 2007.

[13] Goland, M., "The Flutter of a Uniform Cantilever Wing", *Journal of Applied Mechanics*, 12(4):197-208 (December 1945).

[14] Lee, D. and Chen, P., "Nonlinear Aeroelastic Studies on a Joined-Wing with Wing Buckling Effects", AIAA Paper 2004-1944, April 2004**.**

[15] Wang, Z. Chen, P., and Lui, D., "Nonlinear Aeroelastic Analysis for HALE Wing Including Effects of Gust and Flow Separation", AIAA 2007-2106, 47th AIAA/ASME/ASCE/AHS/ASC Structures, Structural Dynamics and Materials Conference, Honolulu, HI, April 2007.

[16] Patil, M., "Nonlinear Aeroelastic Analysis Of Joined-Wing Aircraft", AIAA 2003-1487, 44th AIAA/ASME/ASCE/AHS Structures, Structural Dynamics, and Materials Conference, Norfolk, Virginia, 7-10 April 2003.

[17] Tyler, C., Schwabacher, G., and Carter, D., "Comparison Of Computational and Experimental Studies For A Joined-Wing Aircraft", AIAA-2002-0702, January 2002.

[18] Livne, E. "Aeroelasticity of Joined-Wing Airplane Configurations: Past Work and Future Challenges - A Survey," AIAA Paper 2001-1370. 42d AIAA/ASME/ASCE/AHS/ASC Structures, Structural Dynamics and Materials Conference, Seattle WA, 16-19 April 2001.

[19] Weisshaar, T.A. and Lee, D.H., *"Aeroelastic Tailoring of Joined-Wing Configurations,"* AIAA Paper 2002-1207, April 2002.

[20] Lin, H.H., Jhou, J. , and Stearman, R., "Influence of Joint Fixity on the Aeroelastic Characteristics of a Joined Wing Structure," AIAA Paper 1990-0980. 31st AIAA/ ASME/ASCE/AHS/ASC Structures, Structural Dynamics and Materials Conference, Long Beach CA, April 1990.

[21] Pendleton, E. Lee, M., Wasserman, L., "An Application Of The Active Flexible Wing Concept To An F-16 Derivative Wing Model", AIAA Paper 91-0987-CP.

[22] Bond V., Canfield, R. Suleman, A., Pereira, P., and Blair, M., "Aeroelastic Scaling of the Goland wing for verification on a Joined-Wing Aircraft," 12th AIAA/ISSMO Multidisciplinary Analysis and Optimization Conference, Victoria, British Columbia, Canada, September 2008.

[23] Corneille, J., and Franke, M., "Wind Tunnel Tests of a Joined-Wing Missile Model", AIAA Paper 2000-0938, January 2000.

[24] Lee, D. and Chen, P., "Nonlinear Aeroelastic Studies on a Joined-Wing with Wing Buckling Effects", AIAA Paper 2004-1944, April 2004.

[25] Roberts, Ronald, *Sensor-Craft Analytical Certification*, MS Thesis, Graduate School of Engineering, Air Force Institute of Technology (AETC), Wright-Patterson AFB, Ohio, March 2003. AFIT/GAE/ENY/03-06

[26] Sitz, Jennifer. *Aeroelastic Analysis of a Joined-Wing Sensorcraft*, MS Thesis, Graduate School of Engineering, Air Force Institute of Technology (AETC), Wright-Patterson AFB, Ohio, June 2004. AFIT/GAE/ENY/04-J12.

[27] Craft, Ryan. *Drag Estimated for the Joined-Wing Sensor Craft*, MS Thesis, Graduate School of Engineering, Air Force Institute of Technology (AETC), Wright-Patterson AFB, Ohio, June 2005. AFIT/GAE/ENY/05-J02.

[28] Kimler, F. and Canfield, R., "Structural Design of Wing Twist for Pitch Control of Joined Wing SensorCraft", AIAA 2006-7134, 11th AIAA/ISSMO Multidisciplinary Analysis and Optimization Conference, Portsmouth, Virginia, September 2006.

[29] Pope, A., Wind Tunnel Testing, 1954.

[30] Bisplinghoff, R., Ashley, H., and Halfman, R., Aeroelasticity, Cambridge, Mass., Addison-Wesley Pub. Co., 1955.

[31] Anderson, J., Introduction to Flight, 2nd Ed.

[32] Anderson, J., <u>Introduction to Flight</u>, 3rd Ed.

[33]   Hodges, D. and Pierce, G., <u>Introduction to Structural Dynamics and Aeroelasticity</u>, Cambridge, [England], New York: Cambridge University Press, 2002.

[34] Zona Technology, Inc. *ZAERO 7.1 Theoretical Manual*. Scottsdale, AZ: Zona Technology, Inc., September 2004.

[35] Meirovitch, L. <u>Fundamentals of Vibration</u>, 2001.

[36] MSC/NASTRAN *Handbook for Nonlinear Analysis Based on Version 67*, Los Angeles, CA: MacNeal-Schwendler Corp., March 2002.

[37] Smith, S.C., Cliff, S.E., and Kroo, I.M., "The Design of a Joined-Wing Flight Demonstrator Aircraft", AIAA/AHS/ASEE Aircraft Design, Systems and Operations Meeting, St. Louis, MO, September 1987.

[38] Eastep, F.E and Olsen, J.J, "Transonic Flutter Analysis of a Rectangular Wing with Conventional Airfoil Sections", *AIAA Journal* 1980, 0001-1452 vol.18 no.10 (1159-1164).

[39] Discussions with Dr. Raj Nangia, Nangia Aero Research Associates , 28 November 2006.

[40] Adams, Brandon. *Structural Stability of a Joined-Wing Sensorcraft*, MS Thesis, Graduate School of Engineering, Air Force Institute of Technology (AETC), Wright-Patterson AFB, Ohio, June 2007. AFIT/GAE/ENY/07-J01.

[41] Armani, C., Nye, A., Stevens, C., Swenson, E., Mechanical Engineering 542 class project, solid modeling of the Boeing Joined-Wing Sensorcraft, Spring quarter 2008.

[42] Noll, T, Brown, J.M., Perez-Davis, M., Ishmael, S., Tiffany, G., and Gaier, M. "Investigation of the Helios Prototype Aircraft Mishap, Volume I, Mishap Report", January 2004.

[43] Box, G.E.P., *Robustness in the strategy of scientific model building, in Robustness in Statistics*, R.L. Launer and G.N. Wilkinson, Editors. 1979, Academic Press: New York.

A. Appendix: Wind Tunnel Model Dimensions, Experimental Parameters and Set-up

The following tables and figures provide illustration of the dimensions of the wind tunnel test article used in Task 1 to determine aerodynamic forces such that pitch control is realizable.

Table A-1. Dimensions of wind tunnel model.

Dimensions	
fore wing chord, c_m*	0.097m
aft wing chord	0.045m
vehicle half-span	0.600m
½ fore wing area, S*	0.04m^2

*used in coefficient calculations

Table A-2. Dynamic Pressure, q (Pa)*

Test Run	Nominal	Twist Up	Twist Down
20 m/s	236.96	235.64	235.27
30 m/s	530.65	527.85	526.94
40 m/s	927.27	927.27	916.51
50 m/s	1427.5	1438.6	1423.5

*Outside air pressure and tunnel flow temperature were used in calculating air density for dynamic pressures listed.
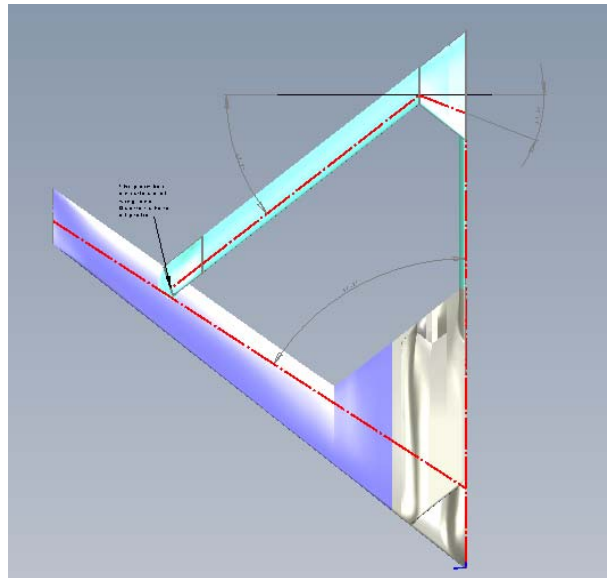
Figure A-1. Top view, dimensions in mm.

775

225

d = 306

Wind tunnel balance point

c.p
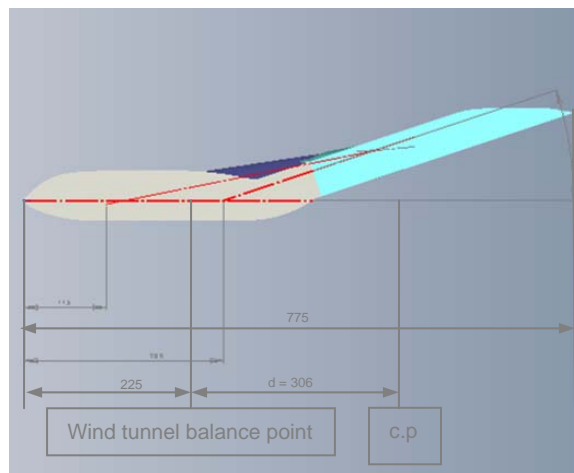
Figure A-2. Side view with wind tunnel balance position and center of pressure, dimensions in mm.
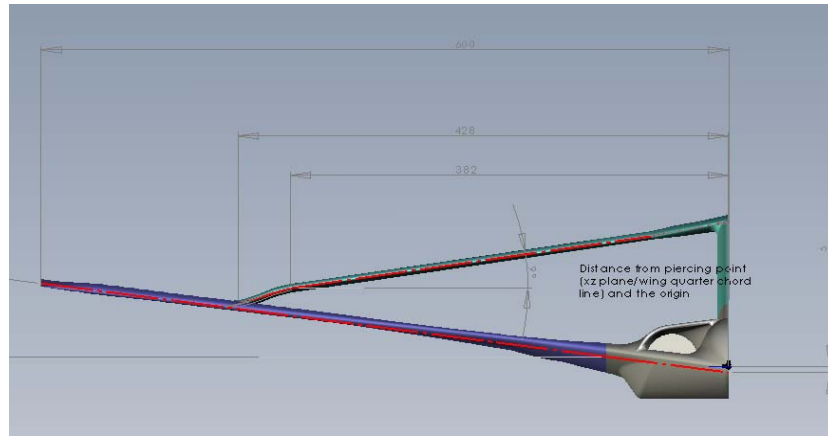
Figure A-3. Front view, dimensions in mm.
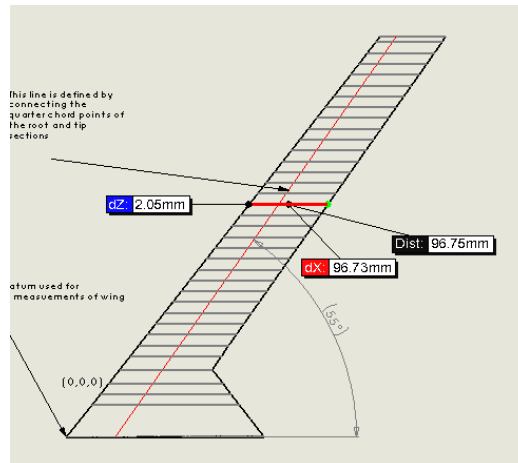
Figure A-4. Front wing, dimensions in mm.
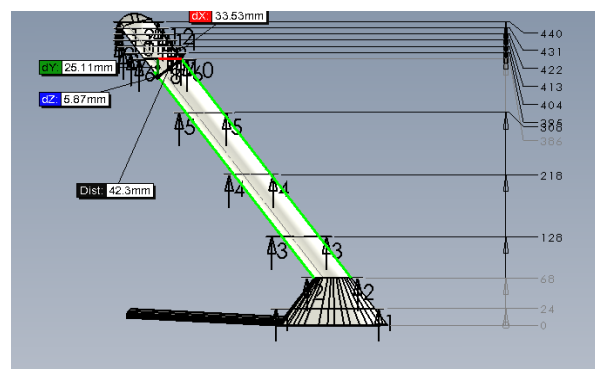
Figure A-5. Aft wing, dimensions in mm.

146

Figure A-6. Control room during wind tunnel testing.

Figure A-7. Tunnel power controller.

Figure A-8. Tunnel cooling system controller.

Figure A-9. Controller/display for wind tunnel.
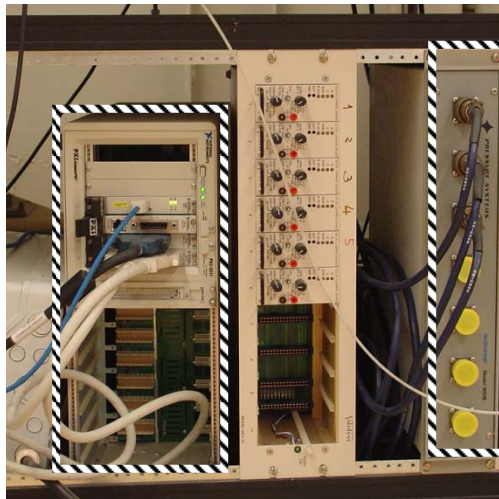
Figure A-10. Pressure data acquisition system and transducers for pressure (left to right in hashed boxes).

Figure A-11. Pressure transducers and pressure tubes (blue cables and clear tubes).
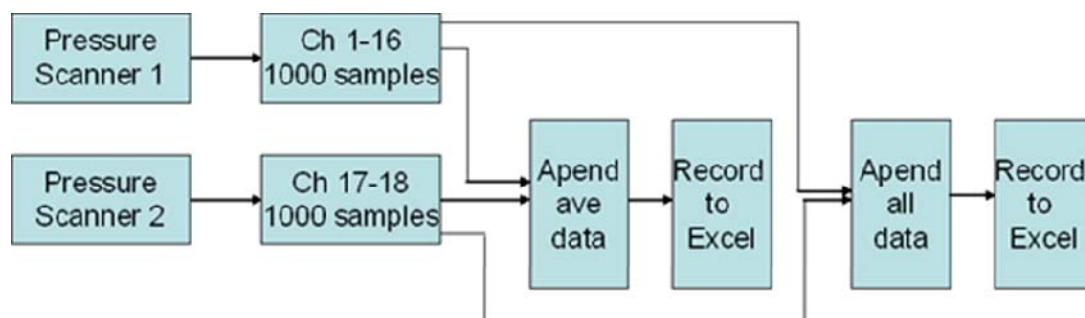
Figure A-12. LabVIEW sequence.
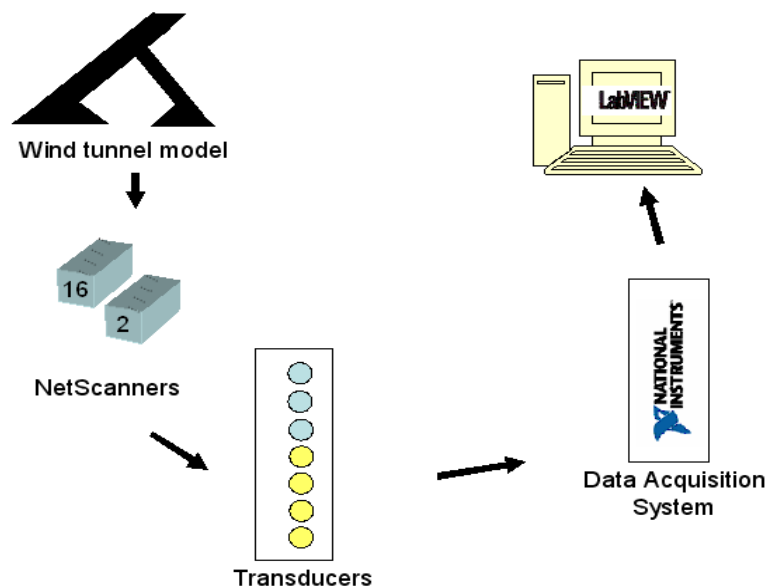
Figure A-13. Pressure Measurement Test Set-up.
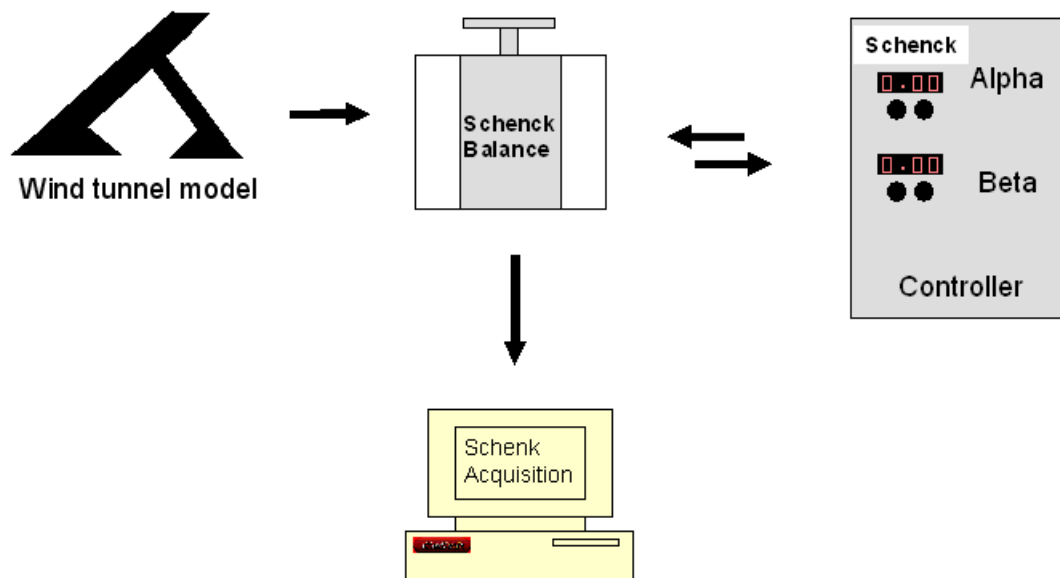
Figure A-14. Force balance set-up.

B. Appendix: Complete Experimental Test Force and Moment Results

The following plots provide the full complement of force and moment data analyzed from the wind tunnel tests described in Chapter 5. They include the force and moment data for 20 to 50 m/s.
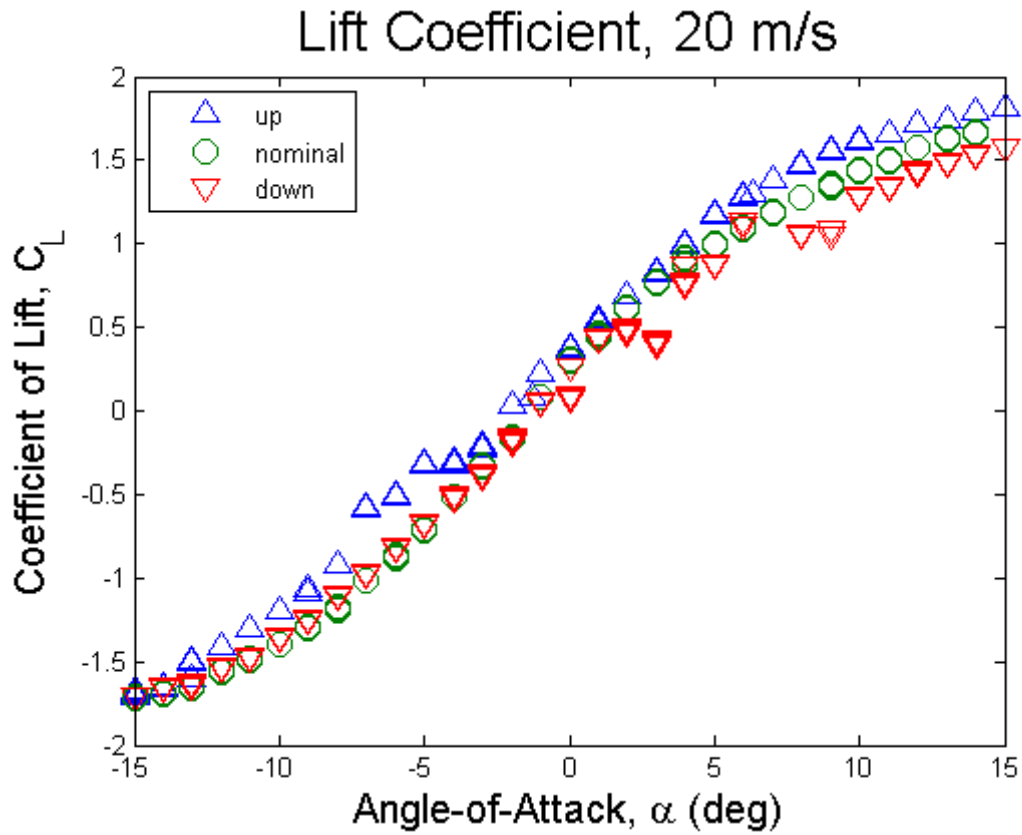
Figure B-1. Lift curves, 20 m/s.
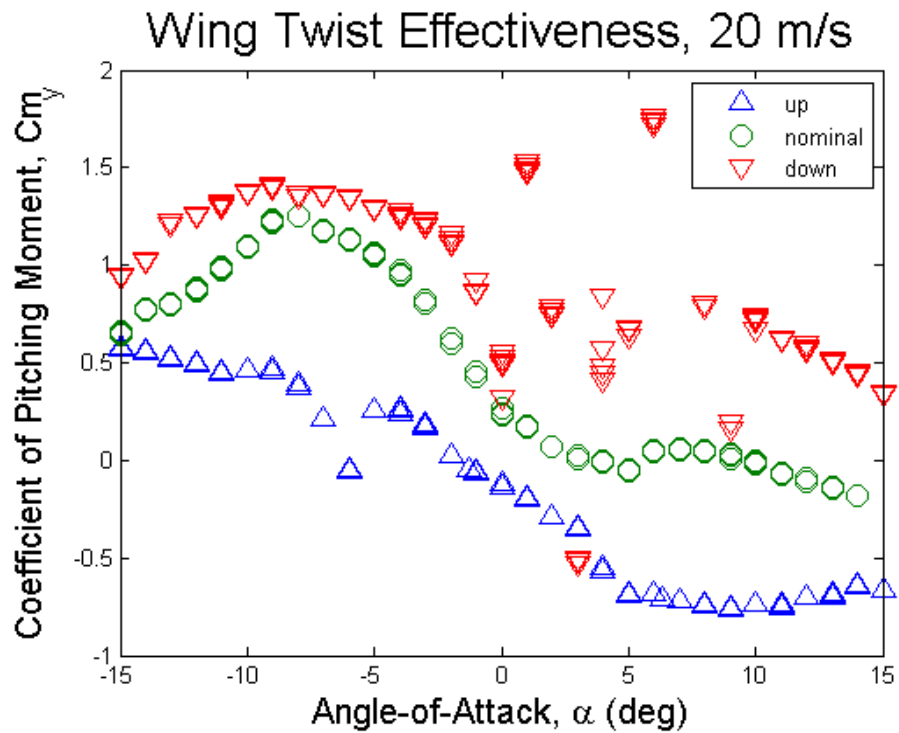
Figure B-2. Wing Twist Effectiveness Curves, 20 m/s.
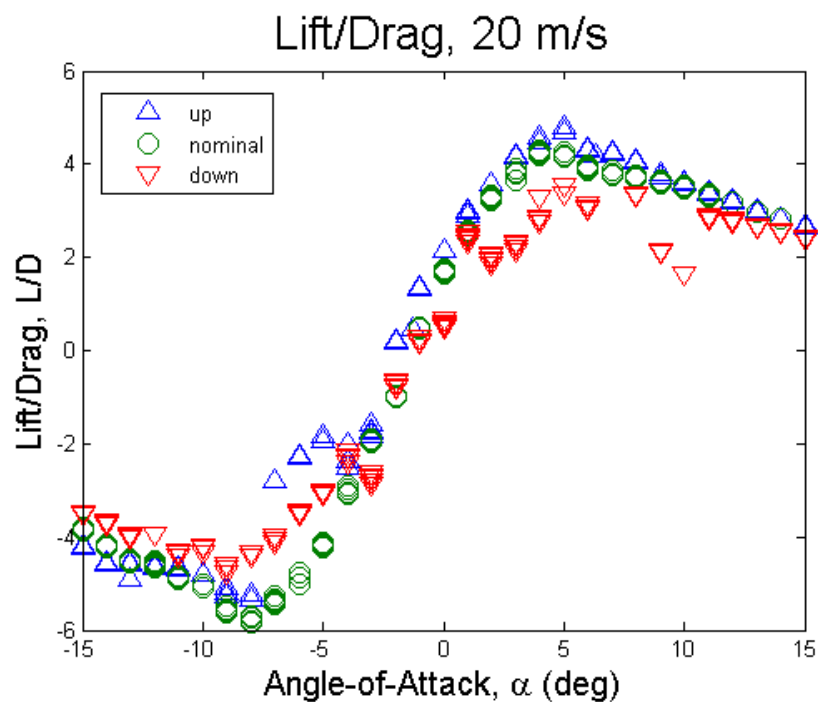
Figure B-3. Lift-to-Drag Curves, 20 m/s.
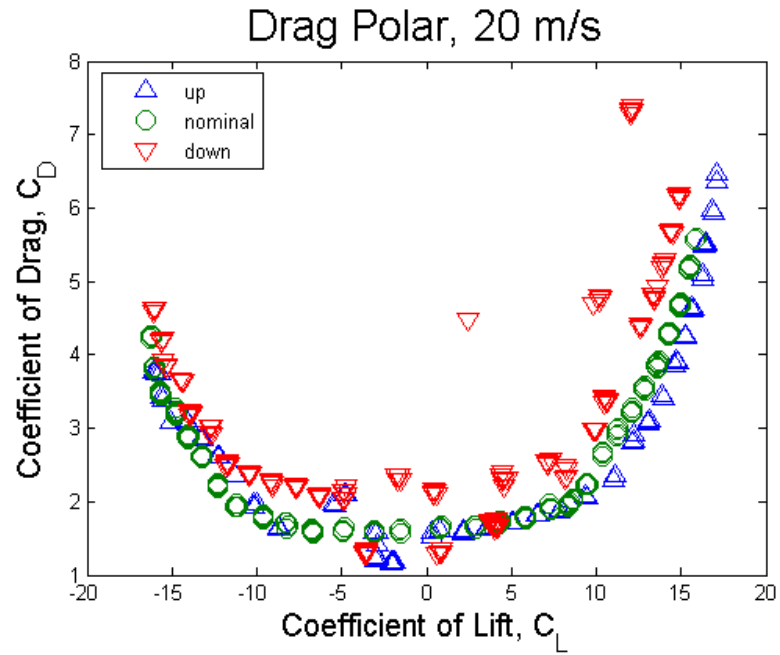
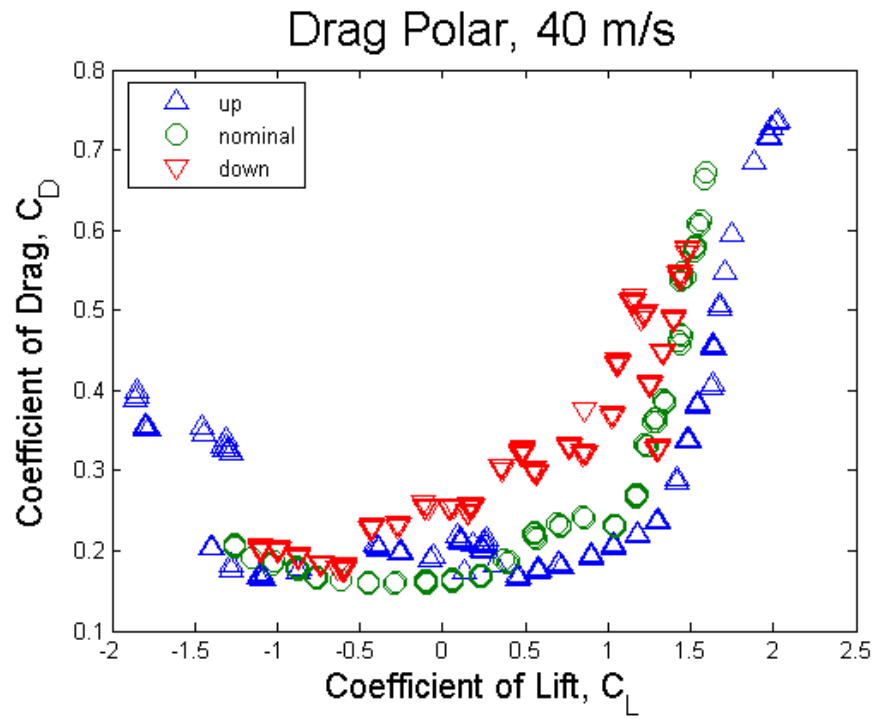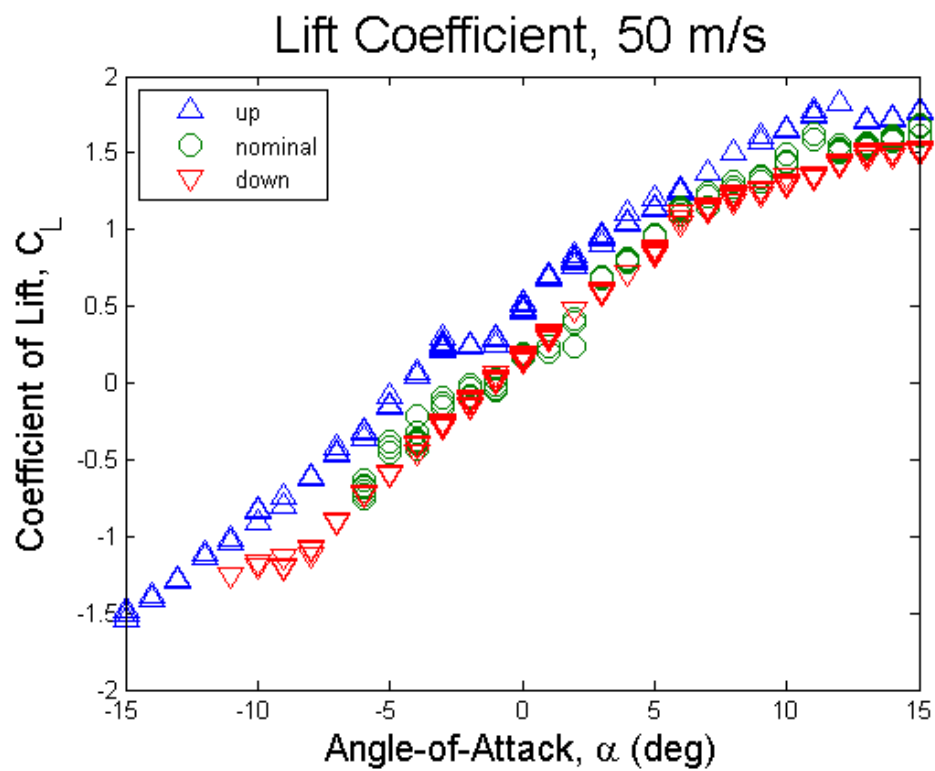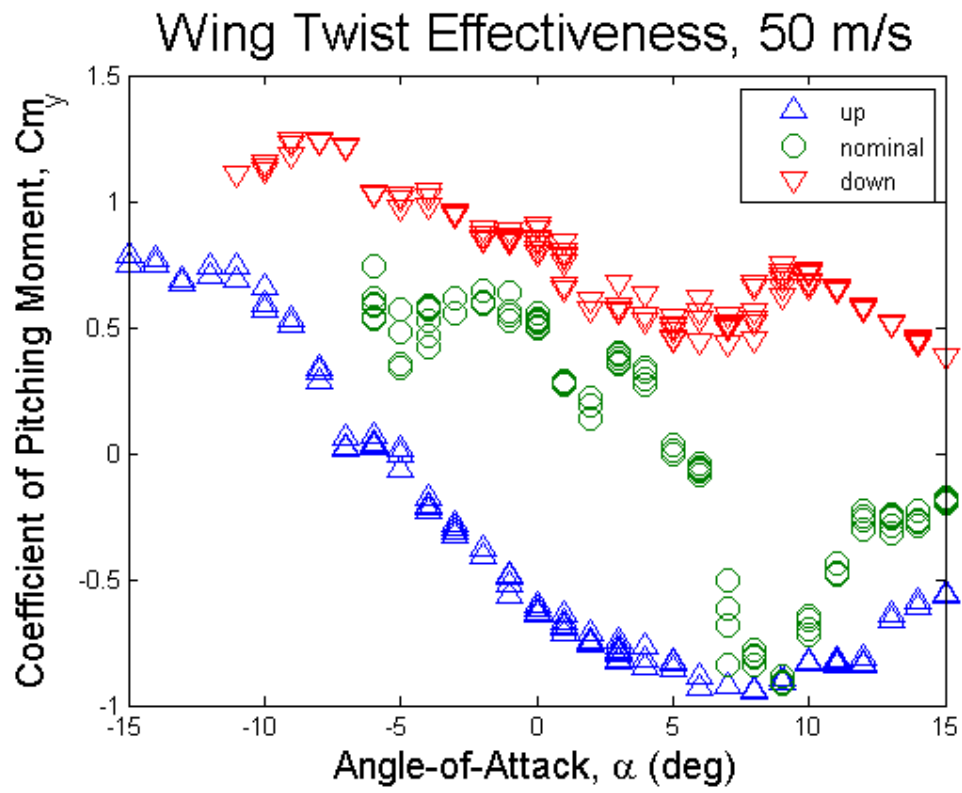**Figure B-4. Drag Polar, 20 m/s.**
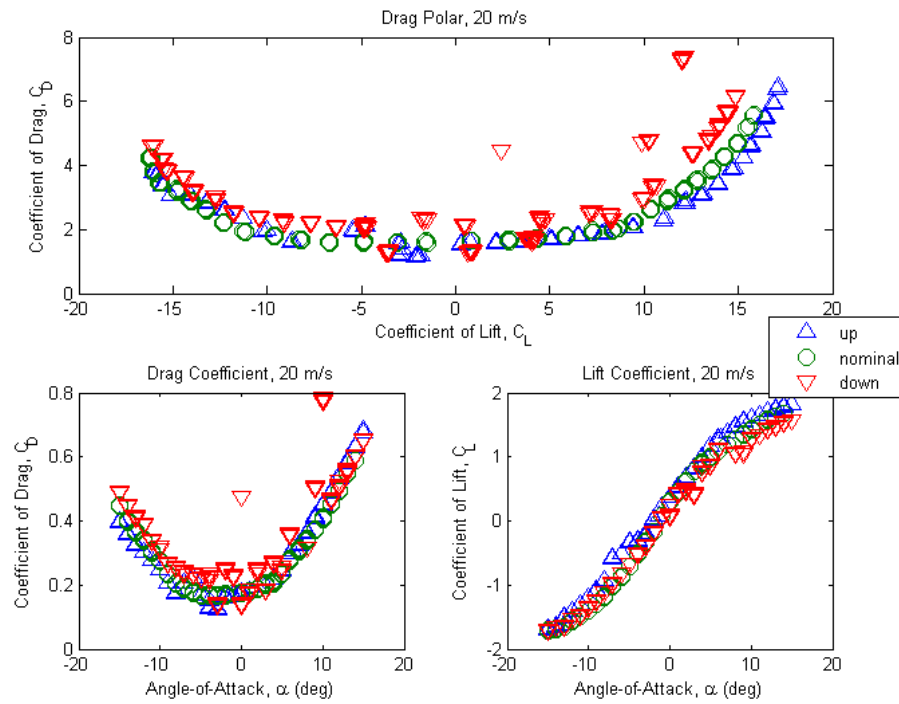
Figure B-5. Lift and Drag Curves, 20 m/s.

153
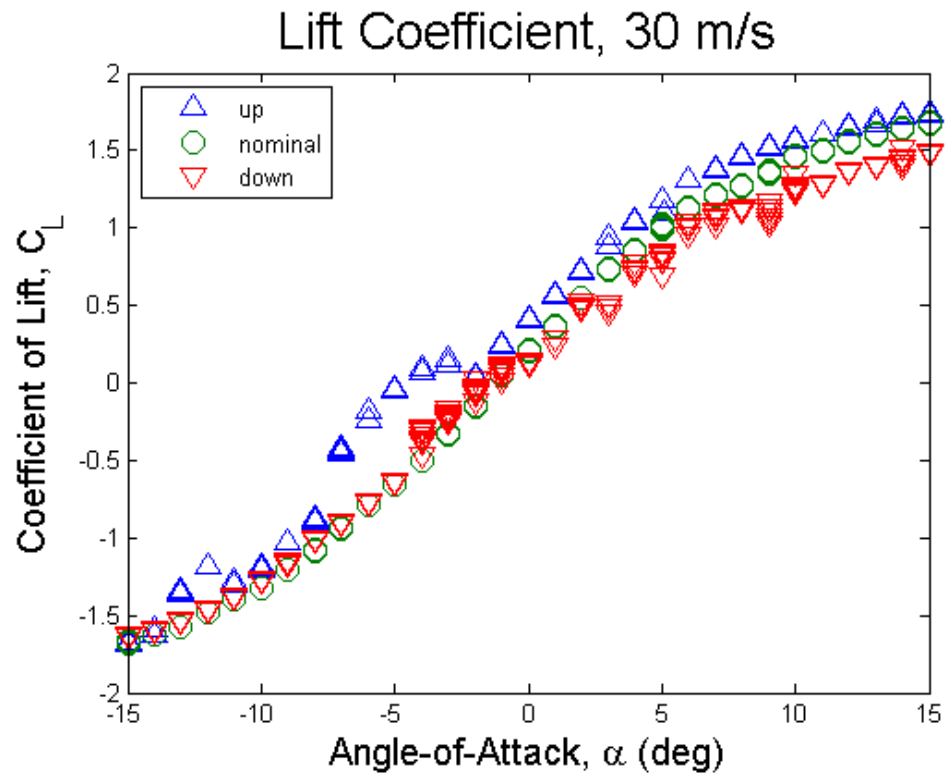
Figure B-6. Lift curves, 30 m/s.
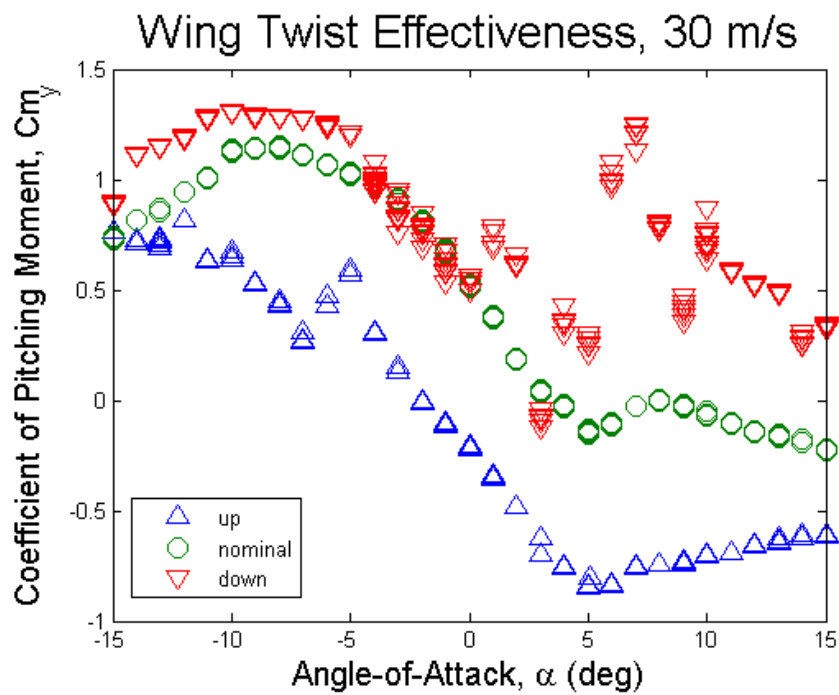
Figure B-7. Wing Twist Effectiveness Curves, 30 m/s.

154
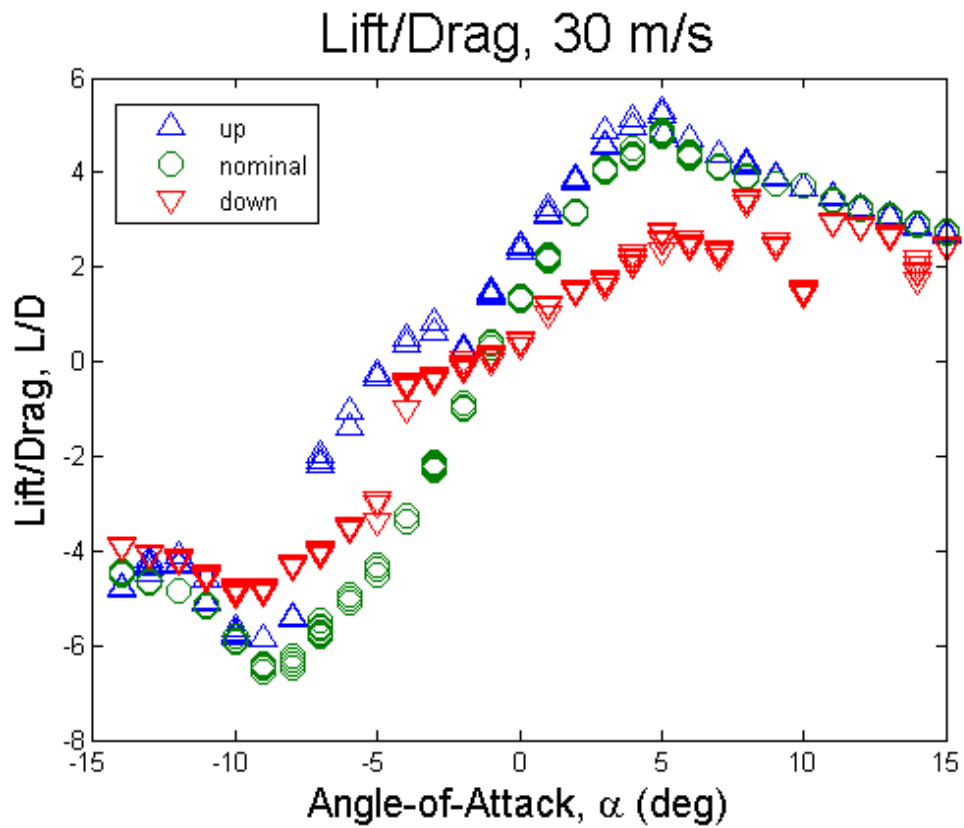
Figure B-8. Lift-to-Drag Curves, 30 m/s.
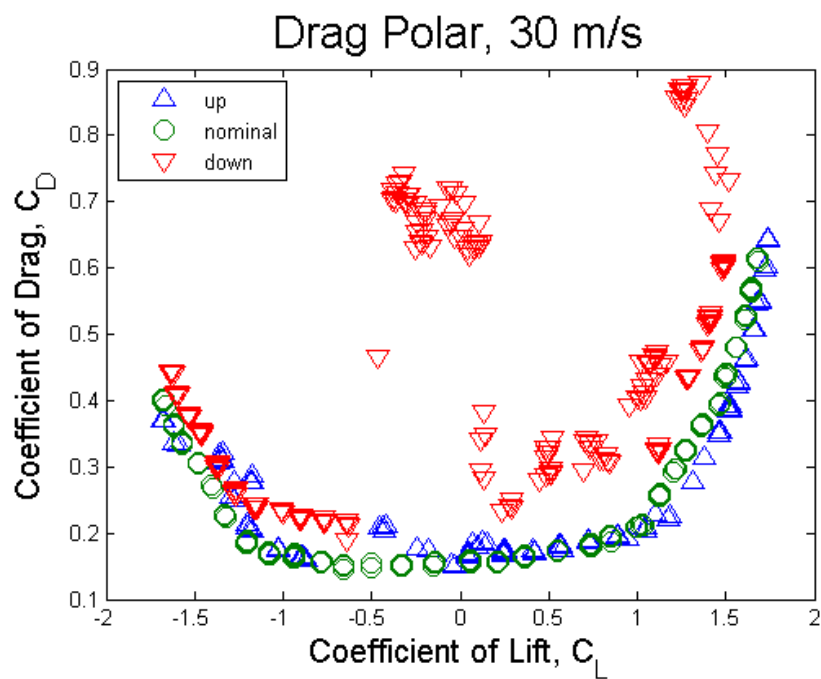
Figure B-9. Drag Polar, 30 m/s.

155
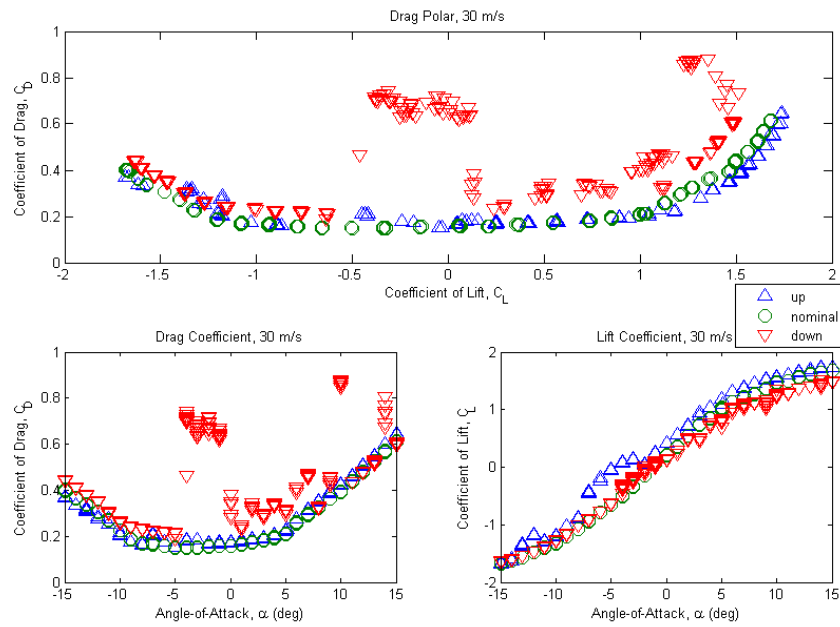
Figure B-10. Lift and Drag Curves, 30 m/s.
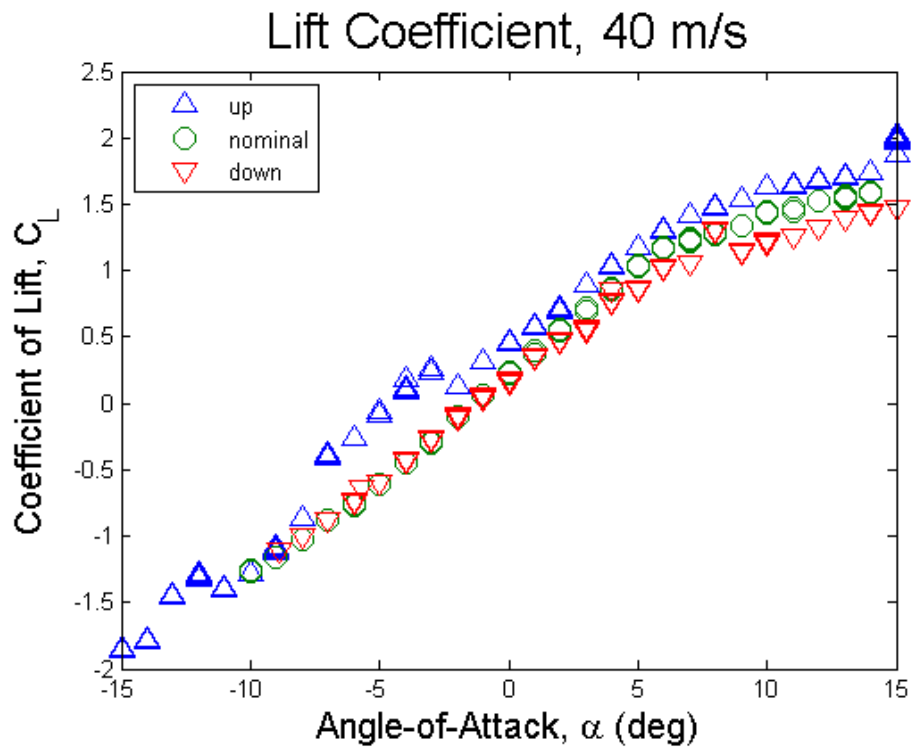
Figure B-11. . Lift curves, 40 m/s.
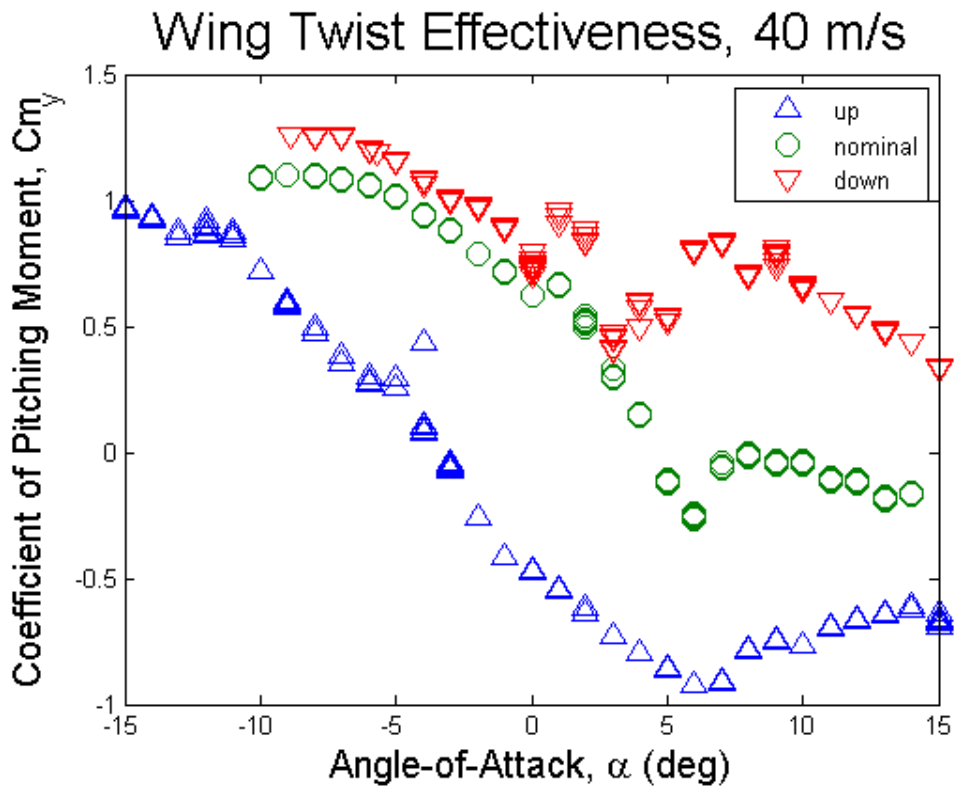
Figure B-12. Wing Twist Effectiveness Curves, 40 m/s.
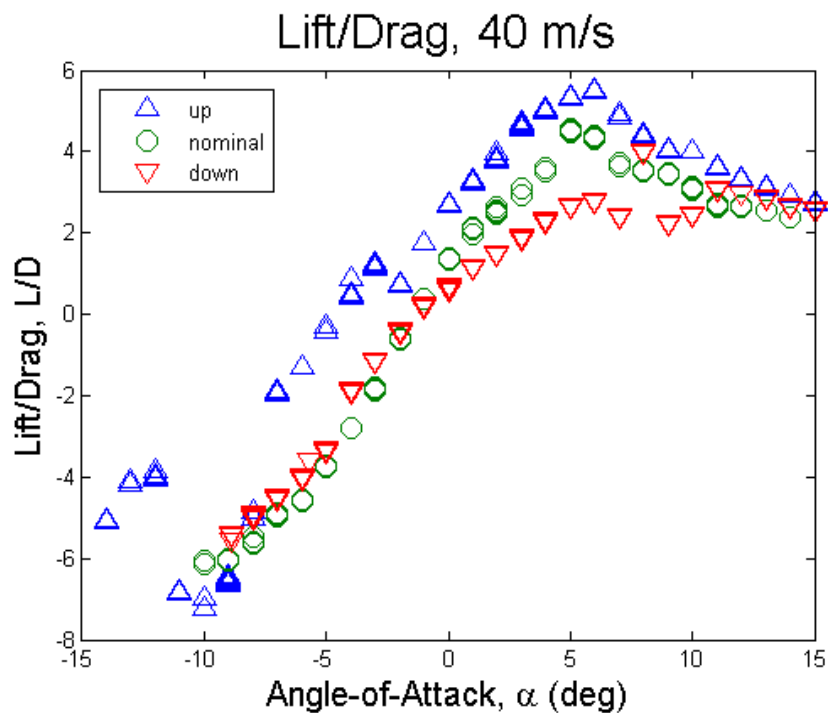
Figure B-13. Lift-to-Drag Curves, 40 m/s.

Figure B-14. Drag Polar, 40 m/s.

Figure B-15. Lift curves, 50 m/s.

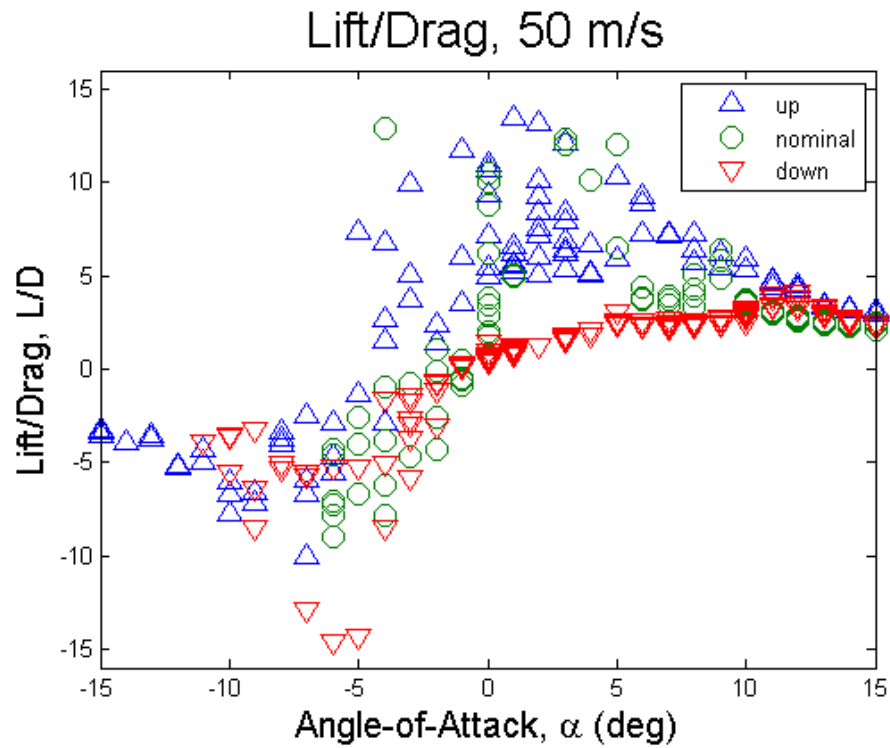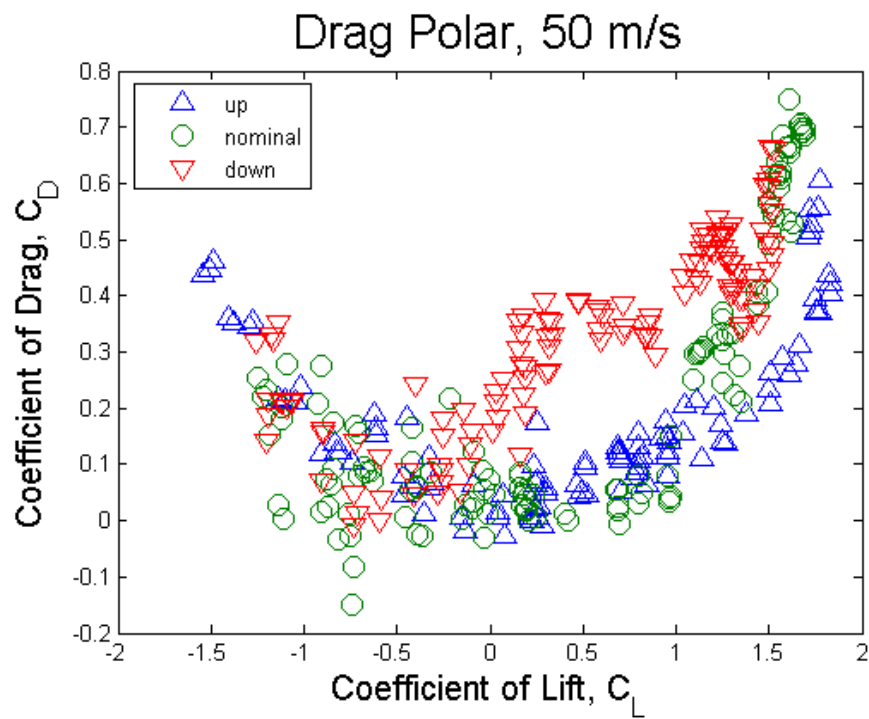158

Figure B-16. Wing Twist Effectiveness Curves, 50 m/s.

Figure B-17. Lift-to-Drag Curves, 50 m/s.

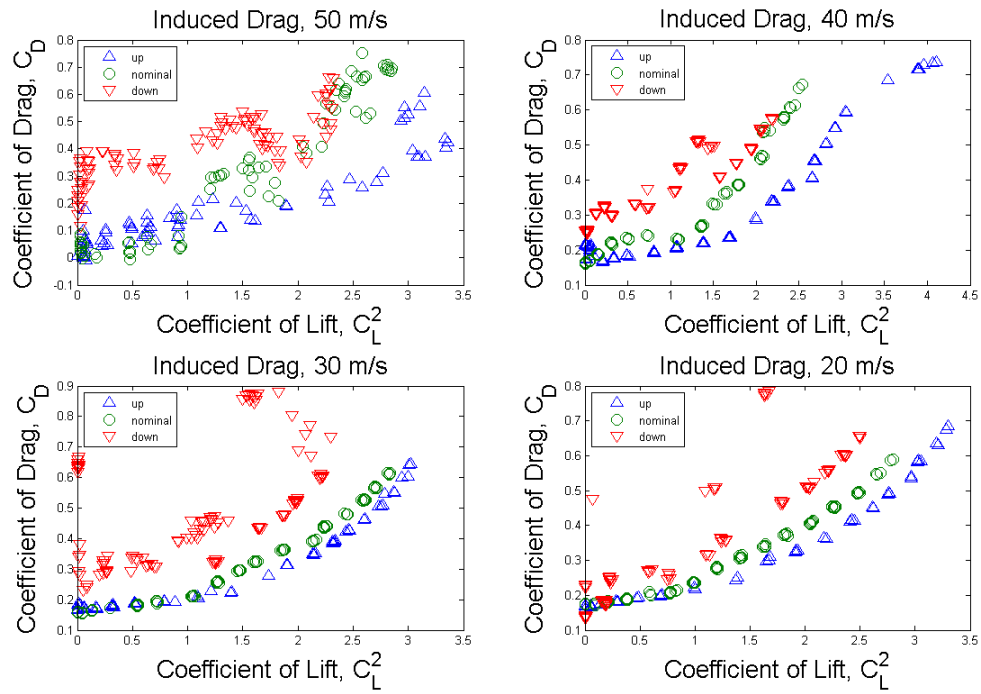**Figure B-18. Drag Polar, 50 m/s.**

Figure B-19. Induced Drag, 20 – 50 m/s.
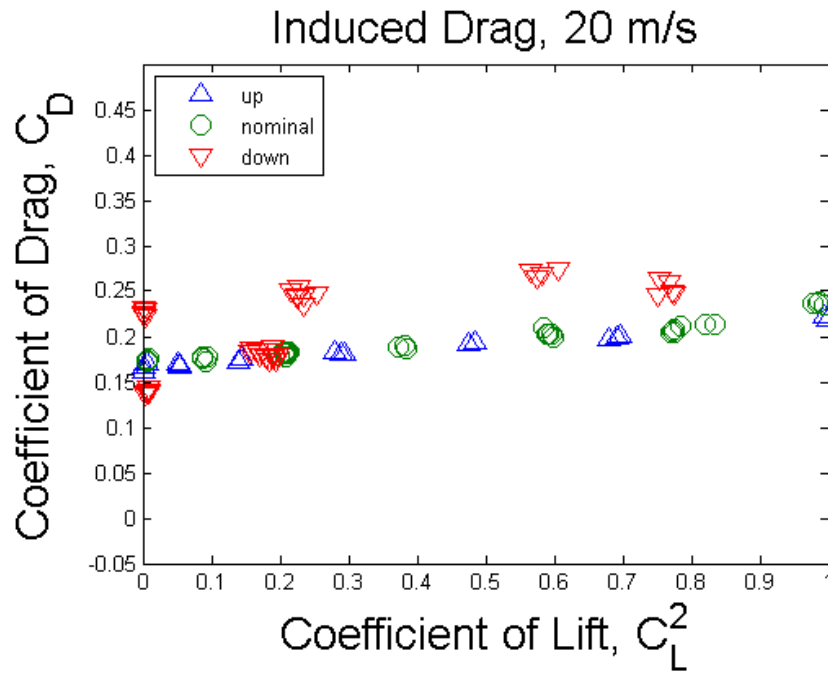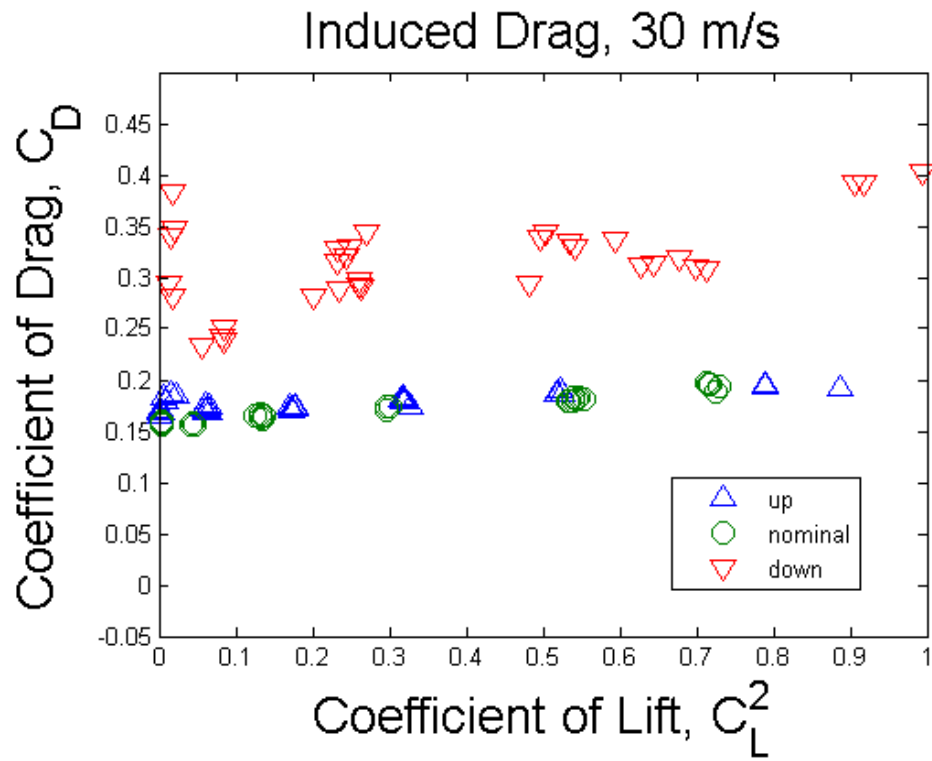

Figure B-20. Induced Drag, 20 m/s.

Figure B-21. Induced Drag, 30 m/s.
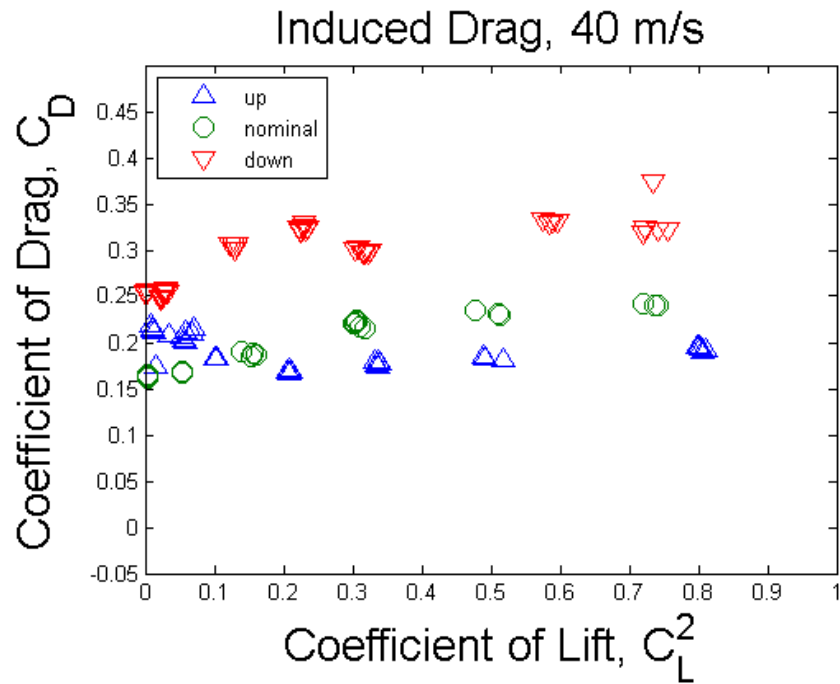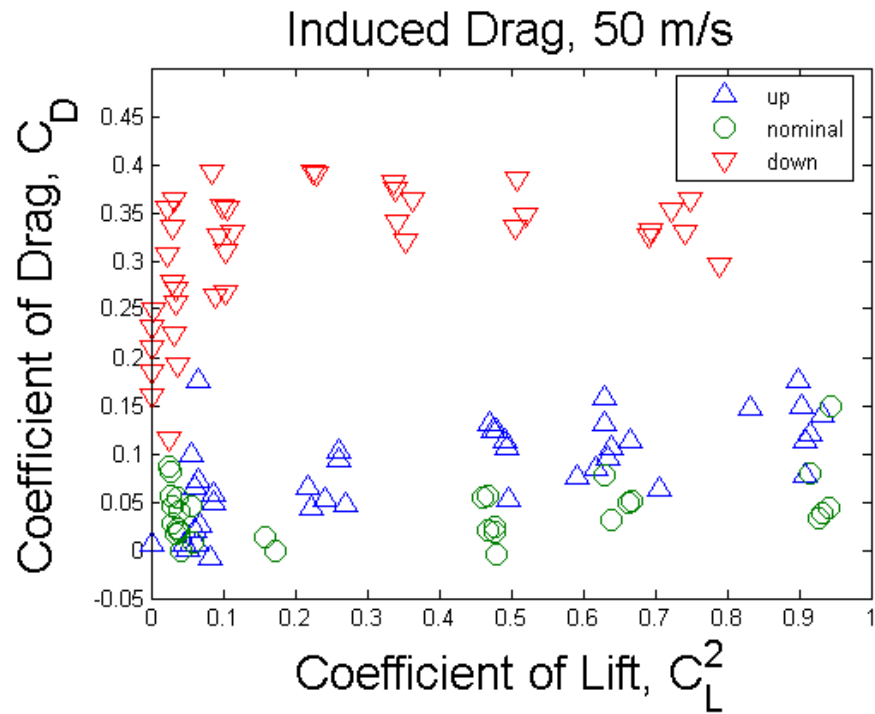

Figure B-22. Induced Drag, 40 m/s.

162

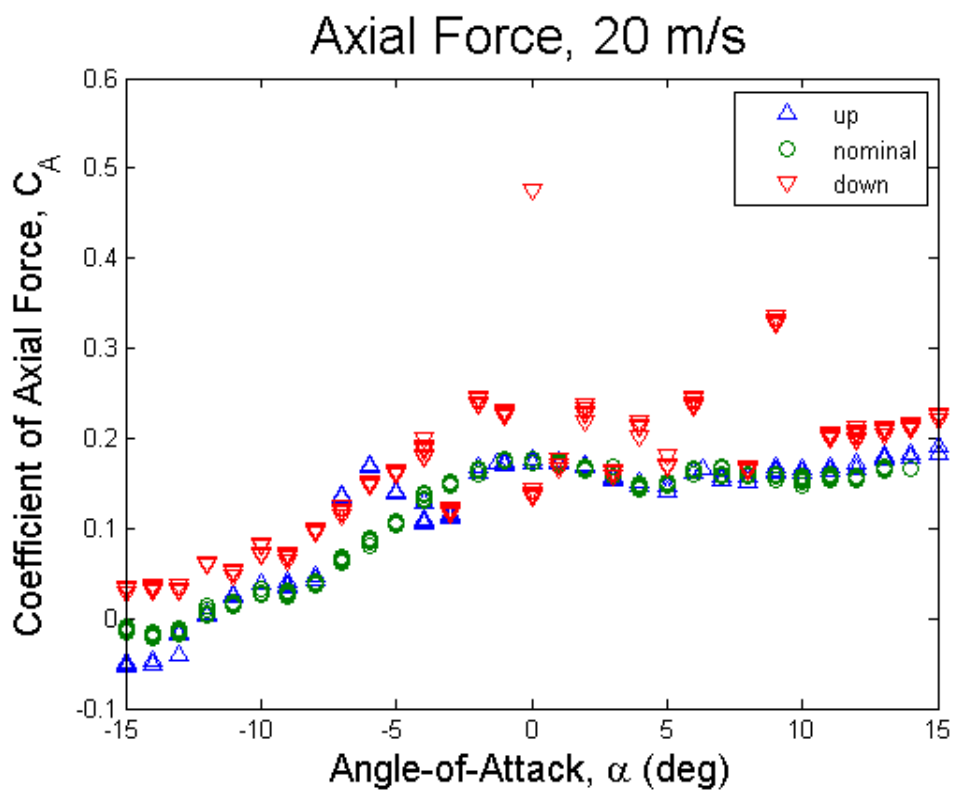**Figure B-23. Induced Drag, 50 m/s.**

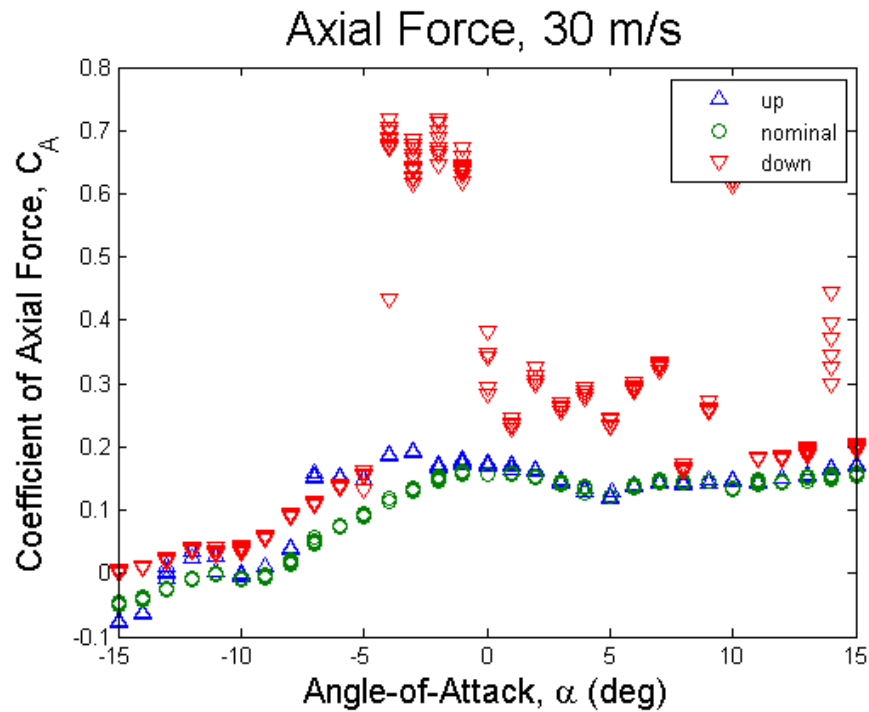**Figure B-24. Axial Force, 20 m/s.**

163

Figure B-25. Axial Force, 30 m/s.
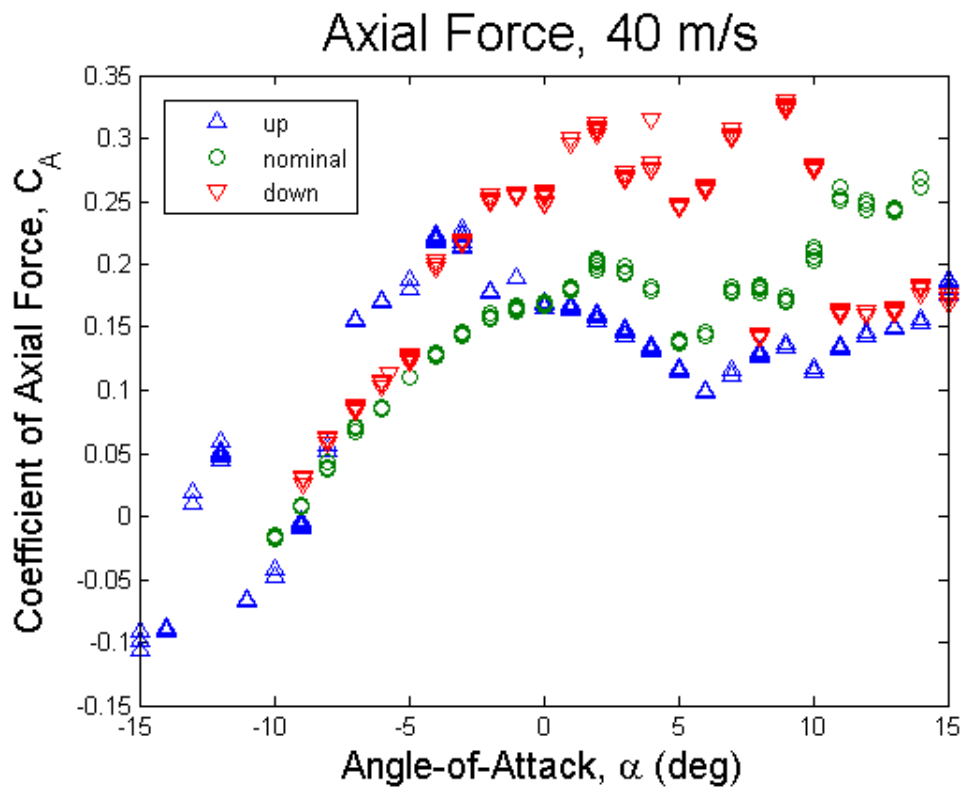
Figure B-26. Axial Force, 40 m/s.
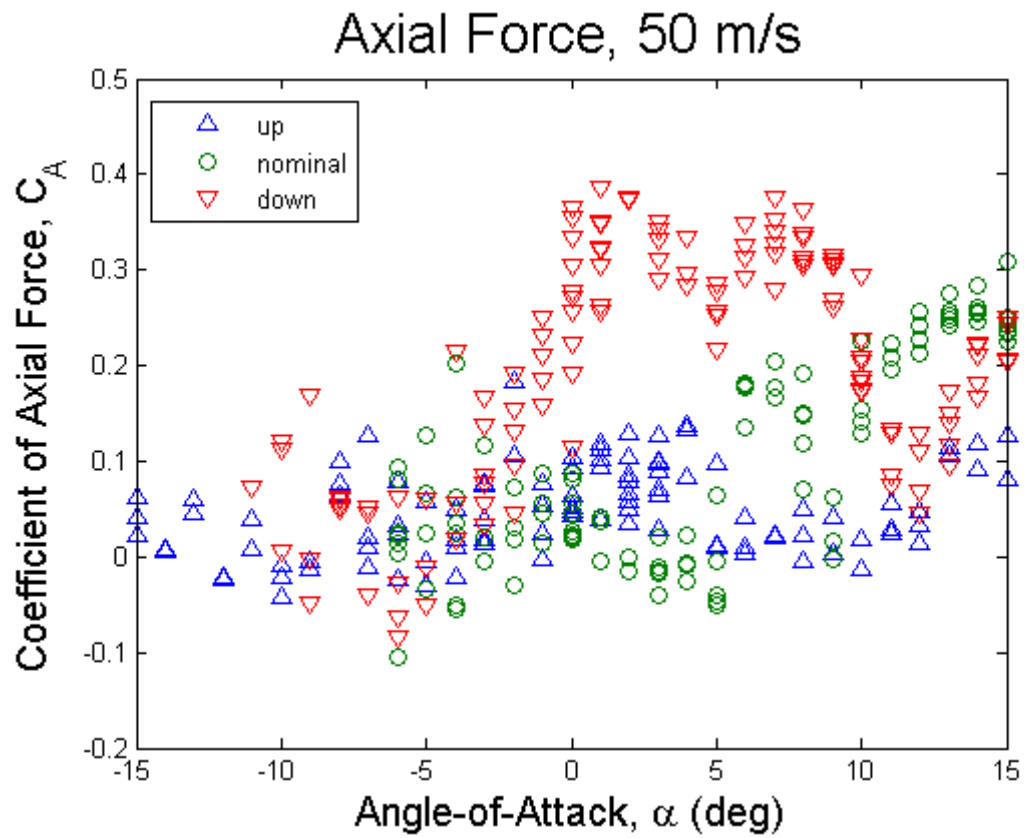
Figure B-27. Axial Force, 50 m/s.

C. Appendix: Complete Experimental Test Pressure Results

The following plots provide the full complement of pressure data analyzed from the wind tunnel tests described in Chapter 5. They include the pressure data for 20 to 50 m/s.

Note: The pressure data measurements at 20 m/s are not reliable since they were less than the resolution of the measuring apparatus.

Figure C-1. Nominal Delta Coefficient of Pressure, 20 m/s.

Figure C-2. Twist Up Delta Coefficient of Pressure, 20 m/s.
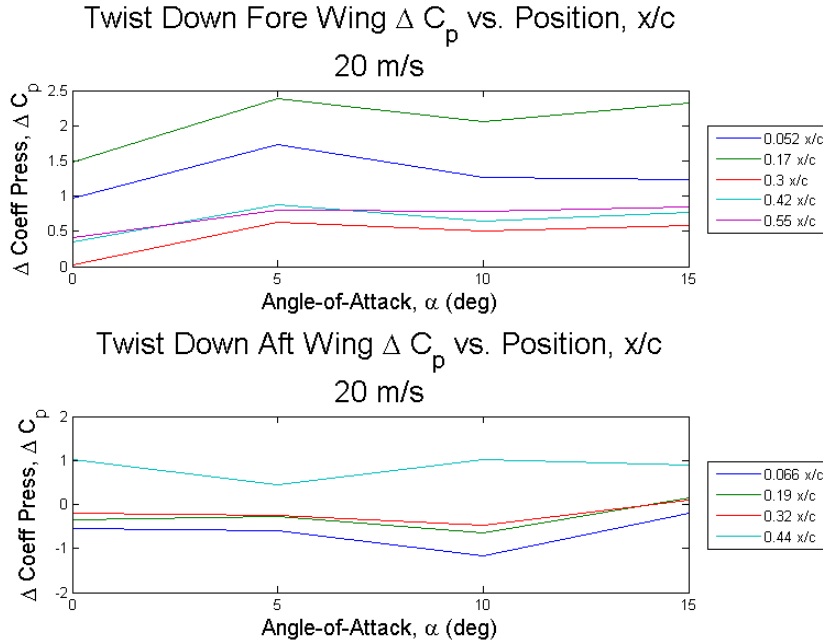
Figure C-3. Twist Down Delta Coefficient of Pressure, 20 m/s.
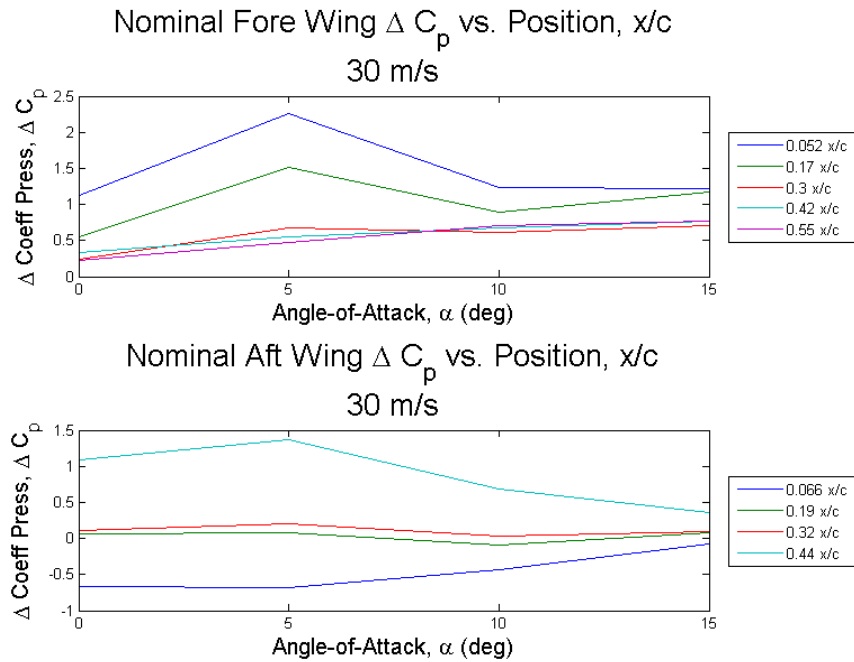
Figure C-4. Nominal Delta Coefficient of Pressure, 30 m/s.
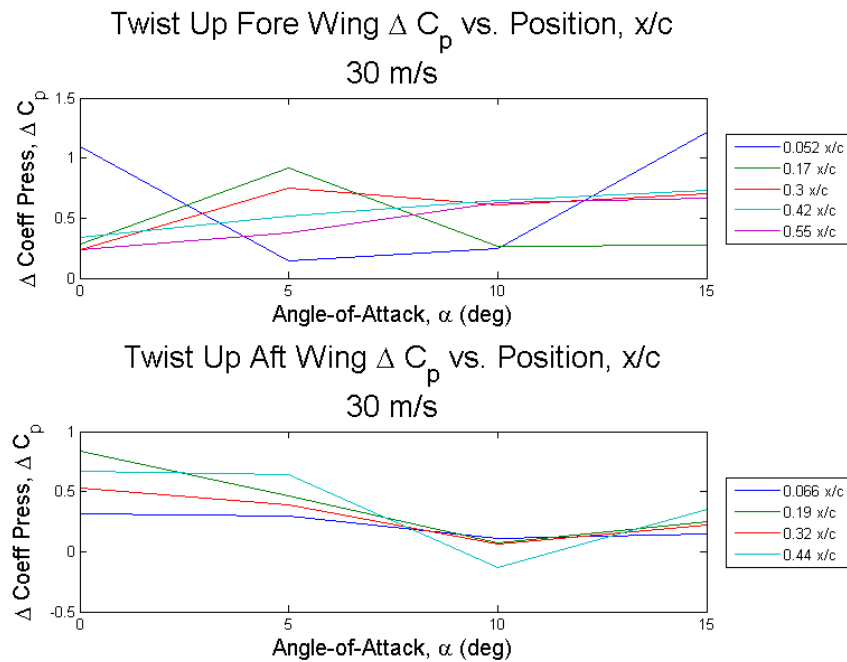
Figure C-5. Twist Up Delta Coefficient of Pressure, 30 m/s.
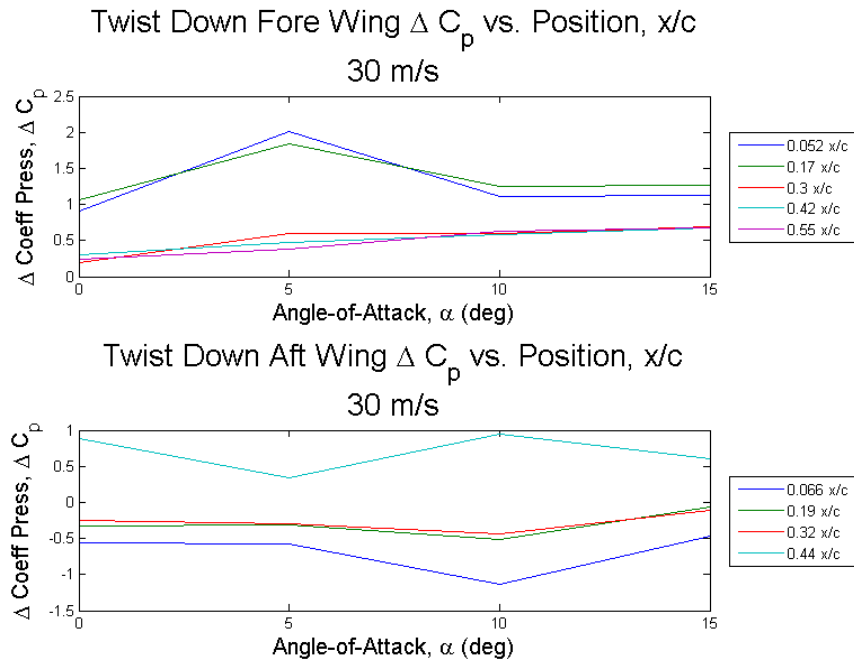
Figure C-6. Twist Down Delta Coefficient of Pressure, 30 m/s.
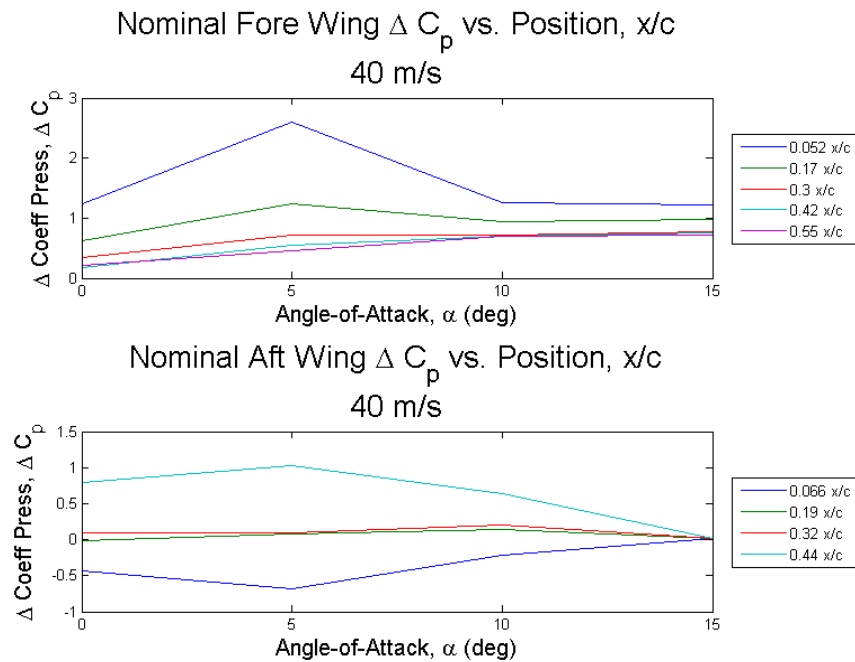
Figure C-7. Nominal Delta Coefficient of Pressure, 40 m/s.
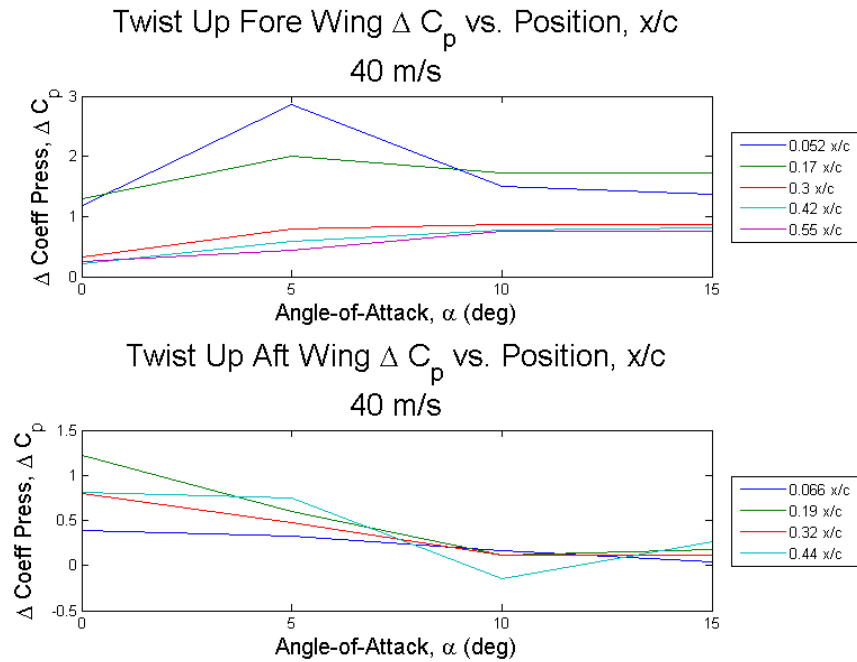
Figure C-8. Twist Up Delta Coefficient of Pressure, 40 m/s.

Note: The plots were there is data absent (40 and 50 m/s twist down, the pressure port was blocked.
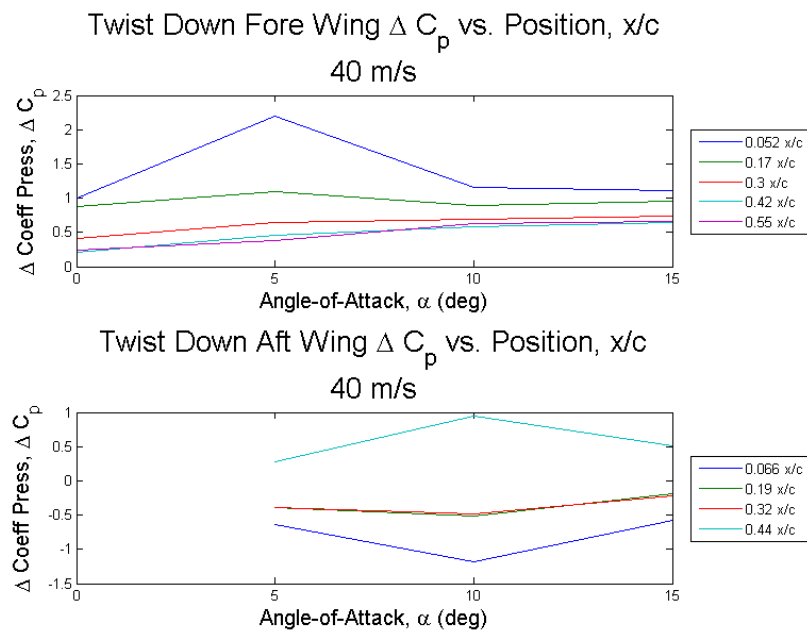
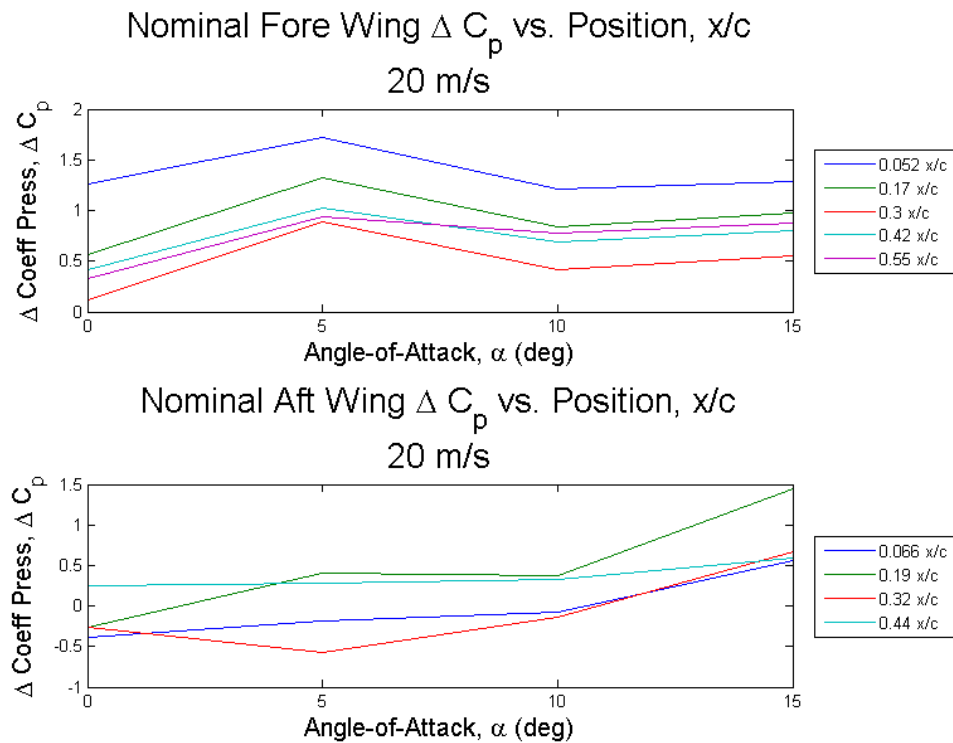**Figure C-9. Twist Down Delta Coefficient of Pressure, 40 m/s.**
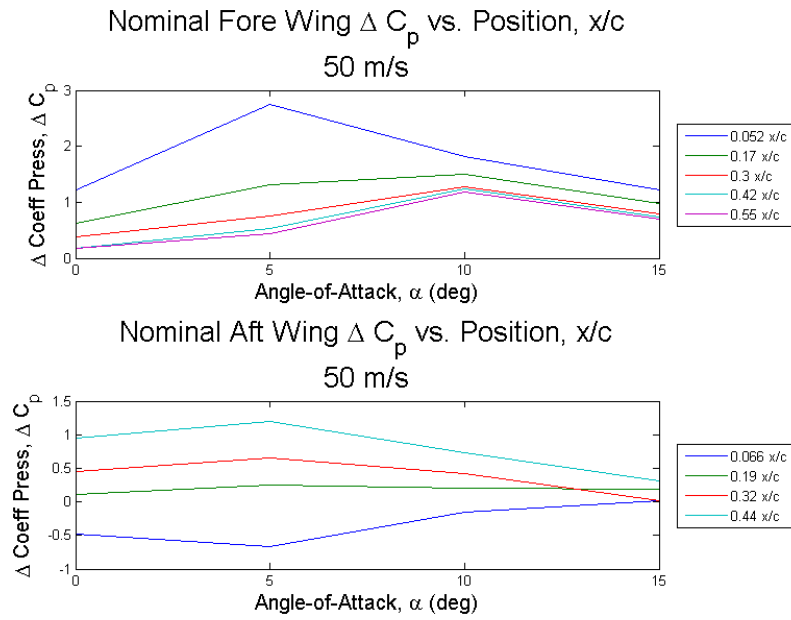
Figure C-10. Nominal Delta Coefficient of Pressure, 50 m/s.
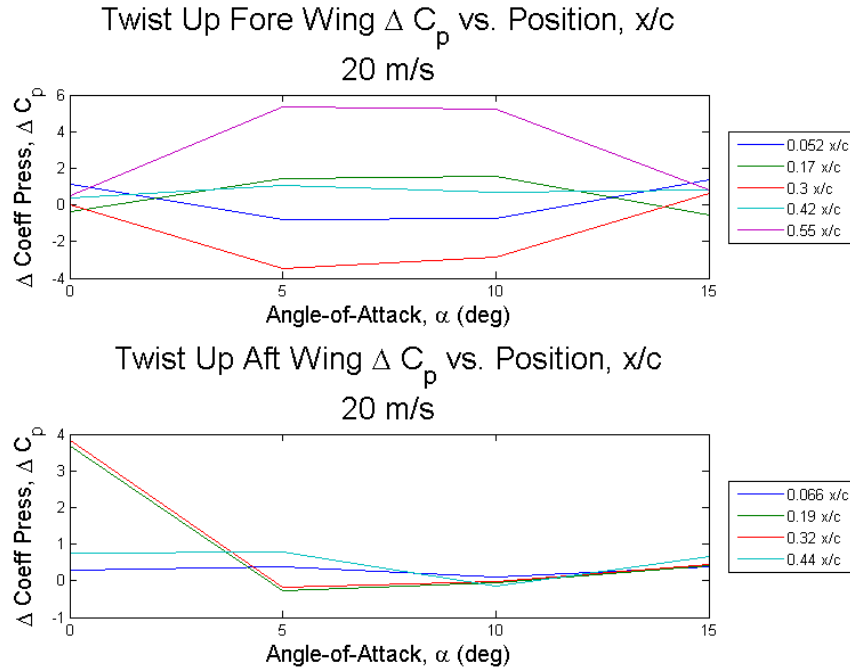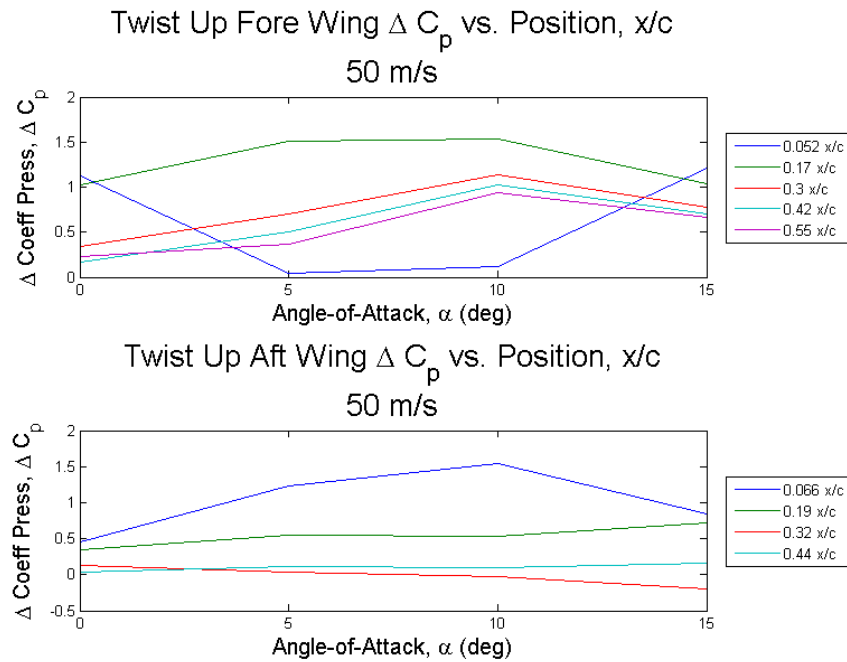

Figure C-11. Twist Up Delta Coefficient of Pressure, 50 m/s.

Figure C-12. Twist Down Delta Coefficient of Pressure, 50 m/s.

Figure C-13. Nominal Delta Coefficient of Pressure, 20 m/s, 0° AoA.

172

Figure C-14. Nominal Delta Coefficient of Pressure, 20 m/s, 5° AoA.

Figure C-15. Nominal Delta Coefficient of Pressure, 20 m/s, 10° AoA.

173

Figure C-16. Nominal Delta Coefficient of Pressure, 20 m/s, 15° AoA.

Figure C-17. Twist Up Delta Coefficient of Pressure, 20 m/s, 0° AoA.

Figure C-18. Twist Up Delta Coefficient of Pressure, 20 m/s, 5° AoA.

Figure C-19. Twist Up Delta Coefficient of Pressure, 20 m/s, 10° AoA.
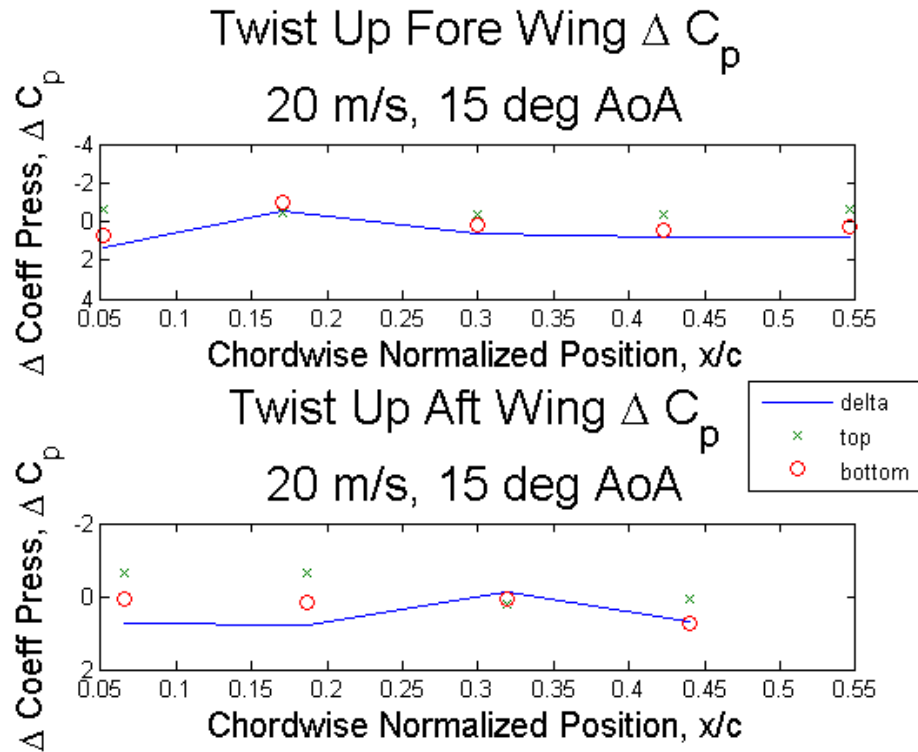
Figure C-20. Twist Up Delta Coefficient of Pressure, 20 m/s, 15° AoA.

Figure C-21. Nominal Delta Coefficient of Pressure, 30 m/s, 0° AoA.
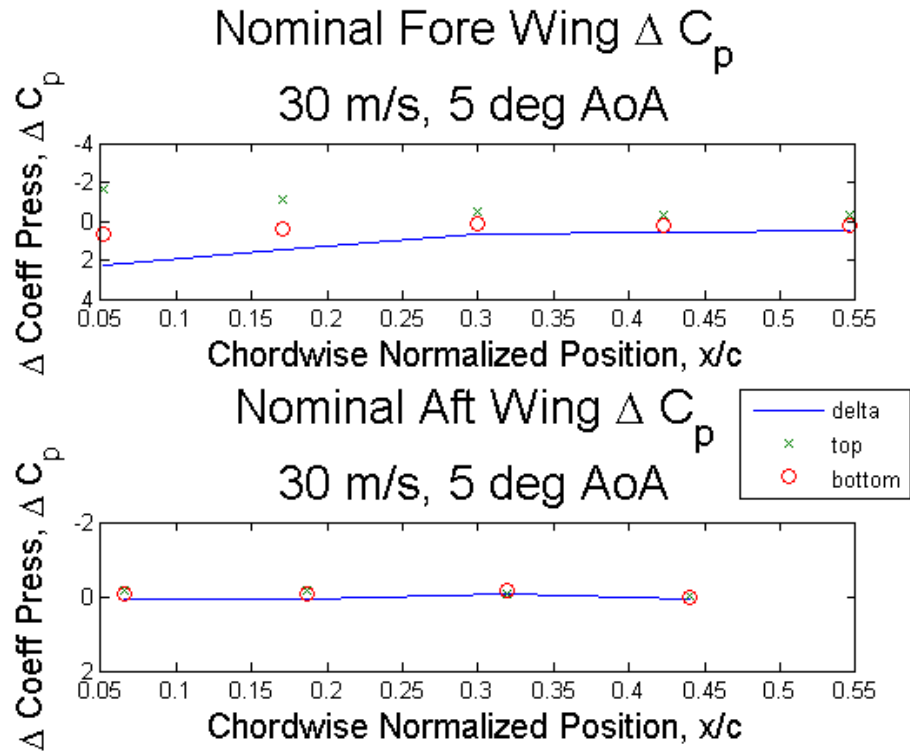
Figure C-22. Nominal Delta Coefficient of Pressure, 30 m/s, 5° AoA.
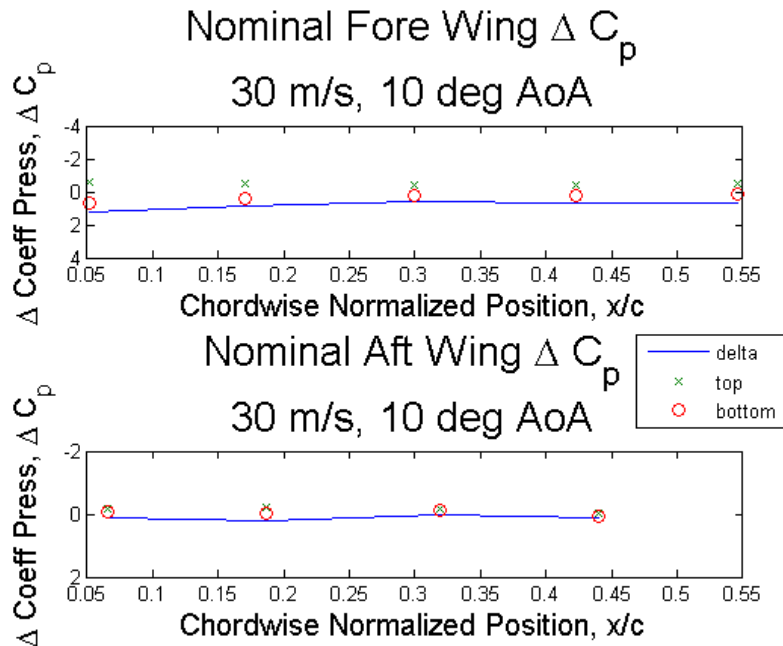
Figure C-23. Nominal Delta Coefficient of Pressure, 30 m/s, 10° AoA.
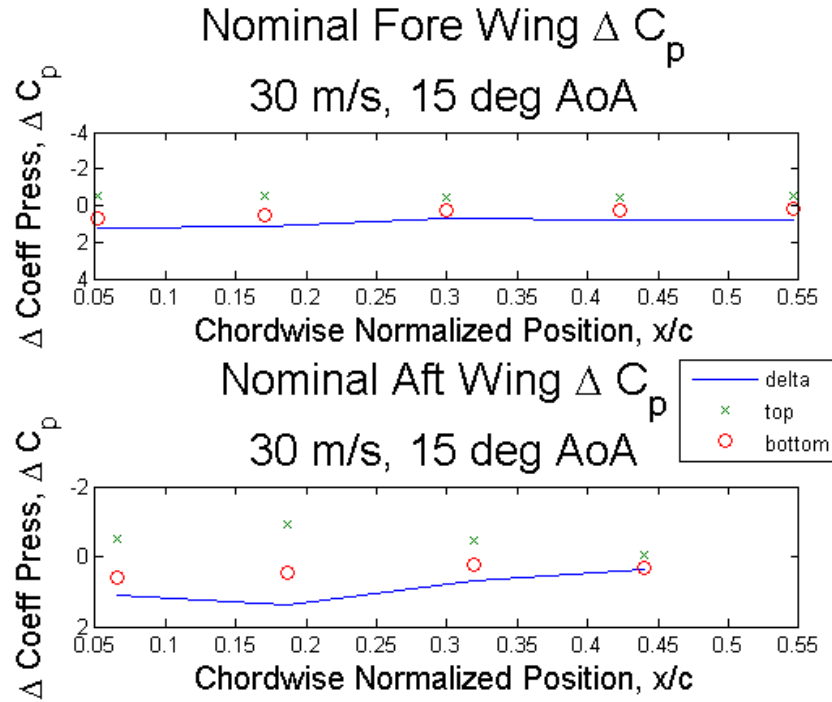
Figure C-24. Nominal Delta Coefficient of Pressure, 30 m/s, 15° AoA.
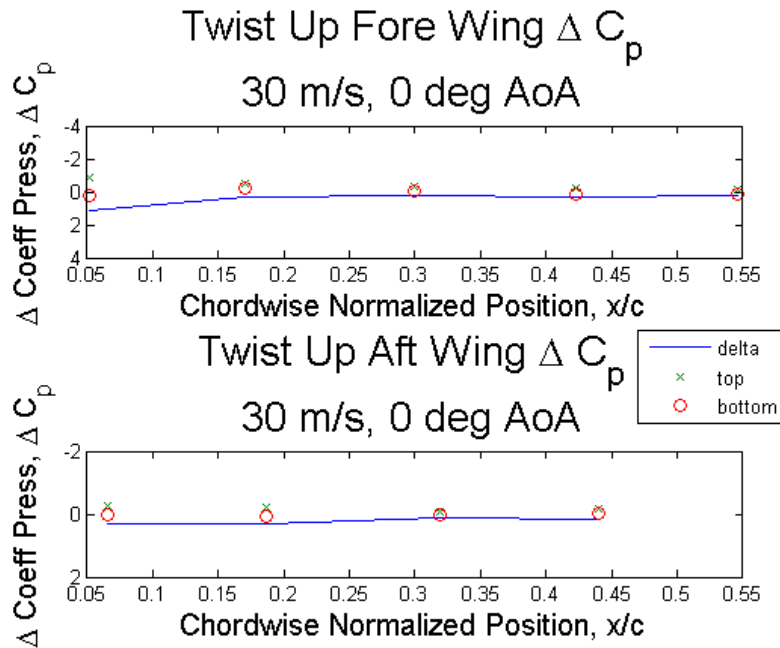
Figure C-25. Twist Up Delta Coefficient of Pressure, 30 m/s, 0° AoA.
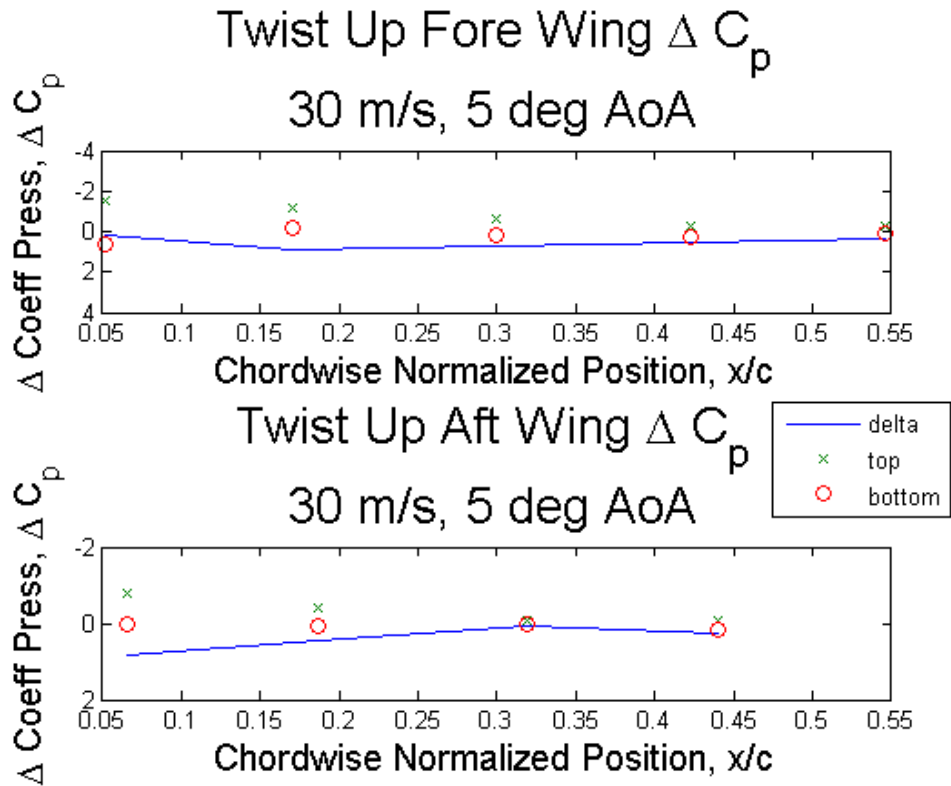
Figure C-26. Twist Up Delta Coefficient of Pressure, 30 m/s, 5° AoA.
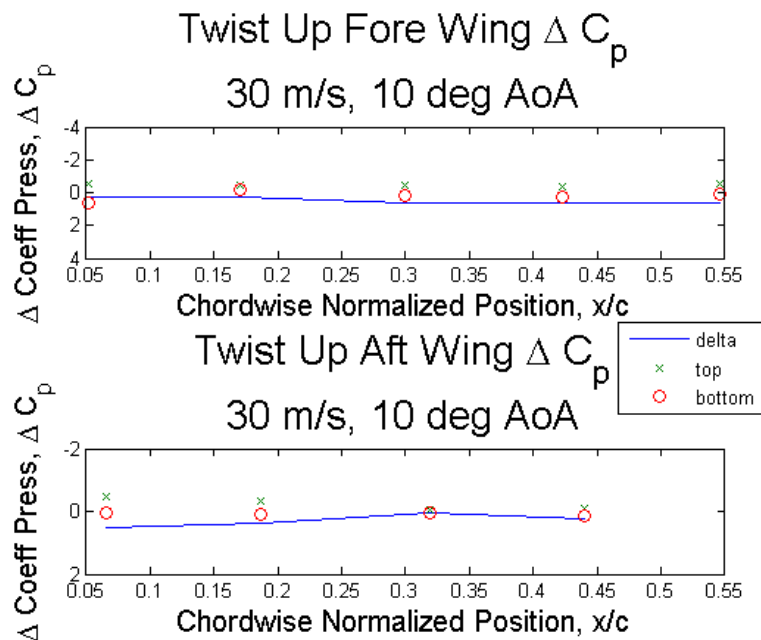
Figure C-27. Twist Up Delta Coefficient of Pressure, 30 m/s, 10° AoA.

179
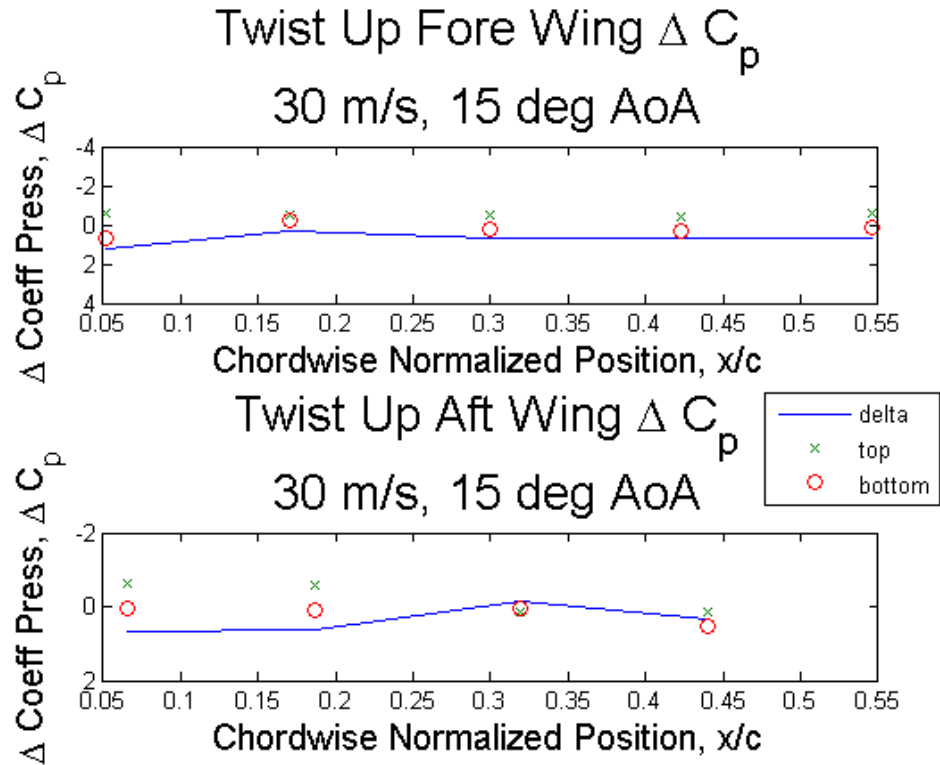
Figure C-28. Twist Up Delta Coefficient of Pressure, 30 m/s, 15° AoA.
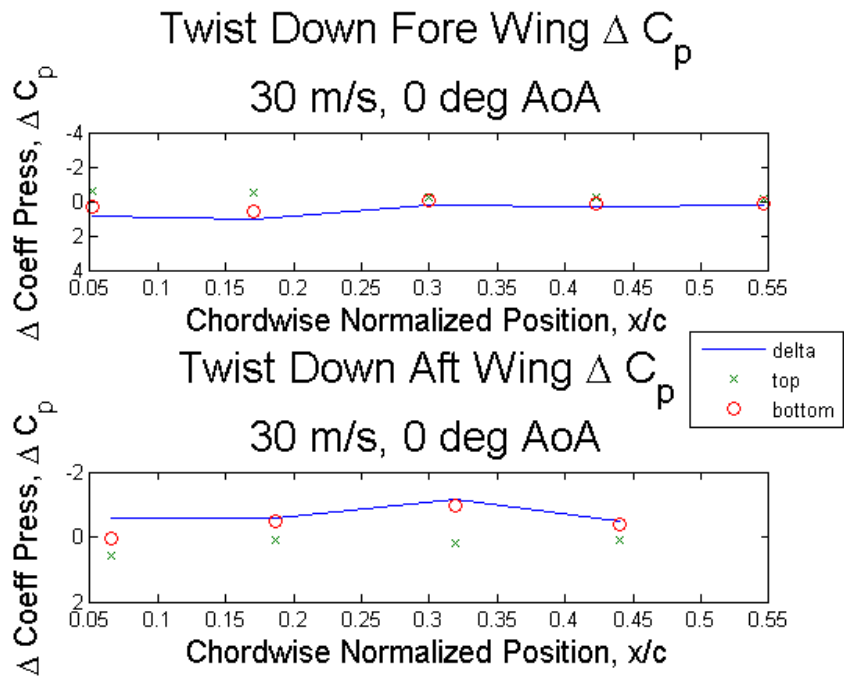
Figure C-29. Twist Down Delta Coefficient of Pressure, 30 m/s, 0° AoA.
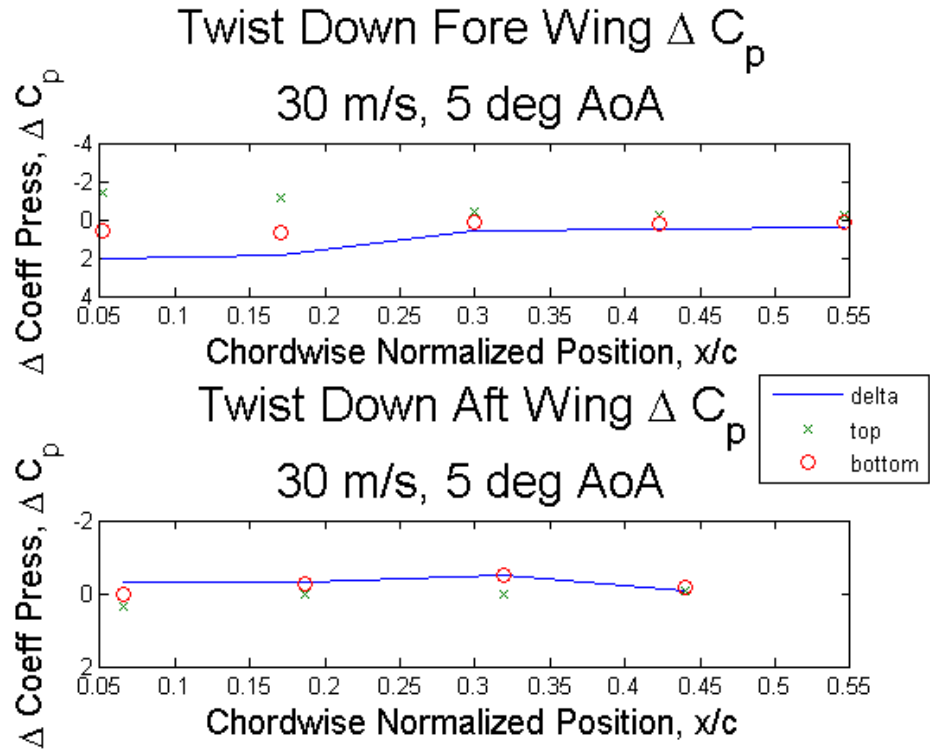
Figure C-30. Twist Down Delta Coefficient of Pressure, 30 m/s, 5° AoA.
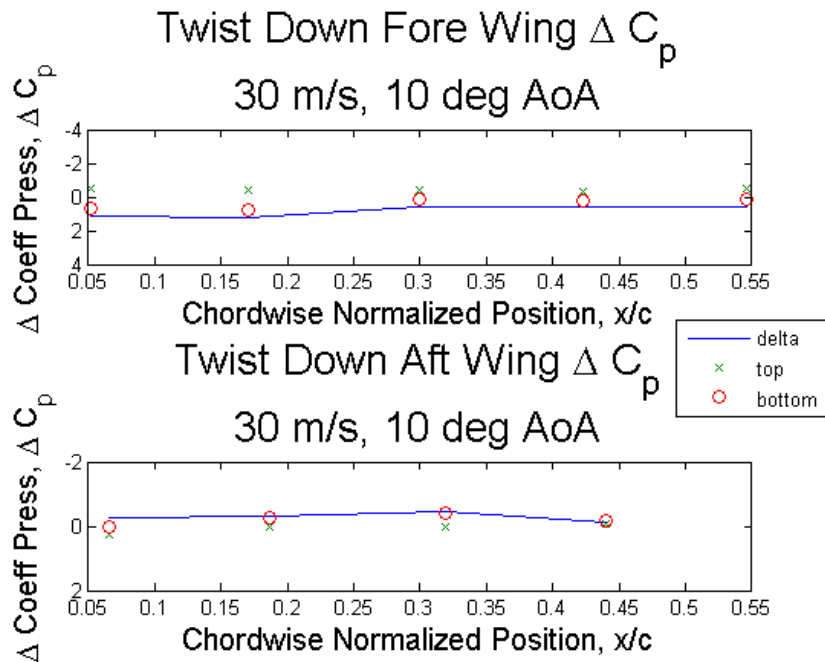
Figure C-31. Twist Down Delta Coefficient of Pressure, 30 m/s, 10° AoA.

181
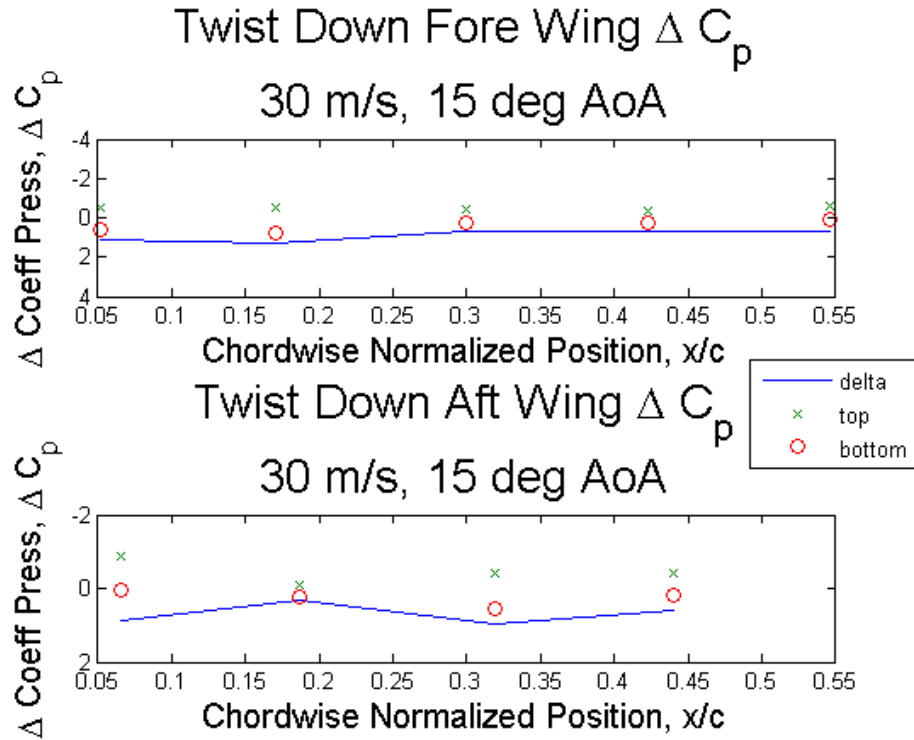
Figure C-32. Twist Down Delta Coefficient of Pressure, 30 m/s, 15° AoA.
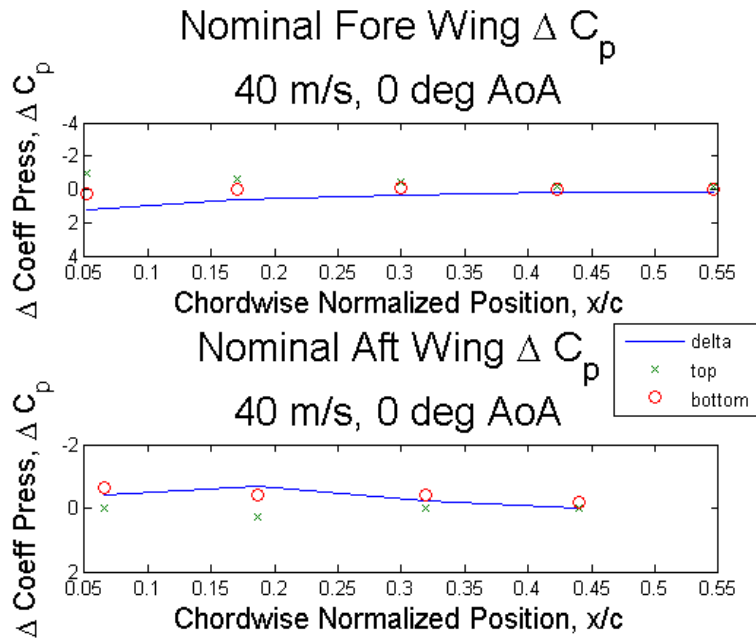
Figure C-33. Nominal Delta Coefficient of Pressure, 40 m/s, 0° AoA.

182
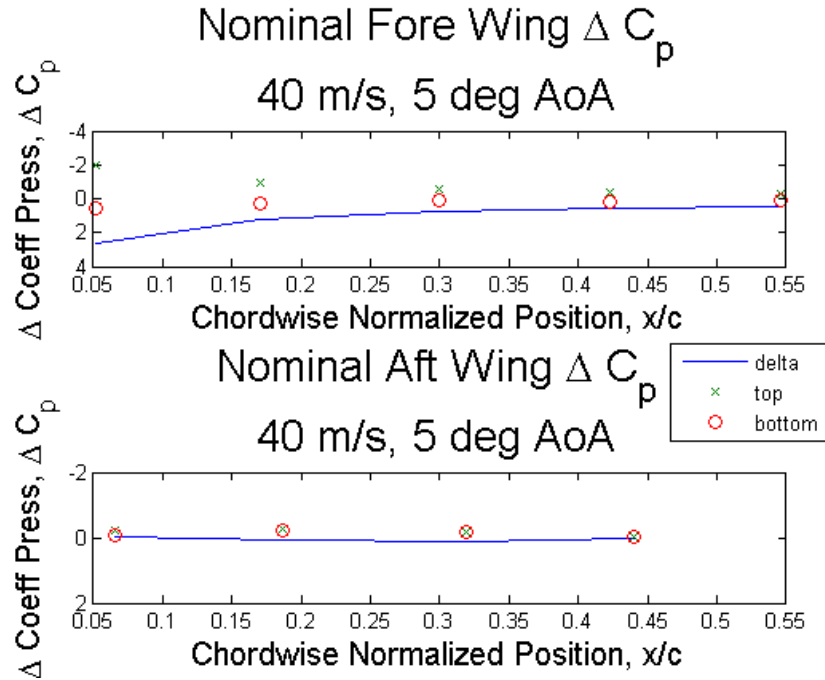
Figure C-34. Nominal Delta Coefficient of Pressure, 40 m/s, 5° AoA.
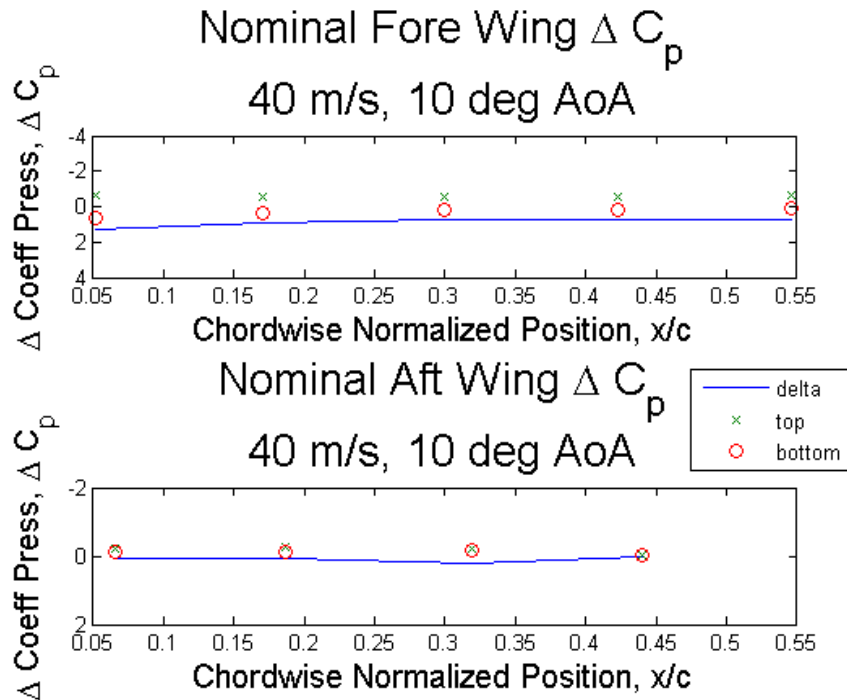
Figure C-35. Nominal Delta Coefficient of Pressure, 40 m/s, 10° AoA.

183
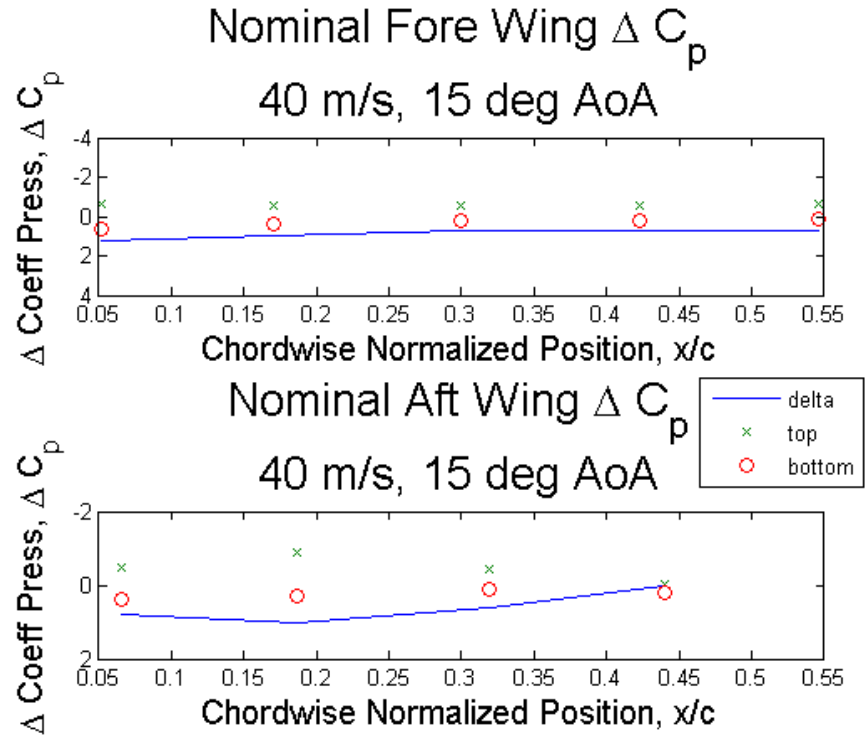
Figure C-36. Nominal Delta Coefficient of Pressure, 40 m/s, 15° AoA.
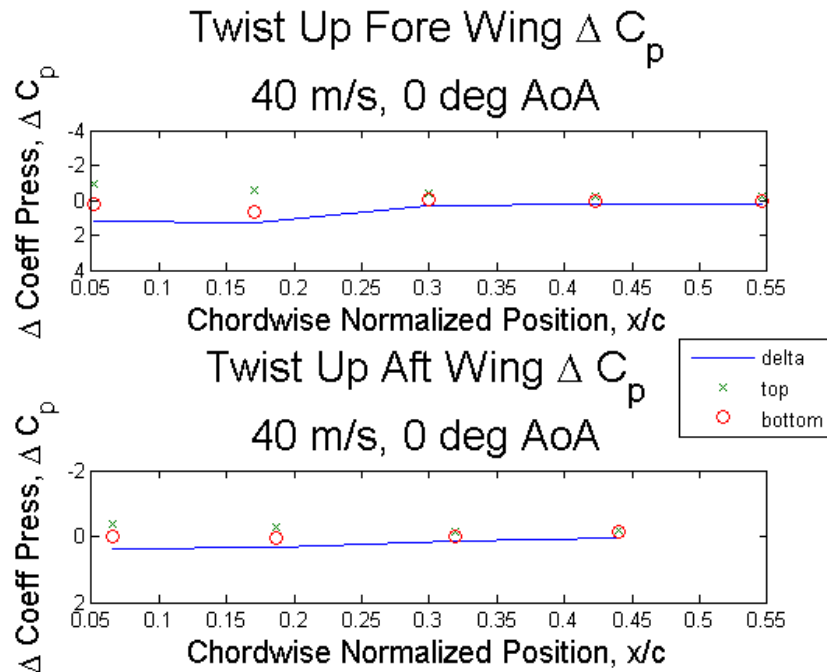
Figure C-37. Twist Up Delta Coefficient of Pressure, 40 m/s, 0° AoA.
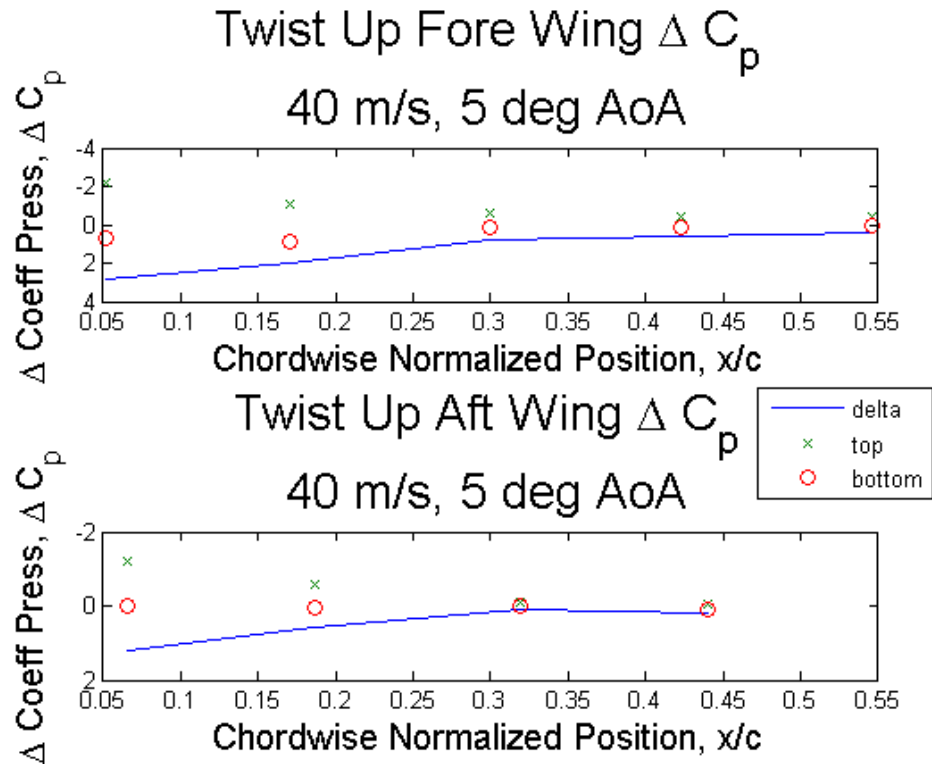
Figure C-38. Twist Up Delta Coefficient of Pressure, 40 m/s, 5° AoA.
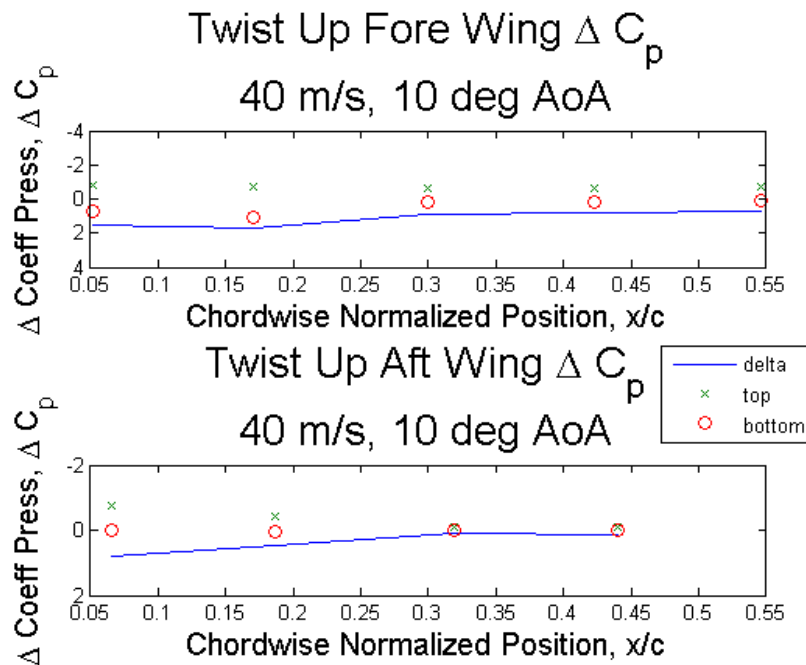
Figure C-39. Twist Up Delta Coefficient of Pressure, 40 m/s, 10° AoA.
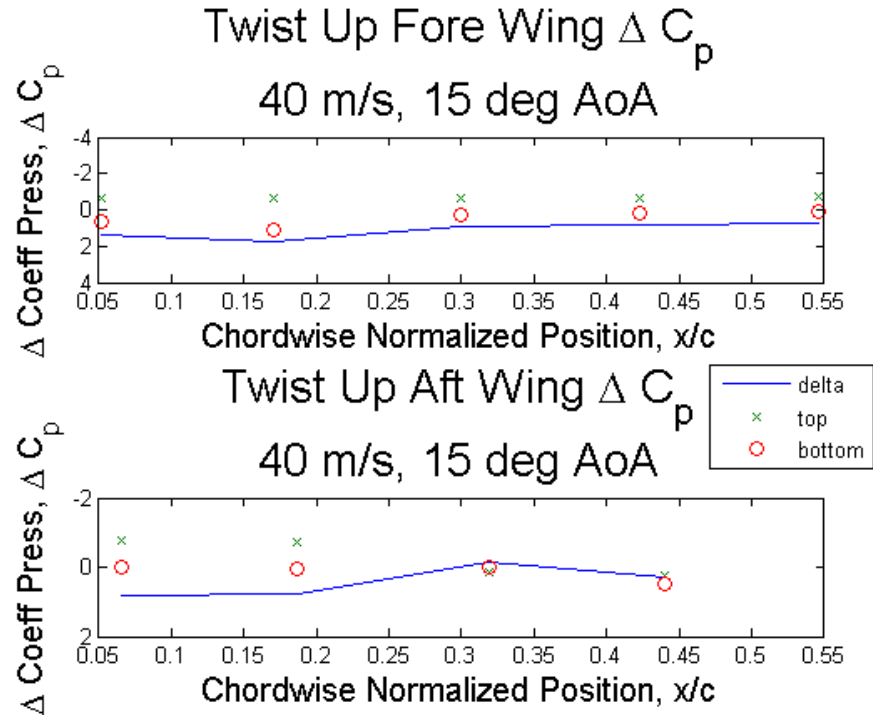
Figure C-40. Twist Up Delta Coefficient of Pressure, 40 m/s, 15° AoA.
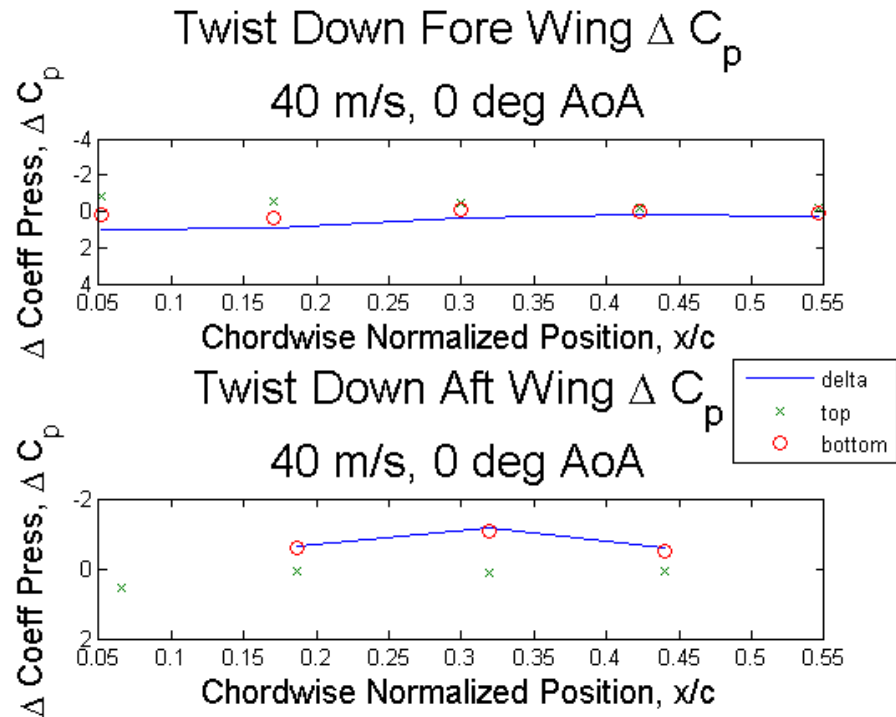
Figure C-41. Twist Down Delta Coefficient of Pressure, 40 m/s, 0° AoA.
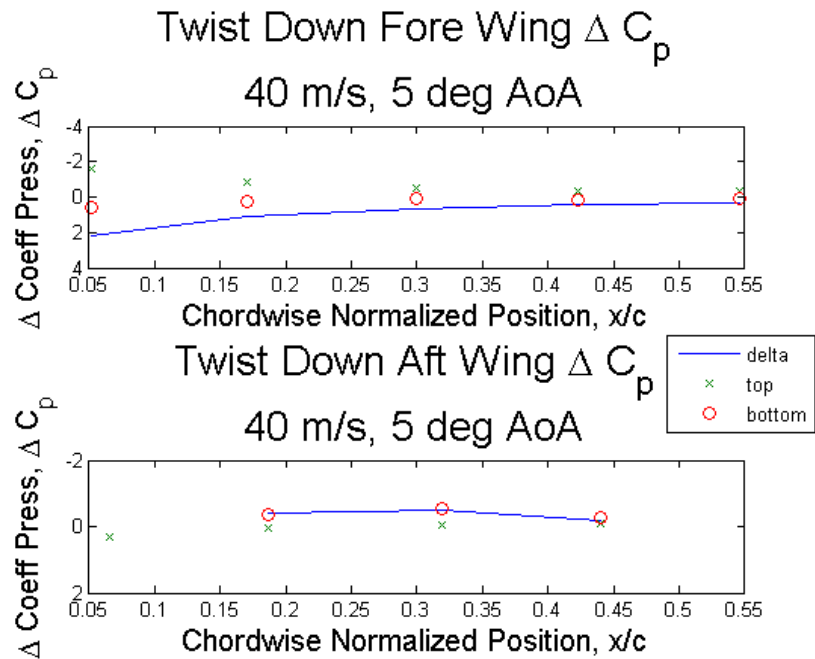
Figure C-42. Twist Down Delta Coefficient of Pressure, 40 m/s, 5° AoA.
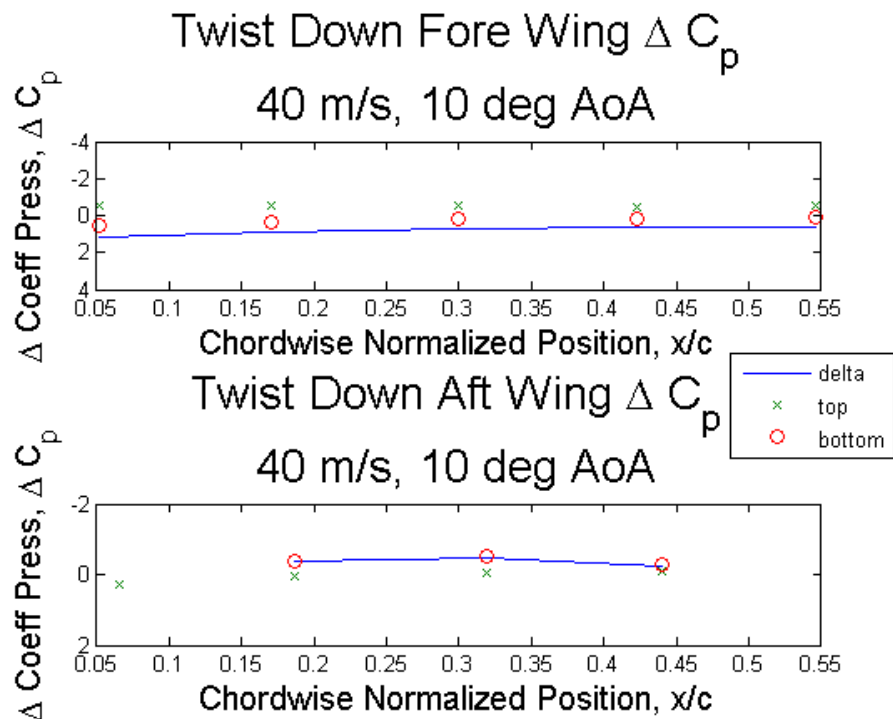
Figure C-43. Twist Down Delta Coefficient of Pressure, 40 m/s, 10° AoA.
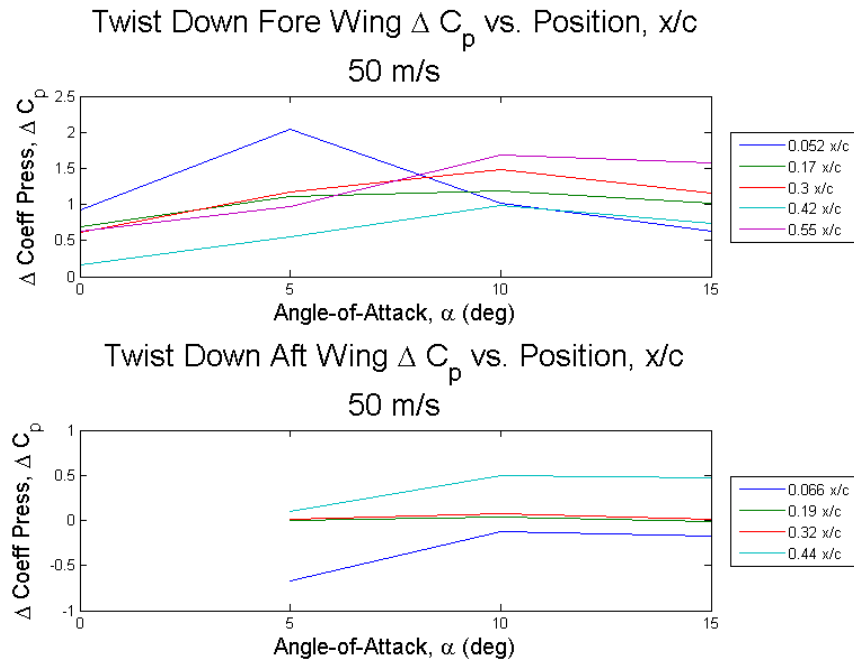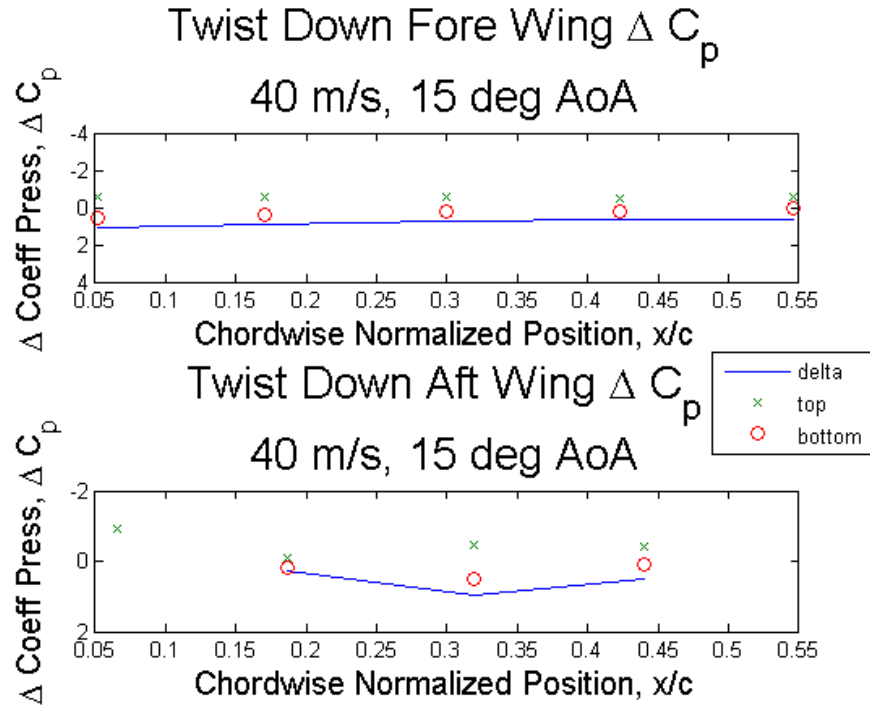
Figure C-44. Twist Down Delta Coefficient of Pressure, 40 m/s, 15° AoA.
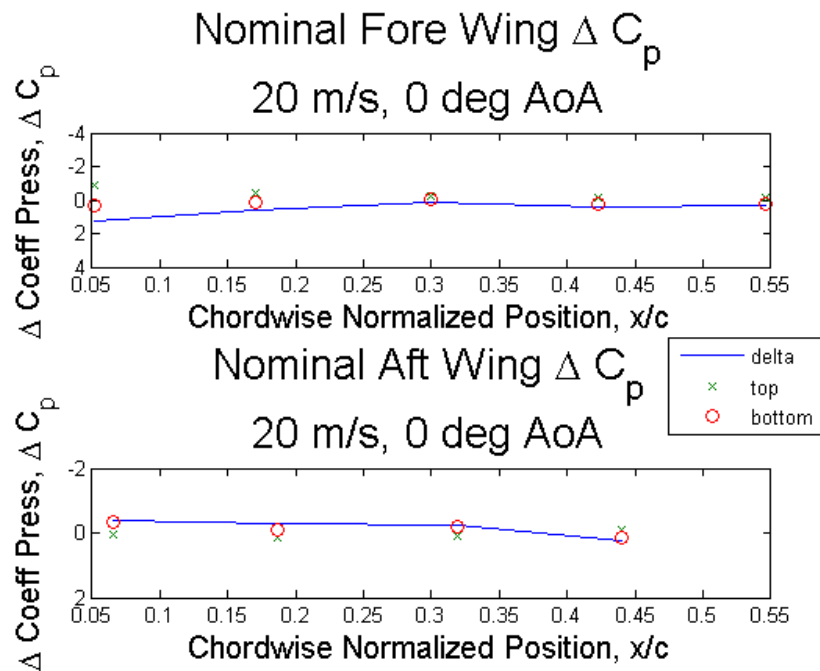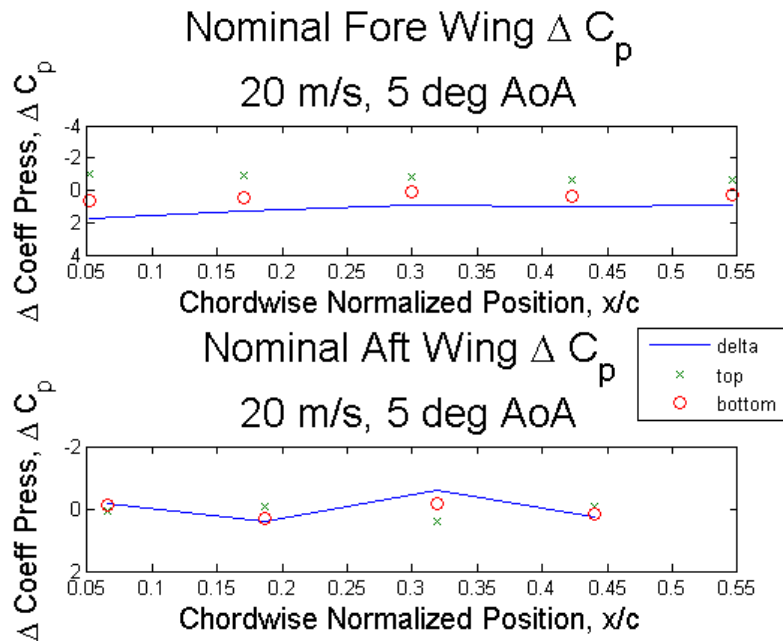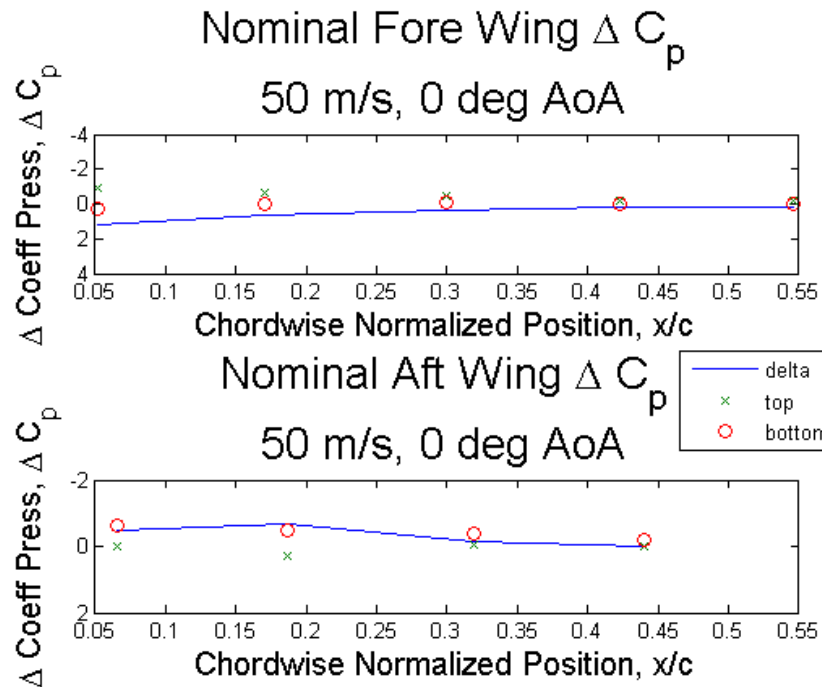

Figure C-45. Nominal Delta Coefficient of Pressure, 50 m/s, 0° AoA.
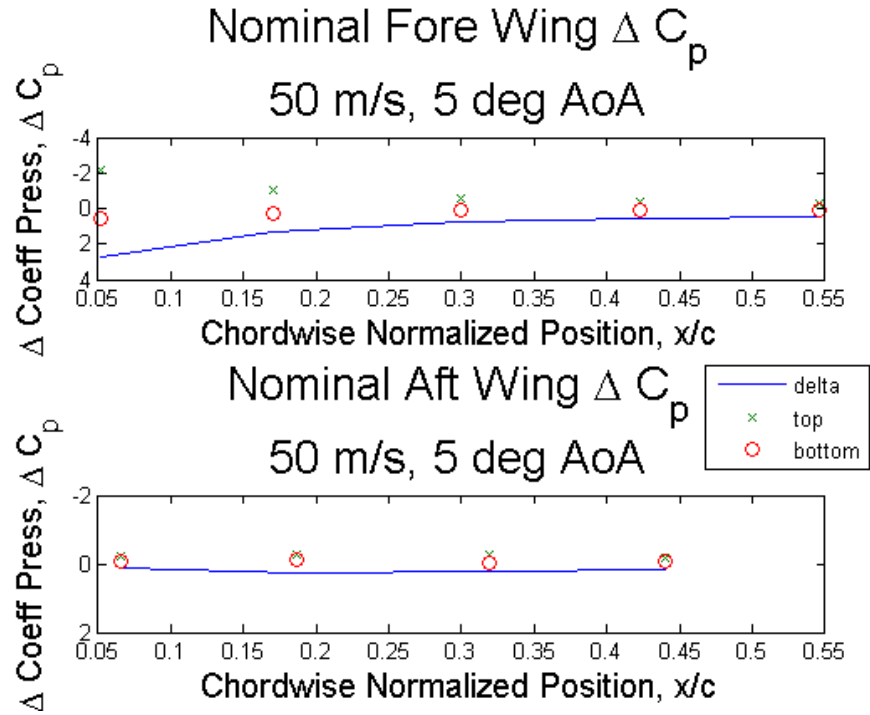
Figure C-46. Nominal Delta Coefficient of Pressure, 50 m/s, 5° AoA.
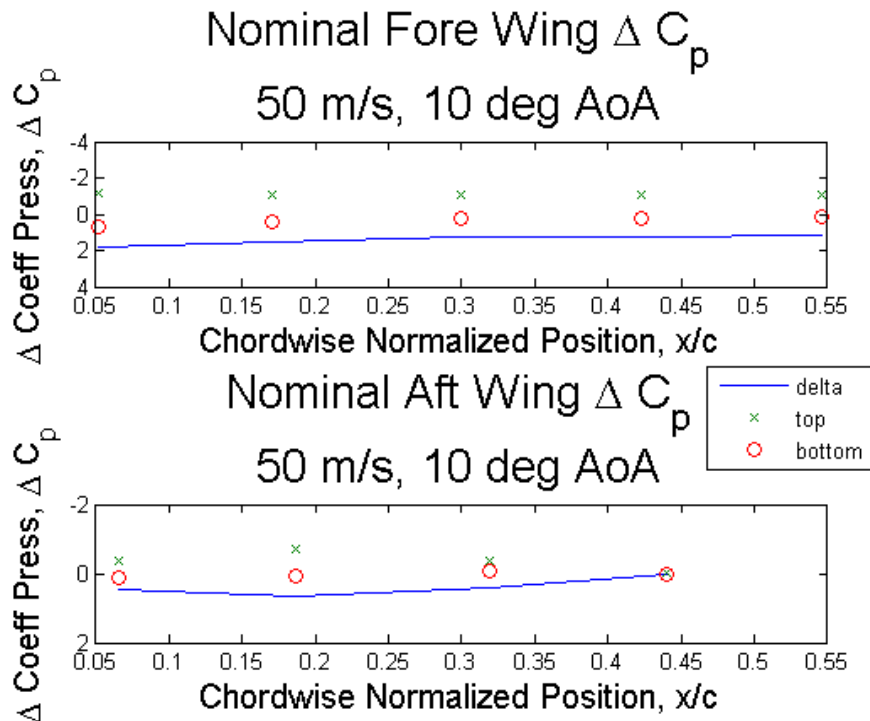
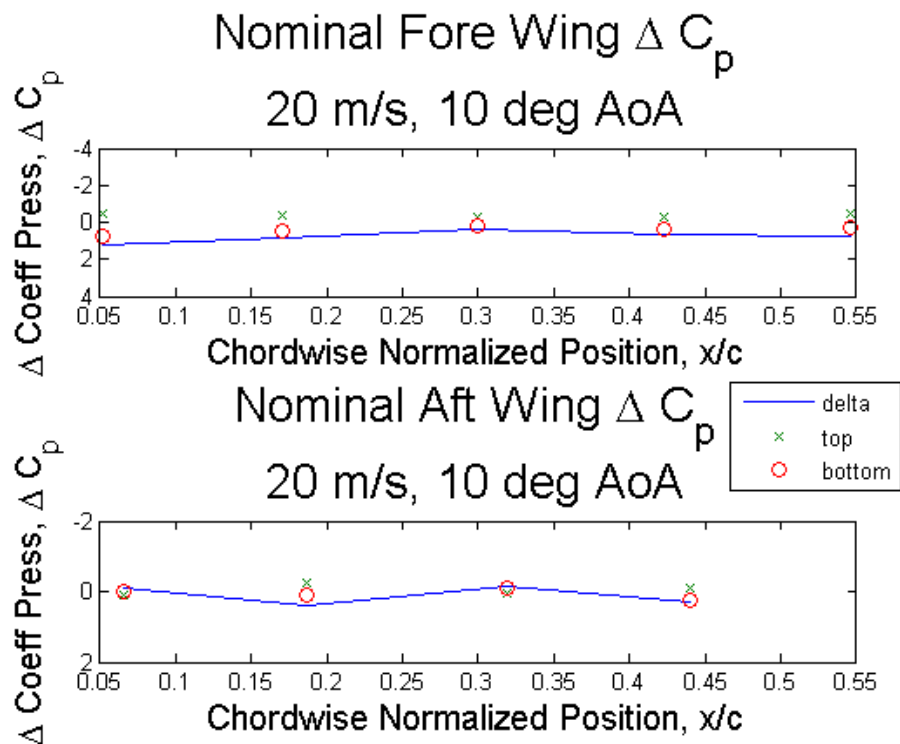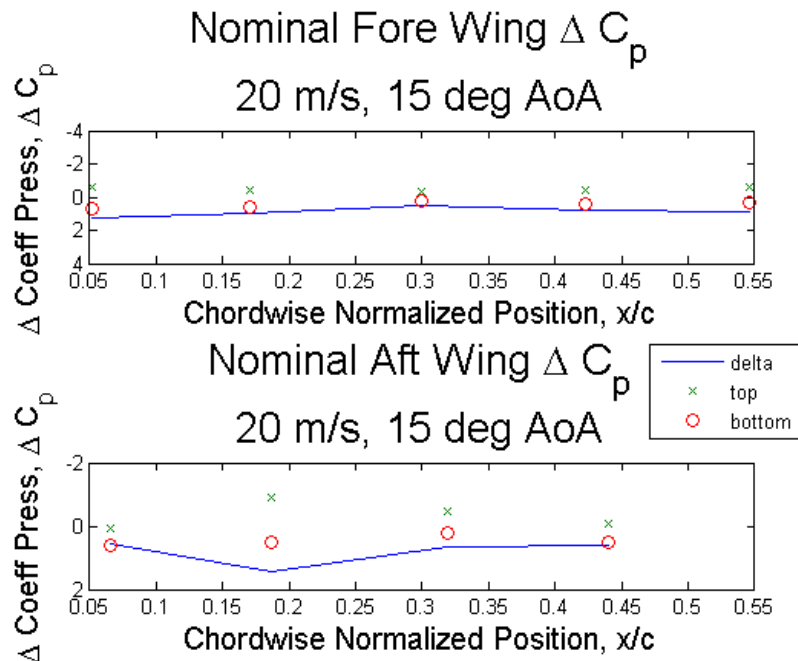**Figure C-47. Nominal Delta Coefficient of Pressure, 50 m/s, 10° AoA.**

189
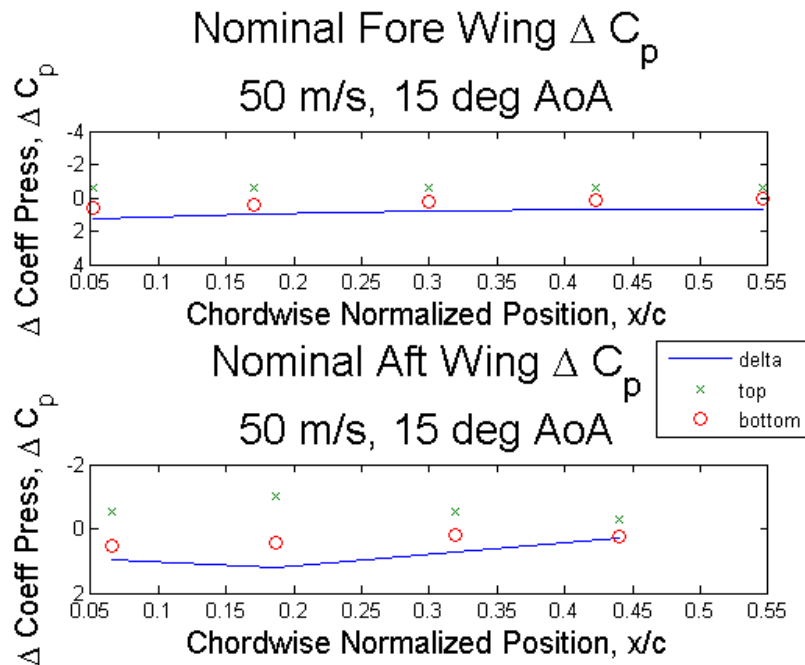
Figure C-48. Nominal Delta Coefficient of Pressure, 50 m/s, 15° AoA.
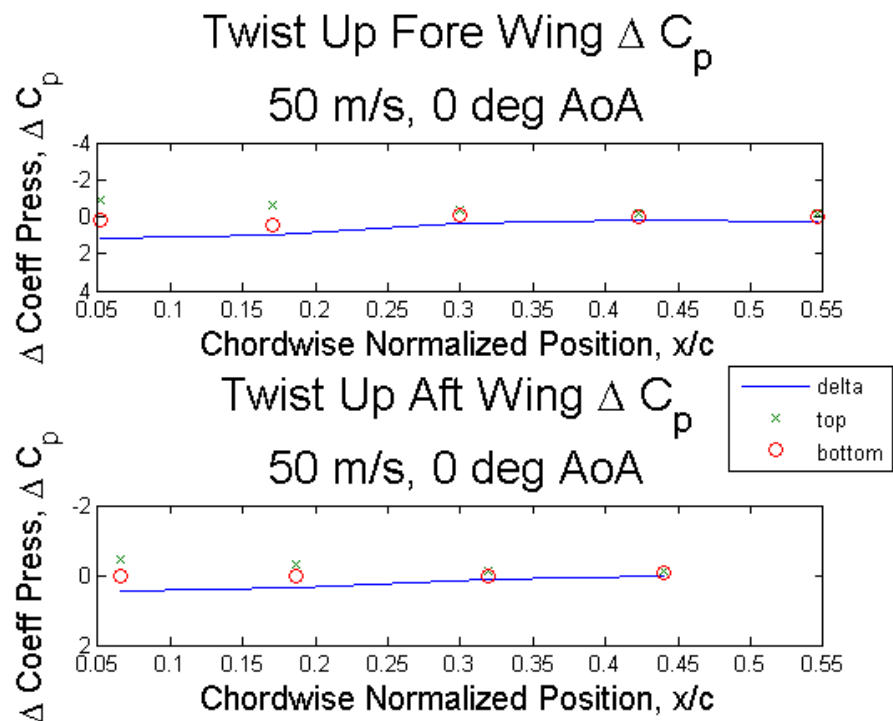
Figure C-49. Twist Up Delta Coefficient of Pressure, 50 m/s, 0° AoA.
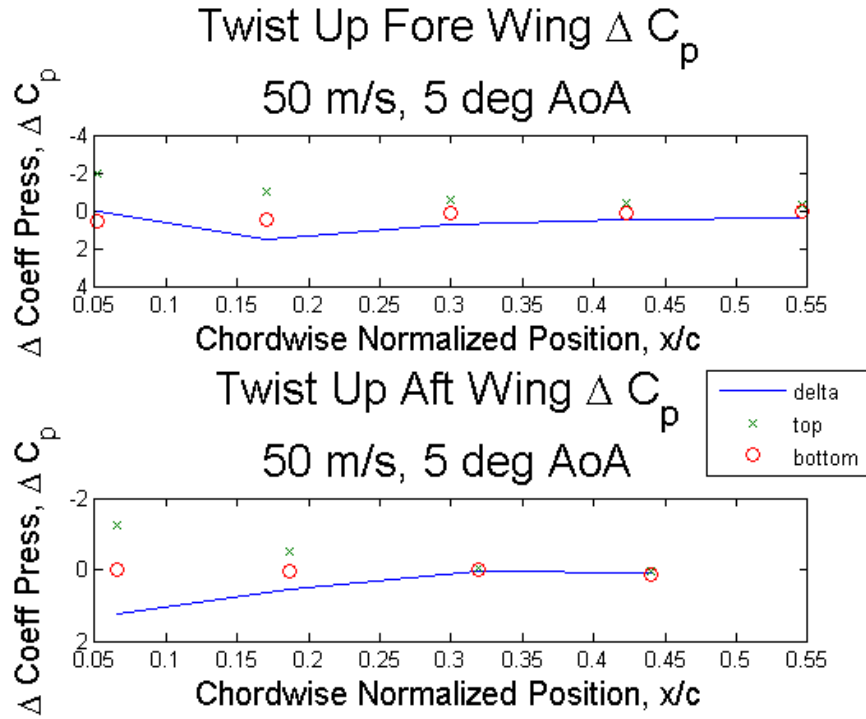
Figure C-50. Twist Up Delta Coefficient of Pressure, 50 m/s, 5° AoA.
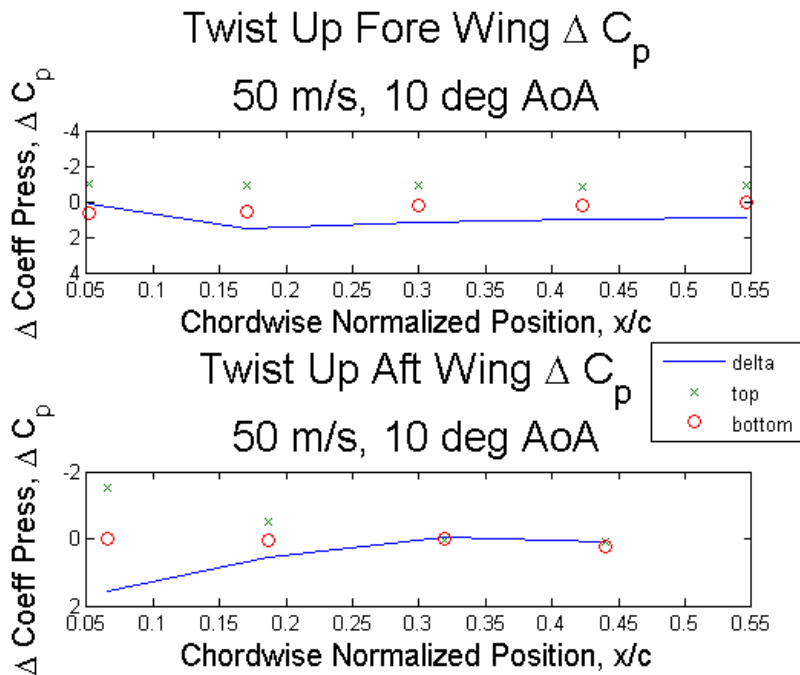
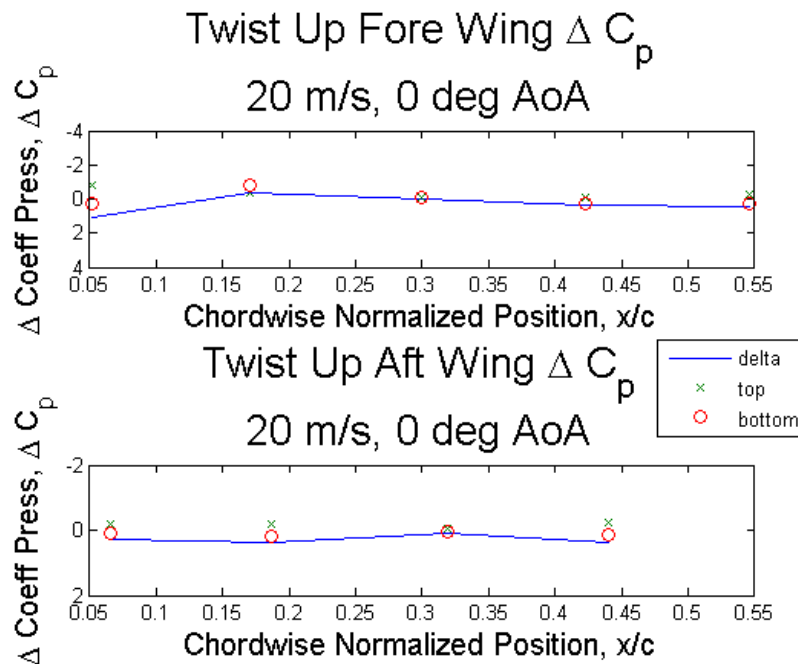**Figure C-51. Twist Up Delta Coefficient of Pressure, 50 m/s, 10° AoA.**
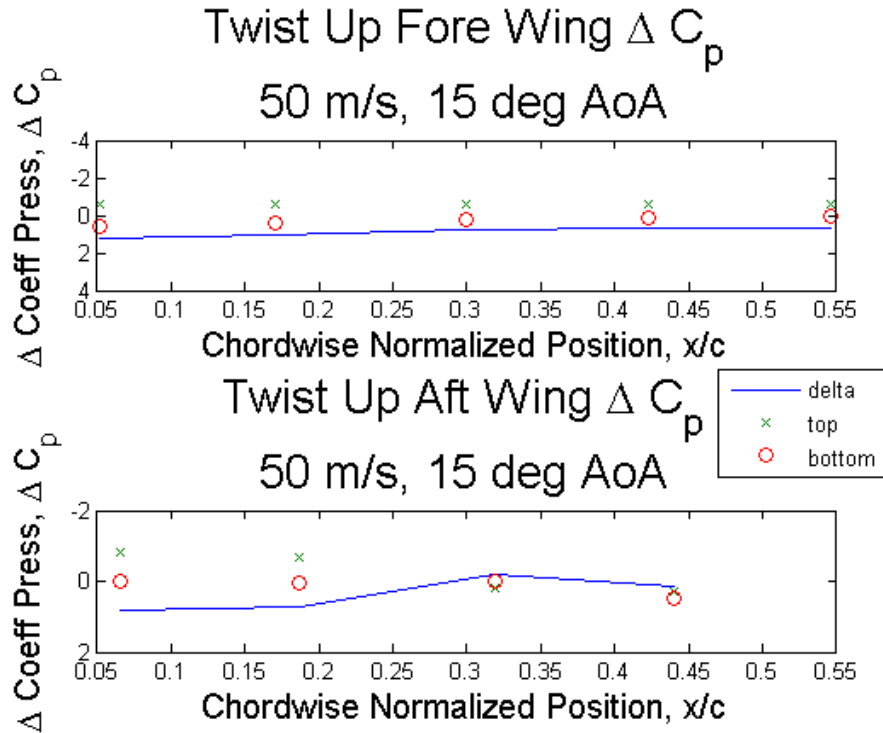
Figure C-52. Twist Up Delta Coefficient of Pressure, 50 m/s, 15° AoA.
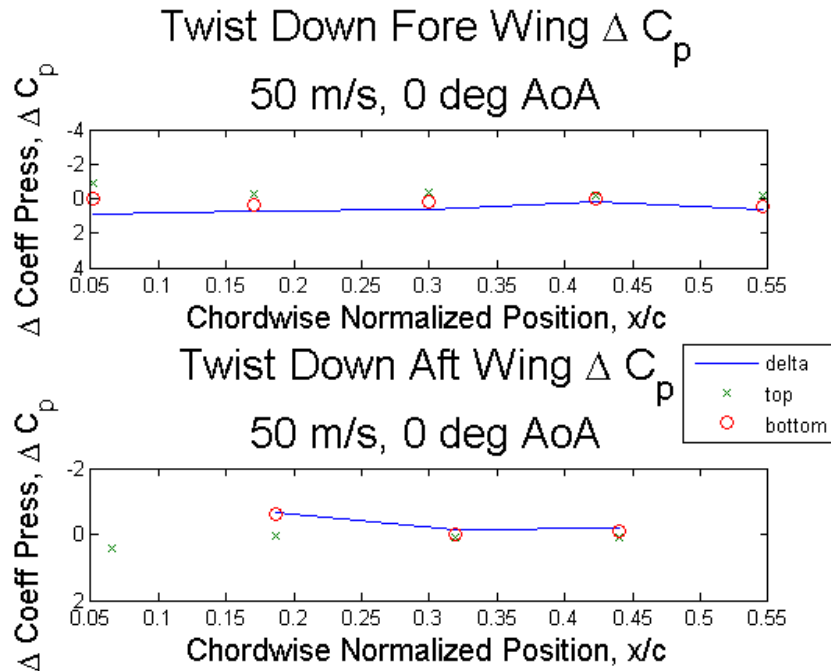
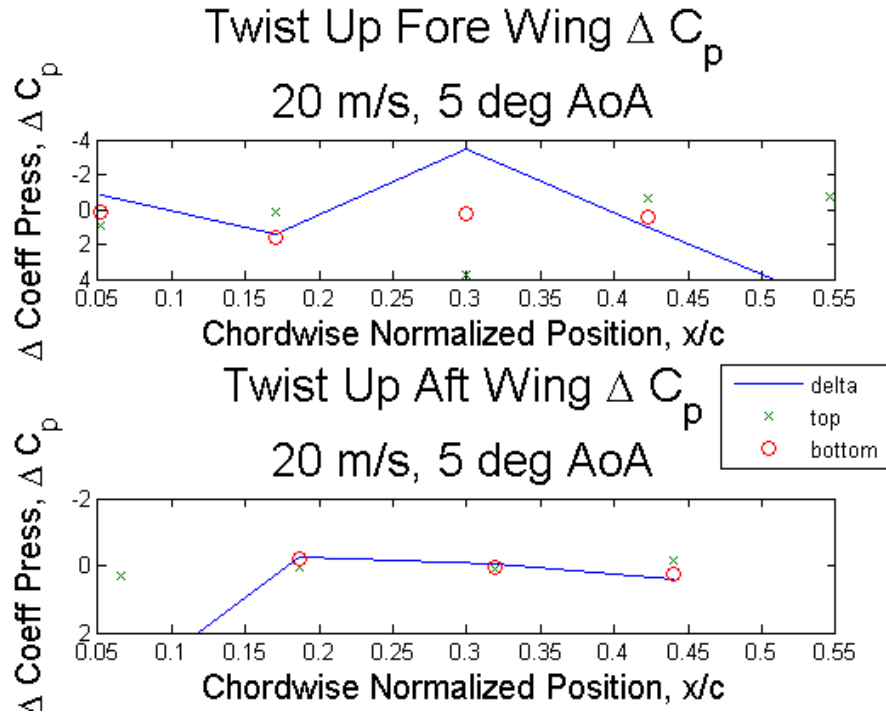**Figure C-53. Twist Down Delta Coefficient of Pressure, 50 m/s, 0° AoA.**
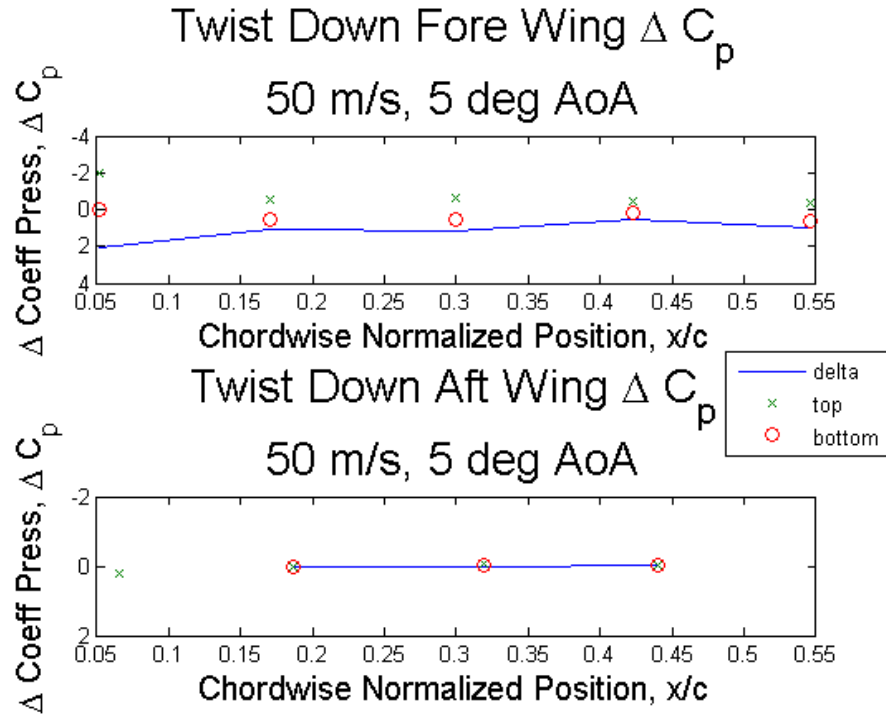
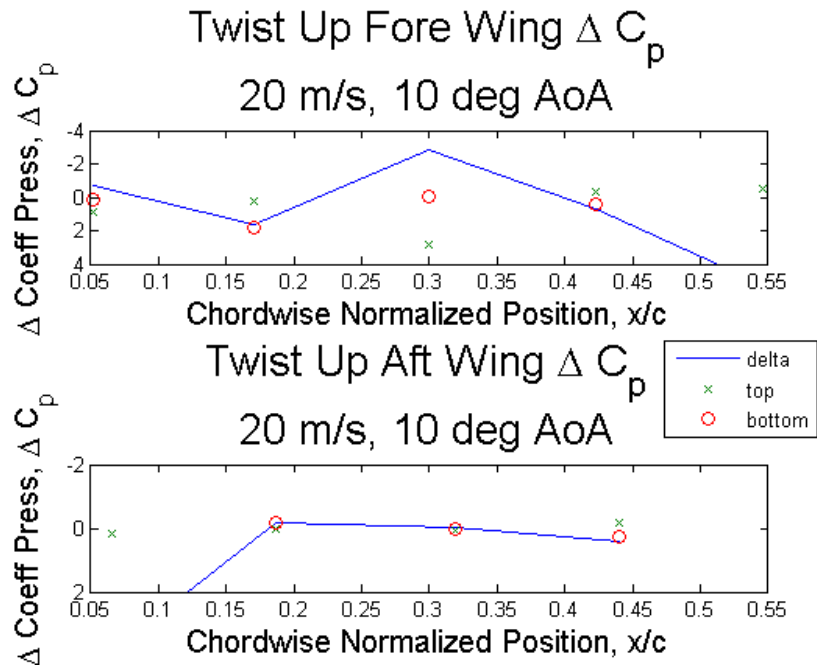**Figure C-54. Twist Down Delta Coefficient of Pressure, 50 m/s, 5° AoA.**
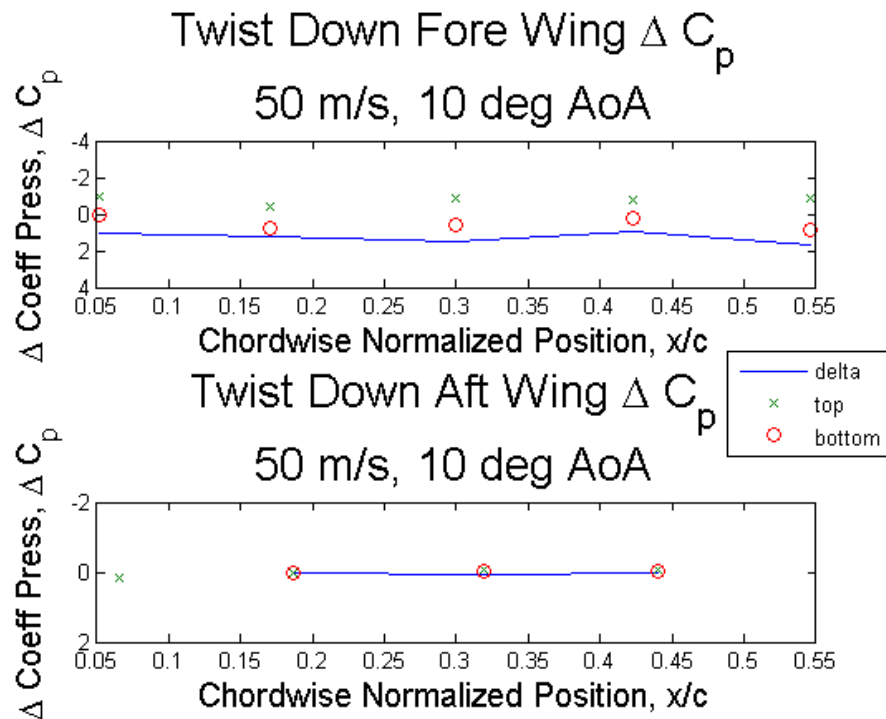
Figure C-55. Twist Down Delta Coefficient of Pressure, 50 m/s, 10° AoA.

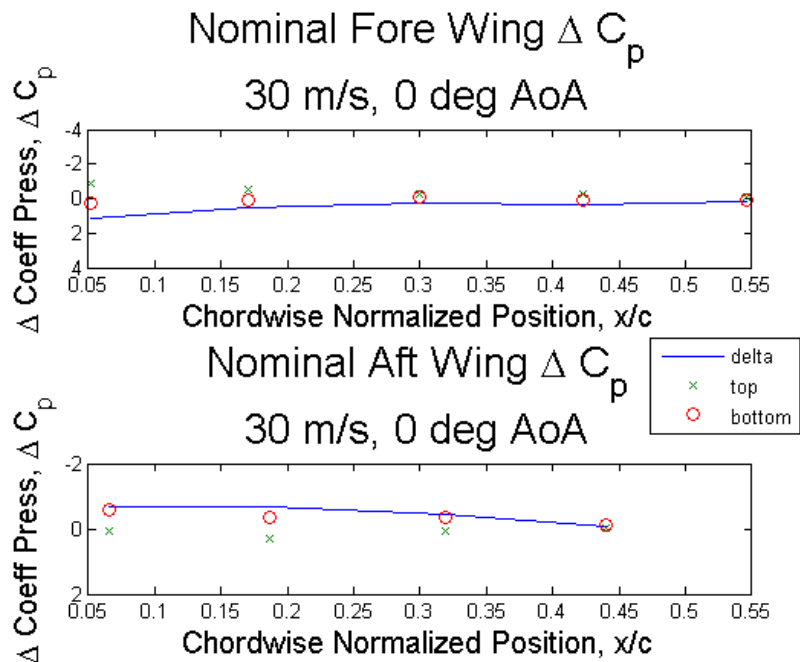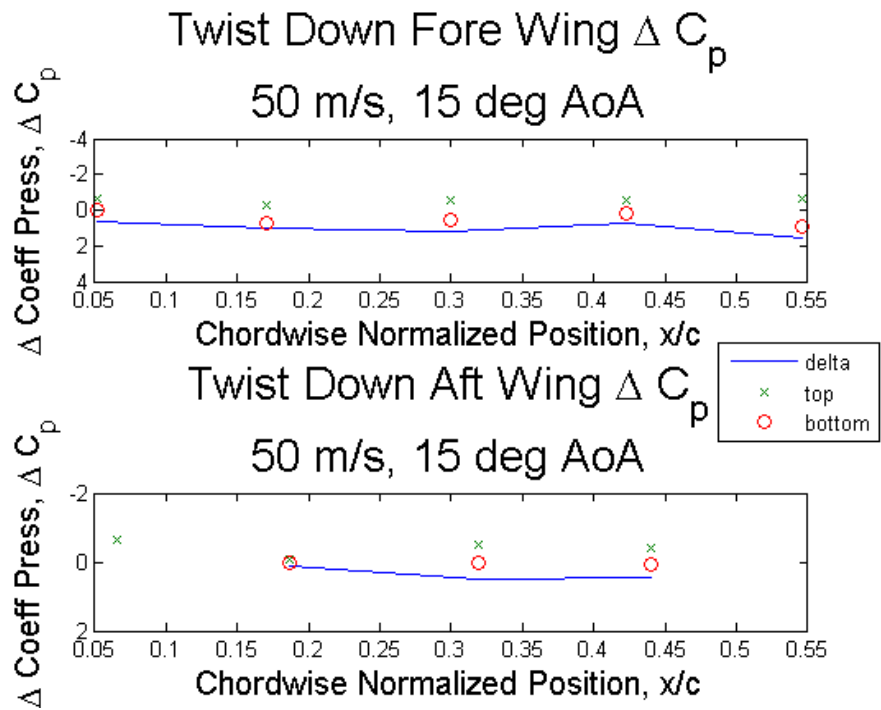**Figure C-56. Twist Down Delta Coefficient of Pressure, 50 m/s, 15° AoA.**

D. Appendix: Complete Experimental Nonlinear Static Response Test Results

The following provide additional data analyzed from the static nonlinear tests described in Chapter 6.

Table D-1. Measurement position change of outboard location

Approx % Total gust equivalent load	Incline (°)	spanwise (mm)	chordwise (mm)
0%	10	0	0
10%	13	5	4.5
20%	15	6	5
25%	15	8	6
30%	16	10	8
32%	17	14	9
34%	19	13	11
36%	19	17	13
38%	19	17	13
40%	20	18	14
42%	20	18	14
44%	20	20	16
46%	22	25	17
48%	23	29	19
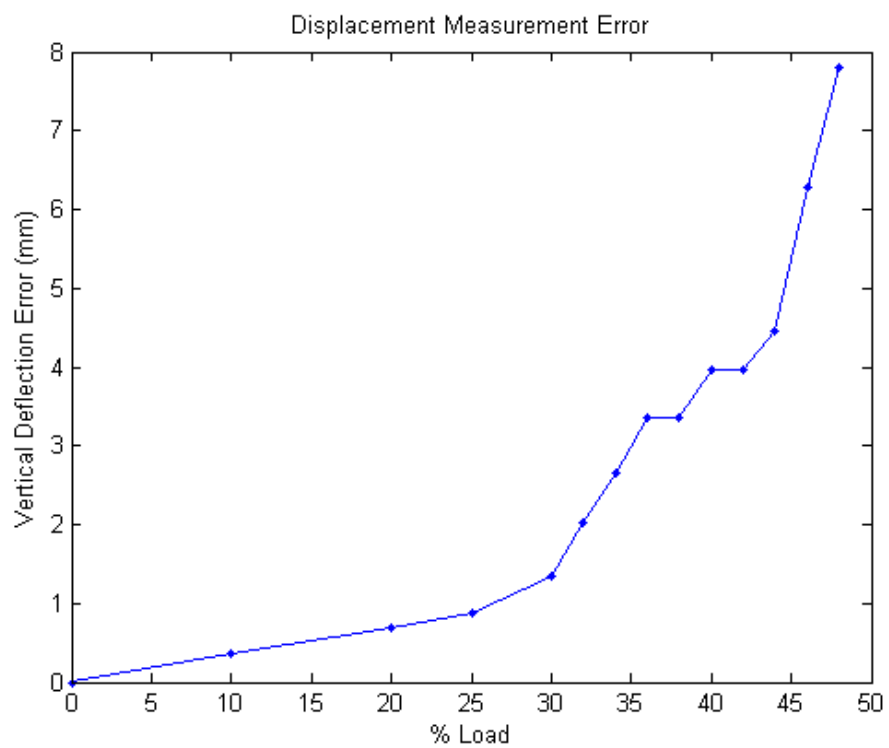
Figure D-1.   Displacement error verses applied load.

Table D-2. Experimental Percent Load and displacement

Approx % Total gust equivalent load	Displacement (mm)			Approx % Total gust equivalent load	Displacement (mm)		
	AW	OB	Joint		AW	OB	Joint
-3.18	-0.159	-0.58	-0.363	34	29.9621	95.55	72.801
-3.18	-0.159	-0.6	-0.368	34	29.9619	95.542	72.799
-3.18	-0.159	-0.615	-0.37	36	31.1854	102.729	77.7261
0	5.13	14.4945	10.799	36	31.1826	102.732	77.7159
0	5.13	14.4873	10.813	36	31.182	102.685	77.7005
0	5.129	14.4425	10.801	36	31.1351	102.543	77.7598
0	5.13	14.5011	10.816	36	31.1352	102.577	77.7667
0	5.129	14.472	10.798	36	31.1354	102.567	77.7722
5	8.247	25.0249	19.214	38	32.9199	107.694	82.037
5	8.246	25.0731	19.231	38	32.9194	107.683	82.0418
5	8.246	25.0801	19.233	38	32.9188	107.678	82.0587
10	12.651	35.9174	27.897	40	34.1294	113.543	86.0079
10	12.648	35.9022	27.886	40	34.1297	113.522	85.9947
10	12.649	35.9209	27.9	40	34.1297	113.532	85.9924
20	19.898	59.4194	45.388	42	35.4036	120.222	90.7186
20	19.898	59.4328	45.384	42	35.4049	120.225	90.7042
20	19.897	59.4506	45.41	42	35.4045	120.2	90.7256
25	23.6625	70.605	53.85	44	36.8377	128.303	96.5759
25	23.6625	70.5571	53.835	44	36.8377	128.309	96.5763
25	23.6623	70.5341	53.825	44	36.8377	128.282	96.5551
30	26.9674	83.7297	63.8	46	37.7113	139.236	104.31
30	26.961	83.7814	63.812	46	37.7006	139.265	104.334
32	28.5293	89.723	68.357	46	37.7014	139.263	104.36
32	28.529	89.743	68.345	48	38.748	150.121	111.923
32	28.5276	89.746	68.351	48	38.7483	150.103	111.913
34	29.9639	95.549	72.781				

Table D-3. Experimental μStrain for Each Location

Approx % Total gust equivalent load	Location 1 (rosette gage)			Location 2 (rosette gage)			Location 3 (rosette gage)			Location 4 (linear gage)	Location 5 (linear gage)	Location 6 (rosette gage)			Location 7 (rosette gage)		
	0	45	90	0	45	90	0	45	90	0	0	0	45	90	0	45	90
-3.18	1.8	2.6	0.7	1.5	2.5	1.4	2.7	3.1	1.2	0.9	0.6	2.6	3.6	0.9	2.1	2.2	1
-3.18	1.6	3.3	1.3	0.9	2.6	1.5	2.7	2.2	2.3	0.2	1.7	3.7	3.5	2.3	2	2.5	1.9
-3.18	2	3.7	2	1.2	2.1	1.7	3.2	2.6	2.5	-0.8	2	3.5	4.1	1.7	1.7	2.4	1.5
0	-36.8	-21.3	11.5	10.8	6.1	-1.1	-114.6	-64.1	26.9	-43.6	-185.9	-119.4	-85.4	28.7	-42.5	40.7	23
0	-35	-21.2	11	10.8	5.8	-0.3	-117.5	-64.7	26.5	-43.5	-185.8	-118.6	-85	28.2	-41.6	41.1	23.5
0	-36.1	-19.9	11.5	10.5	5.6	-0.2	-114	-63.9	27.2	-43.1	-184.8	-118.3	-84.3	29.3	-41.1	41.5	24.3
0	-36.2	-20.5	11	11.7	5.4	-0.7	-114	-64.6	26.6	-43.6	-185.3	-118.2	-85	28.6	-41.4	41.2	24.4
0	-36	-20.2	11.8	10	6.6	-0.3	-113.1	-63.8	27.4	-43.1	-185.8	-117.7	-84.9	27.7	-41.4	41	23.7
5	-62.7	-36.6	17.2	13.9	7.7	-1.1	-194.1	-110.7	36.9	-87.2	-319.4	-203.5	-148.4	44.8	-66.5	75	37.9
5	-62.6	-32.4	17.4	13.4	7.6	-0.8	-194	-110.3	37.3	-87	-319	-203.8	-148	45.5	-65.6	75.7	38.5
5	-63.3	-35.8	17.3	13.9	7.5	-1	-194.2	-110.7	37.6	-87	-319.4	-203.8	-148	44.7	-65.8	75	38.5
10	-90.7	-49.8	24.6	13.7	8.3	0	-278.5	-154.1	43.5	-146.6	-463.8	-292.7	-207.7	62	-80.3	116.4	49.6
10	-89.5	-49.7	25	13.9	9.9	-0.2	-277	-153.9	44	-146.3	-462.4	-293	-207.2	62.4	-79	116.5	50.5
10	-89.6	-49.1	25	13.7	10.5	0.7	-277.3	-153.6	44.7	-146.3	-462.2	-292.5	-207	62.9	-79.4	116.1	50.5
20	-142.4	-74.1	38.4	4.3	11.8	3	-434.6	-239.9	34.4	-288.3	-750.4	-477.2	-332.7	90.6	-114.7	208.8	78.2
20	-142.2	-73.2	38.6	4.3	12.3	3.6	-435	-240.1	35	-288.2	-749.7	-476.6	-331.7	91.6	-114.8	209.5	77.7
20	-141.9	-73.7	39.3	5.1	12	3.1	-434.1	-240.1	35.1	-288.9	-749.8	-477.7	-331.5	91.7	-113.5	208.9	77.9
25	-167.7	-84	45.3	-6.5	12.2	5.4	-514.5	-282.9	19.4	-379.3	-902.2	-577.9	-398.3	104.3	-128.2	263	90.5
25	-168	-84	44.8	-5.9	12.2	5.2	-514.1	-283.4	19.9	-378.9	-902.4	-578.2	-398.9	104	-128.4	263.6	90.7
25	-167.6	-83.6	45.3	-5.3	12.9	5.9	-514.3	-282.6	19.7	-379	-902	-577.5	-399.1	105.3	-128.5	263.2	91.2
30	-192.4	-93.4	50.9	-19.8	11.7	8.5	-593.3	-325.9	-0.1	-476.2	-1053.4	-681.7	-465.4	117.5	-140	323.2	103.5

Approx % Total gust equivalent load	Location 1 (rosette gage)			Location 2 (rosette gage)			Location 3 (rosette gage)			Location 4 (linear gage)	Location 5 (linear gage)	Location 6 (rosette gage)			Location 7 (rosette gage)		
	0	45	90	0	45	90	0	45	90	0	0	0	45	90	0	45	90
30	-192.6	-91.9	50.6	-20.6	11.5	9.2	-593.3	-325.5	0	-476.2	-1053	-681.6	-466	117.5	-140.1	322.5	103.8
32	-201.1	-95.4	53.3	-26.7	12.3	10.9	-628.1	-342.7	-9	-522.4	-1117.9	-728.6	-494.6	124.1	-144.5	349.1	112
32	-201.4	-95	53.9	-26.2	11.6	10.4	-627.6	-342.9	-8.9	-521.6	-1118.4	-728	-494.2	124.3	-144.1	349.5	111.3
32	-201.7	-94.4	54.2	-27.1	11.8	10	-627.2	-342.8	-8.5	-521.1	-1118.2	-727.9	-494	124.3	-144.1	350	111.3
34	-211.5	-97.3	56.5	-34.6	11	13.5	-662.2	-360.7	-20.4	-570.5	-1186	-776.7	-523.8	130.7	-143.5	380	115.9
34	-212	-97.3	56.3	-34	11.8	13.4	-661.2	-360.1	-19.6	-569.4	-1185.2	-775.7	-523.8	130.5	-143.3	380.3	115.4
34	-211.6	-97	57.2	-33.8	10.5	13.6	-661.9	-359.8	-19.9	-569.9	-1186.2	-776.2	-522.9	130.1	-143.4	380	116.3
36	-219	-98.4	59.8	-42.1	11.1	16.7	-697.1	-378	-28.4	-617.2	-1250.4	-825.6	-554.4	138.5	-151.6	409.9	125.9
36	-218.7	-97.4	59.9	-41.8	11.9	16	-697.1	-377.7	-28.6	-616.4	-1250.3	-826.3	-553.7	138.8	-150.6	409.7	126.5
36	-218.8	-98.4	60.6	-41.1	11.7	16.5	-697.5	-377.3	-28.5	-615.6	-1249.6	-825.7	-553.8	139.8	-149.9	410.2	125.3
36	-221.4	-99.3	58.7	-43.3	9.6	14.6	-698.2	-379	-30.4	-618.4	-1251.1	-827.6	-555.5	137.1	-151.7	410.2	124.4
36	-219.9	-99.7	58.5	-43.3	9.9	15.2	-697.9	-379	-30.9	-617.7	-1250.4	-826.6	-554.5	137.1	-151.1	409.8	124.9
36	-219.9	-99.5	58.9	-42.2	9.5	15.7	-699.3	-379.1	-29.5	-617.7	-1251.3	-827.2	-555.5	138.1	-152.6	411.7	125.7
38	-230.2	-101.8	61.6	-52.8	9.3	17.8	-735.1	-395.7	-43.2	-671.4	-1321.1	-879.6	-584.2	144.9	-151.1	440.7	129.2
38	-230.8	-100.7	62.1	-52.7	10	18.5	-734.4	-396.7	-43.8	-671.6	-1321.2	-878.7	-585.3	145.1	-151.5	441.1	130.1
38	-231	-101.2	62	-53.7	9.5	17.9	-734.3	-396.1	-43.6	-671.9	-1321.2	-878.6	-584.4	144.2	-151.5	441.2	130
40	-239.1	-101.8	63.2	-61.7	8.6	20.4	-766.9	-410.3	-56.3	-720.6	-1382.3	-926.3	-612.5	151.1	-154	467.6	135.1
40	-239	-101.6	64.5	-61.2	9	20.3	-765.8	-409.7	-56	-720.5	-1381.6	-925.7	-611.6	151.4	-154	467.4	134.9
40	-237.9	-101.6	64.2	-61.1	9.4	20.1	-765.1	-410.1	-55.8	-720.1	-1381	-926.1	-611	151.4	-153.8	465.6	135.2
42	-247.3	-103.1	67.4	-72.1	7.3	23.1	-803.6	-428.4	-68.9	-776.9	-1450.5	-981.6	-643.4	158.7	-156	497.2	141.4
42	-247.7	-102.7	66.8	-71.8	7.4	24.5	-803.3	-428	-68.2	-776.3	-1451.4	-981.4	-644	160.2	-155.9	498.4	141.4
Approx	Location 1			Location 2			Location 3		Location	Location		Location 6			Location 7		

% Total gust equivalent load	(rosette gage)			(rosette gage)			(rosette gage)			4 (linear gage)	5 (linear gage)	(rosette gage)			(rosette gage)		
	0	45	90	0	45	90	0	45	90	0	0	0	45	90	0	45	90
42	-247.5	-102	67.4	-71.8	8.4	23.1	-803.5	-427.1	-68.8	-776.1	-1450.6	-980.7	-643.7	159.4	-155.5	498.3	141.8
44	-256.3	-101.7	71.1	-85.2	8.3	28	-844.8	-443.7	-89.3	-845.6	-1529.8	-1048.5	-678.7	169.9	-155.9	537	149.4
44	-255.1	-101.2	71.2	-85.4	7.6	28.1	-843.9	-444.2	-89.1	-845.7	-1530.1	-1048.7	-679	167.6	-154.9	537.7	149
44	-255.7	-101.2	70.5	-84.8	8	29.1	-843.5	-444.4	-88.7	-845.2	-1530.5	-1048.2	-678.4	170.2	-155.4	538.6	149.8
46	-265.9	-100.3	75.3	-99.2	7.2	34.3	-896	-467.7	-106.8	-925.2	-1623.2	-1129.7	-724.2	183.8	-159.9	586.1	161.3
46	-265.3	-99.2	75.4	-100	7.8	34.4	-895.2	-466.9	-107.7	-925.1	-1622.7	-1129.5	-724.8	184.4	-159	585.5	161.9
46	-264.5	-99.8	76.1	-100.5	7.4	34.8	-895.5	-466.8	-107.2	-925.8	-1622.3	-1130	-724.7	184.1	-159.6	586.3	160.6
48	-274	-97.5	79.9	-117.9	7.1	40.2	-949	-487.3	-128.2	-1013.2	-1717.6	-1214.4	-768.5	199	-152.8	641.3	172.5
48	-274.5	-97.3	78	-117.9	7	41.1	-947.8	-487.5	-128.5	-1012.3	-1718.1	-1213.4	-767.9	200	-152.6	641.4	172

200

Approx % Total gust equivalent load	Location 8 (rosette gage)			Location 9 (rosette gage)			Location 10 (rosette gage)			Location 11 (rosette gage)			Location 12 (linear gage)	Location 13 (linear gage)	Location 14 (rosette gage)		
	0	45	90	0	45	90	0	45	90	0	45	90	0	0	0	45	90
-3.18	1.9	1.2	1.3	3.1	2.8	2.2	3	3.9	2.2	2.3	2.5	1.3	1.7	2.8	2.2	3.1	2.8
-3.18	2	2.4	1.6	3.6	3.1	2.3	3.2	4.3	3.6	2.9	3	2.3	2	2.7	2.5	3.7	3.3
-3.18	1.7	2.7	2	2.2	3.6	2.7	2.3	4.3	3	3.9	3	1.7	2.5	2.2	2.6	3.9	2.6
0	-153.6	-151.3	50.6	5.9	55.2	7.8	4.6	-38.3	-6.3	6.8	-14.6	-21.9	-92.4	206.8	-83.8	-36.1	-3
0	-154	-150.8	51.2	7.1	55.6	7.9	5.4	-38.8	-4.9	6.8	-14.2	-21.2	-91.8	208.2	-84.1	-35.5	-2.9
0	-152.9	-150.8	51.4	6.9	56.5	7.7	5	-38.3	-5.4	7.8	-13.4	-21.4	-92.5	207	-83.5	-35.5	-2.7
0	-153.3	-150.5	52.3	7.6	56.7	8	6	-38.5	-5.6	6.9	-13.4	-20.9	-91.2	207.5	-83.3	-35.2	-2.9
0	-153.2	-151.2	51.2	7.8	56.1	7.7	6.1	-38.1	-5.3	6.7	-13.3	-20.6	-91.7	208.3	-83.2	-35.5	-2.2
5	-251.9	-247.3	84.5	9.9	98.5	15.3	5.7	-68.4	-8.7	10.5	-25.2	-42.3	-147.4	343.5	-126.1	-55.2	-9.2
5	-251.1	-247	86.5	10	98.8	14.6	5.5	-68.6	-8.5	11.7	-24.9	-42.2	-147.3	343.5	-125.9	-55.2	-9.1
5	-250.4	-247.5	84.9	10.7	97.9	14.9	5.8	-68.7	-8.8	11	-25.5	-41.8	-147.5	344.5	-126.2	-56	-9.2
10	-344.1	-338.3	117.6	19	143.6	16.8	7.1	-98	-14.6	14	-44.1	-49	-232.6	509.1	-186.6	-79.7	-15.2
10	-344.6	-337.2	118.7	19.8	143.7	17.1	8.2	-97.4	-14.1	14.5	-43.5	-48.7	-231.3	509.8	-186.2	-78.5	-15.1
10	-344.2	-338.4	118.4	20.2	143.1	16.2	7.9	-97.5	-14.6	13.8	-43.5	-48.7	-231.3	509.5	-186.5	-78.6	-14.6
20	-544.8	-535.2	189.4	33.4	245.3	30.2	5.4	-159.2	-19.6	20.3	-79.3	-75.5	-369.8	810.9	-253.4	-104.2	-38.4
20	-546	-534.9	190.7	33.4	245.1	30.2	6.4	-158.9	-18.7	20.3	-78.6	-75.1	-369.5	810.9	-253.8	-104.9	-39
20	-545.4	-534.3	190.8	32.7	245.7	30	6.9	-159.2	-19.3	21	-79.7	-74.5	-368.9	810.9	-253.9	-103.8	-38.7
25	-648.8	-638.3	227.7	39.7	303.3	40.5	3.6	-191.5	-18.9	22.7	-100.3	-88.4	-433	959	-269.1	-109.3	-57.9
25	-648.3	-637.4	228.4	39.5	302.6	41	3.4	-191.6	-19.5	23	-100.9	-89	-432.2	959.5	-269.3	-107.6	-58.3
25	-648.5	-638	228.3	40	303	40.1	4.5	-191.1	-19.1	23.3	-100	-88.6	-432.9	959.6	-268.6	-108.8	-57.6
30	-747	-735	264.6	44.3	362.5	53.2	-0.2	-222	-16.4	25.3	-120.6	-105.4	-479.9	1089.2	-262.4	-105.2	-81.3

Approx % Total gust equivalent load	Location 8 (rosette gage)			Location 9 (rosette gage)			Location 10 (rosette gage)			Location 11 (rosette gage)			Location 12 (linear gage)	Location 13 (linear gage)	Location 14 (rosette gage)		
	0	45	90	0	45	90	0	45	90	0	45	90	0	0	0	45	90
30	-746.9	-735.1	265.1	44.8	362.4	53.3	-0.2	-221.4	-15.3	25.6	-119.8	-105.7	-479.2	1089.2	-261.9	-103.9	-80.9
32	-789.4	-777.3	281.5	47	388.5	58.5	-2	-233.5	-14.6	27.7	-128	-108.5	-500.1	1145.8	-256.6	-100.1	-92.1
32	-789.6	-777.3	281.9	46.7	389.1	57.8	-2.3	-233.3	-13.5	26.9	-128.4	-108.9	-499	1146	-257.3	-99.7	-91.6
32	-789.9	-776.6	282.6	46.9	389.1	57.8	-1.9	-233.5	-13.1	27.8	-130	-109	-499.1	1146	-256.8	-99.6	-91.9
34	-824.3	-811.4	296.6	48.3	414	63.6	-4.4	-243.5	-9.5	28.3	-137.8	-114.9	-512.8	1195.3	-245.1	-93.2	-104.5
34	-824.2	-811	296.5	48.2	414.4	64.5	-4.3	-242.6	-10	28.6	-136.6	-114	-513.3	1194.8	-244.8	-93.2	-103.8
34	-824.2	-811.3	296.7	48.6	415.1	63.7	-4.5	-243.2	-9.3	29.4	-136.4	-114.2	-513	1195	-245.3	-93.6	-103.4
36	-871.1	-858.1	315.9	50	443.8	71.4	-5.9	-254.7	-5.1	31.9	-144	-122.5	-518.6	1235	-223.6	-84.7	-118
36	-871.6	-858.2	316.2	50.1	443.6	72.1	-6.3	-253.6	-3.8	31.6	-145.1	-122.1	-518.2	1233.4	-223.3	-84.4	-117.1
36	-870.9	-857.7	316.5	49.7	444.1	71.9	-5.6	-253.2	-3.4	32.4	-143.5	-121.7	-517.1	1234.7	-223.1	-84	-118
36	-872.5	-860.2	314.8	46.3	439.9	69.3	-7.8	-255.8	-5.5	30	-146.7	-123.7	-517.7	1231.2	-225	-85.6	-118.5
36	-873.7	-861.1	314.6	46.4	440.2	69.2	-7.4	-254.8	-5.9	29.6	-145.6	-122.9	-518.2	1231.2	-224.1	-85.3	-119.4
36	-872.2	-860.8	316.1	46.4	440.3	68.9	-7.3	-255.6	-5.7	30.6	-145.7	-123.2	-518.3	1231.8	-224	-85.2	-118.8
38	-911.6	-899.3	330.3	50.3	468.8	75.5	-9.1	-266	-2.6	31.2	-156.4	-123.1	-535.1	1284.9	-210	-75.3	-132.1
38	-912	-899.2	331.3	50.9	469.3	76	-9.3	-265.6	-1.9	31	-155.7	-122.4	-535.1	1285.1	-209.1	-74.9	-132.6
38	-911.7	-899.1	330.9	50.5	469.8	77	-8.2	-264.1	-1.6	31.4	-155.8	-122.2	-535.1	1285.3	-208.8	-75	-132.7
40	-948.1	-934.2	344.2	51.6	493.6	83.5	-11.4	-274	2.5	31.9	-163.7	-126.6	-540.1	1316.2	-186.9	-65.8	-146.8
40	-947.1	-934.2	344.7	51.7	494.2	84	-11.8	-272.7	2.2	32.3	-164.2	-126.3	-539.7	1316.1	-185.7	-65.4	-146.6
40	-948.1	-934.2	345.5	51.9	494.6	84.2	-11.1	-271.9	3.5	32.7	-164	-125.5	-540	1316.7	-185.9	-65.3	-146.3
42	-985.5	-971.5	361.3	53.1	522.9	93.2	-14.7	-280.4	11.3	34.3	-172.5	-132.4	-536.9	1340	-151.1	-51.8	-165
42	-985.1	-971.3	360.5	52.8	523	94	-13.6	-280.2	11.6	34.1	-171.7	-132.4	-536.7	1340.2	-150.4	-52.1	-164.6
42	-984.6	-971	360.7	52.8	522.2	94.1	-14.7	-279.5	11.6	33.6	-172.1	-131.9	-535.6	1339.8	-150	-52.1	-164

Approx % Total gust equivalent load	Location 8 (rosette gage)			Location 9 (rosette gage			Location 10 (rosette gage)			Location 11 (rosette gage)			Location 12 (linear gage)	Location 13 (linear gage)	Location 14 (rosette gage)		
	0	45	90	0	45	90	0	45	90	0	45	90	0	0	0	45	90
44	-1032	-1019.3	379.9	52.3	556.2	106.9	-19.9	-284.8	25.2	34.8	-179.2	-135.9	-523.7	1362.5	-100.8	-30.7	-184.2
44	-1031.2	-1019.4	380.5	52.8	556.4	107.6	-18.7	-284.9	26.7	35.3	-179.2	-135.2	-523.5	1362.4	-100.8	-30.7	-184
44	-1032.2	-1019.2	381.3	51.9	555.9	108.3	-19.2	-284.8	25.8	35.9	-180.1	-135.3	-523.5	1362.6	-100.2	-29.4	-183.4
46	-1081.9	-1068.5	404	50.3	598.9	127.7	-26.4	-290.4	45.5	36.8	-184.5	-150.7	-479.2	1351.5	-25	-2.4	-211.4
46	-1080.6	-1067.3	404.6	50	598.4	127.4	-26.1	-289.7	45.6	38.2	-184	-150.1	-478.1	1351.8	-24.9	-2.3	-210.9
46	-1080.8	-1067.7	404.3	50.4	598.9	127.3	-25.5	-289.7	46.1	37.8	-183.4	-149.8	-478.7	1352	-24.8	-2.1	-210.8
48	-1116.1	-1105.5	423.2	45.6	636.7	148	-32	-290.5	68.9	38.3	-184.7	-159.8	-432.4	1331.3	49.9	25.4	-241.1
48	-1115.5	-1104.5	424.1	45.6	636.9	147.6	-32.7	-290.4	70.1	38.2	-185.1	-159.5	-432.9	1331.5	50.3	26.4	-241.1

E. Appendix: Calculations and Data used in Scaling

Equations for determining mass in the leading and trailing edge and the centerline for the uncoupled Goland[±]:

$$J_m = 38.86 = \left(\tfrac{h}{2}\right)^2 m_{cl} + \left(\left(\tfrac{h}{2}\right)^2 + \left(\tfrac{b}{2}\right)^2\right)\left(m_{LE} + m_{TE}\right)$$

$$\sum m = 14.92 = m_{cl} + m_{LE} + m_{TE} \tag{E.1}$$

$$\Rightarrow m_{cl} = 5.3086 \text{ and } m_{LE} = m_{TE} = 9.6114$$

$$I_{ea} = J_m = 38.94 = \left(\tfrac{h}{2}\right)^2 m_{cl} + \left(\left(\tfrac{h}{2}\right)^2 + \left(\tfrac{b}{2}\right)^2\right)\left(m_{LE} + m_{TE}\right)$$

$$\sum m = 14.92 = m_{cl} + m_{LE} + m_{TE}$$

$$I_{cg} = 33.57 \tag{E.2}$$

$$= \left(\left(\tfrac{h}{2}\right)^2 + \left(x_{ea} - x_{cg}\right)^2\right)m_{cl} + \left(\left(\tfrac{h}{2}\right)^2 + \left(x_{cg} - x_{LE}\right)^2\right)\left(m_{LE}\right) + \left(\left(\tfrac{h}{2}\right)^2 + \left(x_{TE} - x_{cg}\right)^2\right)\left(m_{TE}\right)$$

$$\Rightarrow m_{cl} = 5.2886 \, , \ m_{LE} = 2.5779 \text{ and } m_{TE} = 7.0534$$

Table E-1. Goland Strut wingbox properties after buckling and vibration optimization.

title	area (ft^2)	thickness (ft)
fore wing posts	0.0008	
fore wing front top spar cap	0.038408	
fore wing mid top spar cap	0.167923	
fore wing rear top spar cap	0.038408	
aft wing spar caps	0.008931	
fore wing front bottom spar cap	0.038408	
fore wing mid bottom spar cap	0.167923	
fore wing rear bottom spar cap	0.038408	
fore wing rib top spar cap	0.0422	
fore wing rib bottom spar cap	0.0422	
top skins		0.020603
bottom skins		0.020603
aft wing skins		0.002002
fore wing front spar		0.000391
fore wing mid spar		0.090325
fore wing rear spar		0.000391
aft wing spars		0.021811
rib shear property		0.041644

REPORT DOCUMENTATION PAGE

1. REPORT DATE (DD-MM-YYYY)	2. REPORT TYPE	3. DATES COVERED (From - To)
30-09-2008	PhD Dissertation	Dec 06 - Sep 08

4. TITLE AND SUBTITLE
FLEXIBLE TWIST FOR PITCH CONTROL IN A HIGH ALTITUDE LONG ENDURANCE AIRCRAFT WITH NONLINEAR RESPONSE

5a. CONTRACT NUMBER

5b. GRANT NUMBER

5c. PROGRAM ELEMENT NUMBER

6. AUTHOR(S)
Bond, Vanessa L.

5d. PROJECT NUMBER

5e. TASK NUMBER

5f. WORK UNIT NUMBER

7. PERFORMING ORGANIZATION NAME(S) AND ADDRESS(ES)
Air Force Institute of Technology
2950 Hobson Way
Wright Patterson, OH 45433-7765

8. PERFORMING ORGANIZATION REPORT NUMBER
AFIT/DS/ENY/08-D11

9. SPONSORING/MONITORING AGENCY NAME(S) AND ADDRESS(ES)
Air Force Research Laboratory/Vehicles Directorate
Attn: Dr. Maxwell Blair
2210 8th St.
B146 R220
Wright Patterson, OH 45433   DSN: 785-8430 email: maxwell.blair@wpafb.af.mil

10. SPONSOR/MONITOR'S ACRONYM(S)
AFRL/RB

11. SPONSOR/MONITOR'S REPORT NUMBER(S)

12. DISTRIBUTION/AVAILABILITY STATEMENT
APPROVED FOR PUBLIC RELEASE; DISTRIBUTION UNLIMITED.

13. SUPPLEMENTARY NOTES

14. ABSTRACT
The goal was to demonstrate that scaling the nonlinear response of a full-scale finite element model of a high-altitude long-endurance (HALE) aircraft was possible if the model was aeroelastically and "nonlinearly" scaled. A straight-forward method of scaling the first three natural vibration frequencies and mode shapes, and the first buckling eigenvalue was attempted. In addition to analytical scaling several experiments were accomplished to understand and overcome design challenges of HALE aircraft. One such challenge is combated by eliminating pitch control surfaces and replacing them with an aft-wing twist concept. This design was physically realized through wind tunnel measurement of forces, moments and pressures on a subscale experimental model proving that pitch control with aft-wing twist is feasible. Another challenge is predicting the nonlinear response of long-endurance aircraft. This was addressed by experimental validation of modeling nonlinear response on a subscale experimental model. The validation accomplished during this experiment on a subscale model will reduce technical risk for full-scale development of such pioneering craft. Nonlinearities can be attributed to follower forces, which were found to be a significant influence in HALE aircraft.

15. SUBJECT TERMS
Aeroelastic, high-altitude long-endurance (HALE) aircraft, Joined-Wing, Sensorcraft, Nonlinear, Scaling, Buckling, Vibration, Pitch Control, Follower forces

16. SECURITY CLASSIFICATION OF:

a. REPORT	b. ABSTRACT	c. THIS PAGE	17. LIMITATION OF ABSTRACT	18. NUMBER OF PAGES	19a. NAME OF RESPONSIBLE PERSON
U	U	U	UU	233	Robert A. Canfield

19b. TELEPHONE NUMBER (Include area code)
937-255-3636 x4723 robert.canfield@afit.edu

Reset

Standard Form 298 (Rev. 8/98)
Prescribed by ANSI Std. Z39.18
Adobe Professional 7.0